Modeling and Control of Voltage-Controlling Converters for Enhanced Operation of Multi-Source Power Systems

Igor Cvetkovic

Dissertation submitted to the faculty of the Virginia Polytechnic Institute and State University in partial fulfillment of the requirements for the degree of

Doctor of Philosophy

In

Electrical Engineering

Dushan Boroyevich, Chair

Rolando Burgos

Paolo Mattavelli

Jaime De La Reelopez

John J. Lesko

Slobodan Vukosavić

August 30, 2017

Blacksburg, Virginia

Keywords: Terminal-behavioral model, small signal model, small-signal stability, inward and outward immittances, voltage-controlling converter, virtual synchronous machine, electronic machine, frequency-locked loop

Modeling and Control of Voltage-Controlling Converters for Enhanced Operation of Multi-Source Power Systems

Igor Cvetkovic

ABSTRACT

The unconventional improvements in the power electronics field have been the primary reason for massive deployment of renewable energy sources in the electrical power grid over the past several decades. This needed trend, together with the increasing penetration of micro-, and nano-grids, is bringing significant improvements in system controllability, performance, and energy availability, but is fundamentally changing the nature of electronically-interfaced sources and loads, altering their conventionally mild aggregate dynamics, and inflicting low- and high-frequency dynamic interactions that never before existed at this magnitude. This problem is not restricted only to the grid; modern electronic power distribution systems built for airplanes, ships, electric vehicles, data-centers, and homes, comprise dozens, even hundreds of power electronics converters, produced by different manufacturers, who provide very limited details on converters' dynamic behavior - distinctiveness that has the highest impact on how two converters, or converter and a system interact. Consequently, substantial dispersion of power electronics into the future grid will significantly depend on engineers' capability to understand how to model and dynamically control power flow and subsystem interactions. It is therefore essential to continue developing innovative methods that allow easier system-level modeling, continuous monitoring of dynamic interactions, and advanced control concepts of power electronics converters and systems.

The dissertation will start with a "black box" approach to modeling of three-phase power electronics converters, introducing a method to remove source and load dynamics from *in-situ* measured terminated frequency responses. It will be then shown how converter, itself, can perform an online stability assessment knowing its own unterminated dynamics, and being able to measure all terminal immittances. The dissertation will further advance into an approach to control power electronics converters based on the electro-mechanical duality with synchronous machines, and end with selected examples of system-level operation, where small-signal instability in multi-source power systems can be mitigated using this concept.

Modeling and Control of Voltage-Controlling Converters for Enhanced Operation of Multi-Source Power Systems

Igor Cvetkovic

GENERAL AUDIENCE ABSTRACT

The modern technological advancements and ever-increasing needs for a sustainable future silently demand a serious revision of the conventional practice in electricity production, distribution, and utilization. These technologies are already challenging the limits of the biggest and most complex system ever built by humankind - the electrical grid. One practical solution to this problem is much higher dispersion of electronic power conversion systems capable of decoupling dynamics between system sources, distribution, and loads, while improving system controllability, reliability, and efficiency. Such a trend is already happening, and there has been an increased immersion of power electronics converters in electric cars, ships, airplanes, and the grid, in an effort to replace their traditional thermal, mechanical, hydraulic, and pneumatic systems. The goals have been to reduce the size, weight, and operational costs while increasing efficiency and reliability. In all these applications, a majority of energy sources and loads are interfaced to the power system through power electronics converters ranging in power from few watts to hundreds of megawatts. However, massive dispersion of power electronics into the future grid will significantly depend on engineers' capability to understand how to model and dynamically control power flow and subsystem interactions. It is important to continue researching innovative methods that allow easier system-level modeling, continuous monitoring of interactions, and advanced control concepts of power electronics converters and systems. This dissertation hence addresses modeling of power electronics converters using their behavioral models, and shows how these models can assist the stability assessment of the system converters operate in. Additionally, dissertation presents an alternative way to control power electronics converters to behave as synchronous machines, and how this concept can be used to mitigate some stability problems.

In memory of my Grandfather
who inspired me the most

Jovan Ljubenović
1933-2015

Acknowledgments

I am immensely grateful to all the people who inspired and challenged my work directly or indirectly, to those that taught me, and equally to those who critiqued. This has been an unbelievable journey filled with excitement and gratification.

I owe my deepest gratitude to an exceptional person, a mentor, a boss, and a friend Dr. Dushan Boroyevich for his impeccable guidance, support, and encouragement. His immensely broad knowledge, intelligence, enthusiasm, vision, and outstanding work ethic, coupled with his extraordinary attention to detail, completely changed my standards of what a good engineer should be. On the other hand, his natural emotional intelligence, caring personality, great sense of humor, and positive attitude, entirely changed my perception of life. Forever.

I am also very grateful to Dr. Rolando Burgos for our numerous hours of discussions, guidance, support, and encouragement, as well as his honest and apposite critique, conveyed just enough to cause an instant desire for improvement on the receiving end.

Another outstanding person I also wish to thank for enormous contributions and help with this dissertation, and my research in general, is Dr. Paolo Mattavelli. It is his intelligence combined with his calm and respectful nature that made our countless discussion hours enjoyable, rewarding, and productive.

I am also grateful to Dr. Jaime De La Ree for many challenging discussions, comments, and suggestions regarding the practical implementation of the concepts addressed in this dissertation.

Additionally, I would like to express my gratitude to Dr. Jack Lesko for numerous talks, support, encouragement, and recommendations for great improvement in the flow of ideas presented here.

It was an honor for me to have Dr. Slobodan Vukosavić serving as my committee member. He is another extraordinary person to whom I am extremely thankful for a long-time mentoring, my first hands-on contact with power electronics, my first job in the industry, invaluable encouragement, and recommendation to CPES that I begin my graduate studies here.

I am also endlessly thankful to:

- Dr. Fred Lee for his support, guidance, and numerous technical discussions that constantly challenged my research results;
- Dr. Khai Ngo for lots of encouragement and great advice;
- Dr. Zeng Liu for his immense help with this dissertation, and for the numerous hours he spent away from his family in order to help me with testing in the lab. Thank you Zeng, very much!
- Dr. Zhiyu Shen for countless hours of discussion, help, and all the fun we had working together. Thank you for designing and creating hardware that was instrumental in the completion of my work reported in this dissertation;
- Dr. Marko Jakšić for numerous discussions, help, and friendship, as well as for creating hardware that enabled the major part of my experimental work in this dissertation;
- Dr. Chi Li for great discussions and help with building the power converter I used for the experimental demonstrations shown in this dissertation;
- Ms. Christina DiMarino for her help and countless discussions;
- Dr. Dong Dong, Dr. Gerald Francis, Dr. Tim Thacker, and Dr. Luis Arnedo, for their help and our great time working together at the beginning of my graduate studies at CPES;
- Dr. Glenn Skutt for numerous technical discussions, help, and invaluable guidance;
- Dr. Milisav Danilović for great discussions, encouragement, and friendship;
- Mr. Yi-Hsun (Eric) Hsieh for discussions and help with the experiments;
- Dr. Xuning Zhang for numerous discussions and help;
- Dr. Qiang Li for help and support;
- Dr. G.Q. Lu, Dr. Ming Xu, and Dr. Shuo Wang for our technical discussions.

I am so grateful to the wonderful people at CPES whose unselfish help greatly influenced my work on this dissertation, their constant encouragement, great advice, and immense help: an exceptional person, colleague and a friend Ms. Teresa Shaw, Ms. Linda Long, Mr. David Gilham, Ms. Marianne Hawthorne, Ms. Trish Rose, and Ms. Lauren Shutt. You all are my second family, thank you for all you did for me!

I am also indebted to numerous CPES colleagues, faculty, and staff with whom I have worked either directly or indirectly over the past 10 years: Ms. Emma Raszmann, Dr. Qiong Wang, Dr. Bingyao Sun, Dr. Alinaghi Marzoughi, Dr. Niloofar Rashidi Mehrabadi, Mr. Joshua Stewart, Ms. Sarah El-Helw, Mr. Hao Xue, Mr. Vladimir Mitrović, Ms. Qian Li, Mr. Yue Xu,

Ms. Yu Rong, Mr. Slavko Moćević, Mr. Joseph Kozak, Mr. Jianghui Yu, Mr. Sungjae Ohn, Ms. Rebecca Rye, Mr. Lujie Zhang, Ms. Ye Tang, Ms. Jiewen Hu, Ms. Grace Watt, Mr. Owen Jong, Mr. Ahmed Mohamed, Ms. Virginia Li, Mr. David Nam, Mr. Junjie Feng, Mr. Lee Gill, Mr. Patrick Gu, Dr. Fang Chen, Ms. Amy Romero, Mr. Paul Rankin, Dr. Zhengyang Liu, Dr. Ming Lu, Dr. Chao Fei, Dr. Syed Bari, Ms. Nidhi Haryani, Dr. Yang Jiao, Dr. Zhemin Zhang, Dr. Xiucheng Huang, Dr. Zichen Miao, Ms. Yingying Gui, Dr. Ting Ge, Dr. Yuchen Yang, Mr. Alex Chu, Mr. Mudit Khanna, Dr. Han Cui, Dr. Yincan Mao, Mr. Ruiyang Qin, Mr. Vahid Najmi, Dr. Lingxiao Xue, Dr. Woochan Kim, Mr. Chen Li, Dr. Hanguang Zheng, Dr. Yi Yan, Dr. Pei-Hsin Liu, Dr. Pengju Kong, Mr. Shu (Alex) Ji, Dr. Shishuo Zhao, Dr. Dongbin Hou, Dr. Carson Baisden, Mr. Vladimir Podosinov, Dr. Fang Luo, Dr. Sara Ahmed, Dr. Zheng Chen, Mr. Wei Zhang, Dr. Ruxi Wang, Dr. David Reusch, Dr. Di Zhang, Dr. Rixin Lai, Dr. Dong Jiang, Mr. Jeremy Webb, Dr. Hemant Bishnoi, Dr. Xiao Cao, Dr. Weiyi Feng, Ms. Qian Li, Dr. Mingkai Mu, Dr. Chanwit Prasantanakorn, Dr. Yadong Lyu, Dr. Yipeng Su, Dr. Shuilin Tian, Dr. Zijian Wang, Dr. Haoran Wu, Dr. Yingyi Yan, Dr. Yiying Yao, Mr. Doug Sterk, Dr. Wenli Zhang, Mr. Bob Martin, Ms, Linda Gallagher, and many, many other great people whom I may have missed to name but will never forget.

I am also very grateful to Dr. Victor R. Stefanovic for his encouragement, immense help, and support, as well as for countless hours of inspirational talks.

This dissertation would not have happened without the enormous support, love and understanding of my wife Marina and my great boys, Veljko and Lazar. Their constant encouragement, love, and care have inspired me to overcome the most difficult moments and achieve what I thought was impossible. I love you guys!

To my beloved sister Ivana and my parents Dušica (Duda) and Zoran, I am deeply grateful for the endless love, support and care.

To my grandparents, uncles and aunties, cousins, and family-in-law, I am thankful for encouragement and help I received during my graduate studies at Virginia Tech.

I am grateful to Ms. Emily York for all the help and support that I received from her throughout my graduate studies. I feel so fortunate to know her and have her as a very close friend.

Last but not least, I would like to thank my numerous friends for their encouragement and constant support.

Table of Contents

List of Figures

List of Tables

1. Introduction

The modern technological advancements, and ever-increasing needs for a sustainable future, silently demand a serious revision of the conventional practice in electricity production, distribution, and utilization, and are already impelling what is considered the biggest and most complex system ever built by humankind - the electrical grid, into the dire straits of performance, stability, and reliability. One feasible solution to this problem is much higher dispersion of electronic power conversion mediums capable of effectively decoupling dynamics between system sources, distribution, and loads, while improving system controllability, reliability, and efficiency. Such a trend is already happening at the grid-level, and there has been an increased immersion of power electronics converters in electric cars, ships, and airplanes, in an effort to replace their traditional thermal, mechanical, hydraulic, and pneumatic systems. The goals have been to reduce the size, weight, and operational costs while increasing efficiency and reliability. In all these applications, a majority of energy sources and loads are interfaced to the power system through power electronics converters ranging in power from few watts to hundreds of megawatts.

1.1 Predominance of the Electric Energy

Shown in Figure 1-1a, is a close approximation of the total energy production and consumption in the United States [1]. The primary energy sources are: petroleum, natural gas, coal, nuclear, and renewables (including the hydro-power generation). The residential and commercial consumption

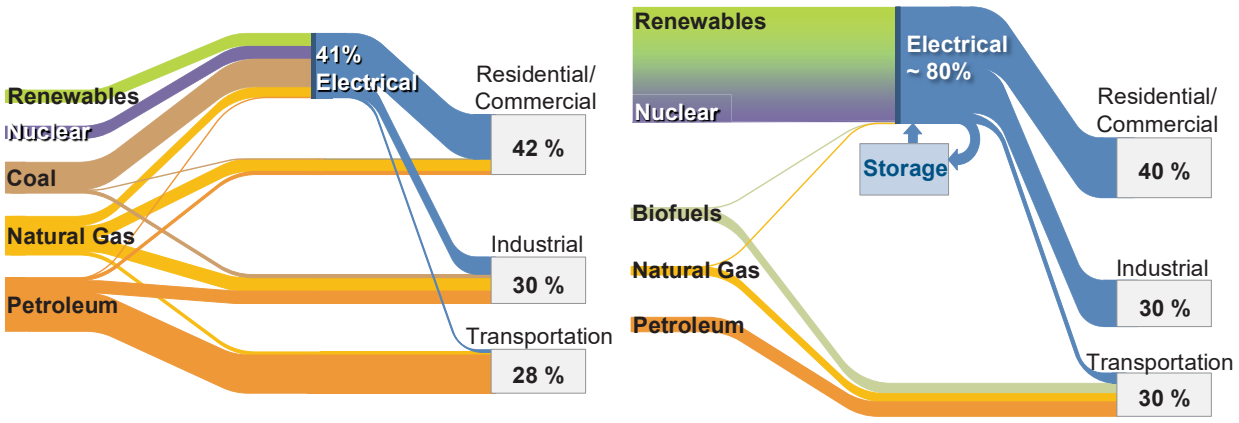

a) Approximate US energy flow in the last decade b) A possible energy flow in sustainable future

Figure 1-1: Total energy production and consumption in developed societies

(buildings and public spaces) is around 40%, while the remainder is almost equally split between industrial and transportation usage.

A hypothetical energy flow that can exist in the developed world in 20-30 years is illustrated in Figure 1-1b [2]. The flow is based on the assumption that most of the energy coming from the sustainable sources will be converted to electricity before it is used elsewhere. Obviously, due to large variability of renewable sources, their large penetration cannot happen without significant energy storage capacity and increased long-distance transmission capability. If the energy flow scenario from Figure 1-1b could be expected in 20-30 years, it would require double the electric energy infrastructure of today. Furthermore, the existing power system infrastructure is aging and inescapably facing not only an update but more likely a complete reconstruction in the future [3]-[5]. The statistics show an increase in grid outages and blackouts in the last 30 years [6], and the grid infrastructure is a global concern, since the majority of installed transmission and distribution equipment have experienced service duty in excess of 30 years [3],[7]. All of this implies that in the developed world, we can be facing the need to build a new electric power system with twice the size of the one we have today. This trend unquestionably opens a variety of new and interesting challenges and opportunities.

1.2 Electric Power System Today

From its beginning in the early 20th century, the structure and organization of the power grid underwent a very slow evolution. The generation has always been centralized; the transmission features a mesh network structure, and the distribution which is organized as a radial network provides electric energy at the lower voltage level to the end consumers. This very well-known structure is demonstrated through a simplified form in Figure 1-2 (left side), which illustrates the major components of a power system: production, transmission, distribution and consumers, interconnected through the power lines and substations.

This conventional power system is intrinsically slow due to the fact that it is mechanically controlled, where due to the frequent actions, electromechanical devices such as switchgear, tap changers, reactors and capacitors, tend to wear out very quickly compared to static electronic devices [8]. Future grid should be controlled electronically rather than mechanically [9], [10], and the stability of the power system could be improved by an advanced control of active and reactive power flow. For instance, it has been anticipated that before year 2030, a grid will be fully

automated hybrid AC-, and DC- electronic power network, featuring two-way flow of electricity and information between the production, consumption, and all points in-between [11]-[15]. This is illustrated in Figure 1-2 (right).

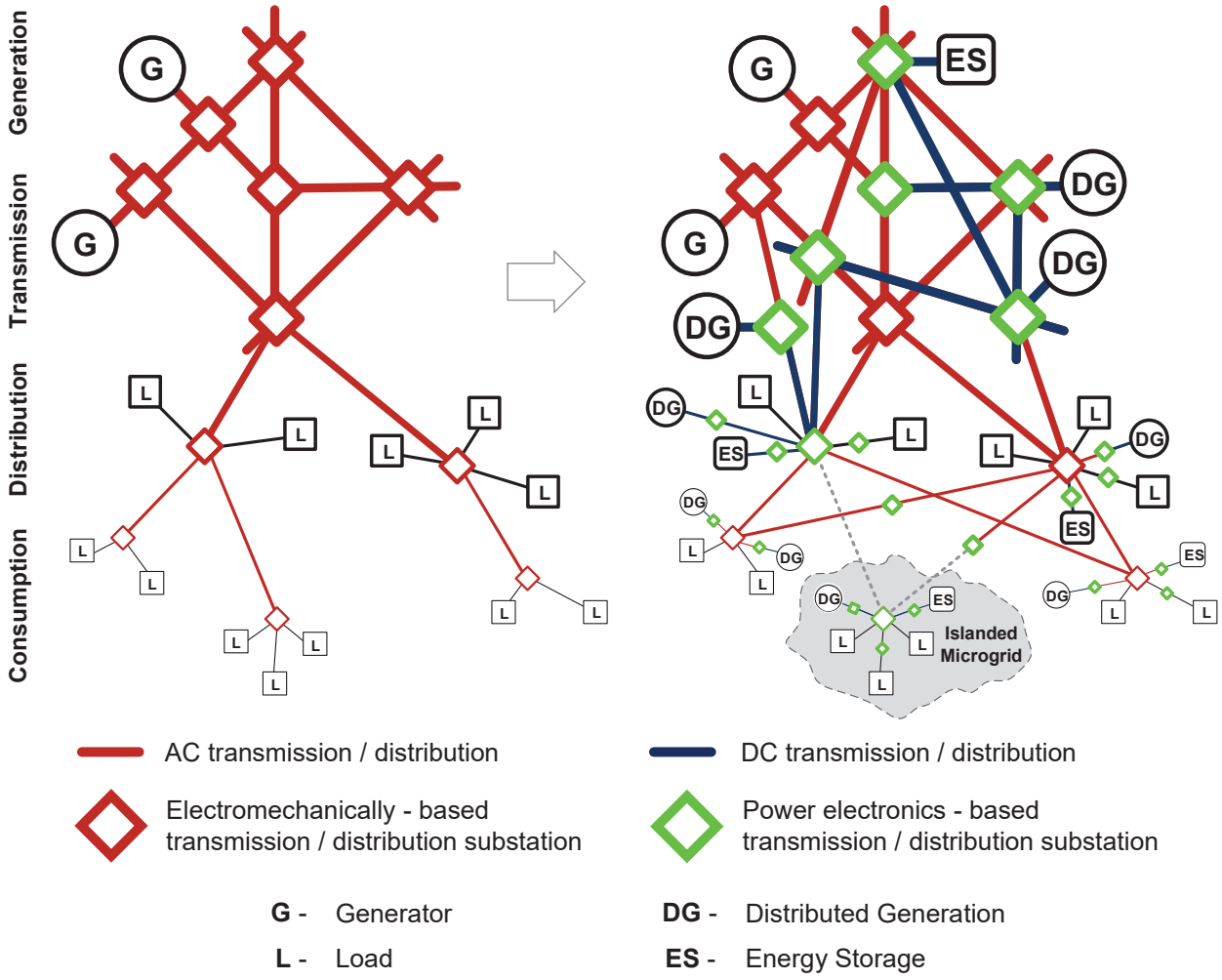

Figure 1-2: An illustrative example of the grid evolution

As seen in this figure, power electronics converters can separate a complex system into a large number of smaller, well-defined, and easily optimized subsystems. The utilization of the energy sources and the power delivery to loads can then be optimized independently of the power distribution architecture, which is primarily determined by the type of application and the power level. In such electronic power distribution systems, the dynamics of electric energy generation, distribution, and delivery can be fully decoupled by using separate source converters, load converters, and power distribution converters, as is already a common practice in smaller autonomous power management systems [16].

Undoubtedly, it takes time to reach these goals, and the future power grid will not emerge instantaneously, but will be a "migration rather than a sudden transformation" [17], [18]. This course has already started with the smart grid initiative [19]-[21], a concept that features enhanced sensing, actuation, control and operational benefits. However, even in a smart grid vision, the power system control centers are still dominantly relying on operators' responses and actions, which vastly increases decision time constants, and can lead to massive power system blackouts as seen numerous times in the history of the electric grid [22]. Therefore, it will take effort to progress beyond today's concepts unless we find a way to significantly increase penetration of power electronics into all aspects of electric power generation, transmission, distribution, and consumption.

1.3 Power Electronics in the Power Grid

Anticipated widespread usage of new power electronics technologies in electrical energy generation and consumption is expected to provide major efficiency improvements, while the deployment of *smart* grid technologies should improve the utilization and availability of the electricity. Over the last 40 years there has been an overwhelming trend to provide all electric energy to the final load equipment through fast electronic power converters in order to improve load performance and energy efficiency [23]-[26]. None of the electronic devices that have pervaded our lives – from phones to the life-support equipment – can directly use the electricity from AC mains; it must first be converted to DC of appropriate voltage-level by electronic power supplies. Most of the electric motors used in elevators, ventilation, pumping, heating, air-conditioning, refrigeration, food processing, fabric care, etc., are today being powered through electronic motor drives. With the LED becoming the dominant technology for lighting, all electrical energy used for this purpose will be processed electronically. Likewise, with traditional cooking equipment being replaced with microwaves and induction heating, over 80% of the total energy usage in newly equipped commercial and residential buildings will be processed through power electronics. Similar percentages of the total electric energy consumed in industry and transportation are already being processed by power electronics converters.

Although distributed generation (DG) was the rule rather than an exception in the early days of electric energy production [27], it has been almost completely replaced by the large-scale centralized generation in the second half of the 20th century. Recently, rapid commercialization

of the renewable energy sources [28] has resulted in increased deployment of low, medium and high power DG sources as well as energy storage (ES) systems. Invariably, renewable DG and ES sources are interfaced to the grid with the assistance of power electronics converters. Fast digitally controlled converters offer endless possibilities for the most optimal utilization of renewable resources. Moreover, power electronics based DG can enhance power system controllability due to the fast dynamic response to the power system disturbances and deviations of the voltage and frequency.

The future energy sources will unavoidably represent a mix of different technologies. However, wind generation is most likely to remain a dominant segment of the renewable industry [29] [31]. The most common, doubly-fed induction generator (DFIG) wind turbines [32], [33] require power converters rated at about 30% of the nominal power. However, with the recent fault-ride-through requirements [34], DFIG will need power converters rated at 100% of the nominal power, which could create a shift towards the full-power converter wind turbine systems, which also provide significant flexibility and performance improvements.

A network able to handle intermittent distributed renewable generation, and supply fast and widely variable electronic loads, can be implemented by utilizing power converters for fast control of the energy flows in the power system. However, today's power grid employs power electronics only for the fast dynamic control at transmission level [35],[36]. The high voltage direct current (HVDC) transmission has been developed and used for bulk power transmission over very long distances and to interconnect two AC systems with the different operating frequencies; furthermore, it can significantly influence and improve the transient stability of the power system. There are two major types of HVDC systems: the older thyristor-based, line-commutated, current source HVDC is usually used with overhead lines, and the newer IGBT-based voltage source converter (VSC) HVDC is often employed for cable and multi-terminal transmission. The line-commutated HVDC is used for long-distance very high power transmission, up to 6.5 GW through the lines with up to ±800 kV [37] whereas the VSC HVDC systems have been used for transmission up to 1.2 GW with the ±320 kV cables and could be suitable even for some distribution-level applications, for example, through underwater or underground cables. As the latest developments in high-voltage DC (HVDC) transmission illustrate [38], the performance, reliability and affordability of electronic power converters at 10-1000 MW power levels have achieved a remarkable progress, but still need further improvements, together with fundamental

concepts of energy flow and protection in electric power systems. Similarly, flexible AC transmission systems (FACTS) have been offering new solutions and opportunities for controlling power and improving the transmission capacity utilization [8]. In the form of the thyristor-based static VAr compensators (SVC) and VSC-based static synchronous compensators (STATCOM) and universal power flow controllers (UPFC), FACTS devices are opening numerous possibilities in controlling the power and improving the performance and reliability of centralized, bulk-power transmission systems.

Line-commutated HVDC has large reactive power consumption and cannot operate in weak systems. VSC-based HVDC can dynamically reverse the direction of the power flow very fast and has the ability to supply reactive power to the grid independent of its active power transmission, thus providing a major capability for the grid stability improvement [39],[40]. Furthermore, the recent resurgence of the modular multi-cell converter concepts [41]-[43] opens new possibilities for the massive use of lower-cost power conversion technologies in the high-power medium- and high-voltage applications. This is expected to enable wider usage of full-power electronics conversion in the distribution as well as in transmission networks.

1.4 Dynamic Interactions

Increased deployment of power electronics in all areas of electricity production, distribution, and consumption is undeniably bringing significant improvements in system controllability, performance, and energy availability, but is at the same time fundamentally changing the nature of fast and actively controlled sources and loads, imposing dynamics interactions that did not exist before in the passively cushioned and inefficient systems with very slow dynamics.

Figure 1-3 shows the notional hybrid AC/DC power distribution system that exemplifies the structure of those found in many different applications. The interactions between power electronics converters illustrated in this figure can happen at all frequencies, from very low, to very high, and if not carefully addressed, can be detrimental to the system stability. Below is the list of a few dynamic properties that have that potential; each will be briefly addressed.

- AC-, and DC- constant power loads
- Dynamic synchronization
- Aggregate load uncertainty
- Harmonics

1.4.1 Small-Signal Stability

There are numerous methods developed for small-signal stability assessment in order to address above listed system interactions. One of them is an eigenvalue-based approach where system eigenvalues are calculated and their location in the complex plane examined [194]-[198], [206]. A drawback of such approach is a need to know all system parameters that comprise a particular evaluated system, including its topology, passive components, control loops, etc., which in many cases presents quite complex and even impossible task.

Another popular stability assessment method is via loop gain measurements at different operating points, often performed using popular Middlebrooks's injection technique [210]. As system conditions constantly change during operation, some authors propose an online monitoring of the loop gain stability margins [208].

One of the most common and widely adopted method for small-signal stability evaluation is impedance-based stability method. Once source output impedance (Z_S), and load input impedance (Z_L) of a DC system are known, Nyquist stability criteria can be applied to the minor loop-gain defined as a ratio of these two ($L=Z_S/Z_L$) [46]. To quantify stability margins, a phase margin (PM) and a gain margin (GM) of the minor loop-gain can be defined, and numerous authors proposed forbidden regions in the complex plane where minor loop-gain is allowed to have excursions, allowing load impedance specifications to be determined [182]-[184], [211]. On the other hand, a small-signal stability assessment in three-phase AC systems is often done using Generalized Nyquist stability Criterion (GNC) [54], [55]. Although this is a powerful, widely used method for stability analysis, measuring impedances, and quantifying stability margins for AC systems is not as straightforward as in DC systems, and still presents a challenging task for system-level researchers and engineers.

1.4.2 AC-, and DC- Constant Power Loads

In general, three types of loads dominate in the power system: constant power, constant impedance, and constant current loads. Lumping constant power and constant current loads into one category, and looking at the typical industrial area, the constant power and constant current loads take about 80%, leaving only 20% for the constant impedance load category [44]. The ratio in the residential areas is not much different, getting to a 70/30 ratio in favor of the constant power load. These constant power loads (CPL) react to a voltage sag with the increased current draw in

order to maintain the power delivered to the load. The consequence of that action is that these loads present a "negative incremental resistance" behavior to the grid, disreputable for causing small-signal system instability.

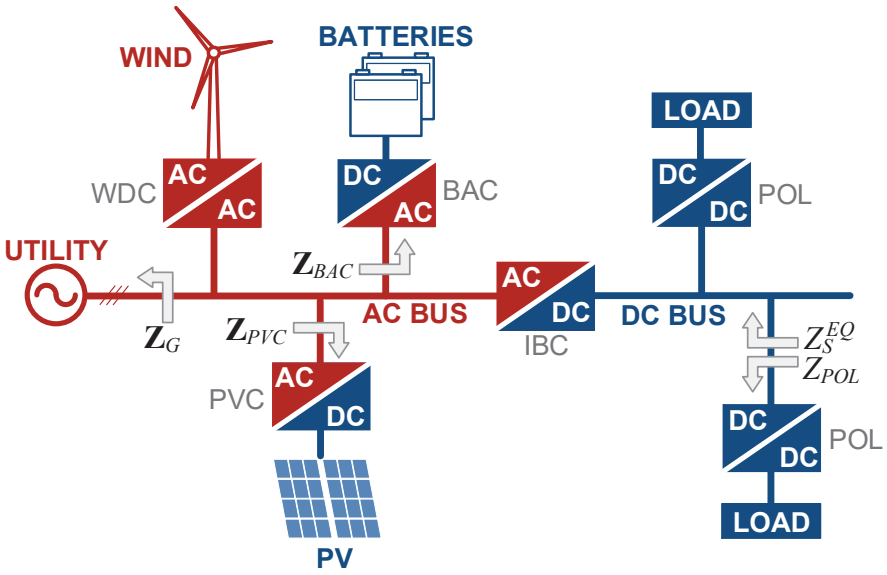

$\mathbf{Z}_G$	Grid output impedance	$\mathbf{Z}_{BAC}$	Battery converter output impedance
$\mathbf{Z}_{PVC}$	PV converter output impedance	Z_S^{EQ}	Equivalent (aggregate) source output impedance
Z_{POL}	Point of load converter output impedance		

Figure 1-3: Notional, hybrid AC/DC microgrid subsystem

If the point-of-load converter (POL) from Figure 1-3 above supplies the load with the constant power, its input impedance "seen" from the DC bus will feature the shape as shown in Figure 1-4, with negative incremental resistance ($-R_{POL}$) property maintained from DC to the frequency corresponding to the control bandwidth (in this case about 100 Hz). If now equivalent source impedance Z_S^{EQ}, intercepts Z_{POL} anywhere within the point-of-load converter control bandwidth, when the phase is around 180°, instability can happen [45]-[47].

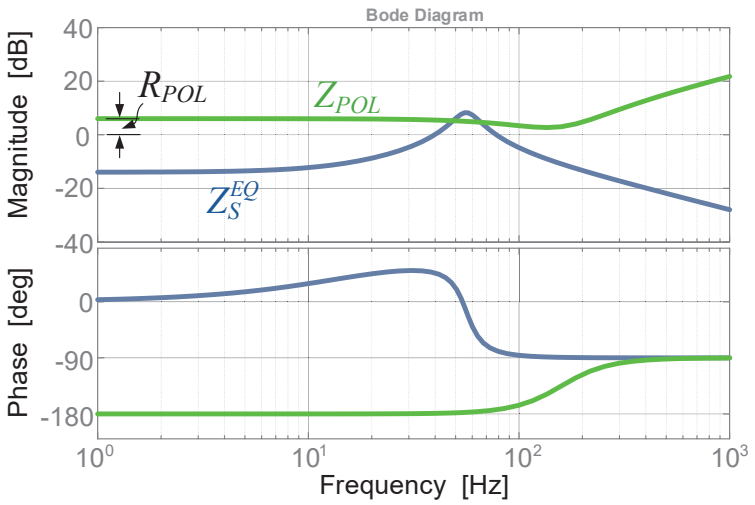

Figure 1-4: Input impedance of the regulated converter with negative incremental resistance, and equivalent output impedance at the DC interface point shown in Figure 1-3.

The same conclusion can be made for input impedance $\mathbf{Z}_{BAC}$ of the active rectifier (BAC converter) at the three-phase AC interface. Wen *et al.* [48] show experimentally that active rectifier regulating its output voltage also features negative incremental resistance property in the direct axis of its input impedance, within the control loop bandwidth, which increases chances for the small-signal instability if interaction with the equivalent source impedance (seen from converter's input towards the rest of the system) happens.

In general, negative incremental resistance cannot be avoided, as it is an inherent small-signal property of the constant power loads, but its impact can significantly be mitigated by proper system and control loop design.

1.4.3 Frequency Synchronization

The common, and with some exceptions, the only method to interconnect high power renewable energy sources and energy storage systems to the power system has been using power electronics converters that operate as current sources to the grid, for the purpose of achieving maximum primary-source power tracking and synchronization with the grid through low-bandwidth phase-locked loops. These "source inverters" also demonstrate negative incremental output resistance which makes them susceptible to the low-frequency dynamic interactions with other sources and loads on the grid that are trying to synchronize at the same time.

By looking again at the notional microgrid subsystem from Figure 1-3, it is evident that photovoltaics (PV) are connected to the AC distribution line via the voltage source inverter PVC

(in practice, there is almost always another converter (DC-DC) between the actual PV and inverter stage, but is not shown here for simplicity). This inverter should feature some form of the dynamic phase-locked loop (PLL) [49] in order to acquire knowledge of the grid angular frequency and angle, and to be able to properly position its control variables and provide desired active and reactive power to the grid. Wen *et al.*, show in [48], another negative incremental resistance property in the quadrature axis of the output impedance of the inverter featuring the PLL (e.g. PVC in Figure 1-3). If now equivalent load impedance, seen from the PVC, intercepts with $\mathbf{Z}_{PVC}$ anywhere within the PLL control bandwidth, instability can occur. Dong *et al.* [50] experimentally demonstrate instability caused by PLL-based interactions between two converters when grid output impedance Z_G shown in Figure 1-3 becomes high.

1.4.4 Aggregate Load Uncertainty

Another challenging problem for system designers and integrators is the unknown nature (dynamics) of the source and load seen from the terminals of the bus converter installed in-between. Although usually not as severe as negative incremental resistance from the small-signal stability point of view, dynamics of the source and the load will deviate performance of the converter from the original design done in the lab environment using, for instance, electronic loads, and consequently impact control bandwidth and, more alarming, its phase margin. Figure 1-5 shows an example of the load influence on the control loop gain of the intermediate bus converter (IBC) from Figure 1-3.

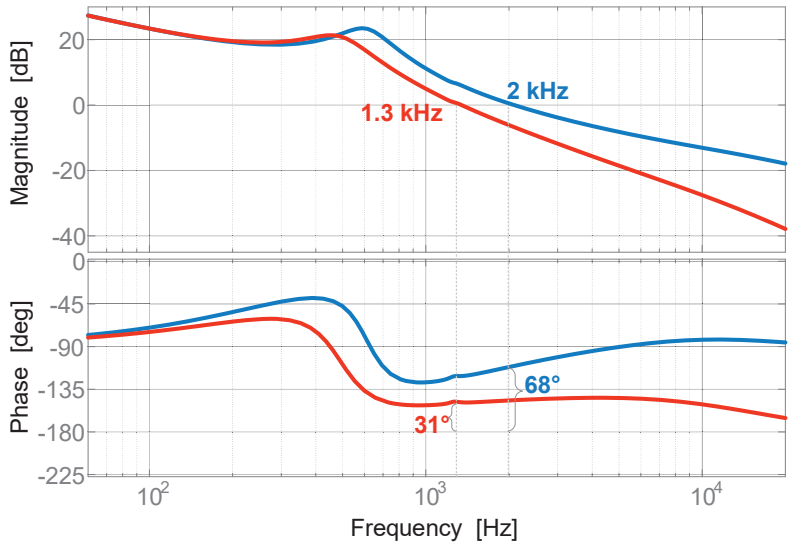

Figure 1-5: An example of the possible impact of the load dynamics on the converter loop gain

The converter control was, as an example, originally designed to feature the loop gain shown in blue in Figure 1-5, with the bandwidth of about 2 kHz, and phase margin of 68°. However, connecting different loads to the IBC converter (in this case aggregate load impedance of the DC subsystem from Figure 1-3) can cause a significant reduction of the control bandwidth, and phase margin which could have detrimental effects on this converter, and consequently, system stability.

1.4.5 Harmonics

Power electronics-based processing systems produce harmonics at the grid side that span from very low to very high frequencies. In addition to the instability problems associated with the negative incremental resistance, or synchronization loops, interactions of the converter control loops may result in harmonic instability phenomena [51] - typically from hundreds of hertz to several kilohertz [52], [53].

1.5 Measurement of Small-Signal Impedances

Equipment made to measure *in-situ* AC system impedances are rare and not commercially available. There are, however, examples of impedance measurement unit prototypes made in academia. In addition to [59],[60] reported by Shi and Familiant respectively, Center for Power Electronics Systems (CPES) developed several impedance measurement units (IMU) for its industry members, ranging from 50 kVA to 2 MVA during the last decade [56]-[58], [61] [66]. The newest addition to the family of IMUs built by CPES is a medium-voltage, 2.2 MVA unit sponsored by the U.S. Office of Naval Research (ONR), shown in Figure 1-6.

Figure 1-6: Medium-voltage impedance measurement unit developed by CPES in 2014

This IMU is capable of characterizing impedances of the medium-voltage systems, both MVAC (4.16 kV, 60 Hz) and MVDC (6 kV, DC) in the frequency range from 0.1 Hz to 1 kHz. The IMU employs the power electronics building block modular concept developed using novel 10 kV SiC MOSFET modules.

1.6 Motivation and Objective

1.6.1 Terminal Behavioral Modeling – Overview and Contribution

The requirements for improved power availability and quality require higher penetration of power electronics not only at all levels of the electric grid - new electronic power distribution systems are constantly being built for airplanes, ships, electric vehicles, data-centers and even homes, by comprising variety of power electronics converters with very different dynamic characteristics. If system-level behavior is not carefully examined before the system is integrated, there can be detrimental effects on the system performance, and stability. These complex systems consist of a wide assortment of different power converters, usually made by different manufacturers. The design of such systems entirely relies on the information provided in the datasheets and manuals, the experience of system engineers, and their ability to test the system under different operating conditions. System engineers will hardly ever have converters average or switching models available, thus the "black-box" terminal-behavioral modeling has become an attractive topic used in engineering practice for DC-DC converters and systems.

A practical way to represent DC-DC converter as a black-box is through the so-called two port network, where only converter input and output terminals are accessible. The first reported attempt to represent converter in a form of a two-port network was in 1985 by Cho [67]. That structure is shown in Figure 1-7, representing a small-signal DC-DC power converter with a single, two wire input and output (1.1). Here v_i, v_o, i_i, i_o represent input and output voltages and currents, while tilde sign (~) above these variables denotes a small-signal perturbation around an equilibrium operating point of the converter.

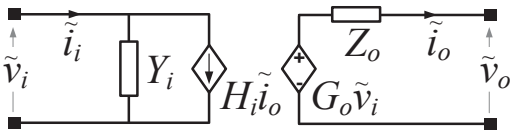

Figure 1-7: Two-port network representation of a DC-DC converter

$$\begin{bmatrix} \tilde{v}_o \\ \tilde{i}_i \end{bmatrix} = \begin{bmatrix} G_o(s) & -Z_o(s) \\ Y_i(s) & H_i(s) \end{bmatrix} \cdot \begin{bmatrix} \tilde{v}_i \\ \tilde{i}_o \end{bmatrix} \tag{1.1}$$

where: $$G_o(s) = \left.\frac{\tilde{v}_o}{\tilde{v}_i}\right|_{i_o=0}, \; Z_o(s) = \left.\frac{\tilde{v}_o}{\tilde{i}_o}\right|_{v_i=0}, \; Y_i(s) = \left.\frac{\tilde{i}_i}{\tilde{v}_i}\right|_{i_o=0}, \; H_i(s) = \left.\frac{\tilde{i}_i}{\tilde{i}_o}\right|_{v_i=0} \tag{1.2}$$

can be defined as: G_o - audio susceptibility, Z_o - output impedance, Y_i - input admittance and H_i – current-back gain. Minus sign in (1.1) mathematically takes into an account direction of the output current as shown in the Figure 1-7, which corresponds to the power flow from input towards the output.

These models very well capture dynamic behavior of linear or "mildly" non-linear converters up to a half of the switching frequency, hence called low-frequency models, and have been well understood and applied to DC-DC converters [67]-[75] due to the easiness of performing small-signal measurements and existence of the operating point. This concept has even been further extended to address non-linear behavior [76]-[81].

Equipment made to perform frequency response measurements on DC-DC converters exist on the market, and are commonly used to obtain transfer functions of these converters as well as of the passive filters [201]-[203]. However, compared to DC-DC converters, terminal-behavioral modeling of three-phase converters is a far less popular engineering practice, possibly due to the difficulties associated with the small-signal measurements. Also, terminal AC voltages and currents are time variant, hence linearization around some desired operating point must be done in rotating *d-q* coordinates that are in synchronism with input and/or output frequencies. Small-signal frequency-domain models can now be obtained by linearization around the desired operating point, but the difficulty has always been access to the measurement equipment that will be able to perform frequency response measurements on the AC-converters or networks *in-situ.*

Although more complex, three-phase converters and networks can be as well represented by (1.1), replacing its parameters with corresponding matrices comprising two or four transfer functions each, depending of the type of converter as it will be seen later in the Chapter 3. Hiti's work from early 90's [82], followed by the work of Arnedo *et al.* [79],[16] more than ten years later, expands the two-port network model into three-, and four-network directly applicable to

three-phase converters; additionally, [79] reports some initial simulation results of dynamic characterization of a three-phase converter.

Valdivia *et al.* [83]-[85] used three-port networks to model three-phase converters, and propose to perform their dynamic characterization by transient response analysis on input and output sides of the converter. Experiments were performed using switches, diodes, and passive loads, and recorded transient waveforms were later post-processed using available identification algorithms in order to obtain behavioral transfer functions. Ala *et al.* [86] propose injection of Gaussian zero-mean noise in the process of dynamic characterization of converters, but only demonstrate the technology in simulation, while reference [87] applies the terminal-behavioral methodology to obtain the model of the inverter with a LCL filter.

Moreover, terminal-behavioral modeling can be used to develop high-frequency EMI models. Bishnoi *et al.* present the concept of an EMI filter design of motor drives using these models [88], as well as an EMI modeling of a half-bridge converter [92]. In [89] Cuellar and Idir develop the method using a black-box model to calculate insertion loss of the EMI filter taking into account input and output impedances, while Frantz *et al.* [90], and Baisden *et al.* [92] present methodical approaches for developing EMI terminal models.

1.6.1.1 Problem Statement and Contribution to the Existing Art of Terminal-Behavioral Modeling

Regardless of the type of the converter that is being characterized (AC-, or DC-), the final goal is to obtain the set of unterminated transfer functions that only describe the internal dynamic of a converter at a particular operating point. However, a problem of *in-situ* terminal characterization in general is that it always contains aggregate, terminated dynamics – one that includes not only the behavior of the converter, but as well the dynamics of the source and the load. Figure 1-8 illustrates the termination effects. Labeled with a red color, Y_i and Z_o represent unterminated input admittance and output impedance, while blue colored labels denote terminated input admittance Y_{im} and output impedance Z_{om} that contain terminated dynamics (hence blue color arrow goes all the way to each end, illustrating pictorially that both Y_{im} and Z_{om} "see" reflected dynamics from the opposite sides). Transfer functions G_o, Z_o, Y_i and H_i are defined above in section 1.6.1.

As described in [72],[75],[79], input admittance Y_i can be obtained by perturbing the input side and output impedance Z_o by perturbing the output side. These two perturbations are not performed

simultaneously, but rather one after another. The converter operating point should not change until both perturbations are done.

Prior to the methodology proposed in [93], and consequently this dissertation, termination was neglected due to the fact that the converter under test was connected to the low impedance voltage source and high impedance current sink, seen as "ideal" voltage and current source respectively. In this case perturbations of the input voltage and output current are negligibly small, so that the problem of extracting unterminated impedances and admittances can be significantly simplified ($Y_{im} \approx Y_i$ and $Z_{om} \approx Z_o$). In situation where this assumption was made only for input or output side of the converter, the opposite side impedance or admittance can be calculated out as a solution to the quadratic equation. This solution was reported in [94], as one of the first attempts to decouple source and load dynamics from the converter under test. Additionally, the converter under test would often need to be removed from the original environment and connected to a known source and load before measurements were performed.

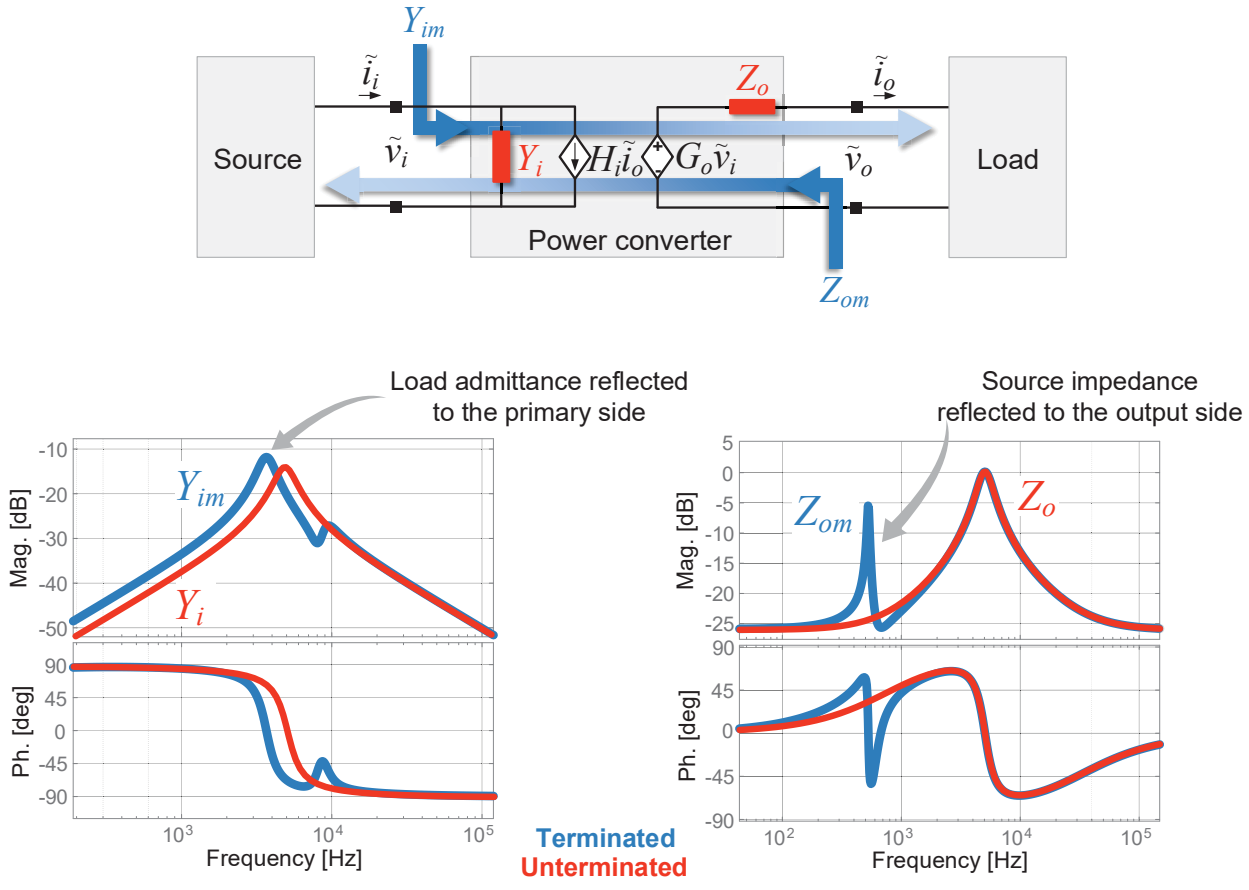

Figure 1-8: (top) DC-DC converter under test and, (bottom) terminated and unterminated immittances (example)

This part of the dissertation complements the work of Arnedo [79], and proposes an *in-situ* converter characterization procedure where the converter under test can remain working in the original environment, at a particular operating point, being connected to any type of the source and the load while the terminated frequency responses are obtained performing the frequency sweep method. Using the proposed linear transformation (decoupling procedure), converter dynamics can be fully decoupled from the source and the load, leaving only internal converter dynamics in the model. Decoupling matrix can be defined from the variables that will be measured anyway during the characterization tests [79],[93],[95].

1.6.2 Online System Observation and Stability Assessment – Overview and Contribution

There have been numerous papers published on different techniques for obtaining system impedances via *in-situ* measurements. A detailed survey of impedance measurement techniques for stability analysis of AC and DC power systems is systematically presented in [58],[60],[101], showing several practical realizations of three-phase power electronics-based perturbation injection units. An alternative solution for impedance extractions based on unbalanced single-phase injection is presented in [102],[103]. Here, the injection unit is compacted into a single-phase structure, significantly reducing the size of the whole unit. Another approach reported in the literature is time-domain identification of impedances via step load changes [105], where only two transient responses are needed to characterize the small-signal impedances at low frequencies, but the drawback is inability to do so precisely at higher frequencies.

To perform a methodical stability assessment of a system (for instance the one shown in Figure 1-3), stability has to be checked at every interface point in the system, by physically connecting the impedance measurement unit at those interfaces. Although trivial for small distribution systems like those found in computers or even electric cars, this effort becomes significantly complicated when higher-power systems are in question. This is mostly due to the size of the equipment; it is recommended that to have enough perturbation power capability the impedance measurement unit should feature a power rating that is at least 5% of the system rated power - a good example of that is the IMU from Figure 1-6.

Several research groups expanded the impedance measurement concept by proposing an online identification methodology, where a converter already operating in the system can additionally perform impedance characterization of the grid impedance at its terminals.

Barkley and Santi are among the first to assign the impedance measurement functionality to a system converter (DC-DC), and reported measurements of source and load impedance by perturbing the duty-cycle of a converter using white noise injection [106]. Cespedes later proposed in [107] to assign an ancillary function to the three-phase grid-connected inverter to inject a current impulse into the grid (while operating), and perform an online Discrete Fourier Transform (DFT) of the impulse response in order to obtain positive-, and negative-sequence impedances of the grid. He further advanced the technique in [108] by suggesting gain-scheduling adaptive control that can tune the PLL bandwidth online in order to avoid converter interaction with the grid (Dong and Wen address PLL-based interactions in [50],[109]). Though it measures the grid output impedance very well, the scarceness in the work of Cespedes is that it only approximates the input admittance of the grid-converter within the PLL bandwidth, and does not take into account impedance of the source (DC-side) reflected to the inverter output (AC-side) – for more accurate dynamic interaction assessment and PLL tuning.

Riccobono *et al.* propose the similar concept in [110], and report the on-line grid output impedance measurement in the single-phase system measured by hardware in the loop-based implementation of the grid-interface converter using injection of pseudo random binary sequence (digital approximation of the white noise). He later published an extension of this work applied to the three-phase grid-tied converter [111]. Martin *et al.* used a similar concept as well, and in [112] reports online measurement of grid impedance using the three-phase converter.

1.6.2.1 Problem Statement and Contribution to the Existing Art of Online System Observation and Stability Assessment

When performing stability assessment at a particular system interface, it is essential to have measurements of both side impedances "seen" from that interface [55]. Although able to quite successfully perform online impedance measurements, current state-of-the-art is still limited to only one side impedance measurement at the time, dubbed outward impedance – looking at either source or load impedance. Indeed, converters themselves can only measure what they are connected to, not look inward. Accordingly, [106] proposes that the downstream converter can be assigned to measure the upstream one; the upstream one afterwards measures the downstream one, and both impedances at that terminal are obtained. Another suggested solution was to estimate the inward impedance analytically in the frequency range of interest according to the known topology and control scheme [108].

Figure 1-9 shows a DC-DC converter in a two-port network representation. V_S and Z_S represent a voltage source in form of the Thevenin equivalent circuit at the operating point V_S and source output impedance Z_S, while load is represented as the Norton equivalent circuit with constant current I_L and load input admittance Y_L. Immittances Y_L^{EQ} *and* Z_S^{EQ} define equivalent terminated input admittance and output impedance respectively including reflected dynamics from each associated side of the converter.

The concept proposed in this dissertation expands and complements the existing knowledge while contributing to the general stability research. Proposed is the method where converter itself, operating at a particular operating point, can perform frequency sweep *in-situ*, and determine all terminal impedances as illustrated in Figure 1-9. To achieve that, the unterminated transfer functions of a converter have to be known, which allows the converter to actually "see" through itself and determine its own equivalent input admittance, and equivalent output impedance, necessary for stability evaluation at its input and output terminals. While a DC-DC converter is shown in Figure 1-9, the concept can be applied to any type of converter as will be presented in Chapter 4.

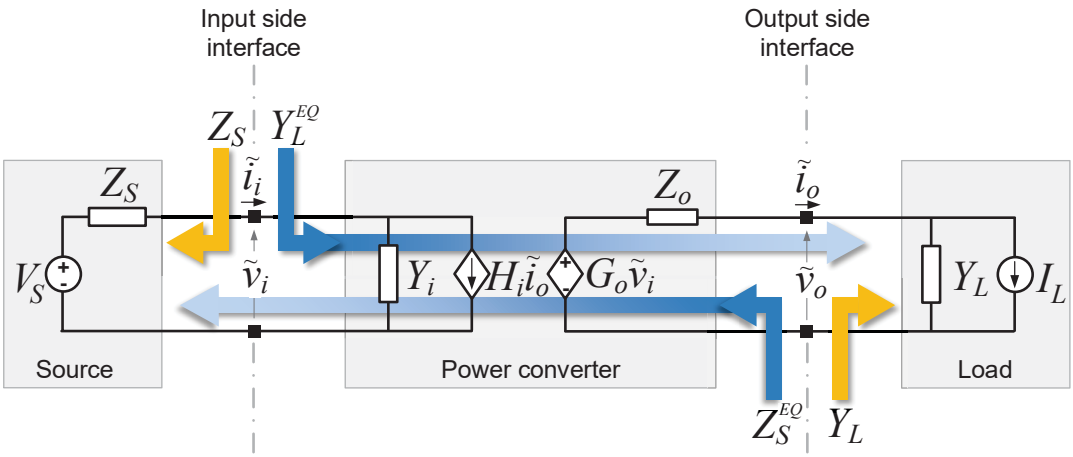

Figure 1-9: Small-signal model of the DC-DC converter in a two-port network representation

1.6.3 Voltage-Controlling Converter (Electronic Synchronous Machine) – Overview and Contribution

The newest (upcoming) revision of the IEEE 1547 standard will allow for the first time distributed generation to regulate the voltage at the point of common coupling [113]. Such change incontrovertibly opens new research opportunities and requires fresh concepts for advanced power

flow control of grid-interface converters in order to improve system stability and energy availability. On the other hand, higher expansion of distributed generation has a negative impact on grid protection coordination, voltage regulation, and voltage flicker where all can be caused by the intermittent behavior of the renewable sources, especially wind turbine systems [114]. Also, the conventional voltage regulation is commonly based on radial power flow so distributed generation can lead to both overvoltage and undervoltage conditions [115], [116]. Additionally, by introducing inversion in the power flow that is not common for the radial networks, distributed generation can affect the stability by directly influencing the hierarchical protection scheme and the relay coordination [117]. Power converters for renewable resources, and in general all distributed generation, work as current sources [118] and every grid-connected inverter forms a dynamic system with the grid, so unintentional dynamic interactions may occur at the interconnection point which causes instability [119], oscillations [120] or harmonic distortions [121].

To enable higher growth of distributed generation into the grid, researchers started exploring unconventional ways to control grid-side power electronics, making their presence in the grid non-disruptive and with the high potential to enhance, not impair grid performance. One such way is to control grid-interface converters as synchronous machines. This concept is seen as a promising methodology for seamless, yet massive, penetration of power electronics into the grid due to the mild properties associated with the well known nature of the synchronous machines. As it will be seen below in this subsection, while going through the literature review, numerous researchers have been giving ample credit to this concept, partially since it offers a new and fresh look at the control of the grid-interface converters, and partially since it gives promising results in suppressing system oscillations through virtual inertia and damping, seamless islanding, and self-synchronization. In general, a power electronics converter operating as a synchronous machine, at the very minimum, can perform much like a generator. The idea of course is to explore how to advance this concept way beyond the limits of an actual synchronous machine.

Although IEEE FACTS Terms & Definitions Task Force [122] introduced the term *Static Synchronous Generator* (*SSG*) in 1997, there was no research in this direction reported until one decade later. In 2007, Beck and Hesse published the *Virtual Synchronous Machine* (*VISMA*) paper [123], using a detailed model of the synchronous machine implemented in the dSPACE platform. The model calculated reference stator currents in ~~the~~ real-time, feeding them back to the current

controlled inverter which consequently operated as a synchronous machine. One year later, Driesen and Visscher introduced the long-term VSYNC demonstration project using the *Virtual Synchronous Generator* (*VSG*) concept, with emphasis on the virtual inertia [124]. References [138], [149] report results of the implementation of the concept.

Zhong and Weiss in 2009 published the *Static Synchronous Generator* concept [125] adding voltage and frequency droop functionality to the simplified machine model that will be implemented in the DSP controller of the voltage source converter. In their approach, a controller will measure inverter output currents that will be input to the machine model running in the DSP, while calculated output voltage will be the control variable used directly to drive the three-phase inverter. Two years later, the authors proposed the term *Synchronverter* [126] for an inverter that emulates a synchronous machine using the same concept described in [125].

In 2010, Zhang *et al.* [127] were among the first recognized that voltage source converters could effectively use the synchronous machine power balance concept to synchronize with the grid frequency without the need for the Phase-Locked Loop (PLL). They used a simplified power swing equation for this purpose, but still only as a supplemental synchronization method to the conventional and often used synchronous-reference frame PLL [128]-[130]. Applying a similar concept, Zhong *et al.* [131], [132], propose the improved operation of the *synchronverters* without a need for the auxiliary PLL, demonstrating capability of inverter self-synchronization using only the synchronous machine power-balance concept. Similar work on the alternative, machine-like synchronization techniques has been reported in [133]-[137], [149], [161].

Rodriguez *et al.* [139], [140] show the concept of the selective synchronous generator emulation, focusing on attenuation of power oscillations using damping and inertia adjustments provided by the power-balance equation. The concept of virtual admittance was also introduced here to mitigate impedance interactions with the grid. Authors named this concept the *Synchronous Power Controller* (*SPC*). More recent work related to *SPC* operation can be found in [141]-[143].

Applying a similar concept and taking advantage of the virtual impedance and inertia, as well as virtual damping, Chi *et al.* report improved operation of STATCOMs in [144]-[146]. Phi-Long *et al.* [147] as well report performance improvement when operating STATCOMs as synchronous machines.

Additionally, high research focus has been put on understanding advantages of virtual inertia algorithms and implementation techniques, all with the goal of providing high-performance, yet simple means of suppressing dynamic oscillations and minimizing vicious system interactions. Torres *et al.* [148] propose in 2014 the online self-tuning virtual impedance and damping factor algorithm in machine-like controlled converters in order to provide dynamic frequency support in the system. Another, inspiring concept published by Alipoor *et al.* [150] proposes the use of the bang-bang control in order to change virtual inertia between two defined values that significantly suppress power oscillations.

Other quite interesting work related to the virtual synchronous machine concept can be found in [151]-[165], focusing on damping the power oscillation [151], [154], [155], [158], [166] power quality improvement [156], [163], islanding [157], and system-level integration benefits [152], [153], [159], [160], [162], [164], [165].

1.6.3.1 Problem Statement and Contribution to the Existing Art of Virtual (Electronic) Synchronous Machine

Widely accepted among researchers who see the virtual synchronous machines (VSM) as solutions to many grid problems is the power-balance concept for synchronization of power electronics converters. Simply, if grid angular frequency changes, angular electrical frequency of the machine rotor will accurately track these changes (statically). More precisely, if we look at the two voltage sources in Figure 1-10 (simplified machine representation with Thevenin equivalent voltage sources demonstrating machine electromotive force and grid voltage, with the inductance L between them). Assuming the balanced and symmetrical three-phase system, the time invariant active power transfer from one source to another exists only if the difference between their angular frequencies is zero. This can be shown by calculating active power in the simplified circuit from Figure 1-10 at the input terminals (before the impedance, looking towards the grid). If the Root Mean Square (RMS) of the electromotive force has a fixed value E, angular frequency ω_e and instantaneous angle θ_e (initial angle θ_{eo} can be assumed to be 0 for simplicity), and if grid voltage with RMS value V, angular frequency ω_s and instantaneous angle θ_s (initial angle θ_{so}) represents the stiff grid, the instantaneous active power (1.3) can be derived.

$$p(t) = i_a v_a + i_b v_b + i_c v_c = \frac{3EV}{L\omega_s} \sin((\omega_e - \omega_s)t - \theta_{so}) \tag{1.3}$$

If two angular frequencies (ω_e and ω_s) are not in synchronism, active power becomes time variant and oscillates with the beat angular frequency (ω_e-ω_s) and zero-average value, as evident from (1.3), and illustrated in Figure 1-10.

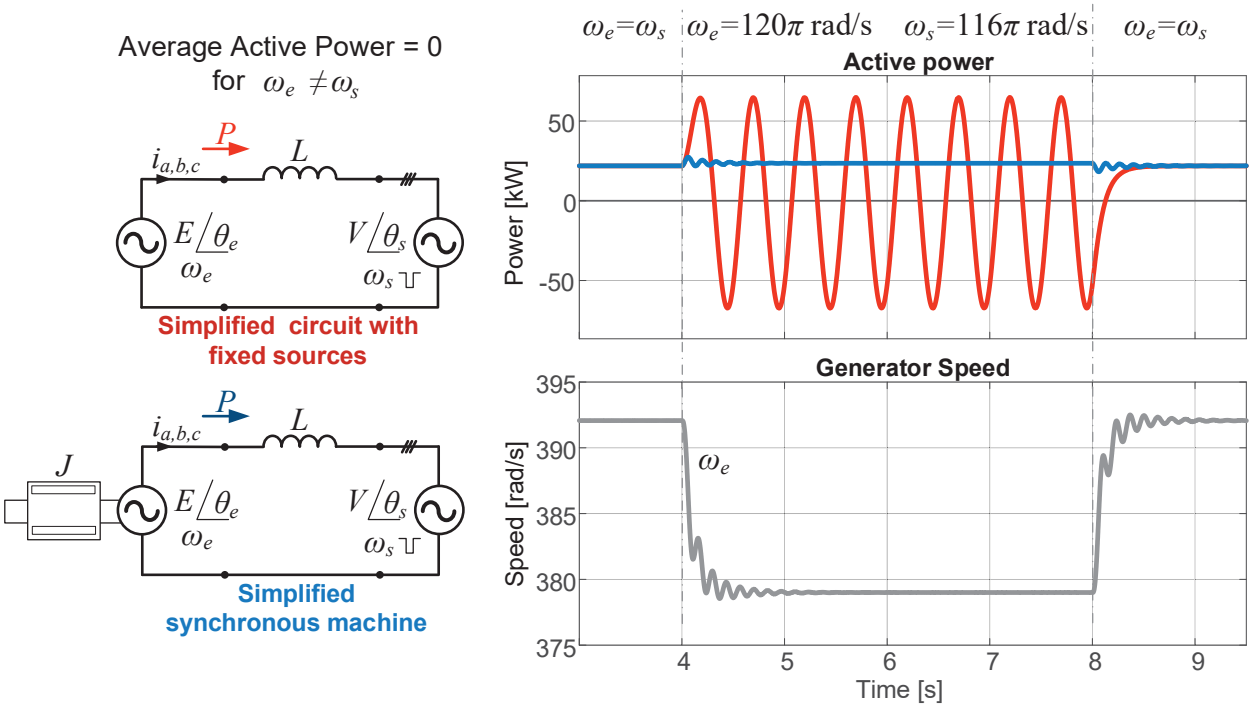

Figure 1-10: Dependence of the active power in synchronous machines on the synchronism with the grid

It can be seen that for the time before 4 s both side sources had the same frequency - 60 Hz (120π rad/s), while between 4 s and 8 s the frequency of the grid was changed to 58 Hz (116π rad/s), demonstrating the oscillating nature of the instantaneous power with the beat frequency of 2 Hz during this time (red waveform in Figure 1-10). Grid frequency recovered at 8 s and voltage source E resumed active power delivery to the grid. This example assumed two stiff sources on both side to emphasize the phenomena of the zero average active power flow if sources are not in synchronism.

In the case machine EMF E is not stiff, and in fact is a consequence of the rotor rotation as illustrated in the bottom circuit in Figure 1-10, then change of a grid frequency causes the machine speed to change, hence demonstrating a self-synchronization capability. Blue waveform in

Figure 1-10 shows the active power after the angular frequency transient, and bottom gray waveform represents the change of machine speed we that follows change in ω_s.

This self -synchronization is the consequence of Newton's law of motion [167], [168], known as the swing equation, where J is moment of inertia, D damping coefficient, and, T_m, T_e mechanical and electrical torque respectively:

$$J\frac{\mathrm{d}\omega_e}{\mathrm{d}t} = T_m - T_e - D(\omega_e - \omega_s) \tag{1.4}$$

Writing it in the form of power, (1.4) can be obtained after linearization with an assumption that ω_s is the constant. M is angular momentum (M=$J\omega_s$), and K_D damping factor (K_D=$D\omega_s$):

$$M\frac{\mathrm{d}\omega_e}{\mathrm{d}t} = P_m - P_e - K_D\omega_e \tag{1.5}$$

Figure 1-11 shows (1.5) applied to a converter control.

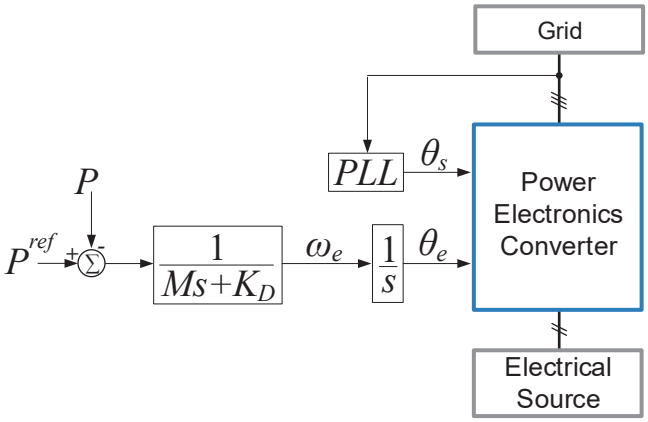

Figure 1-11: Simplified representation of the synchronous machine emulation

This figure evidently represents the oversimplified form of the virtual synchronous machine control concept, but does emphasize the most commonly used approach for power balance-based concept implementation. This is not by chance. Synchronous machines exhibit the swing equation naturally by the physics and their carefully engineered geometry.

With any transient that can happen in the system, measured active power at the output of the VSM converter P is compared with the reference, and the error fed into the simple two-pole compensator structure (low-pass filter followed by an integrator) that will align angle θ_e as required

to assure the power balance is achieved. This structure can be expanded by adding a DC-link voltage regulator which output will provide active power reference.

It can be noticed that there is also a Phase-locked Loop (PLL) added in this figure. This addition demonstrates in a simple form how a large majority of the researchers from the VSM research community implement this concept. The angular momentum M, and damping factor K_D from the swing equation are mostly used to provide virtual inertia and damping respectively, while the PLL would provide the angle θ_s of the grid terminal voltages.

There are several research groups that took advantage of the power balance concept recognizing an opportunity to only use power balance (swing equation) for synchronization with the grid once the VSM converter is connected [127], [131], [134], [136], [137], [139].

Additionally, despite the fact that the virtual synchronous machine concept has been a well understood and widely accepted concept with more than a thousand papers on the topic, there has not been reported a systematic assessment of electromechanical duality between the synchronous machines and the power electronics converters. Furthermore, dynamic, large-signal models of the two are very different, that as a consequence, only engineers who understand well both, machines and converters, would be able to perform system-level analysis encompassing both concepts.

The contributions reported in this dissertation regarding VSM-based operation can be described with the assistance of the helpful (while oversimplified) illustration shown in Figure 1-12.

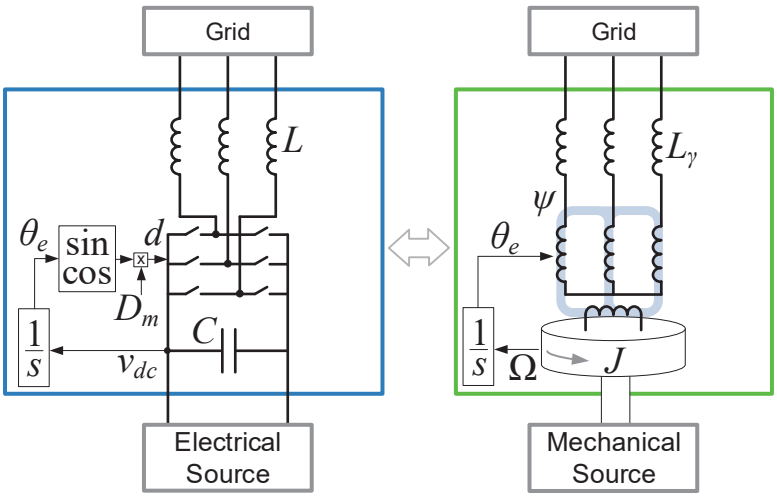

Figure 1-12: Simplified representation of the duality between the power converter and the synchronous machine

The following are the contributions reported in this dissertation:

- Developed is a dynamic model of the synchronous machine based on electromechanical duality with power converters. This model completely resembles the widely used average model of the voltage source converters and represents mathematical alteration of the known machine model [167] with no loss of generality. Having the machine model restructured to resemble the configuration of the power converter model enables two important things: accurate and simple hardware emulation of any type of synchronous machine, and now both synchronous machines and power converters can be modeled using the same model structure.

- Electromechanical duality analysis reveals insights that were not clearly shown previously. A common misconception that inductance of the synchronous machine stator winding is equivalent to the converter output filter inductance is now substituted with the claim that stator leakage inductance L_γ is the one that directly corresponds to the converter output filter inductance L (Figure 1-12 illustrates this in a simple form). Moreover, fluxes in the machine ψ_d, ψ_q, are directly proportional to the converter duty cycles d_d, and $\underline{d_q}$ as the main linking agents in the power conversion process – rotor to stator, and DC-link to AC side respectively. Furthermore, synchronous machine rotation can be emulated by applying a sinusoidal function on the angle θ_e obtained via DC-link voltage integration (this is illustrated in Figure 1-12). This understanding allows for any type of machine to be emulated with a power electronics converter using control approach reported in this dissertation (Chapter 5); in fact, all isotropic or anisotropic machines with any number of poles and damper windings can be effectively emulated using this process.

- Using electrical-mechanical duality, it became apparent that the swing equation (1.4) can be implemented in the converter in a much simpler form which exactly replicates machine synchronization. Figure 1-12 illustrates that converter synchronization can now be achieved by simply measuring and integrating DC-link voltage in power converters and still fully comply with the power balance concept. For instance, assuming modulation index (D_m) from Figure 1-12 is constant representing a fixed flux, integration of the DC-link voltage is

all that needs to be done in the converter to make it emulate the permanent magnet synchronous machine.

- Applying simple replacement of dynamics reported in Chapter 5, converter with a finite capacitor *C* on the DC-link can mimic any inertia *J* as long as there is a sufficient energy available in the primary source. This capability can have a large impact on the small-signal stability, as will be discussed later.

1.7 Dissertation Outline

This dissertation is organized in eight chapters starting with the current one that provides motivation, objectives, and contribution of the reported work.

Chapter 2 offers a background theory (models, equations, etc.) and conventions used throughout the dissertation.

Chapter 3 addresses terminal behavioral modeling of three-phase converters. Models are derived for all types of three-phase converters, together with the generalized decoupling matrix that can be used for any type of AC-converters or networks (AC-DC, DC-AC, and AC-AC), to completely decouple source and load dynamics from the measured frequency responses. At the end, experimental demonstration of the methodology is reported using 30 kW voltage source converter operating as both inverter and active rectifier.

In Chapter 4 an alternative way to access system stability on-line is proposed. It is shown how a converter already operating in the system can perform an AC-sweep *in-situ* (via duty cycle perturbations) and obtain source output impedance and load input admittance. Using the unterminated frequency responses derived in Chapter 3, it is possible to calculate all terminal impedances at both input and output for the online stability assessment. Both simulation and experimental demonstration of the concept are reported at the end of the chapter.

Chapter 5 starts with the synchronous machine model restructuring based on the electromechanical duality with power converters. Once the model is completed, the chapter further progresses into dynamic characterization of a particular 4-pole synchronous generator whose main frequency responses are obtained and used as a basis for the virtual machine emulation. Finally, the last part of the chapter reports successful machine emulation with a 30 kW voltage source converter.

In Chapter 6 the virtual inertia concept is developed and demonstrated experimentally in the droop controlled electronic generator. The same chapter reports the system-level operation where a synchronous machine and an electronic generator operate together, coupled on the AC-side through the inductive interconnection impedance and synchronize to each other with no help of the conventional PLL, using only DC-link voltage integration technique. Multi-source system simulation is shown at the end of the chapter to illustrate how virtual inertia can aid mitigation of small-signal system instability.

Chapter 7 provides a summary of the reported methodologies. Additionally, it discusses possibilities of research extensions offering some new insights that could not have been included in the scope of this dissertation. These insights can possibly be developed into good directions for future research.

A list of references is provided in the last chapter.

2. Dynamic Models of Voltage Source Converters and Synchronous Machines

This chapter presents known mathematical models, and conventions used in this dissertation, with the purpose to provide supporting material for the seamless information flow in the following chapters.

2.1 Dynamic Average Model of a Three-Phase Power Electronics Converter

Although the generic dynamic average model of the three-phase power electronic converters is known and widely used for a very long time, some details will be repeated here for completeness. A two-level voltage source converter representation is illustrated in Figure 2-1, and its dynamic model is shown in Figure 2-2 and described with (2.3)-(2.6).

Derived almost a century ago, the Clarke and Park transformation is one of the most powerful mathematical tools used not only to simulate three phase systems, but to control them as well [167], [168]. Time variant, three-phase variables can be represented as time invariant using simple *d-q* transformation (2.1). The shown form features the coefficient $\sqrt{2/3}$ due to the power-invariance. This form applied to the phase-neutral variables will be used throughout this dissertation, although phase-phase form is often used as well [82].

$$\mathbf{T}_{abc\to dqo} = \sqrt{\frac{2}{3}}\begin{bmatrix} \cos(\theta) & \cos(\theta-2\pi/3) & \cos(\theta+2\pi/3) \\ -\sin(\theta) & -\sin(\theta-2\pi/3) & -\sin(\theta+2\pi/3) \\ 1/\sqrt{2} & 1/\sqrt{2} & 1/\sqrt{2} \end{bmatrix} \tag{2.1}$$

The inverse form (2.2) calculates out *abc* variables from *dqo* ones.

$$\mathbf{T}_{dqo\to abc} = \mathbf{T}_{abc\to dqo}^{-1} = \mathbf{T}_{abc\to dqo}^{T} = \sqrt{\frac{2}{3}}\begin{bmatrix} \cos(\theta) & -\sin(\theta) & 1/\sqrt{2} \\ \cos(\theta-2\pi/3) & -\sin(\theta-2\pi/3) & 1/\sqrt{2} \\ \cos(\theta+2\pi/3) & -\sin(\theta+2\pi/3) & 1/\sqrt{2} \end{bmatrix} \tag{2.2}$$

.

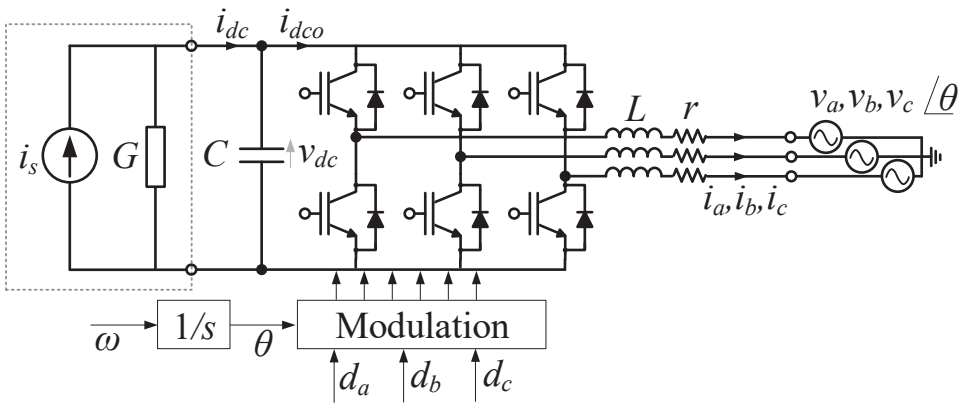

Figure 2-1: Two-level power electronics converter representation

The following is description of variables/parameters:

v_a, v_b, v_c – terminal, grid voltages

i_a, i_b, i_c – output currents

d_a, d_b, d_c – duty cycles

L – output filter inductor

r – resistance of the output inductor

C – DC-link capacitor

i_s – primary source current

i_{dco} – DC current

G – primary source conductance

i_{dc} – primary source DC current

v_{dc} – DC-link voltage

θ – grid voltage angle in rad

ω – grid angular frequency

Using (2.1), and neglecting the homopolar components (balanced and symmetrical system is assumed), the following set of equations delineate the converter *d-q* model [82]:

$$\begin{aligned} v_d &= v_{dc} d_d - r i_d - L \frac{\mathrm{d}i_d}{\mathrm{d}t} + \omega L i_q \\ v_q &= v_{dc} d_q - r i_q - L \frac{\mathrm{d}i_q}{\mathrm{d}t} - \omega L i_d \end{aligned} \tag{2.3}$$

$$C \frac{\mathrm{d}v_{dc}}{\mathrm{d}t} = i_s - i_{dco} - G v_{dc} \tag{2.4}$$

$$i_{dco} = d_d i_d + d_q i_q \tag{2.5}$$

$$\theta = \frac{1}{s}\omega \tag{2.6}$$

Angle θ is typically obtained using the phase-locked loop. The most common and famous for its simplicity is synchronous reference frame (SRF) PLL shown in Figure 2-2 [204].

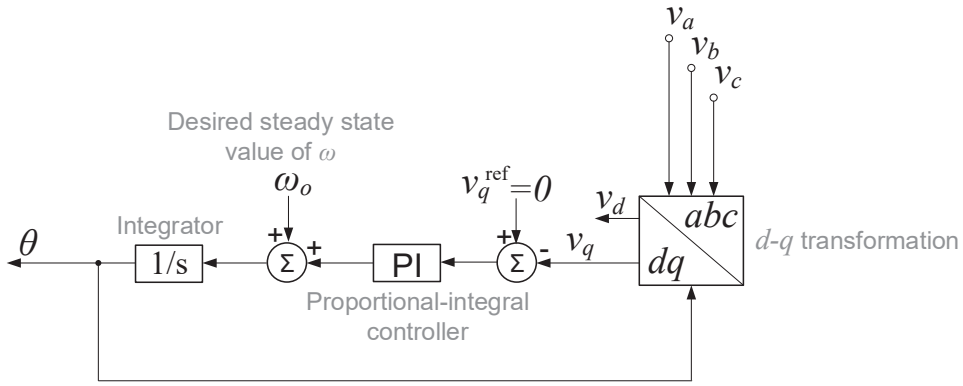

Figure 2-2: Synchronous reference frame PLL

Some other examples of the PLL implementation can be found in [128]-[130].

Finally, the dynamic average model of the converter from Figure 2-1 is shown in Figure 2-3 below.

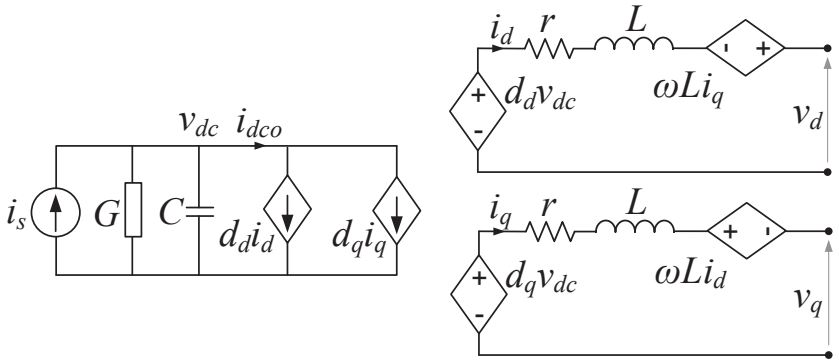

Figure 2-3: *d-q* model of the DC-AC voltage source power converter

2.2 Dynamic Model of a Synchronous Machine

Figure 2-4 illustrates the four-pole synchronous machine with marked *a*,*b*,*c* and *d*-*q* axes. The direct *d*-axis is aligned with the north-pole of the machine while the quadrature *q*-axis is positioned 90 electrical degrees ahead of *d* . The picture below depicts the four pole machine with mechanical

units. The corresponding electrical units are p times higher where p represents the number of pole-pairs of the machine, in this case p=2.

The following equations describe the dynamic model in the synchronous d-q frame [167,168]:

$$\begin{aligned} v_d &= -r_s i_d - \omega_e \psi_q + \frac{\mathrm{d}\psi_d}{\mathrm{d}t} \\ v_q &= -r_s i_q + \omega_e \psi_d + \frac{\mathrm{d}\psi_q}{\mathrm{d}t} \end{aligned} \tag{2.7}$$

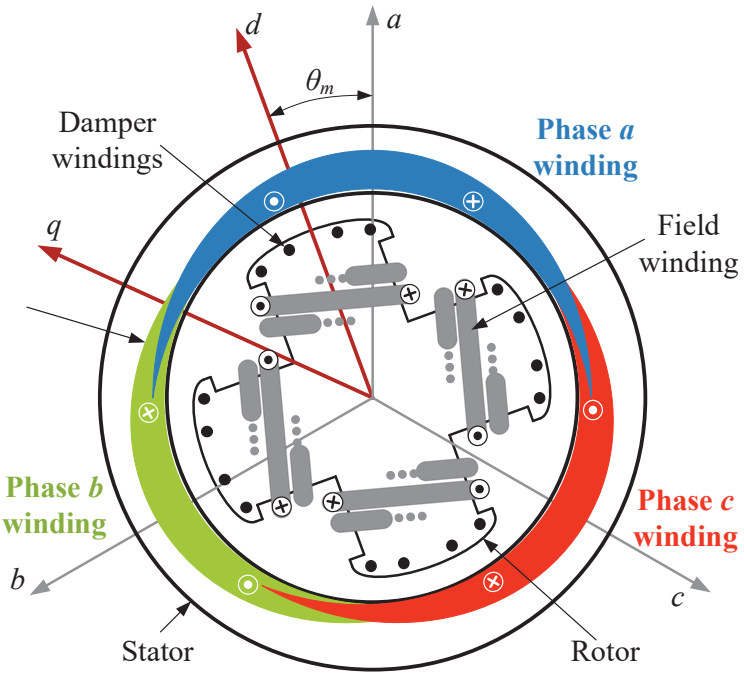

Figure 2-4: Salient-pole synchronous machine representation

$$\begin{aligned} v_F &= r_F i_F + \frac{\mathrm{d}\psi_F}{\mathrm{d}t} \\ 0 &= r_D i_D + \frac{\mathrm{d}\psi_D}{\mathrm{d}t} \\ 0 &= r_Q i_Q + \frac{\mathrm{d}\psi_Q}{\mathrm{d}t} \end{aligned} \tag{2.8}$$

Where fluxes in d and q axis are respectively:

$$\psi_d = -L_d i_d + M_F i_F + M_D i_D \qquad \psi_q = -L_q i_q + M_Q i_Q$$

$$\psi_F = L_F i_F + M_{FD} i_D - \sqrt{\frac{3}{2}} M_F i_d \qquad \psi_Q = L_Q i_Q - \sqrt{\frac{3}{2}} M_Q i_q \tag{2.9}$$

$$\psi_D = L_D i_D + M_{FD} i_F - \sqrt{\frac{3}{2}} M_D i_d$$

$$T_e = p(\psi_d i_q - \psi_d i_q) \tag{2.10}$$

$$\omega_e = p\Omega = \dot{\theta}_e \tag{2.11}$$

$$\theta_e = p\theta_m \tag{2.12}$$

Mechanical equation (Newton's motion equation) is:

$$J \frac{\mathrm{d}\Omega}{\mathrm{d}t} = T_m - T_e - k_f \Omega \tag{2.13}$$

The following are machine parameters:

v_d, v_q – stator terminal voltages

i_d, i_q – stator currents

ψ_d, ψ_q – stator flux linkages

i_D, i_Q – currents in damper windings

ψ_D, ψ_Q – damper winding fluxes

M_D – *d*-axis damper to stator mutual inductance

ψ_F – field winding flux

M_Q – *q*-axis damper to stator mutual inductance

M_F – field to stator mutual inductance

M_{FD} – field to damper winding mutual inductance

i_F – field current

v_F – field voltage

L_d – stator self inductance in *d*-axis

L_F – field self inductance in *d*-axis

L_q – stator self inductance in *q*-axis

L_D – damper self inductance in *d*-axis

J – machine moment of inertia

L_Q – damper self inductance in *d*-axis

T_m – mechanical torque

ω_e, θ_e – electrical speed, angle

T_e – electrical torque

Ω, θ_m – mechanical speed, angle

k_f – machine friction coefficient

r_s – stator resistance

p – pole pairs

r_D, r_Q, r_F – damper and field winding resistances

The coefficient $\sqrt{3/2}$ in the above equations is the consequence of chosen power invariant *d-q* transformation (2.1).

Figure 2-5 shows a dynamic synchronous machine model developed using (2.7) - (2.13). It comprises one damper and field winding in *d* axis and one damper winding in *q* axis.

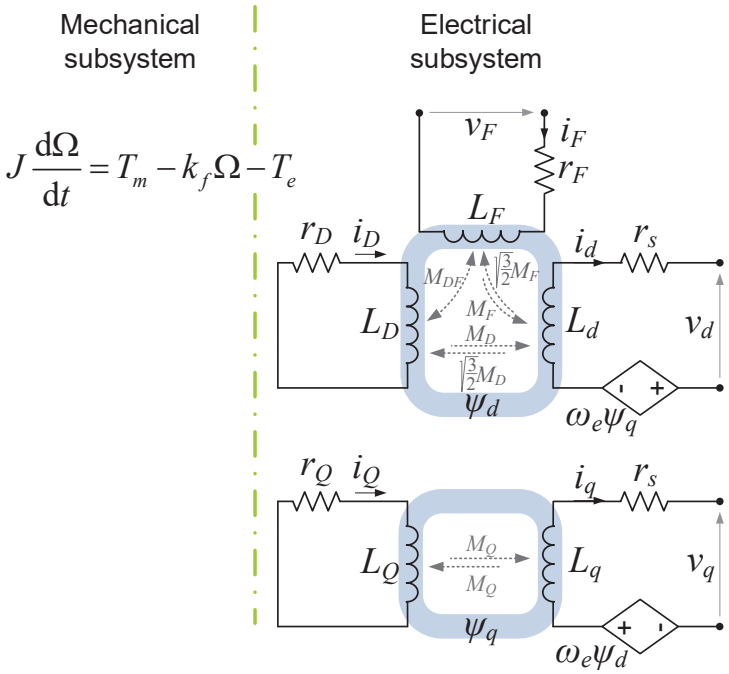

Figure 2-5: Synchronous machine dynamic model representation

It is important to note that several assumptions corresponding to above shown and later derived models are made:

- The stator windings are sinusoidally distributed along the air gap
- Magnetic saturation and hysteresis are neglected
- The three-phase system is balanced and symmetrical

3. Unterminated, Low-Frequency Terminal-Behavioral Model of Three-Phase Converters and Networks

Frequency-domain terminal-behavioral modeling of AC systems is unquestionably attracting more and more interest in engineering practice. As seen in Chapter 1, new electronic power distribution systems built for airplanes, ships, electric vehicles, data-centers, and even homes, dominantly comprise a variety of power electronics converters with very different dynamic characteristics. If their behavior is not examined carefully before a system is integrated, instability can happen at some point during operation.

This chapter addresses low-frequency terminal-behavioral modeling of three-phase converters where the dynamics of the converter can be captured on-line and later decoupled from the source and load in order to get an unterminated model of a particular converter (or a system). These, so-called "black-box" models can be accurate up to half of the switching frequency (due to aliasing), and unfortunately never attained a widespread use in the engineering practice mostly due to the difficulties associated with the transfer functions measurement procedure. In order to obtain an unterminated model of a converter, it had to be removed from the original environment and connected to the high bandwidth voltage source and current sink for easier decoupling of the source and the load dynamics. This problem was a motivation for this work, and this chapter describes an on-line converter characterization procedure where the converter under test can remain working in the original environment, at a particular operating point, being connected to any type of the source and the load while the terminated frequency response characteristics are obtained. The source and load dynamics can then be decoupled from the measured frequency responses using, here proposed, linear transformation matrix. The experimental demonstration of the proposed methodology will be presented as well and at the end of this chapter.

3.1 Terminal-Behavioral Modeling of Three-phase DC-AC Converters (Inverters)

As shown in Figure 3-1, by expanding the two-port network from Figure 2-1 into a three-port network a terminal-behavioral model of three-phase converters can be developed. This figure shows both, a simplified circuit form (with variables in the matrix form) terminated with DC source and three-phase load, and an expanded three-port network form.

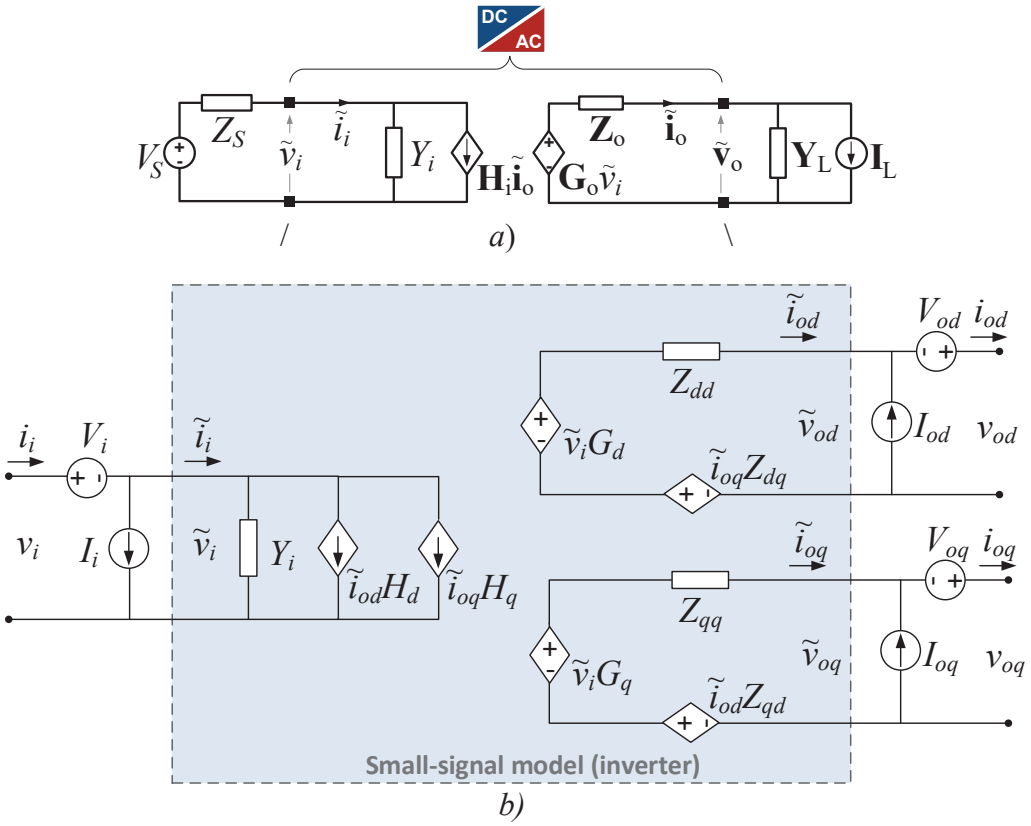

Figure 3-1: Terminal-behavioral model in synchronous *d-q* frame of a three-phase DC-AC converter; three-port network model *a)* simplified, and *b)* expanded form

Its small-signal subsystem can be simply represented by the following expression:

$$\begin{bmatrix} \tilde{\mathbf{v}}_o \\ \tilde{i}_i \end{bmatrix} = \begin{bmatrix} \mathbf{G}_o(s) & -\mathbf{Z}_o(s) \\ Y_i(s) & \mathbf{H}_i(s) \end{bmatrix} \cdot \begin{bmatrix} \tilde{v}_i \\ \tilde{\mathbf{i}}_o \end{bmatrix} \tag{3.1}$$

where

$$\tilde{v}_i,\ \tilde{i}_i,\ \tilde{\mathbf{v}}_o = \begin{bmatrix} \tilde{v}_{od} \\ \tilde{v}_{oq} \end{bmatrix},\ \tilde{\mathbf{i}}_o = \begin{bmatrix} \tilde{i}_{od} \\ \tilde{i}_{oq} \end{bmatrix} \tag{3.2}$$

are small-signal input and output voltages and currents, and

$$\mathbf{G}_o = \begin{bmatrix} G_d(s) \\ G_q(s) \end{bmatrix},\quad \mathbf{Z}_o = \begin{bmatrix} Z_{dd}(s) & Z_{dq}(s) \\ Z_{qd}(s) & Z_{qq}(s) \end{bmatrix},$$
$$Y_i(s),\qquad \mathbf{H}_i = \begin{bmatrix} H_d(s) & H_d(s) \end{bmatrix}; \tag{3.3}$$

are matrices of small-signal, unterminated transfer functions, namely: $\mathbf{G}_o$ - audio susceptibility, $\mathbf{Z}_o$ - output impedance, Y_i - input admittance and $\mathbf{H}_i$ - back current gain.

To expand (3.1) into a system that includes an operating point around which the three-phase converter (network) is linearized, the form (3.4) is obtained by using general expression $x = X + \tilde{x}$.

$$\begin{bmatrix} \mathbf{v}_o \\ i_i \end{bmatrix} = \begin{bmatrix} \mathbf{G}_o(s) & -\mathbf{Z}_o(s) \\ Y_i(s) & \mathbf{H}_i(s) \end{bmatrix} \cdot \begin{bmatrix} v_i - V_i \\ \mathbf{i}_o - \mathbf{I}_o \end{bmatrix} + \begin{bmatrix} \mathbf{V}_o \\ I_i \end{bmatrix} \tag{3.4}$$

where:

$$v_i,\ i_i,\ \mathbf{v}_o = \begin{bmatrix} v_{od} \\ v_{oq} \end{bmatrix},\ \mathbf{i}_o = \begin{bmatrix} i_{od} \\ i_{oq} \end{bmatrix} \tag{3.5}$$

$$V_i,\ I_i,\ \mathbf{V}_o = \begin{bmatrix} V_{od} \\ V_{oq} \end{bmatrix}, \mathbf{I}_o = \begin{bmatrix} I_{od} \\ I_{oq} \end{bmatrix} \tag{3.6}$$

As previously mentioned, this modeling requires transfer functions to be obtained in the *d-q* coordinates. Considering the three-port network shown in Figure 3-1, and assuming that small-signal variables are accessible through measurements (input and output currents and voltages in the *d-q* domain), transfer functions (3.7 – 3.9) can be defined, with the sub-script *m* denoting "measured".

From perturbation at interface **I** (input side) (Figure 3-2):

$$G_{dm} = \frac{\tilde{v}_{od}^{I}}{\tilde{v}_{i}^{I}},\ G_{qm} = \frac{\tilde{v}_{oq}^{I}}{\tilde{v}_{i}^{I}},\ Y_{im} = \frac{\tilde{i}_{id}^{I}}{\tilde{v}_{i}^{I}}; \tag{3.7}$$

from perturbation at interface **II** (*d*-axis, output side):

$$Z_{ddm} = -\frac{\tilde{v}_{od}^{II}}{\tilde{i}_{od}^{II}},\ Z_{qdm} = -\frac{\tilde{v}_{oq}^{II}}{\tilde{i}_{od}^{II}},\ H_{dm} = \frac{\tilde{i}_{i}^{II}}{\tilde{i}_{od}^{II}}; \tag{3.8}$$

from perturbation at interface **III** (*q*-axis, output side):

$$Z_{dqm} = -\frac{\tilde{v}_{od}^{III}}{\tilde{i}_{oq}^{III}},\ Z_{qqm} = -\frac{\tilde{v}_{oq}^{III}}{\tilde{i}_{oq}^{III}},\ H_{qm} = \frac{\tilde{i}_{i}^{III}}{\tilde{i}_{oq}^{III}}; \tag{3.9}$$

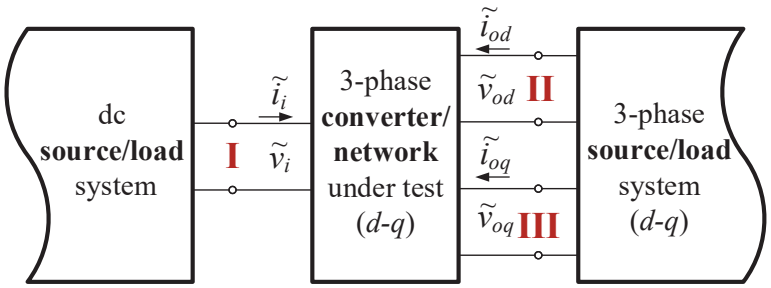

Figure 3-2: Perturbation sequence in *d-q* frame for the inverter

Due to the fact that the above shown (measured) transfer functions comprise source and load dynamics, they cannot be used directly to define the terminal-behavioral model (3.4). Consequently, a termination (or decoupling) procedure has to be performed.

The small-signal model (3.1) can now be rewritten in the following form:

$$\begin{aligned}\tilde{v}_{od} &= G_d \cdot \tilde{v}_i - Z_{dd} \cdot \tilde{i}_{od} - Z_{dq} \cdot \tilde{i}_{oq} \\ \tilde{v}_{oq} &= G_q \cdot \tilde{v}_i - Z_{qd} \cdot \tilde{i}_{od} - Z_{qq} \cdot \tilde{i}_{oq} \\ \tilde{i}_i &= Y_i \cdot \tilde{v}_i + H_d \cdot \tilde{i}_{od} + H_q \cdot \tilde{i}_{oq}\end{aligned} \tag{3.10}$$

Using (3.7) it can be written:

$$\tilde{v}_{od}^I = G_{dm} \cdot \tilde{v}_i^I \tag{3.11}$$

while combining (3.10), and (3.11):

$$\tilde{v}_{od}^I = G_{dm} \cdot \tilde{v}_i^I = G_d \cdot \tilde{v}_i^I - Z_{dd} \cdot \tilde{i}_{od}^I - Z_{dq} \cdot \tilde{i}_{oq}^I \tag{3.12}$$

Now deriving (3.12) with $\tilde{v}_i^I$ further simplifies the expression, and it can be obtained:

$$G_{dm} = G_d - Z_{dd} \cdot \frac{\tilde{i}_{od}^I}{\tilde{v}_i^I} - Z_{dq} \cdot \frac{\tilde{i}_{oq}^I}{\tilde{v}_i^I} \tag{3.13}$$

This gives the first relationship between unterminated and terminated transfer functions, but evidently cannot be solved directly since it has more unknowns than equations.

Continuing the same procedure for the next transfer function from the measurement point **I**, G_{qm}, and combining it with the second equation from (3.10), it can be obtained:

$$G_{qm} = G_q - Z_{dq} \cdot \frac{\tilde{i}_{od}^I}{\tilde{v}_i^I} - Z_{qq} \cdot \frac{\tilde{i}_{oq}^I}{\tilde{v}_i^I} \tag{3.14}$$

Combining expression for Y_{im} and the third equation from (3.10), it can be written:

$$Y_{im} = Y_i + H_d \cdot \frac{\tilde{i}_{od}^I}{\tilde{v}_i^I} + H_q \cdot \frac{\tilde{i}_{oq}^I}{\tilde{v}_i^I} \tag{3.15}$$

By looking at the previous three expressions (3.13-3.15), it can be noticed that all three expressions comprise two common transfer functions:

$$\frac{\tilde{i}_{od}^I}{\tilde{v}_i^I} \text{ and } \frac{\tilde{i}_{oq}^I}{\tilde{v}_i^I} \tag{3.16}$$

Since all of the small-signal variables (input and output currents and voltages) are already obtained from the measurement at point **I**, transfer functions (3.16) can be easily calculated out. Both can be defined as *TG* – transconductance, due to the physical dimension (output current over input voltage).

$$TG_{dm} = \frac{\tilde{i}_{od}^I}{\tilde{v}_i^I} \text{ and } TG_{qm} = \frac{\tilde{i}_{oq}^I}{\tilde{v}_i^I} \tag{3.17}$$

The system (3.13-3.15) can now be rewritten as:

$$\begin{aligned} G_{dm} &= G_d - Z_{dd} \cdot TG_{dm} - Z_{dq} \cdot TG_{qm} \\ G_{qm} &= G_q - Z_{qd} \cdot TG_{dm} - Z_{qq} \cdot TG_{qm} \\ Y_{im} &= Y_i + H_d \cdot TG_{dm} + H_q \cdot TG_{qm} \end{aligned} \tag{3.18}$$

The system above now features three equations but nine unknowns, and cannot be solved for the unterminated transfer functions.

All equations given above were used to build the system of equations for the transfer functions obtained by perturbing the system at the input - interface **I**). Following the same procedure for the measurements at points **II**, and **III**, the results shown below can be obtained.

The system of transfer functions obtained from perturbation at the point **II**:

$$
\begin{aligned}
-Z_{ddm} &= G_d \cdot TR_{dm} - Z_{dd} - Z_{dq} \cdot TI_{qdm} \\
-Z_{qdm} &= G_q \cdot TR_{dm} - Z_{qd} - Z_{qq} \cdot TI_{qdm} \\
H_{dm} &= Y_i \cdot TR_{dm} + H_d + H_q \cdot TI_{qdm}
\end{aligned}
\tag{3.19}
$$

The system (3.19) comprises two additional transfer functions to be defined. The first one can be defined as *TR*-transconductance due to a physical dimension of the ratio of small-signal variables ratio (input voltage over output current), and the second one as a dimensionless transfer function *TI:*

$$
TR_{dm} = \frac{\tilde{v}_i^{II}}{\tilde{i}_{od}^{II}} \text{ and } TI_{qdm} = \frac{\tilde{i}_{oq}^{II}}{\tilde{i}_{od}^{II}}
\tag{3.20}
$$

Finally, a system of transfer functions obtained from perturbation performed at the point **III**:

$$
\begin{aligned}
-Z_{dqm} &= G_d \cdot TR_{qm} - Z_{dd} \cdot TI_{dqm} - Z_{dq} \\
-Z_{qqm} &= G_q \cdot TR_{qm} - Z_{qd} \cdot TI_{dqm} - Z_{qq} \\
H_{qm} &= Y_i \cdot TR_{qm} + H_d \cdot TI_{dqm} + H_q
\end{aligned}
\tag{3.21}
$$

For this set of equations, the following transfer functions have to be defined:

$$
TR_{qm} = \frac{\tilde{v}_i^{III}}{\tilde{i}_{oq}^{III}} \text{ and } TI_{dqm} = \frac{\tilde{i}_{od}^{III}}{\tilde{i}_{oq}^{III}}
\tag{3.22}
$$

At last, the system of nine equations (3.18), (3.19), (3.21), and nine unknowns can be built and solved for the unterminated transfer functions.

$$
\begin{bmatrix} \mathbf{G}_{\mathrm{o}} & -\mathbf{Z}_{\mathrm{o}} \\ Y_i & \mathbf{H}_{\mathrm{i}} \end{bmatrix} = \begin{bmatrix} \mathbf{G}_{\mathrm{om}} & -\mathbf{Z}_{\mathrm{om}} \\ Y_{im} & \mathbf{H}_{\mathrm{im}} \end{bmatrix} \cdot \left[\mathbf{T}^{DC\text{-}AC} \right]^{-1}
\tag{3.23}
$$

where

$$
\mathbf{T}^{dc\text{-}ac} = \begin{bmatrix} 1 & TR_{dm} & TR_{qm} \\ TG_{dm} & 1 & TI_{dqm} \\ TG_{qm} & TI_{qdm} & 1 \end{bmatrix}
\tag{3.24}
$$

is decoupling matrix comprising previously defined transfer functions (3.17), (3.20), and (3.22).

3.2 Terminal-Behavioral Modeling of Three-phase AC-DC Converters (Active Rectifiers)

This case is completely dual to 3.1, with the minor difference in the transfer functions/variable definitions as shown below only for thoroughness. Figure 3-3 shows three-port network of the AC-DC converter (active rectifier) in simplified circuit form terminated with three phase source and DC load.

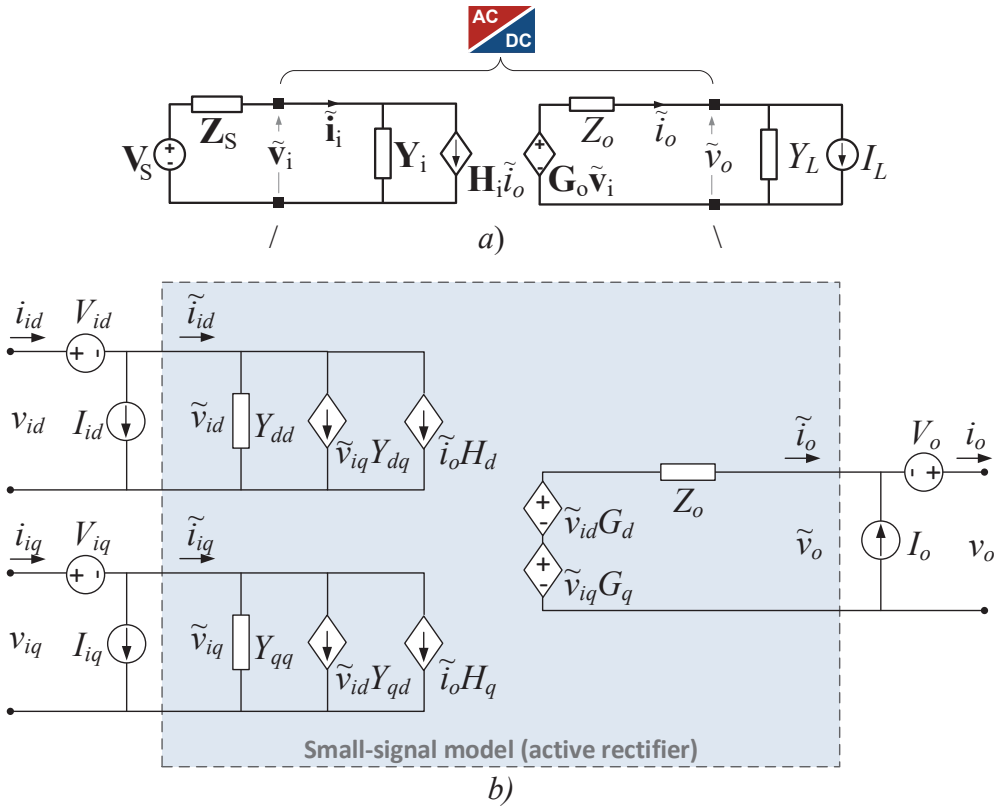

Figure 3-3: Terminal-behavioral model in synchronous *d-q* frame of a three-phase AC-DC converter; three-port network model *a)* simplified, and *b)* expanded form

According to Figure 3-3b, it can be written for its small-signal model:

$$\begin{bmatrix} v_o \\ \mathbf{i}_i \end{bmatrix} = \begin{bmatrix} \mathbf{G}_o(s) & -Z_o(s) \\ \mathbf{Y}_i(s) & \mathbf{H}_i(s) \end{bmatrix} \cdot \begin{bmatrix} \mathbf{v}_i - \mathbf{V}_i \\ i_o - I_o \end{bmatrix} + \begin{bmatrix} V_o \\ \mathbf{I}_i \end{bmatrix} \tag{3.25}$$

where,

$$\mathbf{v}_{\mathrm{i}} = \begin{bmatrix} v_{id} \\ v_{iq} \end{bmatrix}, \mathbf{i}_{\mathrm{i}} = \begin{bmatrix} i_{id} \\ i_{iq} \end{bmatrix}, v_o, i_o \tag{3.26}$$

$$\mathbf{V}_{\mathrm{i}} = \begin{bmatrix} V_{id} \\ V_{iq} \end{bmatrix}, \mathbf{I}_{\mathrm{i}} = \begin{bmatrix} I_{id} \\ I_{iq} \end{bmatrix}, V_o, I_o \tag{3.27}$$

$$\begin{aligned} \mathbf{G}_o &= \begin{bmatrix} G_d & G_q \end{bmatrix}, & Z_o, \\ \mathbf{Y}_{\mathrm{i}} &= \begin{bmatrix} Y_{dd} & Y_{dq} \\ Y_{qd} & Y_{qq} \end{bmatrix}, & \mathbf{H}_{\mathrm{i}} = \begin{bmatrix} H_d \\ H_q \end{bmatrix}; \end{aligned} \tag{3.28}$$

In this case,

$$\begin{bmatrix} \mathbf{G}_{\mathrm{o}} & -Z_o \\ \mathbf{Y}_{\mathrm{i}} & \mathbf{H}_{\mathrm{i}} \end{bmatrix} = \begin{bmatrix} \mathbf{G}_{\mathrm{om}} & -Z_{\mathrm{om}} \\ \mathbf{Y}_{\mathrm{im}} & \mathbf{H}_{\mathrm{im}} \end{bmatrix} \cdot \left[\mathbf{T}^{AC\text{-}DC} \right]^{-1} \tag{3.29}$$

where decoupling matrix has a form:

$$\mathbf{T}^{ac\text{-}dc} = \begin{bmatrix} 1 & TV_{dqm} & TR_{dm} \\ TV_{qdm} & 1 & TR_{qm} \\ TG_{dm} & TG_{qm} & 1 \end{bmatrix} \tag{3.30}$$

and comprises the following transfer functions (according to Figure 3-4):

- dimensionless transfer functions *TV* defined as:

$$TV_{qdm} = \frac{\tilde{v}_{iq}^{I}}{\tilde{v}_{id}^{I}} \text{ and } TV_{dqm} = \frac{\tilde{v}_{id}^{II}}{\tilde{v}_{iq}^{II}}; \tag{3.31}$$

- *TG* – transconductance transfer functions:

$$TG_{dm} = \frac{\tilde{i}_{o}^{I}}{\tilde{v}_{id}^{I}} \text{ and } TG_{qm} = \frac{\tilde{i}_{o}^{II}}{\tilde{v}_{iq}^{II}}; \tag{3.32}$$

- *TR* – transresistance transfer functions:

$$TR_{dm} = \frac{\tilde{v}_{id}^{III}}{\tilde{i}_{o}^{III}} \text{ and } TR_{qm} = \frac{\tilde{v}_{iq}^{III}}{\tilde{i}_{o}^{III}} \tag{3.33}$$

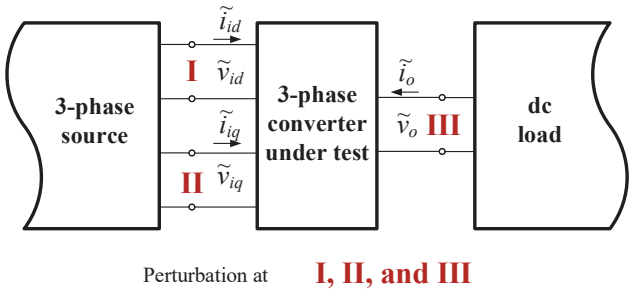

Figure 3-4: Perturbation sequence in *d-q* frame for the active rectifier

3.3 Terminal-Behavioral Modeling of Three-phase AC-AC Converters and Networks

Expanding the three-port network from Figures 3-1, and 3-3 to a four-port network, a terminal-behavioral model of an AC-AC converter (or any three-phase network in general) can be developed. This expanded model is shown in Figure 3-5. This figure shows both a simplified circuit form terminated with a three phase-source and a three-phase load.

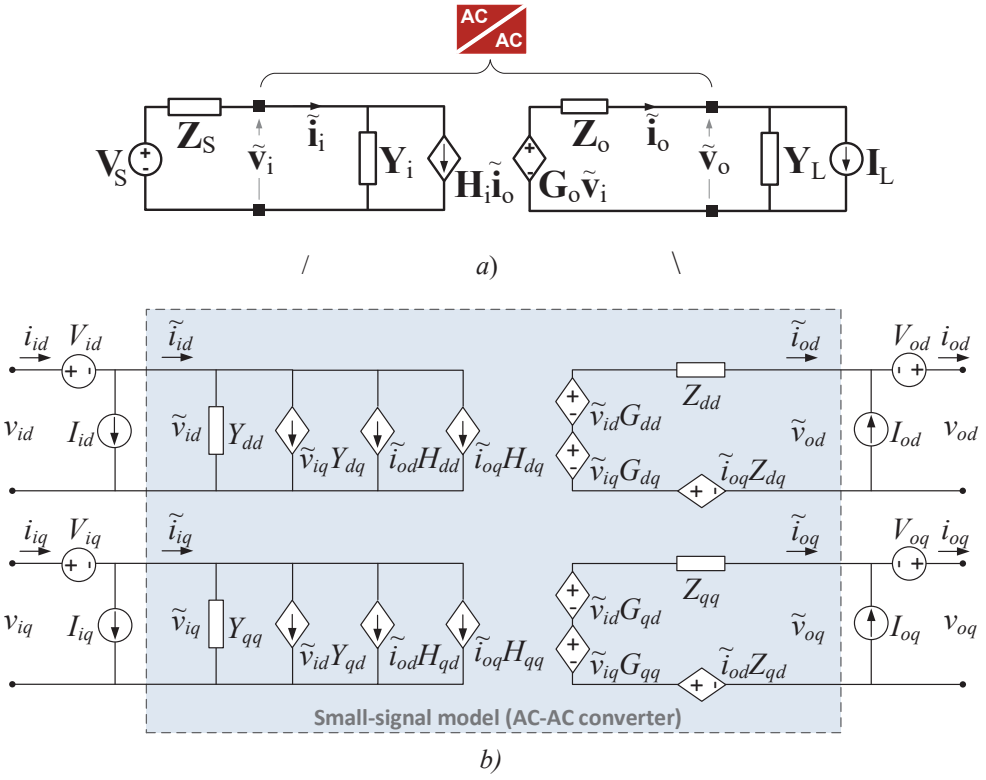

Figure 3-5: Modular terminal-behavioral model in synchronous *d-q* frame of a generic, balanced three-phase AC-AC converter or network

Its small-signal model can be, as well represented by:

$$\begin{bmatrix}\mathbf{v}_{\mathrm{o}}\\ \mathbf{i}_{\mathrm{i}}\end{bmatrix}=\begin{bmatrix}\mathbf{G}_{\mathrm{o}}(s) & \text{-}\mathbf{Z}_{\mathrm{o}}(s)\\ \mathbf{Y}_{\mathrm{i}}(s) & \mathbf{H}_{\mathrm{i}}(s)\end{bmatrix}\cdot\begin{bmatrix}\mathbf{v}_{\mathrm{i}}-\mathbf{V}_{\mathrm{i}}\\ \mathbf{i}_{\mathrm{o}}-\mathbf{I}_{\mathrm{o}}\end{bmatrix}+\begin{bmatrix}\mathbf{V}_{\mathrm{o}}\\ \mathbf{I}_{\mathrm{i}}\end{bmatrix} \tag{3.34}$$

where

$$\begin{aligned}\mathbf{G}_{\mathrm{o}}&=\begin{bmatrix}G_{dd}(s) & G_{dq}(s)\\ G_{qd}(s) & G_{qq}(s)\end{bmatrix},\quad \mathbf{Z}_{\mathrm{o}}=\begin{bmatrix}Z_{dd}(s) & Z_{dq}(s)\\ Z_{qd}(s) & Z_{qq}(s)\end{bmatrix},\\ \mathbf{Y}_{\mathrm{i}}&=\begin{bmatrix}Y_{dd}(s) & Y_{dq}(s)\\ Y_{qd}(s) & Y_{qq}(s)\end{bmatrix},\qquad \mathbf{H}_{\mathrm{i}}=\begin{bmatrix}H_{dd}(s) & H_{dq}(s)\\ H_{qd}(s) & H_{qq}(s)\end{bmatrix};\end{aligned} \tag{3.35}$$

$$\mathbf{v}_{\mathrm{o}}=\begin{bmatrix}v_{od}\\ v_{oq}\end{bmatrix},\mathbf{v}_{\mathrm{i}}=\begin{bmatrix}v_{id}\\ v_{iq}\end{bmatrix},\mathbf{i}_{\mathrm{o}}=\begin{bmatrix}i_{od}\\ i_{oq}\end{bmatrix},\mathbf{i}_{\mathrm{i}}=\begin{bmatrix}i_{id}\\ i_{iq}\end{bmatrix} \tag{3.36}$$

$$\mathbf{V}_{\mathrm{o}}=\begin{bmatrix}V_{od}\\ V_{oq}\end{bmatrix},\mathbf{V}_{\mathrm{i}}=\begin{bmatrix}V_{id}\\ V_{iq}\end{bmatrix},\mathbf{I}_{\mathrm{o}}=\begin{bmatrix}I_{od}\\ I_{oq}\end{bmatrix},\mathbf{I}_{\mathrm{i}}=\begin{bmatrix}I_{id}\\ I_{iq}\end{bmatrix} \tag{3.37}$$

From perturbation at interface **I** (*d*-axis, input side) (Figure 3-6):

$$G_{ddm}=\frac{\tilde{v}_{od}^{I}}{\tilde{v}_{id}^{I}},\ G_{qdm}=\frac{\tilde{v}_{oq}^{I}}{\tilde{v}_{id}^{I}},\ Y_{ddm}=\frac{\tilde{i}_{id}^{I}}{\tilde{v}_{id}^{I}},\ Y_{qdm}=\frac{\tilde{i}_{iq}^{I}}{\tilde{v}_{id}^{I}}; \tag{3.38}$$

from perturbation at **II** (*q*-axis, input side):

$$G_{dqm}=\frac{\tilde{v}_{od}^{II}}{\tilde{v}_{iq}^{II}},G_{qqm}=\frac{\tilde{v}_{oq}^{II}}{\tilde{v}_{iq}^{II}},\ Y_{dqm}=\frac{\tilde{i}_{id}^{II}}{\tilde{v}_{iq}^{II}},\ Y_{qqm}=\frac{\tilde{i}_{iq}^{II}}{\tilde{v}_{iq}^{II}}; \tag{3.39}$$

from perturbation at **III** (*d*-axis, output side):

$$Z_{ddm}=-\frac{\tilde{v}_{od}^{III}}{\tilde{i}_{od}^{III}},\ Z_{qdm}=-\frac{\tilde{v}_{oq}^{III}}{\tilde{i}_{od}^{III}},\ H_{ddm}=\frac{\tilde{i}_{id}^{III}}{\tilde{i}_{od}^{III}},H_{qdm}=\frac{\tilde{i}_{iq}^{III}}{\tilde{i}_{od}^{III}}; \tag{3.40}$$

from perturbation at **IV** (*q*-axis, output side):

$$Z_{dqm}=-\frac{\tilde{v}_{od}^{IV}}{\tilde{i}_{oq}^{IV}},\ Z_{qqm}=-\frac{\tilde{v}_{oq}^{IV}}{\tilde{i}_{oq}^{IV}},\ H_{dqm}=\frac{\tilde{i}_{id}^{IV}}{\tilde{i}_{oq}^{IV}},H_{qqm}=\frac{\tilde{i}_{iq}^{IV}}{\tilde{i}_{oq}^{IV}}; \tag{3.41}$$

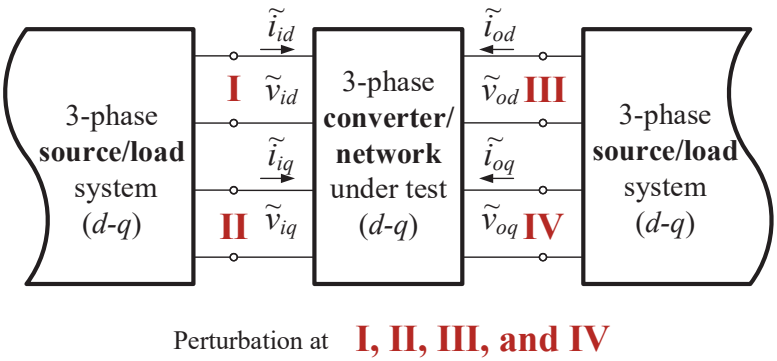

Figure 3-6: Three-phase converter/network in *d-q* frame

Defining

$$TV_{qdm} = \frac{\tilde{v}_{iq}^{I}}{\tilde{v}_{id}^{I}},\ TG_{ddm} = \frac{\tilde{i}_{od}^{I}}{\tilde{v}_{id}^{I}} \text{ and } TG_{qdm} = \frac{\tilde{i}_{oq}^{I}}{\tilde{v}_{id}^{I}} \tag{3.42}$$

obtained via perturbation at the interface **I**, it can be written:

$$\begin{aligned} G_{ddm} &= G_{dd} + G_{dq} \cdot TV_{qdm} - Z_{dd} \cdot TG_{ddm} - Z_{dq} \cdot TG_{qdm} \\ G_{qdm} &= G_{qd} + G_{qq} \cdot TV_{qdm} - Z_{qd} \cdot TG_{ddm} - Z_{qq} \cdot TG_{qdm} \\ Y_{ddm} &= Y_{dd} + Y_{dq} \cdot TV_{qdm} + H_{dd} \cdot TG_{ddm} + H_{dq} \cdot TG_{qdm} \\ Y_{qdm} &= Y_{qd} + Y_{qq} \cdot TV_{qdm} + H_{qd} \cdot TG_{ddm} + H_{qq} \cdot TG_{qdm} \end{aligned} \tag{3.43}$$

Similarly, defining

$$TV_{dqm} = \frac{\tilde{v}_{id}^{II}}{\tilde{v}_{iq}^{II}},\ TG_{dqm} = \frac{\tilde{i}_{od}^{II}}{\tilde{v}_{iq}^{II}} \text{ and } TG_{qqm} = \frac{\tilde{i}_{oq}^{II}}{\tilde{v}_{iq}^{II}} \tag{3.44}$$

system of transfer functions obtained from the perturbation at the interface **II**:

$$\begin{aligned} G_{dqm} &= G_{dd} \cdot TV_{dqm} + G_{dq} - Z_{dd} \cdot TG_{dqm} - Z_{dq} \cdot TG_{qqm} \\ G_{qqm} &= G_{qd} \cdot TV_{dqm} + G_{qq} - Z_{qd} \cdot TG_{dqm} - Z_{qq} \cdot TG_{qqm} \\ Y_{dqm} &= Y_{dd} \cdot TV_{dqm} + Y_{dq} + H_{dd} \cdot TG_{dqm} + H_{dq} \cdot TG_{qqm} \\ Y_{qdm} &= Y_{qd} \cdot TV_{dqm} + Y_{qq} + H_{qd} \cdot TG_{dqm} + H_{qq} \cdot TG_{qqm} \end{aligned} \tag{3.45}$$

Continuing in the same way,

$$TR_{ddm} = \frac{\tilde{v}_{id}^{III}}{\tilde{i}_{od}^{III}},\ TR_{qdm} = \frac{\tilde{v}_{iq}^{III}}{\tilde{i}_{od}^{III}} \text{ and } TI_{qdm} = \frac{\tilde{i}_{oq}^{III}}{\tilde{i}_{od}^{III}} \tag{3.46}$$

$$
\begin{aligned}
-Z_{ddm} &= G_{dd}\cdot TR_{ddm} + G_{dq}\cdot TR_{qdm} - Z_{dd} - Z_{dq}\cdot TI_{qdm} \\
-Z_{qdm} &= G_{qd}\cdot TR_{ddm} + G_{qq}\cdot TR_{qdm} - Z_{qd} - Z_{qq}\cdot TI_{qdm} \\
H_{ddm} &= Y_{dd}\cdot TR_{ddm} + Y_{dq}\cdot TR_{qdm} + H_{dd} + H_{dq}\cdot TI_{qdm} \\
H_{qdm} &= Y_{qd}\cdot TR_{ddm} + Y_{qq}\cdot TR_{qdm} + H_{qd} + H_{qq}\cdot TI_{qdm}
\end{aligned}
\tag{3.47}
$$

and

$$
TR_{dqm} = \frac{\widetilde{v}_{id}^{VI}}{\widetilde{i}_{oq}^{VI}},\ TR_{qqm} = \frac{\widetilde{v}_{iq}^{VI}}{\widetilde{i}_{oq}^{VI}} \ \text{and} \ \ TI_{qdm} = \frac{\widetilde{i}_{od}^{IV}}{\widetilde{i}_{oq}^{IV}}
\tag{3.48}
$$

$$
\begin{aligned}
-Z_{dqm} &= G_{dd}\cdot TR_{dqm} + G_{dq}\cdot TR_{qqm} - Z_{dd}\cdot TI_{dqm} - Z_{dq} \\
-Z_{qqm} &= G_{qd}\cdot TR_{dqm} + G_{qq}\cdot TR_{qqm} - Z_{qd}\cdot TI_{dqm} - Z_{qq} \\
H_{dqm} &= Y_{dd}\cdot TR_{dqm} + Y_{dq}\cdot TR_{qqm} + H_{dd}\cdot TI_{dqm} + H_{dq} \\
H_{qqm} &= Y_{qd}\cdot TR_{dqm} + Y_{dq}\cdot TR_{qqm} + H_{qd}\cdot TI_{dqm} + H_{qq}
\end{aligned}
\tag{3.49}
$$

At last, a system of sixteen equations (3.44), (3.46), (3.48), and (3.50), with sixteen unknowns is defined and can be solved for unterminated transfer functions:

$$
\begin{bmatrix} \mathbf{G}_{\mathrm{o}} & -\mathbf{Z}_{\mathrm{o}} \\ \mathbf{Y}_{\mathrm{i}} & \mathbf{H}_{\mathrm{i}} \end{bmatrix} = \begin{bmatrix} \mathbf{G}_{\mathrm{om}} & -\mathbf{Z}_{\mathrm{om}} \\ \mathbf{Y}_{\mathrm{im}} & \mathbf{H}_{\mathrm{im}} \end{bmatrix} \cdot \left[\mathbf{T}^{AC\text{-}AC} \right]^{-1}
\tag{3.50}
$$

where

$$
\mathbf{T}^{ac\text{-}ac} = \begin{bmatrix} 1 & TV_{dqm} & TR_{ddm} & TR_{dqm} \\ TV_{qdm} & 1 & TR_{qdm} & TR_{qqm} \\ TG_{ddm} & TG_{dqm} & 1 & TI_{dqm} \\ TG_{qdm} & TG_{qqm} & TI_{qdm} & 1 \end{bmatrix}
\tag{3.51}
$$

is decoupling matrix for any three-phase AC-AC converter or network.

3.4 Generalized Unterminated Behavioral Model for any type of Power Converters and Networks

As already apparent, systems (3.23), (3.29), and (3.51) represent terminal-behavioral models in *d-q* coordinates of all types of three-phase converters: AC-AC, AC-DC, and DC-AC. These models can all be generalized and shown using matrix form (3.53) accompanied with the corresponding decoupling matrix (3.24), (3.30), or (3.53).

$$\begin{bmatrix} \mathbf{G}_{o}^{x} & -\mathbf{Z}_{o}^{x} \\ \mathbf{Y}_{i}^{x} & \mathbf{H}_{i}^{x} \end{bmatrix} = \begin{bmatrix} \mathbf{G}_{om}^{x} & -\mathbf{Z}_{om}^{x} \\ \mathbf{Y}_{im}^{x} & \mathbf{H}_{im}^{x} \end{bmatrix} \cdot \left[\mathbf{T}^{x} \right]^{-1} \tag{3.52}$$

$$\text{where } x = \{ AC\text{-}AC,\ AC\text{-}DC\ \ DC\text{-}AC,\ DC\text{-}DC \}$$

It should be noted that everything shown above for three-phase converters applies to DC-DC converters as well; however, the case for DC-DC converters is in details addressed in [95], and will not be reported here.

3.5 Simulation Examples of the Three-Phase Decoupling Procedure

3.5.1 Linear Passive Network

In order to demonstrate the decoupling procedure, a three-phase and balanced linear network with a non-ideal source and load is used as shown in Figure 3-7. All parameters are given, and the circuit is shown in both *abc* and *d-q* domain.

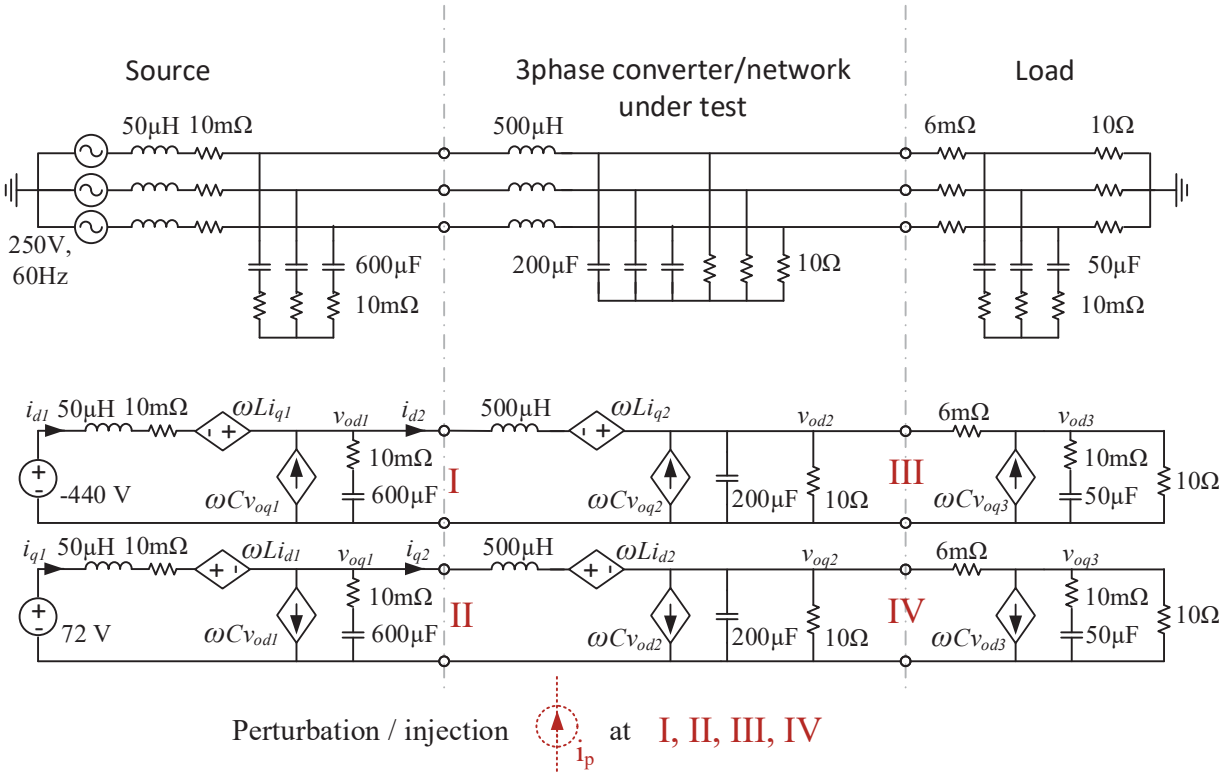

Figure 3-7: Three phase source, linear *R-L-C* network and a load in (top) *abc*, and (bottom) *d-q* coordinates

Small-signal input and output currents and voltages in *d* and *q* axes are obtained by performing linear analysis of the circuit in MATLAB, around a desired operating point and at the terminals I,

II, III and IV as shown in Figure 3-7 (bottom). By applying the above described procedure the required transfer functions are obtained.

To verify the result of the decoupling procedure, unterminated transfer functions of the linear network from Figure 3-7 are analytically derived (with no source and load connected) showing a good match with the ones obtained through the circuit linearization – showed in Figure 3-8 is *dd*-channel output impedance in all three cases: terminated, unterminated and analytically obtained (all overlaid).

The analytical expression for the output impedance Z_{dd} is shown in (3.53).

$$Z_{dd} = \frac{LR(s(R+Ls+CLRs^2)+L(1+CRs)\omega^2)}{(R+Ls+CLRs^2)^2+L\omega^2(L(1+2CRs(1+CRs))-2CR^2)+C^2L^2R^2\omega^4} \tag{3.53}$$

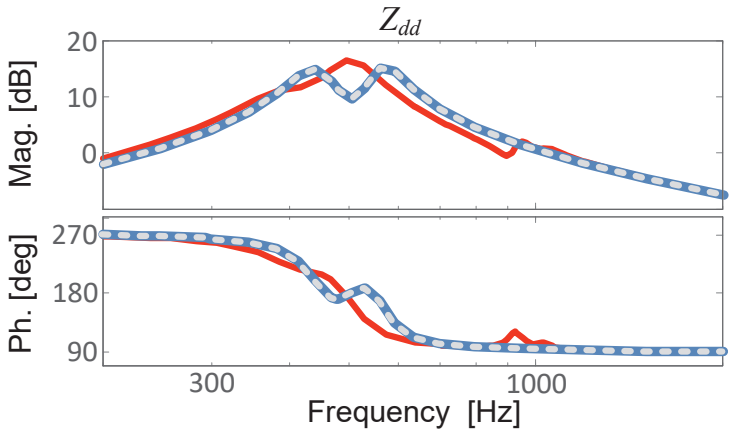

Figure 3-8: Output impedance Z_{dd}, red - before decoupling, terminated, blue - after decoupling (using (42), and gray dotted - analytically obtained and overlaid for the comparison

Moreover, time domain responses of the circuit shown in Figure 3-15 are captured when a load step is applied (at 0.15 s, 4 Ω resistors were added in parallel to 10 Ω ones). Time-domain transient responses of all eight variables (v_{id},v_{iq}, i_{od}, i_{oq}, v_{od}, v_{oq}, i_{id} and i_{iq}) are shown in Figure 3-9 and noted with the color blue. The transfer functions are now obtained via linear analysis in MATLAB, and the system is modeled in frequency domain using Terminal-Behavioral Model (TBM) (3.34). As it can be noticed in this model, input variables to the system are *input voltages* and *output currents*, while output variables are *output voltages* and *input currents*. In order to validate modeling procedure, applying waveforms shown on the left side of Figure 3-9 (input variables for the model), to the model (3.34), the model output must give the same responses (waveforms) as the recorded

output voltage and input currents (from an average model) in order to prove that the model captures all important dynamics. These, model output responses are overlapped with voltages and currents shown on the right side of Figure 3-9, and as evident, a very good match is achieved.

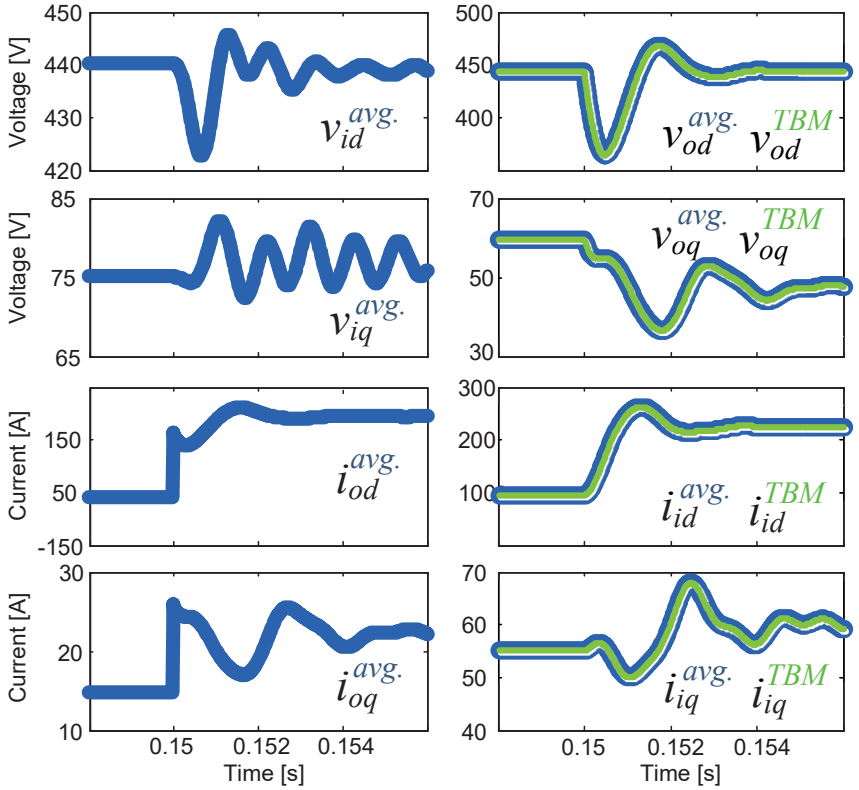

Figure 3-9: Time domain responses in *d* and *q* axes for the given load step, and comparison with the terminal-behavioral model (TBM)

3.5.2 AC-AC Converter (via Average Model)

Another example used for verification purpose is the AC-AC converter (back-to-back converter) shown in Figure 3-10. All of the circuit parameters are given in the same figure. The source and load used in this model are the same as the ones used in the example of the linear network shown in Figure 3-7.

A total of sixteen unterminated transfer functions are obtained using linearization procedure in MATLAB and applying decoupling procedure (3.52). Four of them obtained for *dd*-channel are shown below in Figure 3-11 depicting both terminated and unterminated transfer functions G_{dd}, Z_{dd}, Y_{dd} and H_{dd}, with observable influence of the source and load dynamics.

Finally, the time domain dynamic response is captured from the average model simulation and shown in Figure 3-11b together with the frequency domain model results. Again, a very good match between the two models is achieved.

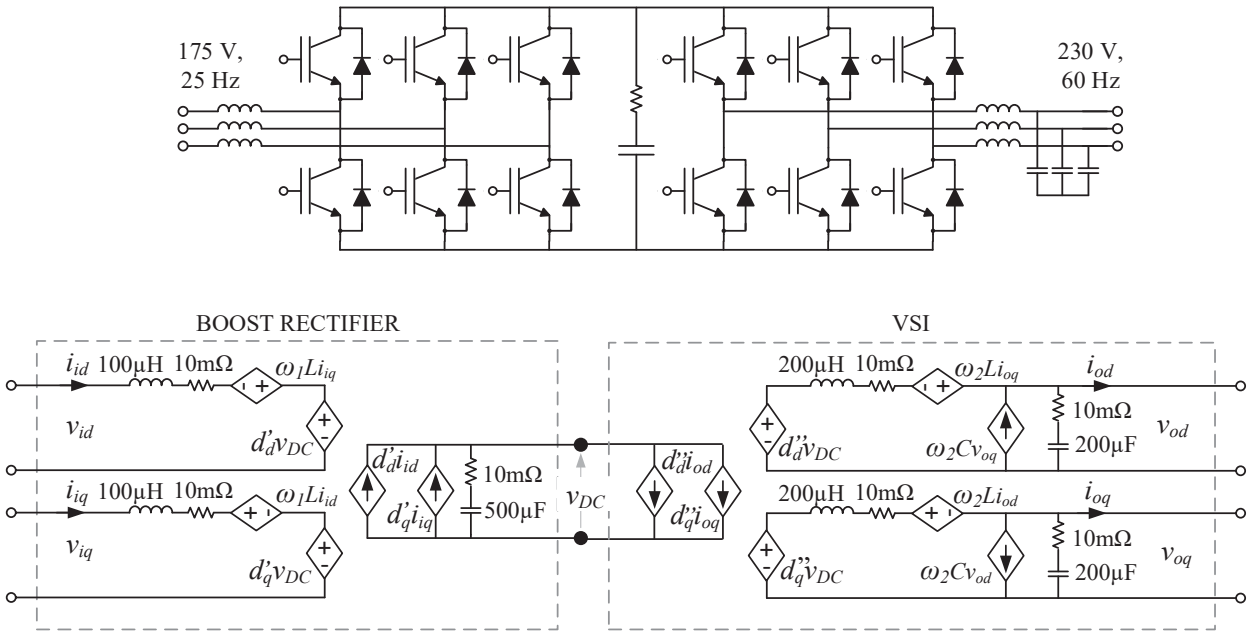

Figure 3-10: Back-to-back converter (top) and its average *d-q* model (bottom)

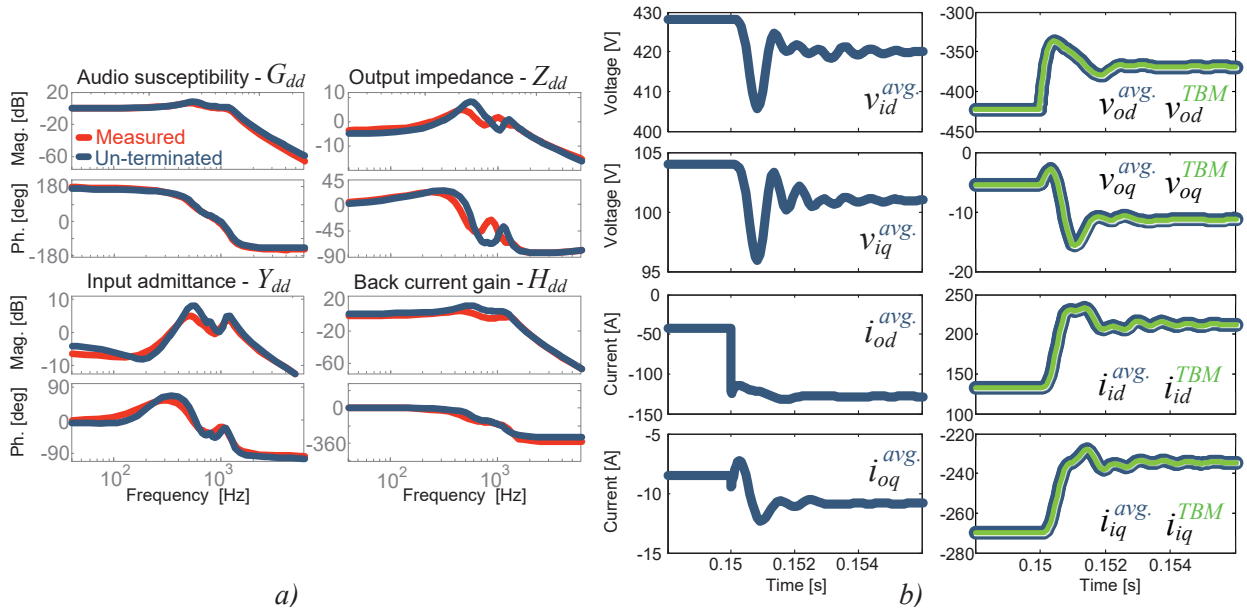

Figure 3-11: *a)* transfer functions: red - before decoupling, terminated, blue - after decoupling, *b)* time domain responses in d and q axes for the given load step, and comparison with the terminal-behavioral model (TBM)

3.5.3 AC-DC Converter (via Switching Model)

The third example used for demonstration is a switching model of a regulated Active Front End (AFE) shown in Figure 3-12 with all circuit parameters. A three-phase non-ideal network is used as a source, while a regulated Voltage Source Inverter (VSI) loaded with resistors is used as a load. The AFE has the voltage and current loop closed, while the VSI features only a current loop. The control parameters for both AFE and VSI are shown in Figure 3-12 (both converters have for simplicity the same control parameters for current loops and both are switching at 20 kHz).

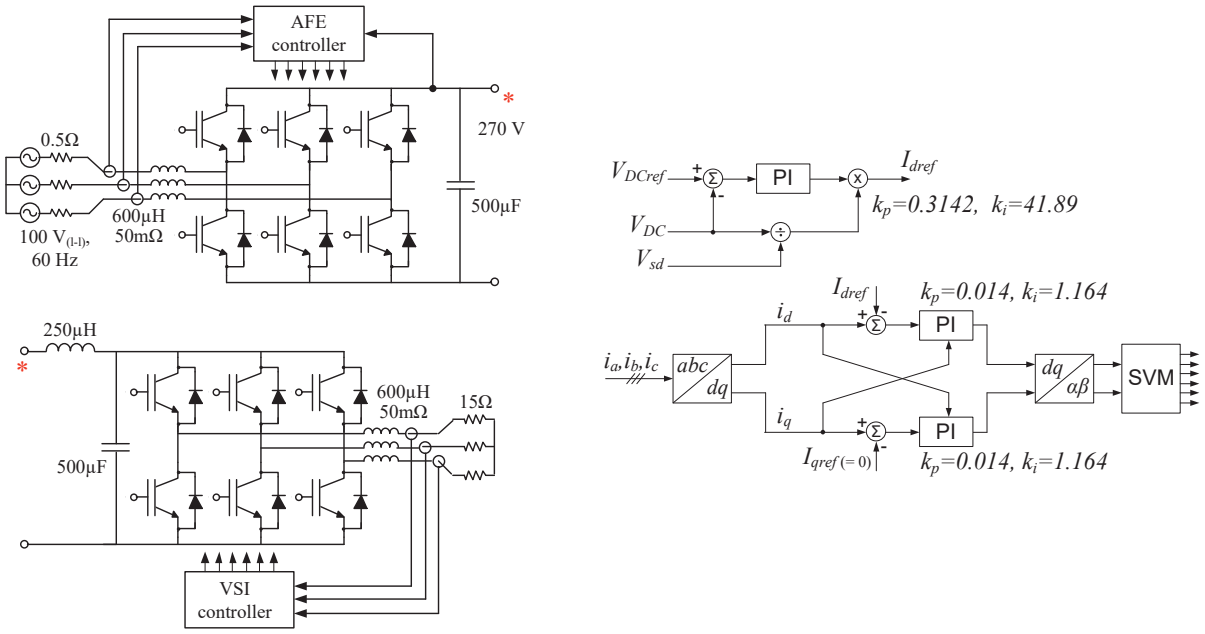

a) *b)*

Figure 3-12: *a)* Active front-end (AFE) and voltage source inverter (VSI); *b)* Voltage controller of the AFE, and current controller of both, AFE and VSI

The AC analysis is performed over the switching model of the AFE circuit using point by point injection in MATLAB [178]. For each of the small-signal variables (v_{id}, v_{iq}, i_{id}, i_{iq}, v_o, and $i_{o,,}$) gain and phase are obtained at 31 frequency points in the range from 100 Hz to 10 kHz. These are shown in Figure 3-13 with yellow dots for the four transfer functions G_d, Z_o, Y_{dd} and H_d. Due to the fact that a terminal-behavioral model (3.25) cannot be straightforwardly simulated with the frequency response data, all transfer functions have to be identified in the *s*-domain using some identification tool. Function '*fitfrd*' is used here (MATLAB) to perform the identification of the frequency response data, and the red colored transfer functions from Figure 3-13 are obtained.

Afterward, the expression (3.30) is used to decouple the source and load from the converter dynamics. The blue colored unterminated transfer functions (in *dd*) are shown in the same figure plotted behind the terminated ones.

Lastly, the load step is applied on the circuit (the current reference of the VSI is stepped up from 5 A to 7 A at 0.5 s in order to simulate load change), and the time domain waveforms are captured. Figure 3-14 shows the time domain response of the three acquired *output* variables from the terminal-behavioral model (3.25) – output votage v_o, input current i_{id} in *d*-axis, and input current i_{iq} in *q*-axis. For comparison, the average and switching models are built for the same circuit (Figure 3-12) and results in the time domain are shown overlaid for all three. A review of Figure 3-12 agrees with the conclusion that the terminal-behavioral model captures dynamics relatively well with a small steady state error after the transient settles down. In addition to being a boost rectifier, the non-linearity is accentuated due to the non-linear controller used (Figure 3-12), and represents one of the downsides of the terminal behavioral model. One possible way to deal with the mild and static nonlinearity is shown in [77] for DC-DC converters, which also can be easily applied to three-phase converters as well.

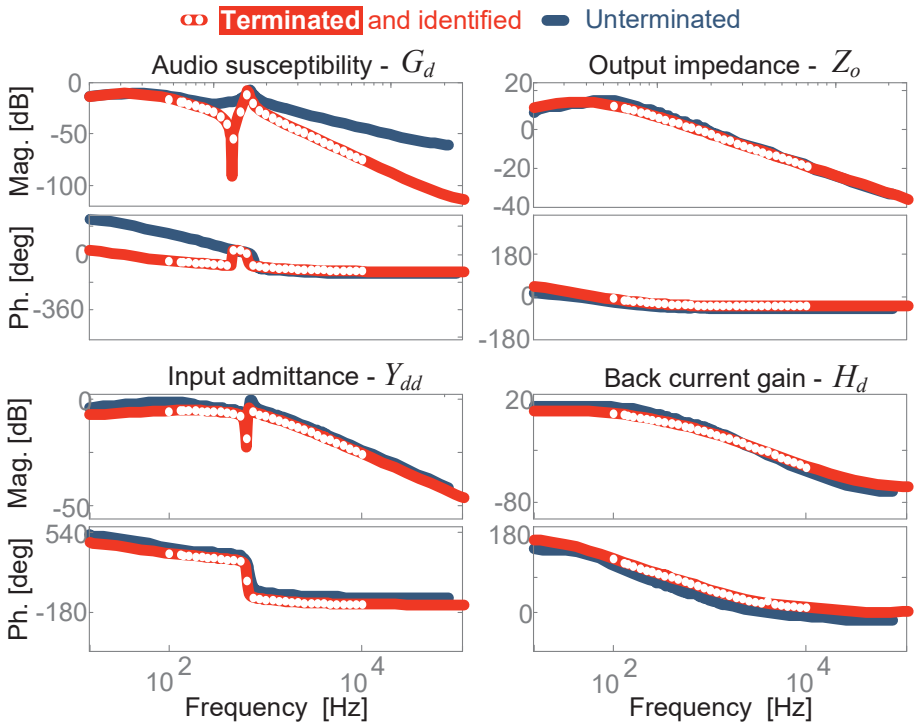

Figure 3-13: Transfer functions obtained from the switching model: white point-by-point response, red – transfer functions identified in the s-domain from the measured points (before decoupling)- terminated, blue - after decoupling (using (3.30))

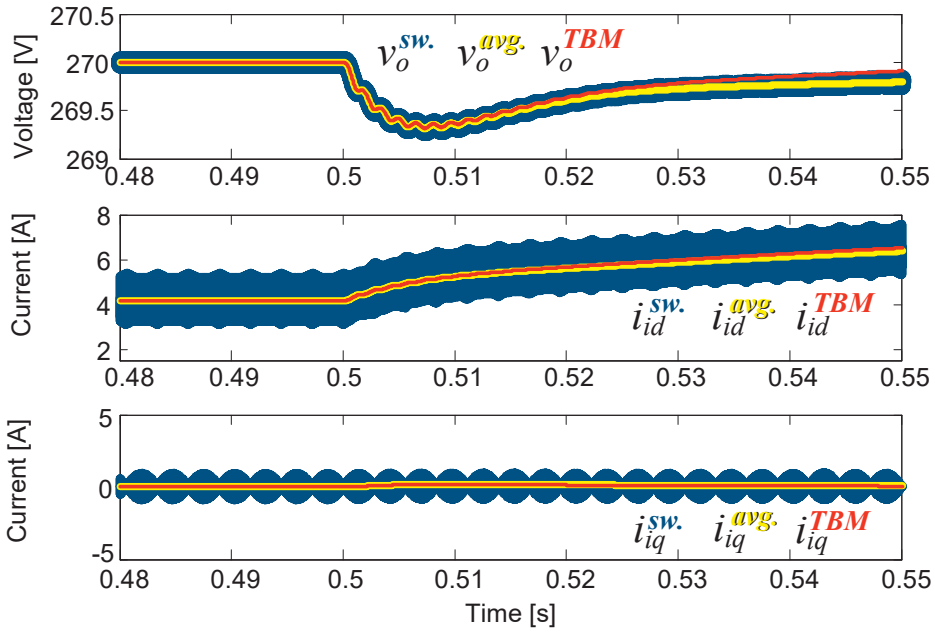

Figure 3-14: Time domain responses in *d* and *q* axes for the given load step, and comparison of switching (sw.), average (avg.) and terminal-behavioral model (TBM)

3.6 Experimental Demonstration of the Terminal-Behavioral Modeling

The experimental demonstration of the behavioral-modeling (and decoupling procedure) described in the last section is performed on 30 kW two-level voltage source converter prototype shown in Figure 3-15.

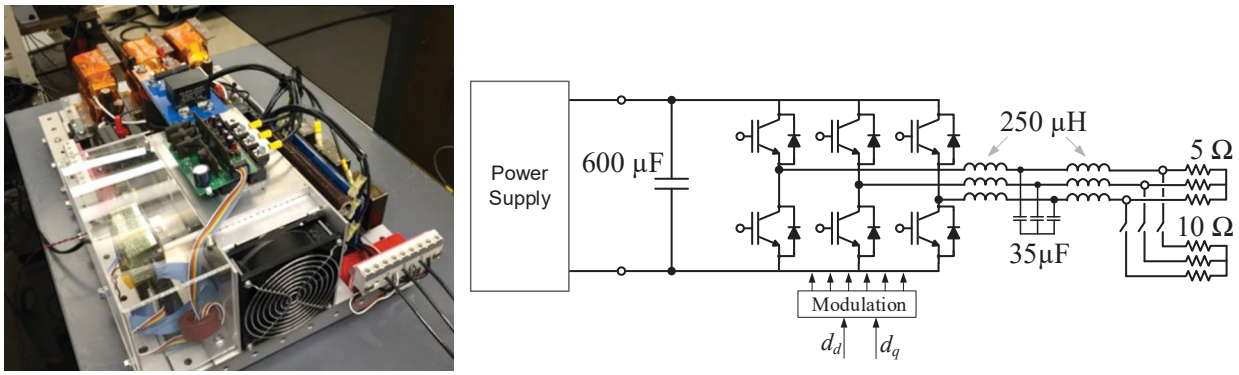

Figure 3-15: Two-level converter prototype used for experimental verification

The converter is built using an IGBT-based integrated power module PM100CL1A060 [179]. Additionally, a custom designed high-speed digital controller featuring *Texas Instruments* TMS320F28343 Delfino MCU [180] and a *Lattice* Complex Programmable Logic Device (CPLD) LCMX02-4000HC [181] is used to control this hardware prototype.

A custom designed Impedance Measurement Unit (IMU) / Frequency Response Analyzer (FRA) [56],[58],[102] shown in Figure 3-16a is used as a perturbation injector. As illustrated in Figure 3-16b, the FRA features a switching perturbation injector unit (PIU) allowing the generation of very low frequency perturbations (down to 0.1 Hz) as well as a linear PIU that extends measurement frequency range to up to 10 kHz. Both injection units can be configured in shunt or series injection mode enabling unparalleled measurement capability.

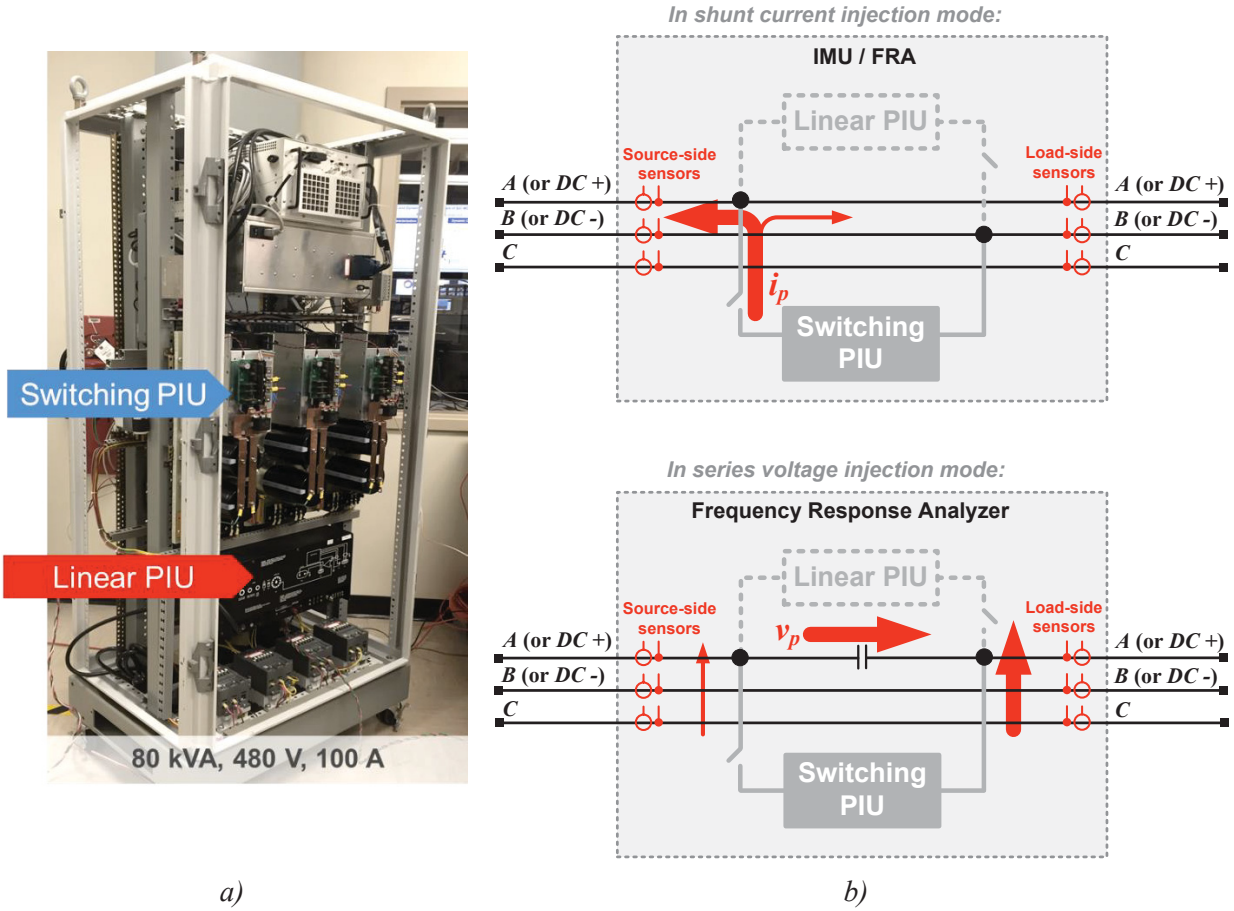

a) *b)*

Figure 3-16: *a)* CPES' Impedance Measurement Unit (IMU) / Freq. Response Analyzer (FRA) *b)* (top) – series current injection mode, (bottom) – series voltage injection mode

Shunt Current Injection Mode

The IMU/FRA configured for shunt current injection mode injects a perturbation current (i_p) between system phase *A* and phase *B* in AC networks (or DC+ and DC- in DC networks). About 5% of the system current is injected into the system. This configuration gives significantly better results when characterization of the source is of interest since source output impedance is lower

than load input impedance, hence a majority of the perturbation current flows into the source. This unequal injection current segregation is illustrated in the top of Figure 3-16b. Current and voltage sensors mounted at the ABC (or DC) terminals of the unit (not explicitly shown in the figures above) measure responses directly sent to a host computer for post-processing.

Series Voltage Injection Mode

The reconfiguration of the PIU from a shunt current injection to a series voltage injection mode, and vice versa, is fully automated. In this mode of operation, the IMU/FRA will impose perturbation to the system by perturbing series voltage (v_p) across the capacitor at about 5% of the nominal system line-to-neutral (or DC) voltage. Not so obvious in the bottom of Figure 3-16b is that the system current of the phase A (or DC+) flows through either a switching or linear PIU. Opposite from the shunt current injection mode, a series voltage injection mode gives significantly better results when load dynamic characterization is of interest. Again, better results are achieved since the source output impedance is lower than load input impedance hence majority of the voltage perturbation occurs at the load side. This unequal voltage division is illustrated in the bottom of Figure 3-16b.

3.6.1 Experimental Demonstration with the Voltage-Source Inverter

As described in section 3.1 (Figure 3-2), three separate measurements should be performed (collecting responses of all six system variables with each measurement - i_{od}, i_{oq}, v_{od}, v_{oq}, v_i and i_i) in order to develop a terminal-behavioral model of the DC-AC converter. Figure 3-17 illustrates placement of the IMU/FRA unit at the input and output for dynamic characterization. Setup from Figure 3-17a provides all required measurements at the interface I, (per Figure 3-2), while setup shown in Figure 3-17b provides measurements at both interfaces II, and III. The IMU/FRA is designed to consecutively perform sweeps, first in *d*, and immediately after in *q* axis (this corresponds to measurements II and III respectively) [56]. As evident from Figure 3-17a, when characterizing the input side (DC) of the power converter, series voltage injection is a much better choice as it will provide higher perturbation level/power at the converter terminals and consequently provide measurements with a better signal to noise ratio than measurements at the terminals on the opposite side of the IMU/FRA facing source.

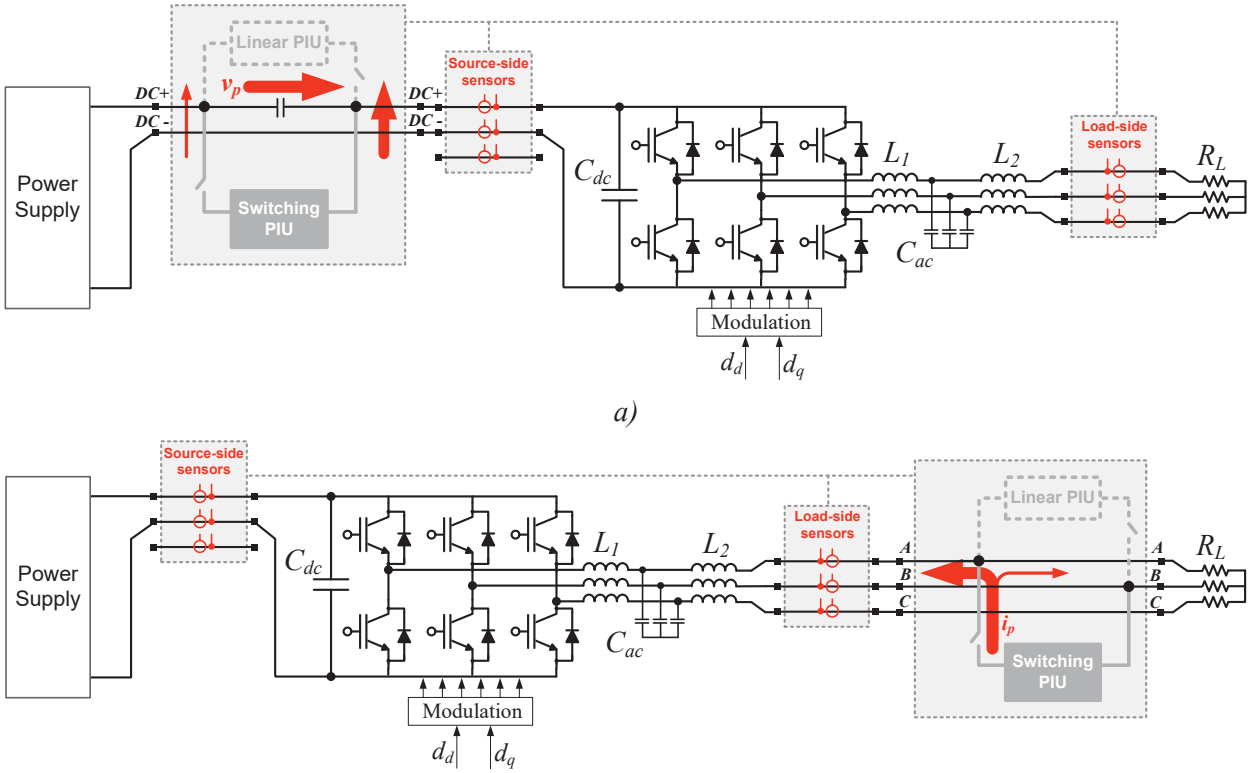

Figure 3-17: Placement of the IMU/FRA for DC-AC converter characterization *a)* at the input (DC), and *b)* at the output (AC)

Similarly, as Figure 3-17b suggests, when characterizing the output side (AC) of the power converter, shunt current injection is a desired choice since it provides a higher perturbation level/power towards the converter output terminals.

With the IMU/FRA connected as shown in Figure 3-17, the power converter is operating as an open loop voltage source converter with fixed duty cycles $d_d = 0.5$, and $d_q = 0$. The power supply is set at 200 V DC output while the converter is loaded with 5 Ω/per phase resistor. These settings and load produces about 10 A DC-link current and about 9 A rms at the AC output.

In order to cover a lower frequency range, the first set of measurements (at the interface "I" as described in the section 3.1) is performed using switching PIU, providing frequency responses of all six variables in the range from 0.1 Hz to 1 kHz - shown with the blue response curves in Figure 3-18.

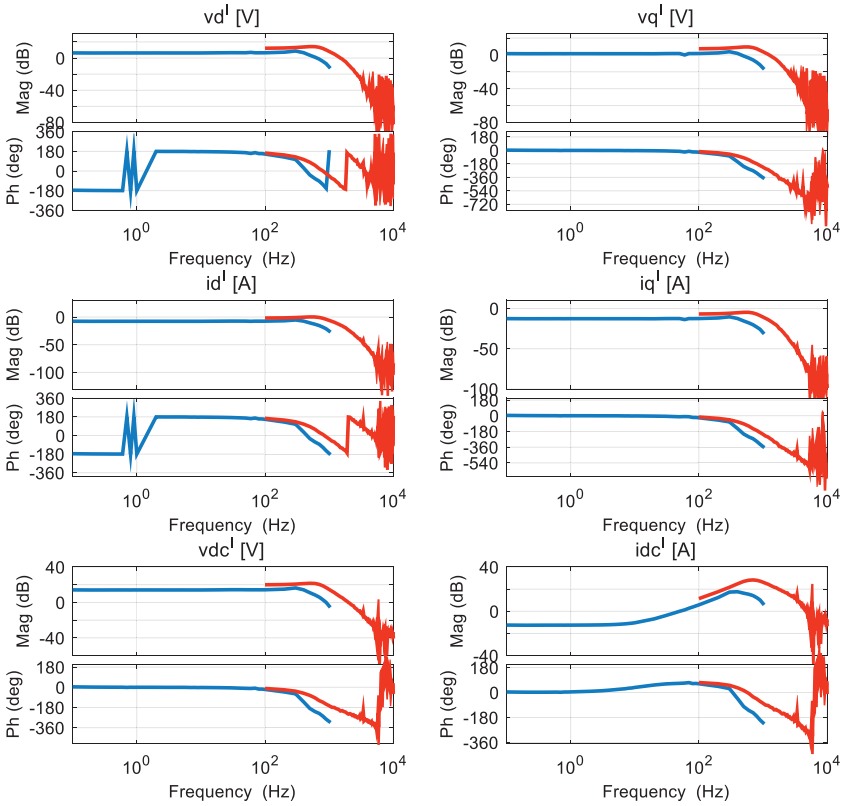

Figure 3-18: Frequency responses obtained using setup from Figure 3-17a (at the interface I - Figure 3-2)

Figure 3-18 also shows frequency responses of all six variables obtained in the range from 100 Hz to 10 kHz when using linear PIU. These frequency responses are shown with the red response curves. The upper frequency limit of 10 kHz corresponds to the Nyquist frequency since the converter switching frequency is 20 kHz. However, as apparent from Figure 3-18, measurements obtained at frequencies above 4-5 kHz are noisy and provide very little useful information about the system/converter dynamics in that frequency range. There can be many different reasons for the elevated noise levels. For example, insufficient current/voltage injection level and low signal to noise ratio, sensor bandwidth, and data acquisition data down-sampling. This phenomena is not analyzed in this dissertation since the IMU/FRA hardware used in this work is a prototype hardware and is still undergoing hardware and software improvements. Currently, there is no commercial hardware available on the market that can perform impedance measurements/frequency responses of AC systems at a similar power level. More details about structure, hardware, and software of this IMU/FRA prototype can be found in references [65],[66]. The following figures show measured variables at the interfaces II, and III as presented in Figure 3-2.

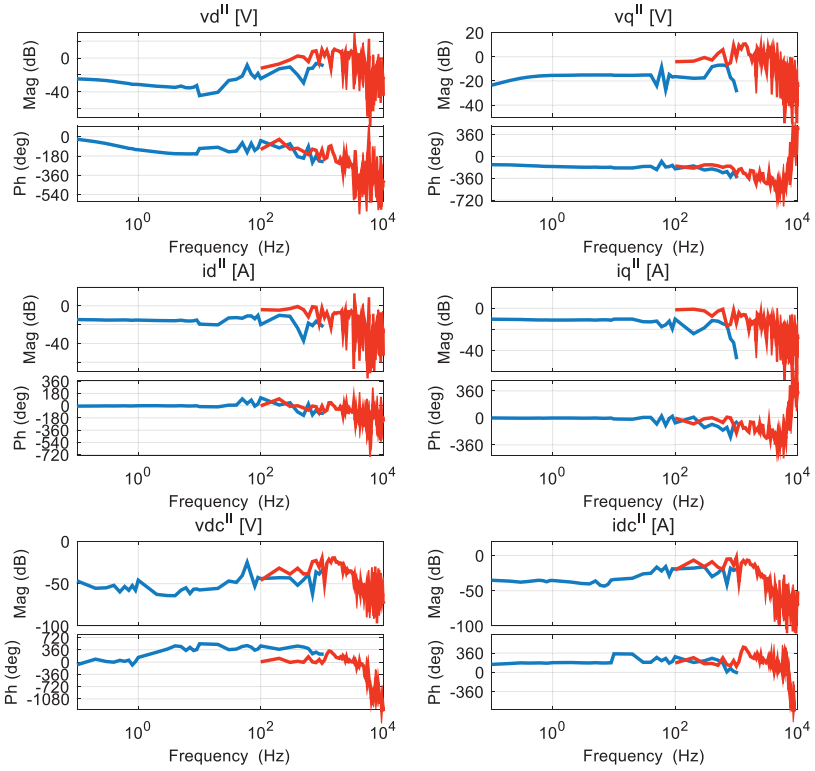

Figure 3-19: Frequency responses obtained using setup from Figure 3-17b (interface II - Figure 3-2)

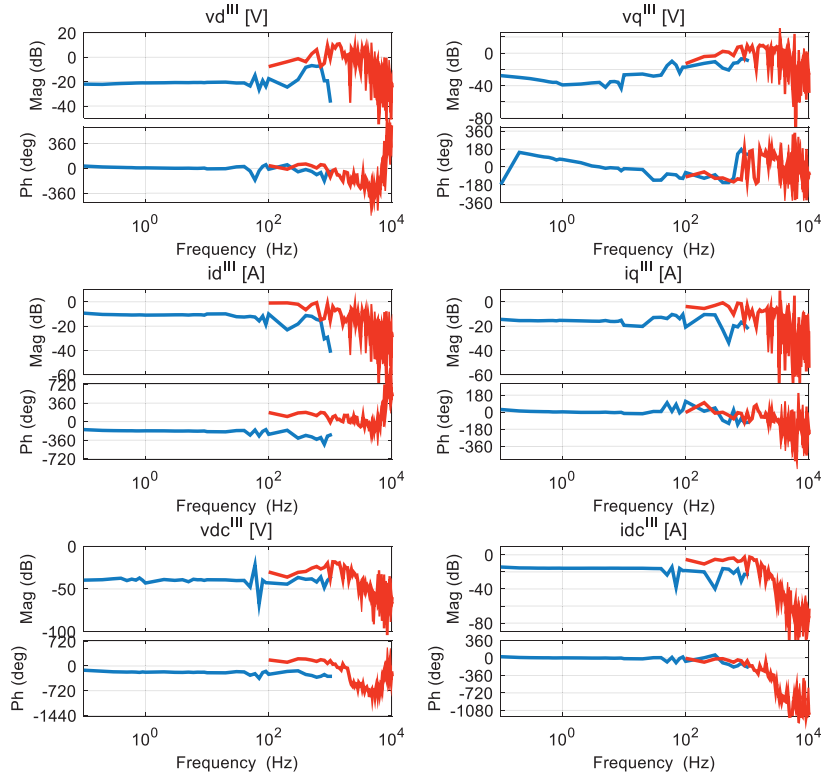

Figure 3-20: Frequency responses obtained using setup from Figure 3-17b (interface III - Figure 3-2)

With the above frequency responses measured, terminated frequency responses from section 3.1 can now be obtained. There is a total of nine frequency responses of which four (those in *d*-axis) are shown in Figure 3-21. It can be noticed that measurement points have very large peak-to-peak data fluctuations which is a consequence of the perturbation choice (Figure 3-17). Series voltage injection is used at the input which causes a high perturbation energy at the converter terminals (as desired). With very little perturbation energy delivered to the source the accurate identification of source output impedance very difficult (low signal-to-noise ratio). A completely analogue situation is at the output side where load input admittance is very hard to be measured using shunt current injection.

However, the proposed methodology does not require an accurate knowledge of the source output impedance and load input admittance; it will, in fact, remove them from the measurement data, which is done quite effectively as presented later in this section when unterminated frequency responses are obtained. As voltage and current frequency responses (Figures 3-18, 3-19, and 3-20) inherently contain source and load dynamics, they all feature noticeable data fluctuations. Consequently, terminated frequency responses feature those as well:

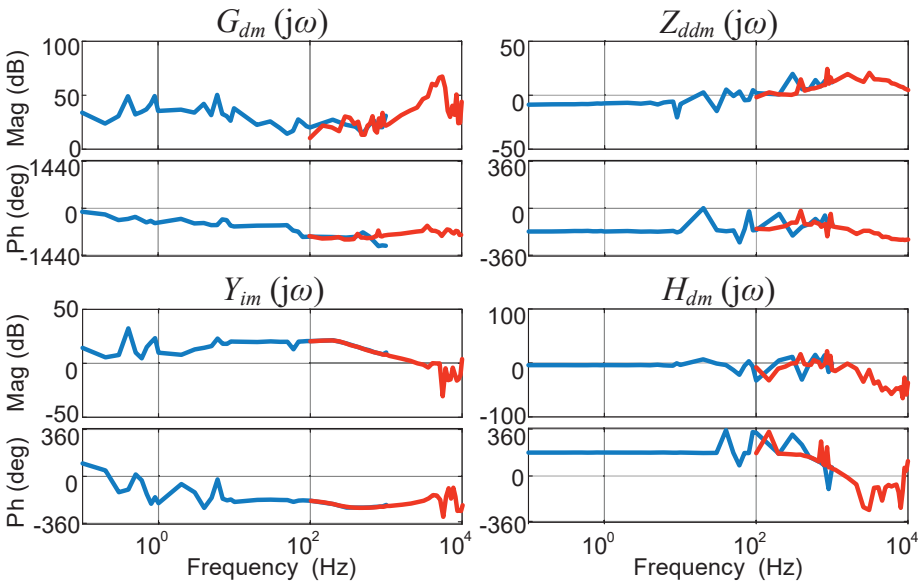

Figure 3-21: Terminated frequency responses of the voltage source inverter

As described in section 3.1, transconductance and transresistance frequency responses can now be obtained from measured voltage and current frequency responses (Figures 3-18, 3-19, and 3-20).

These are shown in Figure 3-22 (again only *d*-axis ones). They feature measurement data fluctuations as well and are the key for successful removal of source and load dynamics.

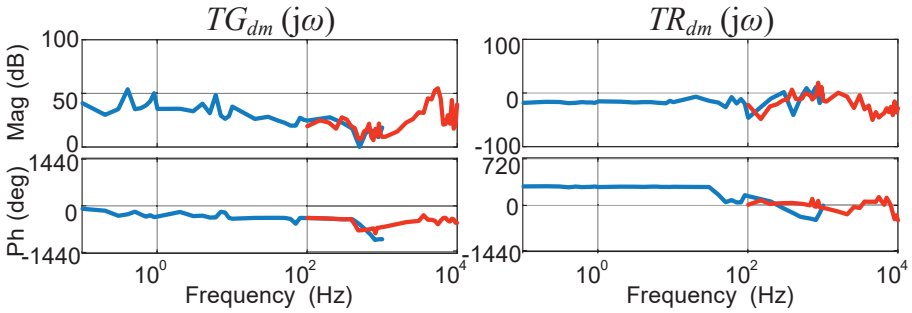

Figure 3-22: Transconductance and transresistance frequency responses

Unterminated frequency responses can now be obtained using (3.30), and are shown in Figure 3-23. It cannot be overlooked that unterminated frequency responses feature more defined shape with a minimal fluctuation of the measurement data in the low frequency range. Noise in the high frequency range is associated with the low signal-to-noise ratio which is quite common with these types of measurements.

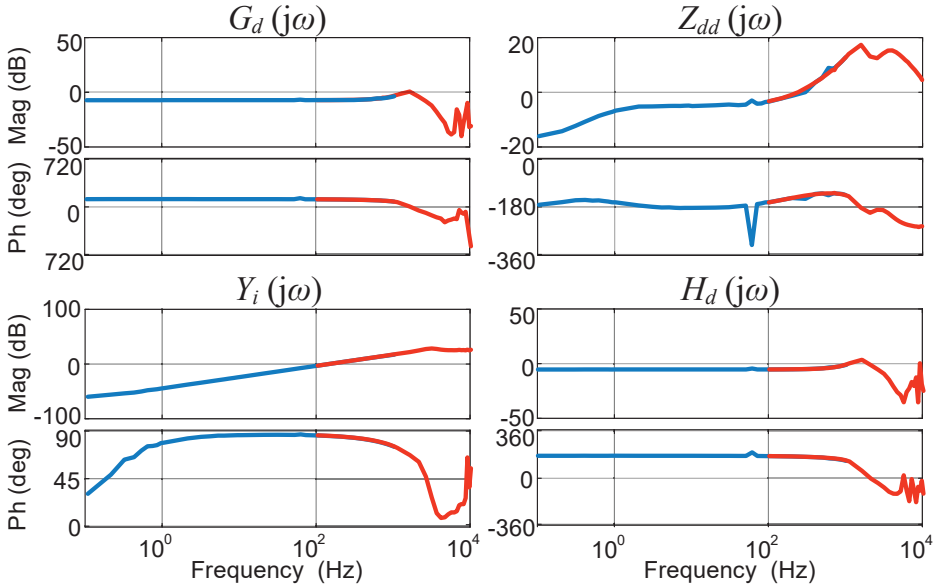

Figure 3-23: Unterminated frequency responses for the voltage source inverter

Furthermore, it can be noticed that frequency responses from Figure 3-23 feature a single data point outlier at 60 Hz (especially pronounced in the output impedance plot). This is a common

issue when perturbation frequency is quite close (or equal) to the system (line) frequency. In many cases this point can be skipped during the sweep. However, it can easily be deleted from the measured frequency response set of data during post-processing.

After unterminated frequency responses are obtained, they can be curve-fitted in MATLAB using one of a few identification tools. Function *'fitfrd'* is used here to perform identification of the frequency response data and provide the stable transfer functions in *s*-domain. Results of the curve fitting are shown in Figure 3-2 (four out of nine transfer functions are shown). Laplace-domain expressions of all nine transfer functions are given in the Appendix.

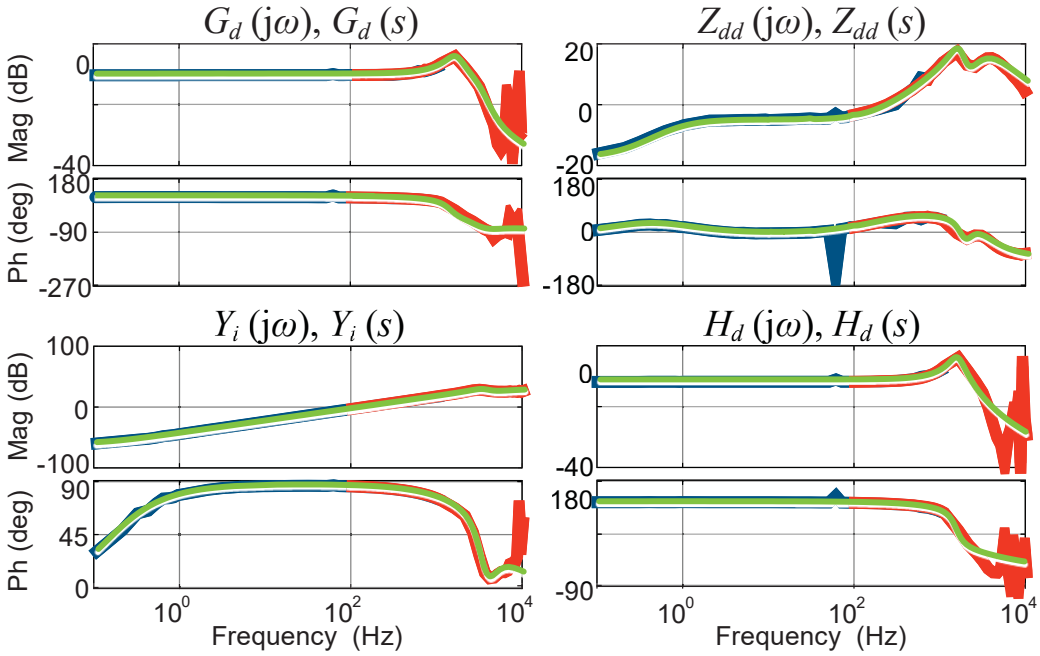

Figure 3-24: Unterminated transfer functions (green) overlaid with unterminated frequency responses

To demonstrate terminal-behavioral modeling and decoupling procedure, the load step transient is applied on the voltage source inverter (Figure 3-15) and transient waveforms are recorded. IMU/FRA (Figure 3-16) also features data acquisition functionality and is used here to record voltage and current waveforms (in *abc* coordinates). Additionally, it can record synchronization angle (internal PLL) that is used to perform *dq* transformation. Figure 3-25 shows captured waveforms data presented in blue.

The small-signal terminal behavioral model of a voltage source inverter is:

$$\left[\begin{array}{c|cc} G_d & -Z_{dd} & -Z_{dq} \\ G_q & -Z_{qd} & -Z_{qq} \\ \hline Y_i & H_d & H_q \end{array}\right] \cdot \begin{bmatrix} v_{dc} \\ i_d \\ i_q \end{bmatrix} = \begin{bmatrix} v_d \\ v_q \\ i_{dc} \end{bmatrix} \tag{3.54}$$

where the matrix on the left comprises all nine unterminated transfer functions obtained above (four of them shown in Figure 3-24). If model (3.54) is simulated in such a way that left column variables from Figure 3-25 (v_{dc}, i_d, and i_q) are inputted into the model, then the model output should be three variables (v_d, v_q, and i_{dc}) that closely resemble those from the right column variables from Figure 3-25. As evident, this is already done in Figure 3-25, displaying simulated variables v_d, v_q, and i_{dc} overlaid with measured ones. A very good match is achieved.

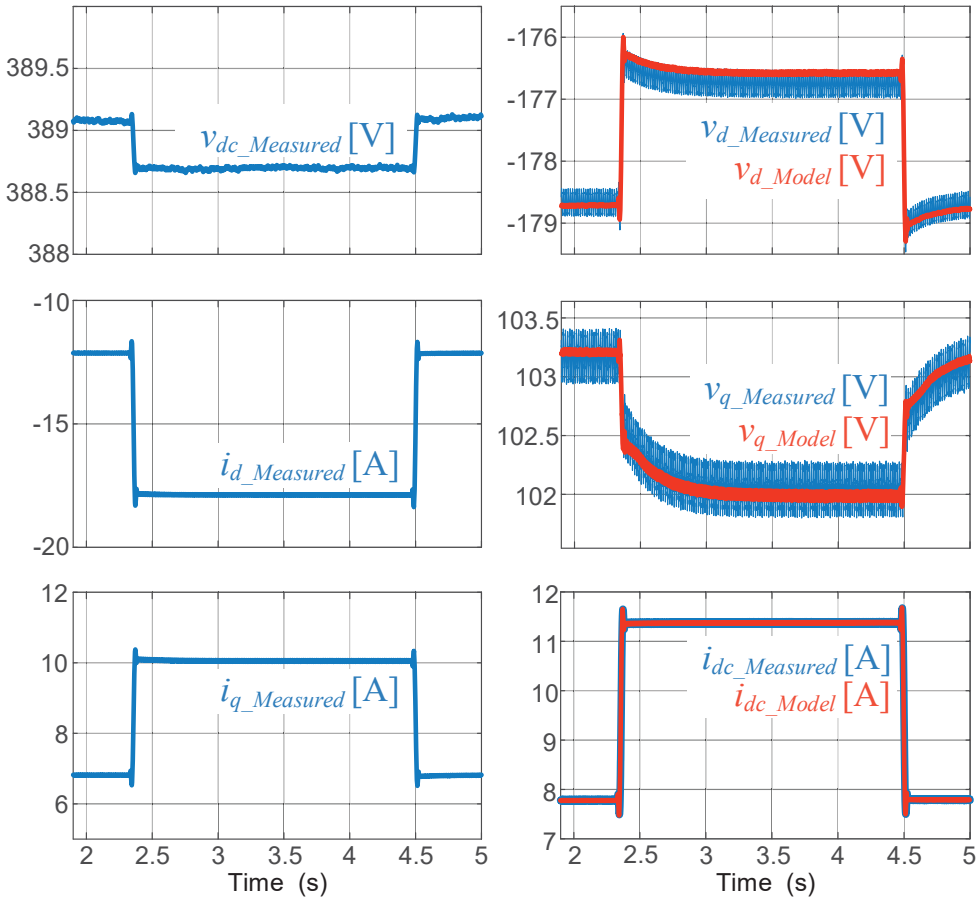

Figure 3-25: Time domain waveforms during transient overlaid with model output (VSI)

3.6.2 Experimental Demonstration with the Active Front-End (Active Rectifier)

A similar experiment is repeated using the same hardware, only now programmed to operate as the active rectifier. This is illustrated in Figure 3-26. The active rectifier control is designed to feature current loops of about 800 Hz bandwidth, while the output DC voltage loop featured about 30 Hz bandwidth. The input voltage is 208 V line-to-line, while the output operated with an adjustable reference up to 400 V DC.

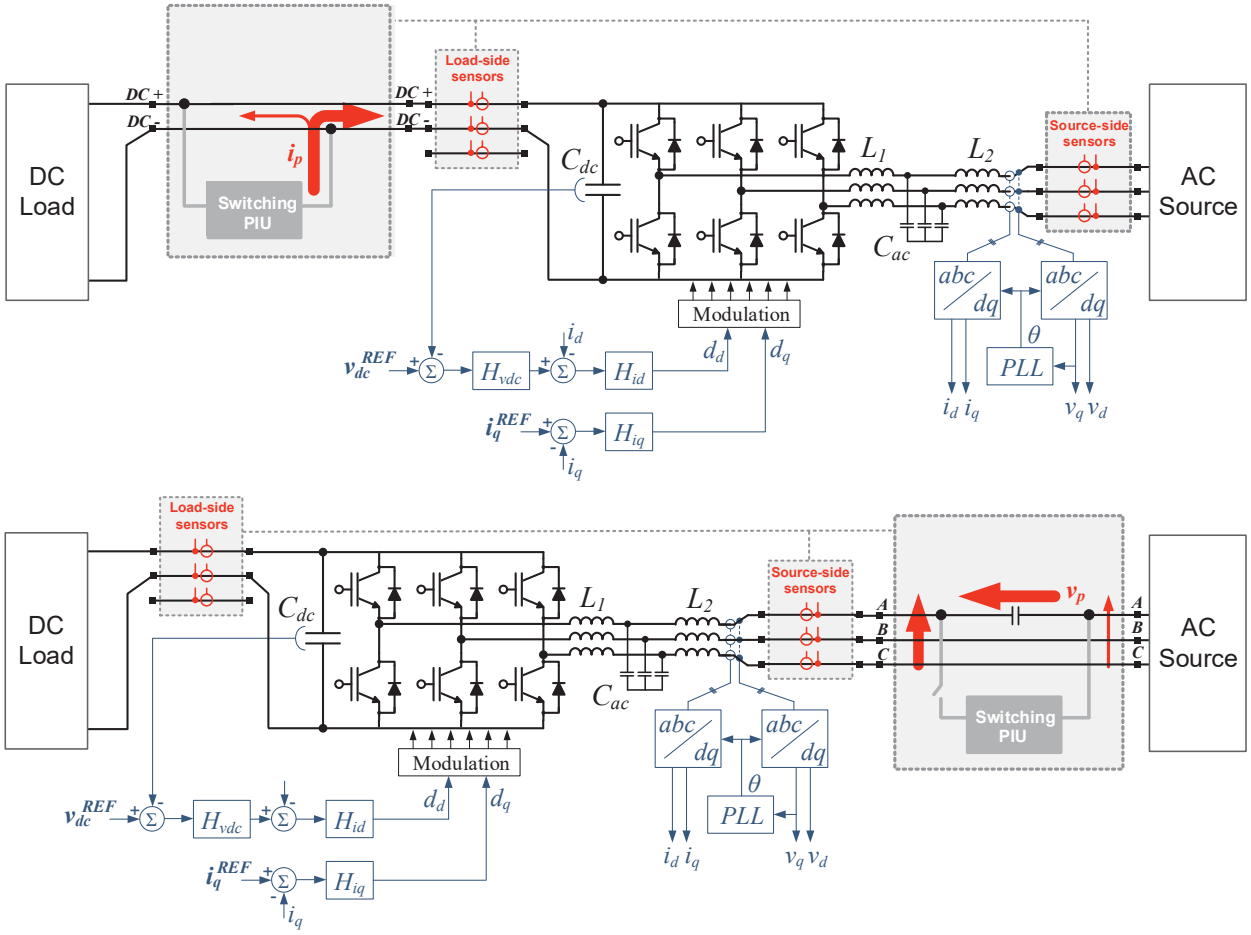

Figure 3-26: Placement of the IMU/FRA for AC-DC **converter characterization *a)* at the output** (DC)**, and *b)* at the input** (AC)

Similar to the voltage source inverter case, the FRA is placed at the input and output of the active rectifier, where now the AC-side is a source side requiring series voltage injection while shunt current injection is needed for the output (DC). Since this is now a controlled converter with the control loop bandwidth slightly lower than 1 kHz, it was sufficient to use only a switching PIU and perform characterization up to 1 kHz capturing dominant dynamics sufficient for the system-

level interaction study. Figure 3-16 illustrates this in a simple manner emphasizing that only a switching PIU was used.

The small-signal terminal behavioral model of an active rectifier is shown in (3.55), while Figure 3-27 shows both, *d*-axis unterminated frequency responses, and their curve-fitted transfer functions in the frequency range from 0.1 Hz to 1 kHz.

$$\left[\begin{array}{cc|c} G_d & G_q & -Z_o \\ \hline Y_{dd} & Y_{dq} & H_d \\ Y_{qd} & Y_{qq} & H_q \end{array}\right] \cdot \begin{bmatrix} v_d \\ v_q \\ i_{dc} \end{bmatrix} = \begin{bmatrix} v_{dc} \\ i_d \\ i_q \end{bmatrix} \tag{3.55}$$

Similarly and as in the previous example, the matrix on the left comprises all nine unterminated transfer functions (four of them are shown in Figure 3-27 plotted over unterminated frequency responses). The time domain voltage and current waveforms are shown in Figure 3-28.

Similarly to the VSI case above, model (3.55) is simulated in such a way that left column variables from Figure 3-28 (now v_d, v_q,and i_{dc}) are inputs to the model, then the model should output three variables (v_{dc}, i_d, and i_q) that resemble those from the right column variables from Figure 3-28. This is already shown in Figure 3-28, displaying simulated variables v_{dc}, i_d, and i_q overlaid with the measured ones. Again, a relatively good match is achieved.

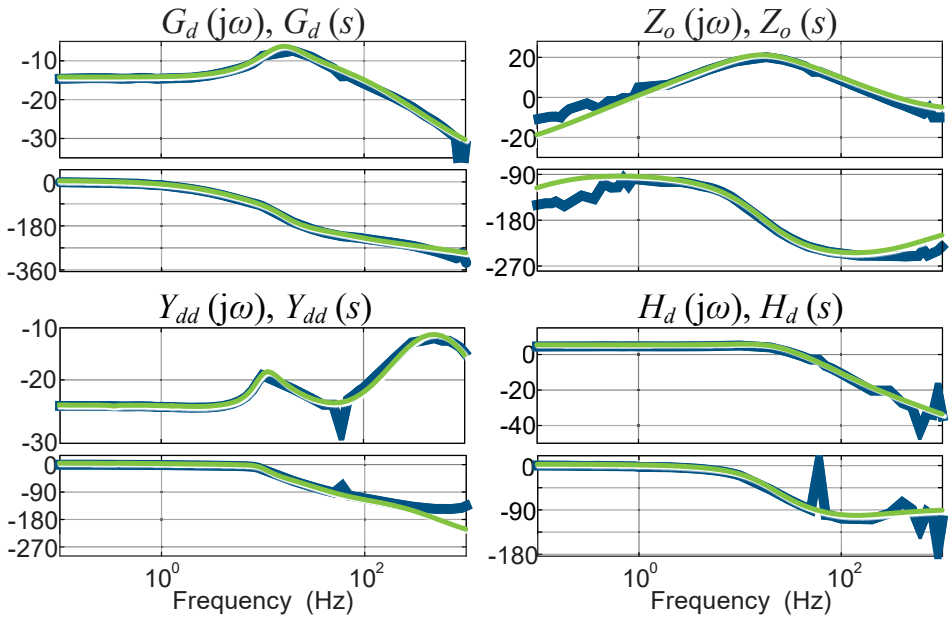

Figure 3-27: Unterminated transfer functions (green) overlaid with unterminated frequency responses

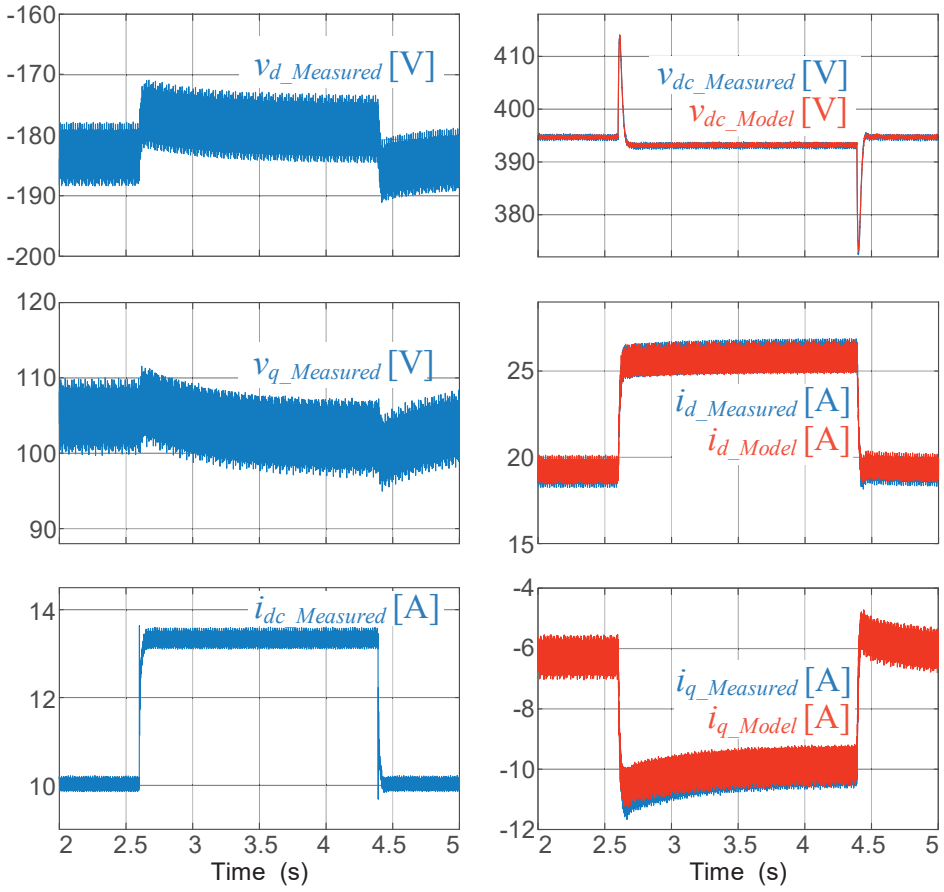

Figure 3-28: Time domain waveforms during transient overlaid with model output (AFE)

Laplace-domain expressions of all nine transfer functions from (3.55) are given in the Appendix.

3.7 Summary

The small-signal, low-frequency terminal behavioral modeling of three-phase power converters is addressed in this chapter. It is shown how power electronics converters can be represented using three-port and four-port dynamic networks obtained using frequency sweep at their input and output terminals. More importantly, a dynamic decoupling matrix in the generalized form is derived enabling decoupling of source and load termination effects from the measured set of terminated frequency responses. This decoupling procedure can be applied to different types of power converters, and can aid system-level simulation of large systems, performance evaluation, analysis of dynamic interactions, and converter control design.

However, there are limitations and engineering challenges associated with this concept aside the difficulty with performing the actual frequency response measurements. Terminal-behavioral modeling is a small-signal representation of converter dynamics at a particular operating point, and does not take into account non-linearity associated with system converters and their control. Some exercise higher linearity than others, but for the meaningful system-level modeling using here shown procedure all system converters have to be relatively accurately characterized. This means that transfer functions of each converter have to be obtained at numerous operating points covering wide operating range. Furthermore, even if obtained and stored in a form of a look-up tables, there are no simple ways to model transitions from one operating point to another using different set of transfer functions. Other than a bit more elaborated on a system-level example shown in Chapter 7, these challenges are not addressed in this dissertation further, and it is clear that additional research efforts have to be made in order to find solutions to some of these problems.

The following chapter will show how unterminated transfer functions allow measurement of converter terminal impedances for online stability assessment.

4. Online System Observation and Stability Assessment

There have been numerous papers published in the last decade that address different small-signal stability assessment methods among which impedance-based criteria present the most common practice. Some of the alternative methods for online and offline stability evaluation are reported in [194]-[200],[206]-[209], while an overview of different ways to measure impedances that can be used for stability analysis using Generalized Nyquist Criterion [55], is given in Chapter 1, section 1.6.2. The work shown in this chapter complementarily contributes to the existing impedance-based stability research for an online, *in-situ*, stability assessment.

The proposed concept utilizes unterminated transfer functions of the converter, and suggests that by knowing those, internal-caused perturbations can be used to generate frequency sweep and obtain all four terminal impedances at both input and output simultaneously. While knowledge of the unterminated transfer functions is unnecessary to obtain system impedances looking out from the converter and towards the system on both sides, it is essential for obtaining impedances that look towards the converter itself. The unterminated transfer functions then form a dynamic input to output ratio offering the opportunity to estimate the reflected impedances on both sides of the converter. With all terminal impedances obtained, Generalized Nyquist stability Criterion (GNC) can be performed online [55].

4.1 Outward and Inward Immittances

Figure 4-1 shows the notional hybrid (AC/DC) electronic power distribution system introduced in Chapter 1, with particular AC and DC interfaces emphasized on both sides of the intermediate bus AC-DC converter. To meaningfully perform a small-signal stability assessment, every interface in this system (in addition to the two highlighted ones) has to be individually examined, one by one, under an assumption that system operating conditions do not change during that process. Moreover, the impedance measurement unit needs to be physically connected to the system (at all DC and AC interfaces) in order to perform *in-situ* impedance measurements and a stability assessment.

Focusing now at the intermediate bus AC-DC converter from Figure 4-1, its outward immittances can be defined as those “seen” out from the converter terminals; more precisely,

aggregate source impedance $\mathbf{Z_S}$ represents the outward impedance related to this bus converter. Similarly, admittance Y_L represents outward admittance "seen" out from the bus converter terminals.

Additionally, inward immittances can be defined as those that "look" towards the particular converter (or towards some other reference point). In Figure 4-1 these are $\mathbf{Y}_{\mathbf{L}}^{EQ}$ and Z_S^{EQ}. This terminology is adequate when related to a particular converter or a fixed reference point in the system.

The only way to inflict internally-caused voltage or current perturbations at the terminal of a converter is by either perturbing its duty-cycles (in the case of an open-loop converter), or voltage and/or current control reference point (in the case of a closed-loop converter). Doing so in a defined frequency range will allow outward system immittances on both sides of the converter to be measured. The following subsections address this for the four types of power converters.

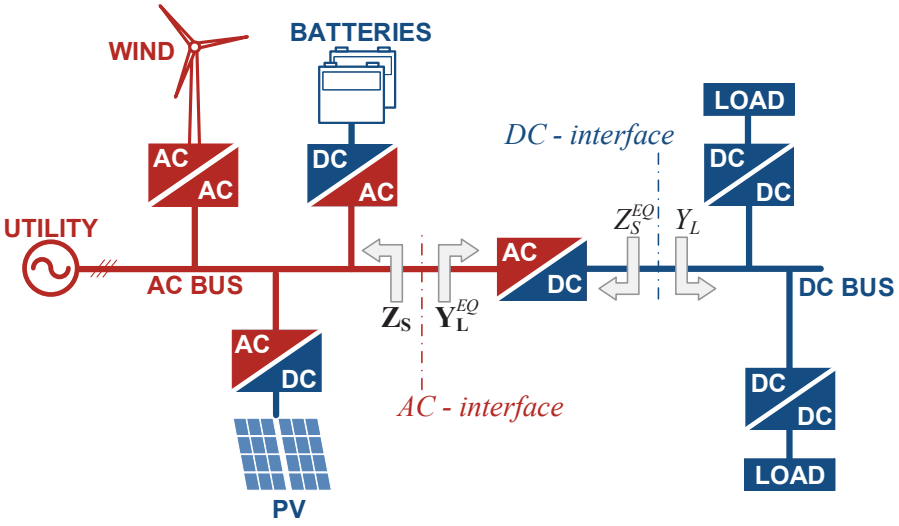

Figure 4-1: Notional hybrid electronic power distribution subsystem

4.1.1 AC-AC Converter Terminal Immittances

As shown in the previous chapter, three-phase converters can be represented with the single-line model, with no loss of generality, where all variables are in the matrix form. This is shown in Figure 4-2, with terminal impedances accentuated on both, input and output side.

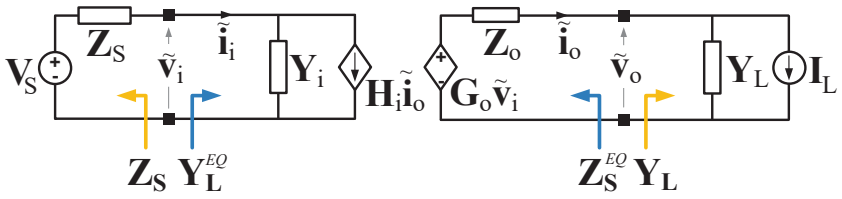

Figure 4-2: Inward and outward immittances in the AC-AC converter model

The perturbation of duty-cycles d_d and d_q in the converter allows outward immittances to be measured as shown in (4.1) and (4.2).

Input side source output impedance (outward):

$$\mathbf{Z_S} = \begin{bmatrix} Z_{dd} & Z_{dq} \\ Z_{qd} & Z_{qq} \end{bmatrix} = \begin{bmatrix} \frac{\tilde{v}_{id}}{\tilde{d}_d} & \frac{\tilde{v}_{id}}{\tilde{d}_q} \\ \frac{\tilde{v}_{iq}}{\tilde{d}_d} & \frac{\tilde{v}_{iq}}{\tilde{d}_q} \end{bmatrix} \begin{bmatrix} \frac{\tilde{i}_{id}}{\tilde{d}_d} & \frac{\tilde{i}_{id}}{\tilde{d}_q} \\ \frac{\tilde{i}_{iq}}{\tilde{d}_d} & \frac{\tilde{i}_{iq}}{\tilde{d}_q} \end{bmatrix}^{-1} \tag{4.1}$$

Output side load input admittance (outward):

$$\mathbf{Y_L} = \begin{bmatrix} Y_{dd} & Y_{dq} \\ Y_{qd} & Y_{qq} \end{bmatrix} = \begin{bmatrix} \frac{\tilde{i}_{od}}{\tilde{d}_d} & \frac{\tilde{i}_{od}}{\tilde{d}_q} \\ \frac{\tilde{i}_{oq}}{\tilde{d}_d} & \frac{\tilde{i}_{oq}}{\tilde{d}_q} \end{bmatrix} \begin{bmatrix} \frac{\tilde{v}_{od}}{\tilde{d}_d} & \frac{\tilde{v}_{od}}{\tilde{d}_q} \\ \frac{\tilde{v}_{oq}}{\tilde{d}_d} & \frac{\tilde{v}_{oq}}{\tilde{d}_q} \end{bmatrix}^{-1} \tag{4.2}$$

Inward immittances measured using (4.3) and (4.4):

Input side equivalent admittance (inward):

$$\mathbf{Y_L^{EQ}} = \mathbf{Y_i} + \mathbf{H_i Y_L (I + Z_o Y_L)^{-1} G_o} \tag{4.3}$$

Output side equivalent output impedance (inward):

$$\mathbf{Z_S^{EQ}} = \mathbf{Z_o} + \mathbf{G_o (I + Z_S Y_i)^{-1} Z_S H_i} \tag{4.4}$$

4.1.2 DC-DC Converter

DC-DC converter two-port network model is shown in Figure 4-3. Assuming open-loop converter, perturbation of its duty-cycle will allow source output impedance and load input admittance (outward immittances) to be measured as shown in (4.5) and (4.6).

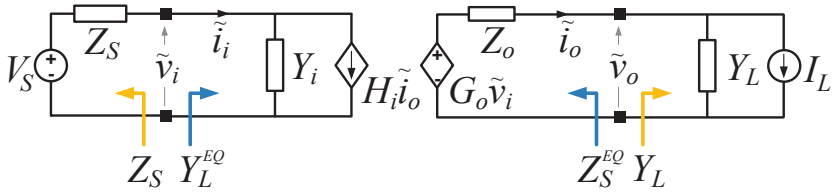

Figure 4-3: Inward and outward immittances in the DC-DC converter model

Input side source output impedance (outward):

$$Z_S = -\frac{\tilde{v}_i / \tilde{d}}{\tilde{i}_i / \tilde{d}} \tag{4.5}$$

Output side load input admittance (outward):

$$Y_L = \frac{\tilde{i}_o / \tilde{d}}{\tilde{v}_o / \tilde{d}} \tag{4.6}$$

Assuming unterminated transfer functions of this converter are known, inward immittances can now be calculated out using (4.7) and (4.8):

Input side equivalent admittance (inward):

$$Y_L^{EQ} = Y_i + H_i Y_L (1 + Z_o Y_L)^{-1} G_o \tag{4.7}$$

Output side equivalent output impedance (inward):

$$Z_S^{EQ} = Z_o + G_o (1 + Z_S Y_i)^{-1} Z_S H_i \tag{4.8}$$

4.1.3 DC-AC Converter (Inverter)

The simplified circuit form of an inverter with variables in the matrix form is shown in Figure 4-3. Perturbation of converter's duty-cycles d_d and d_q allows outward immittances to be measured as shown in (4.9) and (4.10).

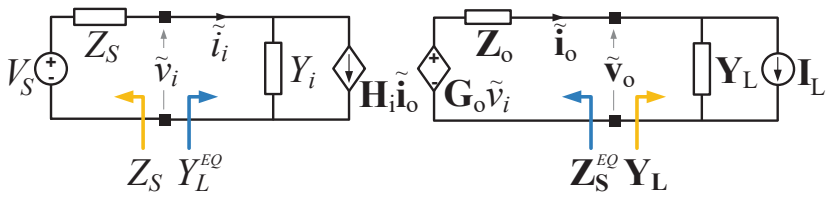

Figure 4-4: Inward and outward immittances in the inverter model

Input side source output impedance (outward):

$$Z_S = -\frac{\tilde{v}_i / \tilde{d}_d}{\tilde{i}_i / \tilde{d}_d} \quad \text{or} \quad Z_S = -\frac{\tilde{v}_i / \tilde{d}_q}{\tilde{i}_i / \tilde{d}_q} \tag{4.9}$$

Both d_d and d_q duty cycles can be used in order to obtain source output impedance as shown above in (4.9). However, although the same results will be obtained, in some cases the same magnitude of perturbation in the duty cycle will yield results with different signal-to-noise ratio. It is probably a good practice to try both forms when performing experiments with the real hardware.

Output side load input admittance (outward):

$$\mathbf{Y_L} = \begin{bmatrix} Y_{dd} & Y_{dq} \\ Y_{qd} & Y_{qq} \end{bmatrix} = \begin{bmatrix} \frac{\tilde{i}_{od}}{\tilde{d}_d} & \frac{\tilde{i}_{od}}{\tilde{d}_q} \\ \frac{\tilde{i}_{oq}}{\tilde{d}_d} & \frac{\tilde{i}_{oq}}{\tilde{d}_q} \end{bmatrix} \begin{bmatrix} \frac{\tilde{v}_{od}}{\tilde{d}_d} & \frac{\tilde{v}_{od}}{\tilde{d}_q} \\ \frac{\tilde{v}_{oq}}{\tilde{d}_d} & \frac{\tilde{v}_{oq}}{\tilde{d}_q} \end{bmatrix}^{-1} \tag{4.10}$$

Inward immittances can now be calculated out using unterminated transfer functions of this converter and measured immittances. Using (4.9) and (4.10) it can be obtained:

Input side equivalent admittance (inward):

$$Y_L^{EQ} = Y_i + \mathbf{H_i Y_L} (\mathbf{I} + \mathbf{Z_o Y_L})^{-1} \mathbf{G_o} \tag{4.11}$$

Output side equivalent output impedance (inward):

$$\mathbf{Z_S^{EQ}} = \begin{bmatrix} Z_{Sdd}^{EQ} & Z_{Sdq}^{EQ} \\ Z_{Sqd}^{EQ} & Z_{Sqq}^{EQ} \end{bmatrix} = \mathbf{Z_o} + \mathbf{G_o} (1 + Z_S Y_i)^{-1} Z_S \mathbf{H_i} \tag{4.12}$$

4.1.4 AC-DC Converter (Active Rectifier)

Rectifier simplified circuit form with variables in the matrix form is shown in Figure 4-5. Outward immittances of the open-loop converter, can be measured by perturbation of its duty-cycles d_d and d_q (4.13) and (4.14).

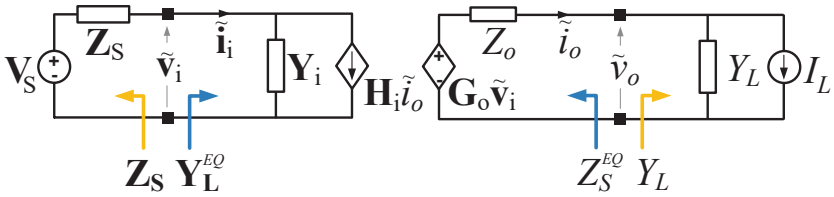

Figure 4-5: Inward and outward immittances in the active rectifier model

Input side source output impedance (outward):

$$\mathbf{Z_S} = \begin{bmatrix} Z_{dd} & Z_{dq} \\ Z_{qd} & Z_{qq} \end{bmatrix} = \begin{bmatrix} \frac{\tilde{v}_{id}}{\tilde{d}_d} & \frac{\tilde{v}_{id}}{\tilde{d}_q} \\ \frac{\tilde{v}_{iq}}{\tilde{d}_d} & \frac{\tilde{v}_{iq}}{\tilde{d}_q} \end{bmatrix} \begin{bmatrix} \frac{\tilde{i}_{id}}{\tilde{d}_d} & \frac{\tilde{i}_{id}}{\tilde{d}_q} \\ \frac{\tilde{i}_{iq}}{\tilde{d}_d} & \frac{\tilde{i}_{iq}}{\tilde{d}_q} \end{bmatrix}^{-1} \tag{4.13}$$

Output side load input admittance (outward):

$$Y_L = \frac{\tilde{i}_o / \tilde{d}_d}{\tilde{v}_o / \tilde{d}_d} \quad \text{or} \quad Y_L = \frac{\tilde{i}_o / \tilde{d}_q}{\tilde{v}_o / \tilde{d}_q} \tag{4.14}$$

Inward immittances calculated using (4.13) and (4.14) are:

Input side equivalent admittance (inward):

$$\mathbf{Y_L^{EQ}} = \mathbf{Y_i} + \mathbf{H_i} Y_L (1 + Z_o Y_L)^{-1} \mathbf{G_o} \tag{4.15}$$

Output side equivalent output impedance (inward):

$$Z_S^{EQ} = Z_o + \mathbf{G_o}(\mathbf{I} + \mathbf{Z_S Y}_i)^{-1} \mathbf{Z_S H_i} \tag{4.16}$$

4.2 Methodology Demonstration

4.2.1 Online System Observation – Simulation Example

Figure 4-6 shows the two-level voltage source converter with current and voltage sensors installed at its end-terminals, all required for online system observation and stability assessment.

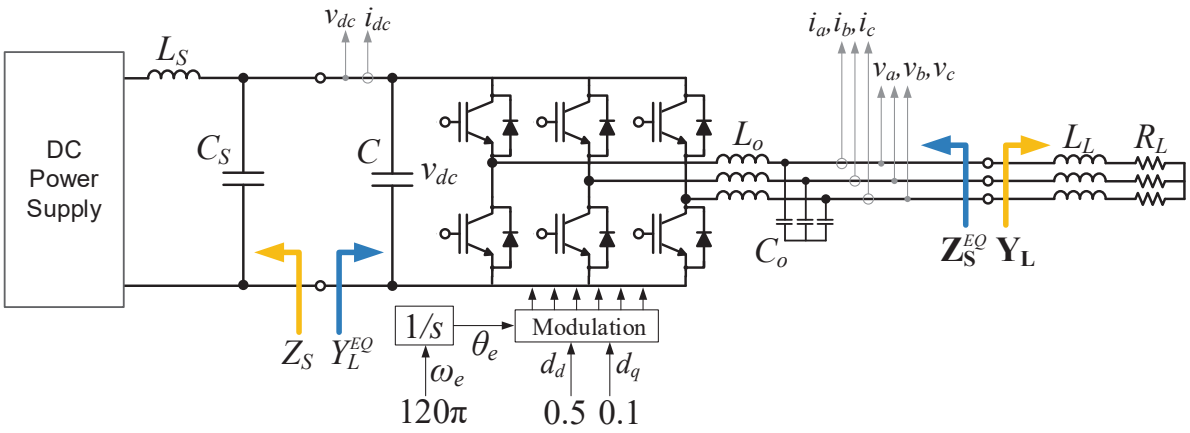

Figure 4-6: Sensor location in the voltage source inverter for online system observation

In general, assuming the three-phase system is balanced, not all of the six sensors are required. Two current and two voltage sensors are enough since the third (dependent) variable in both cases can be calculated out in real-time within the digital signal processor.

The system from Figure 4-6 is modeled in MATLAB/Simulink using the average model (Figure 2-3) with the following parameters:

Table 4.1 Model parameters

Parameter	Value	Parameter	Value
L_S	1.2 mH	L_o	250 µH
C_S	500 µF	R_L	5 Ω → 3.3 Ω
C	600 µF	L_L	250 µH
C_o	130 µF	-	-

Applying the methodology from subsection 4.1.3, more precisely (4.9) and (4.10), the source output impedance and load input admittance are obtained at the operating point determined by the input DC voltage of 400 V, load of 5 Ω, and duty cycles d_d and d_q being respectively 0.5, and 0.1. The same results can be obtained by performing linearization procedure in MATLAB. These

immittances are shown in Figure 4-7, while Figure 4-8 shows terminated and unterminated immittances overlaid. Effects of reflected source impedance and load admittance in terminated transfer functions are apparent.

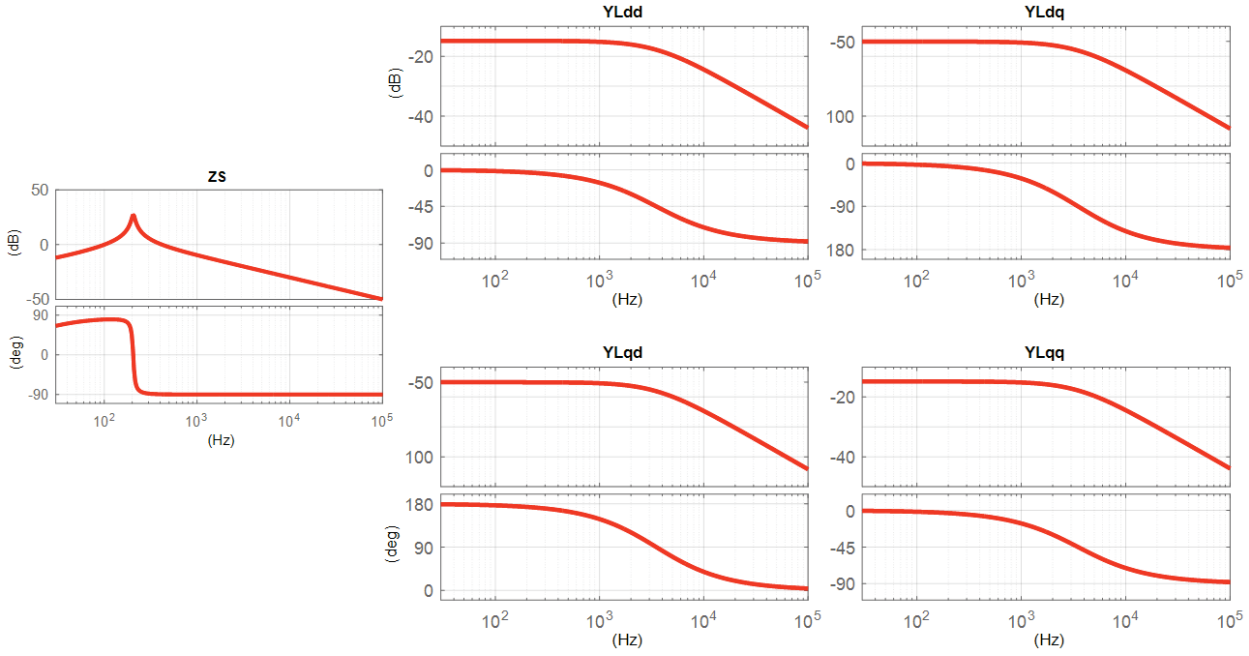

Figure 4-7: Outward immittances - source output impedance and load input admittance

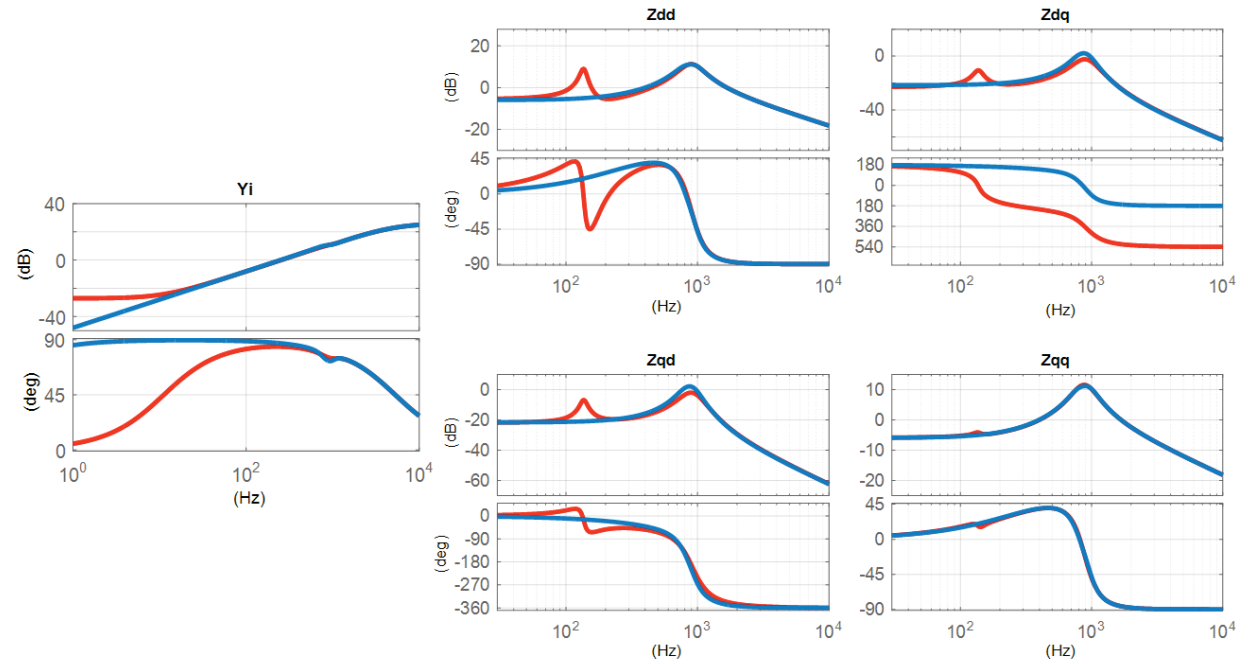

Figure 4-8: Terminated (red) and unterminated (blue) immittances; left – DC input admittance, right – *dq* output impedances

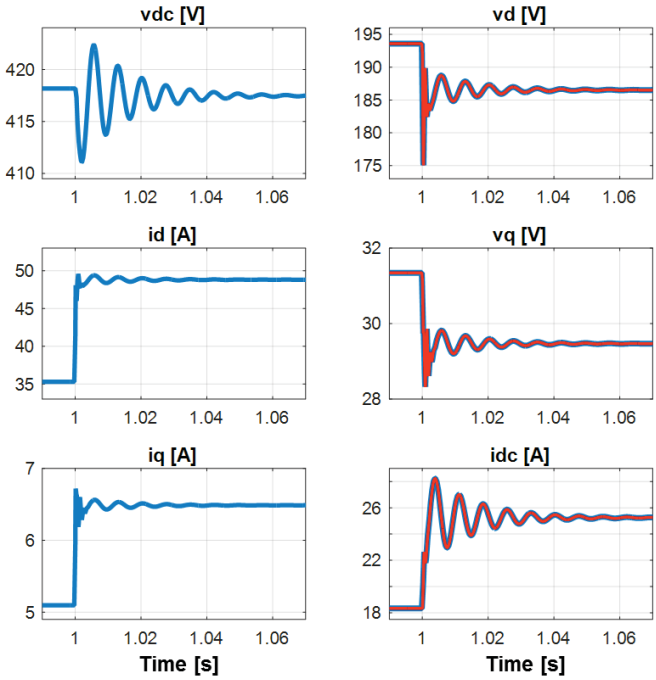

Figure 4-9: Overlaid time domain waveforms; simulation (blue), model output (red)

Figure 4-9 shows that the time domain waveforms are an effective tool to check that the small-signal transfer functions obtained in this case correctly describe the converter dynamics. With the transfer functions being well defined, the next step in the process of calculating out inward immittances - can be performed according to (4.7), and (4.8). Results are shown in Figure 4-10.

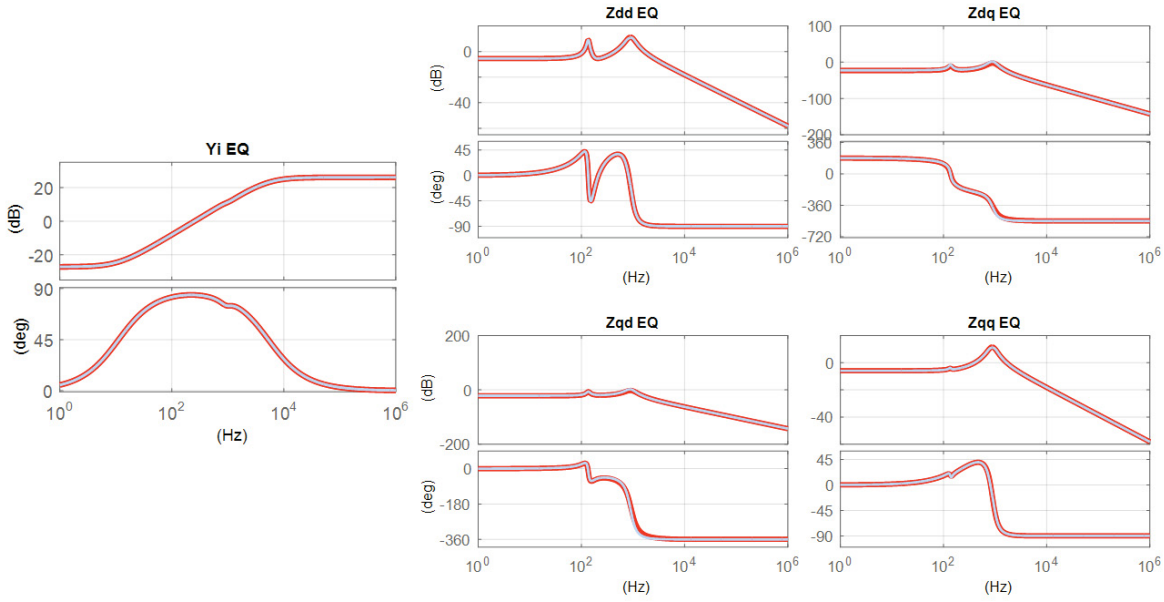

Figure 4-10: Calculated and simulated (model linearization) inward immittances; left -equivalent input admittance, right – equivalent output *dq* impedances

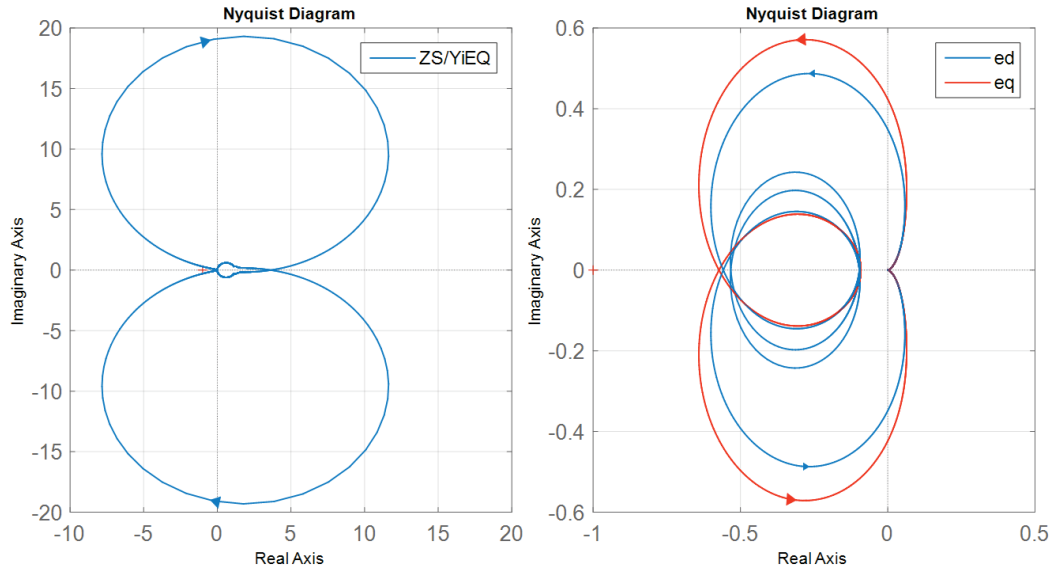

Figure 4-11: Nyquist plot of
left) return ratio – input side; right) return ratio eigenvalue loci – output side

With all terminal impedances now obtained, stability assessment can be performed either off-line or on-line. Figure 4-11 shows the Nyquist plots of the return ratio at the converter input side (DC) and the return ratio eigenvalue loci at the output side (AC). This example represents the stable system since its purpose is only to demonstrate the methodology. Each user now has an opportunity to perform stability assessment per desired stability criteria [55],[182]-[188].

4.2.2 Online System Observation – Experimental Demonstration

The two level converter described in Chapter 3 is used here as well, but is now operating as a DC-DC converter. Figure 4-12 and the Table 4.2 illustrate converter structure and test conditions.

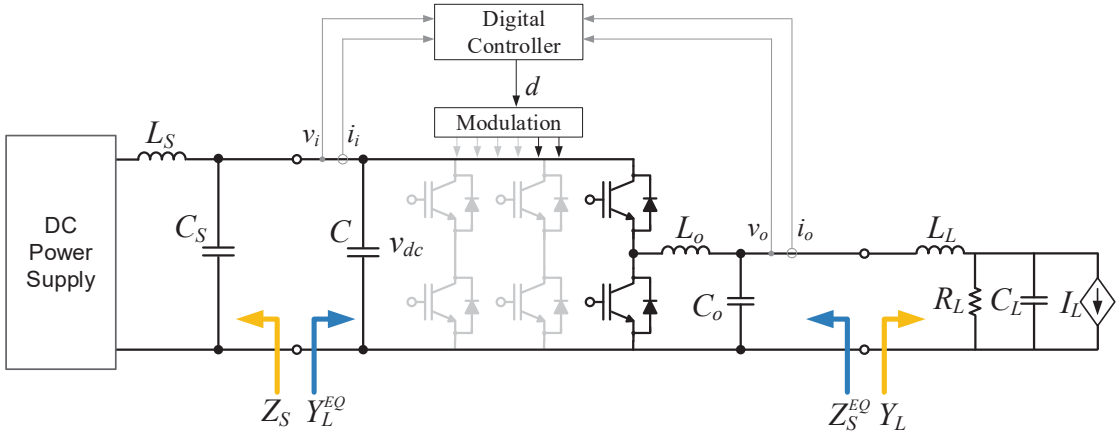

Figure 4-12: Two level converter reconfigured to operate as a buck converter

Table 4.2 Hardware parameters

Parameter	Value	Parameter	Value
L_S	500 µH	L_o	250 µH
C_S	450 µF	R_L	5 Ω
C	600 µF	L_L	500 µH
C_o	450 µF	C_L	160 µF

This converter operates in an open-loop mode with a 50% fixed duty cycle, input voltage of 110 V, and output voltage of 48 V. Constant current load IL is added to increase the output current and was stepped from 10 A to 20 A during the transient test. Operating at the nominal operating point defined by 5 Ω resistive load and 10 A constant current load at 48 V output, source output impedance, and load input admittance are measured in the frequency range from 0.1 Hz to 1 kHz using the impedance measurement unit (IMU) described in Chapter 3.

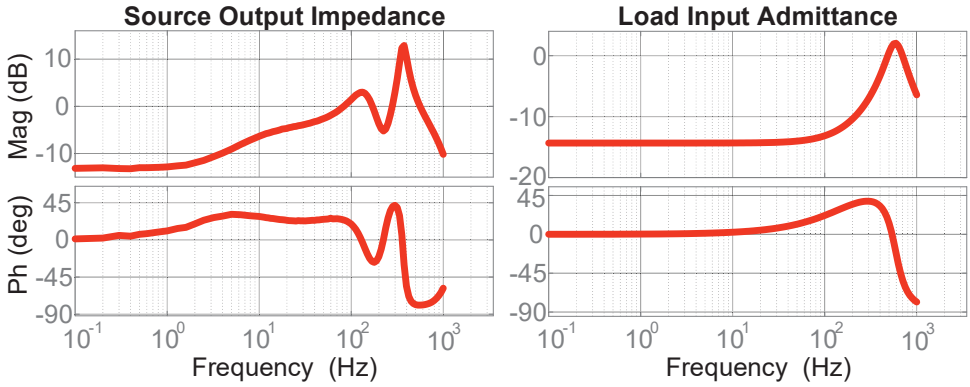

Figure 4-13: Source output impedance and load input admittance

It is required to perturb the converter duty cycle to perform an online immittance characterization. This is achieved using a Texas Instruments Software Frequency Response Analyzer (SFRA) tool offered under the powerSUITE Digital Power Supply Design Software Tools for C2000™ Microcontrollers [189]. This tool was originally developed for online plant and loop-gain measurement, but can be used as well to obtain other numerous frequency responses from the power converter being tested. After being called while the converter operates online at the particular operating point, this function performs perturbation, plots the result, and exports data with comma-separated values, a form convenient for further post-processing.

Although used here, it should be noted that the described methodology does not depend on this tool. The user can program a desired perturbation into the digital signal processor (DSP), collect

the data, and perform post processing. Moreover, if enough processing power and memory for data acquisition is available, the described process, including post-processing, can be done online in the DSP.

The SFRA tool is programed to perform a frequency sweep of the duty cycle with an amplitude of 0.03 in the frequency range from 1 Hz to 3 kHz (one sweep per frequency response). Equations (4.1) and (4.2) are programmed into the main DSP code and the obtained results are shown in Figure 4-14 with the overlaid results from Figure 4-13 obtained by the IMU. It can be seen that a very good match is achieved between the two frequency responses.

The next step is to obtain the unterminated transfer functions of the converter being tested. For this purpose, the IMU is used as the frequency response analyzer (FRA) and the whole procedure described in the Chapter 3 for the three-phase converter was repeated here as well for DC-DC.

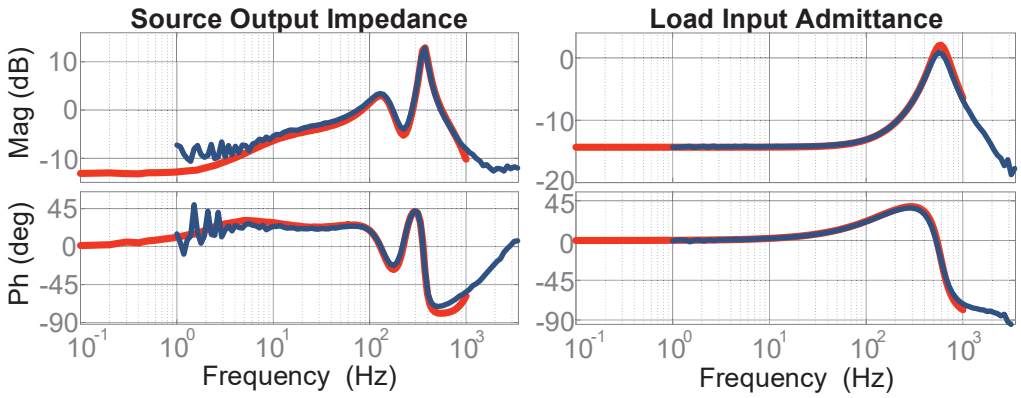

Figure 4-14: Source output impedance and load input admittance obtained using SFRA (blue) and overlaid with those obtained using the IMU (red)

Figure 4-15 shows both terminated frequency responses directly obtained from the IMU measurement and unterminated frequency responses obtained after applying the decoupling procedure – linear transformation over terminated frequency responses.

To perform a check if these frequency responses correctly describe behavior of the converter under test, time domain waveforms during the load step transient are recorded (constant current load stepped from 10 A to 20 A). As described in Chapter 3, transfer functions of the unterminated frequency responses are obtained using curve-fitting and are used in the model (2.5). If this model is now simulated in such a way that the left column variables from Figure 4-16 (v_i and i_o) are inputs to the model, then the model should output two variables (v_o and i_i) that resemble those from the

right side column variables from Figure 4-16. Figure 4-16 displays simulated variables with the measured ones. A very good match of dynamics is achieved.

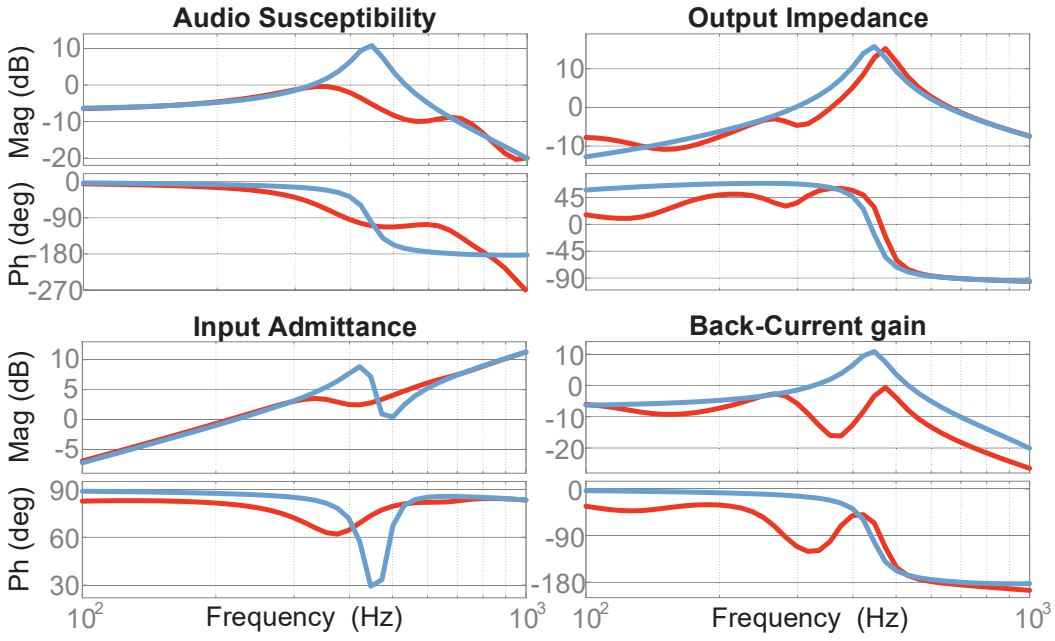

Figure 4-15: Terminated (red) and unterminated (blue) frequency responses of the DC-DC converter under test

.

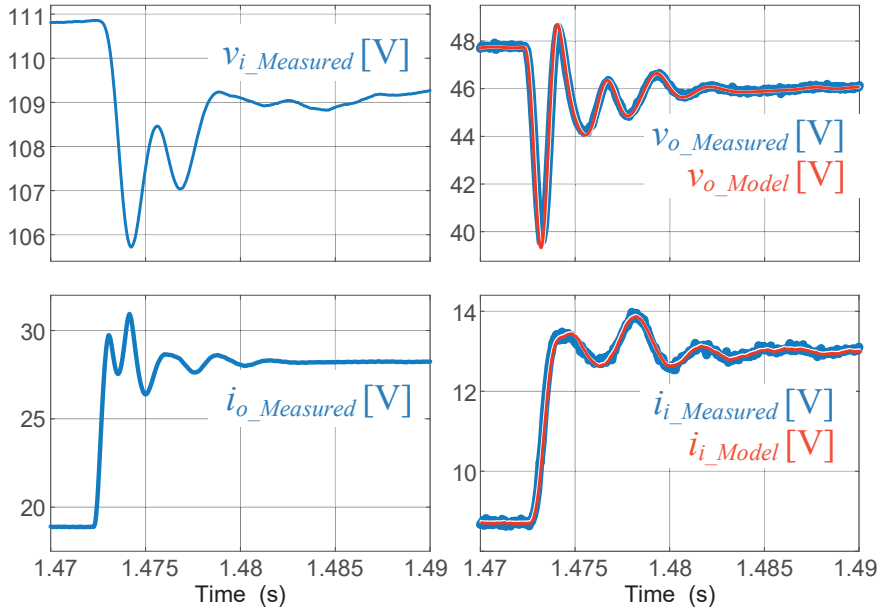

Figure 4-16: Time domain waveforms during transient overlaid with behavioral model output (DC-DC converter)

The inward immittances are now measured with the IMU. Figure 4-17 shows these frequency responses.

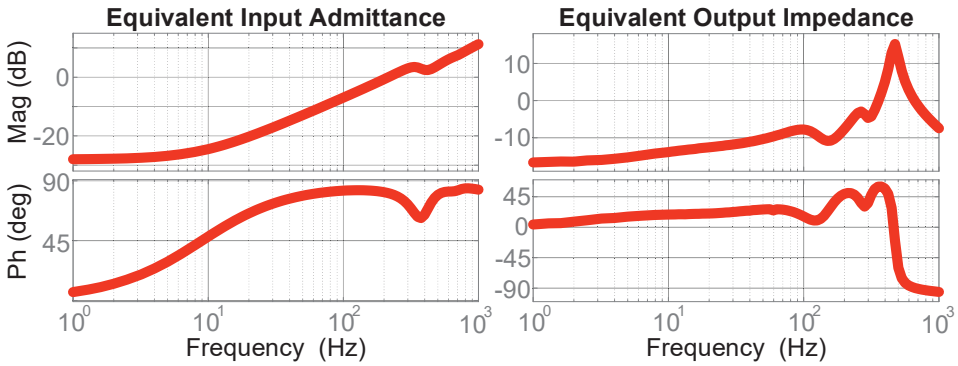

Figure 4-17: Equivalent output impedance and input admittance measured using the IMU

Equations (4.3) and (4.4) are now used together with the unterminated transfer functions and the measured outward immittances (Figure 4-13) to calculate the inward immitances. Results are now shown in Figure 4-18 overlaid with the results from Figure 4-17 obtained using the IMU. It is apparent that the calculated frequency responses match with the measured ones very well.

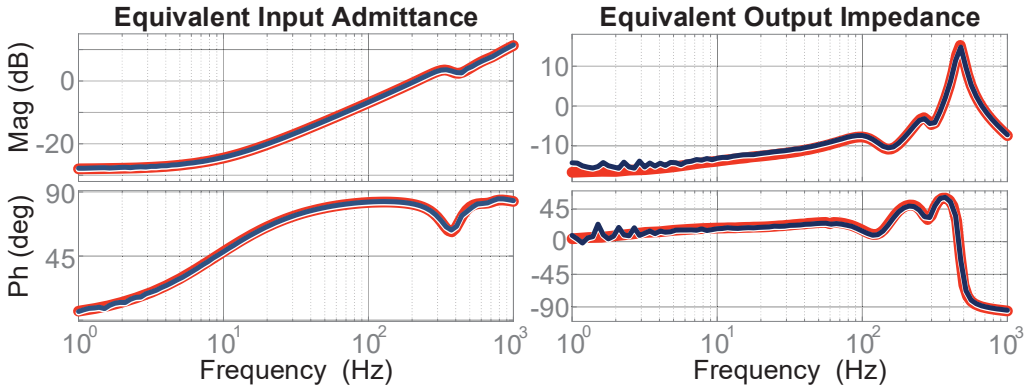

Figure 4-18: Calculated inward equivalent input admittance and output impedance (blue) overlaid with IMU-measured ones (red)

Finally, Nyquist plot of the return ratios at input and output can be produced. Figure 4-19 shows these for the converter under test for both, input and output side.

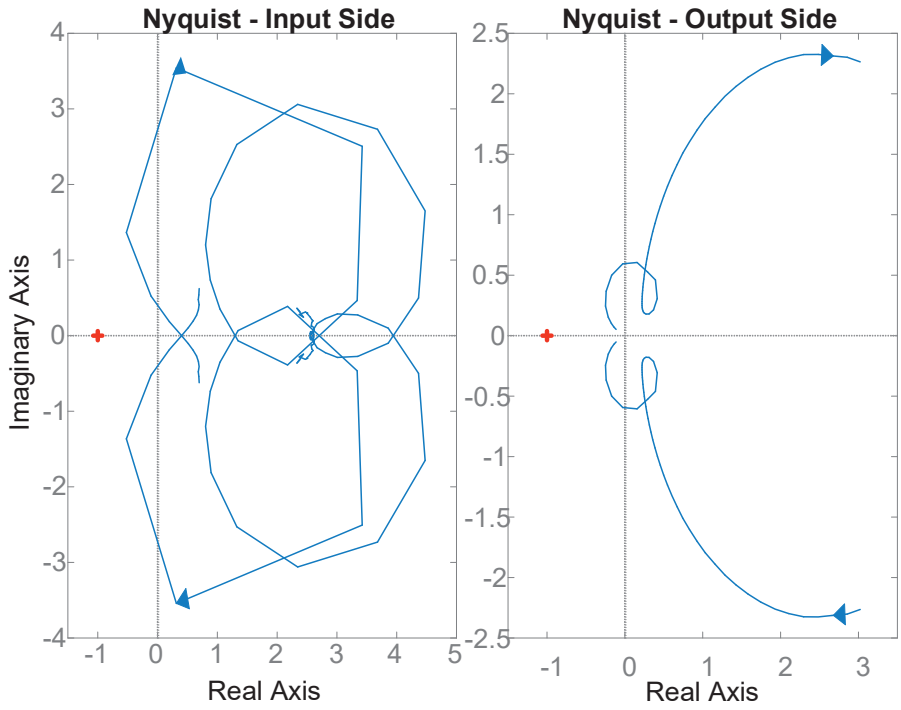

Figure 4-19: Nyquist plot of
left) return ratio – input side; right) return ratio– output side

4.3 Summary

This chapter addresses an online system observation and assessment method where, by performing internal perturbation, the converter itself can simultaneously measure outward impedances, source output impedance, and load input admittance. Combining these measurements with the unterminated transfer functions of the converter, equivalent inward impedances and admittances can be calculated which offers an opportunity to program practically any digitally controlled converter to perform an online stability assessment *in-situ*.

The previous two chapters are highly focused on the small-signal modeling of the three-phase converters and stability assessment. The dissertation will stay focused on the three-phase converters in the following chapters, but will advance into large-signal modeling of converters that emulate synchronous machines. Small-signal terminal behavioral models can still be developed for those converters, and everything described in this chapter regarding online stability assessment can be applied as well.

5. Modeling and Control Design Implementation of Grid-Connected Voltage-Controlling Converter Emulating Isotropic and Anisotropic Synchronous Machine

As the future grid has already started its slow evolution, numerous authors suggest that distributed resources (grid-interface power converters) need to behave as synchronous machines in order to guarantee power system stability, reliability, and availability, pointing to the fact that although occasional blackouts do happen, the current enormously complex power system is undoubtedly very robust and reliable. Numerous published papers discuss in detail the advantages of synchronous machine-based control of grid-interface converters, emphasizing self-synchronization properties, virtual inertia, and damping as important aspects of emulating large synchronous machines. However, distributed generation (DG) of today is not allowed to actively participate in the voltage and frequency regulation of the grid; instead, no matter how much energy is still available from the primary source, DG has to shut down when the particular subsystem of the grid is islanded. It is a good news that the power system community has recognized the benefits of DG participation in voltage control, thus the newest version of the IEEE 1547 standard, currently under ballot, will for the first time allow active voltage regulation of DG at the point of common coupling.

This chapter presents an attempt to develop a method for synchronous machine emulation that very closely replicates real electromechanical and electromagnetic processes in the machine, including saliency, field, and damper windings. The chapter starts with the development of an electrical model of the synchronous machine completely dual to the commonly used electromechanical model, but restructured to resemble the average model of a power electronics converter. As shown later in this chapter, development of this model offers a much better understanding of which power converter parameters relate to which parameters of isotropic (cylindrical) or anisotropic (salient pole) machine, providing a great insight into the required control concept for accurate machine emulation. This can first be achieved by defining electrical parameters that feature physical/mathematical duality with corresponding mechanical parameters, and second by mathematically restructuring the synchronous machine model to resemble a power converter model (without losing generality). Additionally, the goal is to use as many resources of

the chosen converter as possible (to be precise, input and output filters) leaving only complementary parts to be implemented into the converter control algorithm.

5.1 Dynamic Model of the Synchronous Machine Based on the Electro-Mechanical Duality with Power Converters

To achieve the goal of detailed machine emulation by replicating machine physical processes with the power electronics converter, the idea is to first make two dynamically dual models as shown in Figure 5-1.

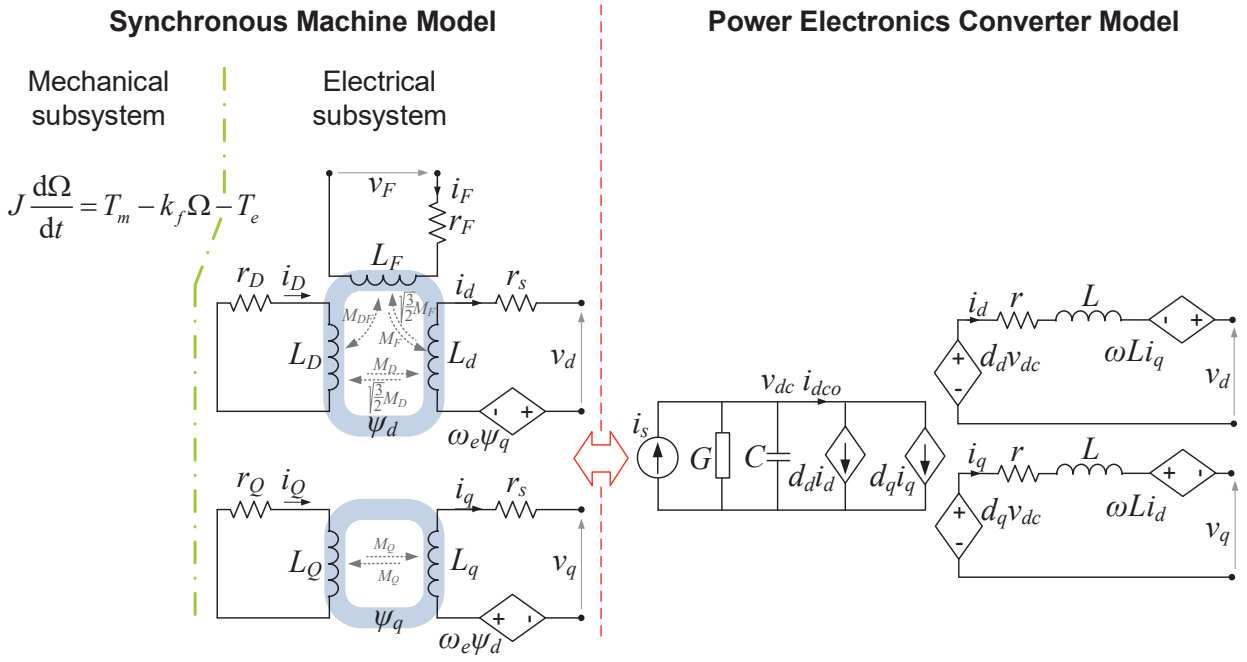

Figure 5-1: Establishing equivalence between two models

The machine equation (5.1) can be rewritten into the following form which define flux derivatives per rotor position rather than time (the main reason to reformat is to factor out the term dependent on the angular speed):

$$\begin{aligned} v_d &= -r_s i_d - \omega_e\psi_q + \frac{d\psi_d}{d\theta_e}\frac{d\theta_e}{dt} = -r_s i_d - \omega_e\psi_q + \frac{d\psi_d}{d\theta_e}\omega_e = -r_s i_d + \Omega\, p\left(\frac{d\psi_d}{d\theta_e} - \psi_q\right) \\ v_q &= -r_s i_q + \omega_e\psi_d + \frac{d\psi_q}{d\theta_e}\frac{d\theta_e}{dt} = -r_s i_q + \omega_e\psi_d + \frac{d\psi_q}{d\theta_e}\omega_e = -r_s i_q + \Omega\, p\left(\frac{d\psi_q}{d\theta_e} + \psi_d\right) \end{aligned} \tag{5.1}$$

Furthermore, active power at the machine terminals comprises the following components: joules losses, rate of change of the energy accumulated in the magnetic field, and mechanical power converted to electrical power [168]:

$$P_{dq} = (i_d^2 + i_q^2)\cdot r_s + i_d \frac{\mathrm{d}\psi_d}{\mathrm{d}t} + i_q \frac{\mathrm{d}\psi_q}{\mathrm{d}t} + \omega_e(\psi_d i_q - \psi_q i_d) \;=\; (i_d^2 + i_q^2)\cdot r_s + P_{gap} \tag{5.2}$$

Assuming lossless electromechanical conversion from rotor to stator, all of the power $P_{d\text{-}q}$ (except joules losses) is delivered from the rotor (P_{gap}). Lumping this power into the form of an "equivalent" torque, it can be written:

$$T_e^{EQ} = \frac{P_{gap}}{\Omega} = \frac{1}{\Omega}\left(i_d \frac{\mathrm{d}\psi_d}{\mathrm{d}t} + i_q \frac{\mathrm{d}\psi_q}{\mathrm{d}t} \right) + \frac{\omega_e}{\Omega}(\psi_d i_q - \psi_q i_d) = i_d \psi_{de} + i_q \psi_{qe} \tag{5.3}$$

where:

$$\begin{aligned} \psi_{de} &= p\left(\frac{\mathrm{d}\psi_d}{\mathrm{d}\theta_e} - \psi_q \right) \\ \psi_{qe} &= p\left(\frac{\mathrm{d}\psi_q}{\mathrm{d}\theta_e} + \psi_d \right) \end{aligned} \tag{5.4}$$

Now if Newton's equation (2.13) is represented in the circuit form together with (2.11) (more on mechanical-electrical equivalence in subsection 5.2), and combined with (5.1) and (5.3), the form that matches the power converter DC-AC conversion stage is obtained. This is illustrated in Figure 5-2.

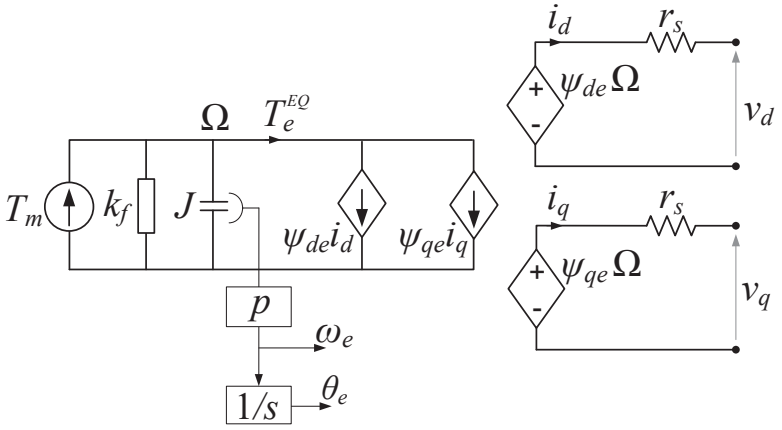

Figure 5-2: Restructured synchronous machine model

It can be noticed that the machine model from Figure 5-2 already structurally resembles quite well the converter model from Figure 5-1, however, the difference is an absence of the converter output inductor. This issue can be addressed by extracting the leakage inductance L_γ out of the flux equations due to the simple fact that it does not contribute to the process of electromagnetic power conversion in the machine.

The fluxes ψ_d and ψ_q (2.14) can be rewritten as:

$$\begin{aligned} \psi_d &= -(L_{\Delta d} + L_\gamma) i_d + M_F i_F + M_D i_D \;=\; \psi_{\Delta d} - L_\gamma i_d \\ \psi_q &= -(L_{\Delta q} + L_\gamma) i_q + M_Q i_Q \;=\; \psi_{\Delta q} - L_\gamma i_q \end{aligned} \tag{5.5}$$

where $L_{\Delta d}$, and $L_{\Delta q}$ represent mutual inductances that complement stator self-inductances with the leakage inductance ($L_d = L_\gamma + L_{\Delta d}$, and $L_q = L_\gamma + L_{\Delta q}$).

This can also be applied to the stator equations:

$$\begin{aligned} v_d &= -r_s i_d - L_\gamma \frac{\mathrm{d}i_d}{\mathrm{d}t} + \omega_e L_\gamma i_q + \Omega\, p\left(\frac{\mathrm{d}\psi_{\Delta d}}{\mathrm{d}\theta_e} - \psi_{\Delta q}\right) \\ v_q &= -r_s i_q - L_\gamma \frac{\mathrm{d}i_q}{\mathrm{d}t} - \omega_e L_\gamma i_d + \Omega\, p\left(\frac{\mathrm{d}\psi_{\Delta q}}{\mathrm{d}\theta_e} + \psi_{\Delta d}\right) \end{aligned} \tag{5.6}$$

and the equivalent torque:

$$T_e^{EQ} = i_d\, p\left(\frac{\mathrm{d}\psi_d}{\mathrm{d}\theta_e} - \psi_q\right) + i_q\, p\left(\frac{\mathrm{d}\psi_q}{\mathrm{d}\theta_e} + \psi_d\right) = i_d\, p\left(\frac{\mathrm{d}\psi_{\Delta d}}{\mathrm{d}\theta_e} - \psi_{\Delta q}\right) + i_q\, p\left(\frac{\mathrm{d}\psi_{\Delta q}}{\mathrm{d}\theta_e} + \psi_{\Delta d}\right) \tag{5.7}$$

Equation (5.7) is obtained using the following:

$$\psi_d i_q - \psi_q i_d \;=\; -L_\gamma i_d i_q + \psi_{\Delta d} i_q + L_\gamma i_q i_d - \psi_{\Delta q} i_d \;=\; \psi_{\Delta d} i_q - \psi_{\Delta q} i_d \tag{5.8}$$

Finally, using (5.6) and (5.7) the machine model that fully resembles the converter model structure from Figure 5-1 is obtained and shown in Figure 5-3.

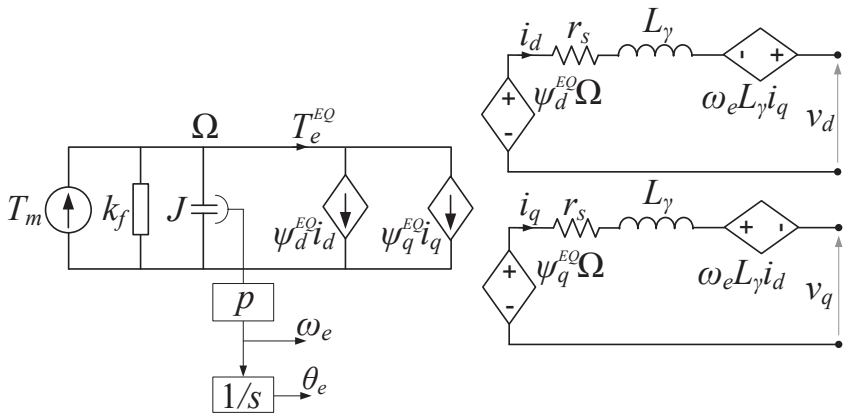

Figure 5-3: Restructured and updated synchronous machine model

Here,

$$\psi_d^{EQ} = p\left(\frac{\mathrm{d}\psi_{\Delta d}}{\mathrm{d}\theta_e} - \psi_{\Delta q}\right)$$
$$\psi_q^{EQ} = p\left(\frac{\mathrm{d}\psi_{\Delta q}}{\mathrm{d}\theta_e} + \psi_{\Delta d}\right) \tag{5.9}$$

Solving equations (2.8) and (2.9), fluxes ψ_d and ψ_q can be expressed as Laplace domain functions of i_d, i_q, and v_F [167]:

$$\psi_d(s) = -L_d(s)\cdot i_d + G(s)\cdot v_F =$$
$$-\frac{L_d\left(r_D(r_F+sL_F)+L_D r_F s + L_D L_F s^2 - M_{FD}^2 s^2\right)}{(r_D+sL_D)(r_F+sL_F)-M_{FD}^2 s^2}\cdot i_d +$$
$$-\frac{\sqrt{3/2}\left(2M_D M_F M_{FD} s^2 - M_F^2(r_D+sL_D)s\right)}{(r_D+sL_D)(r_F+sL_F)-M_{FD}^2 s^2}\cdot i_d + \tag{5.10}$$
$$+\frac{M_F\cdot(r_D+sL_D)-sM_{FD}M_D}{(r_D+sL_D)(r_F+sL_F)-M_{FD}^2 s^2}\cdot v_F$$

$$\psi_q = -L_q(s)\cdot i_q = -\frac{L_q(r_Q + sL_Q) - \sqrt{3/2}M_Q^2 s}{r_Q + sL_Q} i_q \tag{5.11}$$

These forms are more convenient for machine modeling any machine since they do not require knowledge of all machine parameters listed in Chapter 2. Moreover, as it will be seen later, so-called operational inductances L_d (s), L_q (s), and armature-to-field transfer function G(s) can be straightforwardly measured on a particular synchronous machine.

As evident from (5.10), the only control variable is actually v_F, while currents i_d, and i_q, are measured and fed back for flux calculation. Figure 5-4 shows the final restructured machine model that will be used as a basis for this work. Any isotropic or anisotropic synchronous machine, with any number of poles and damper windings can be modeled using this general model.

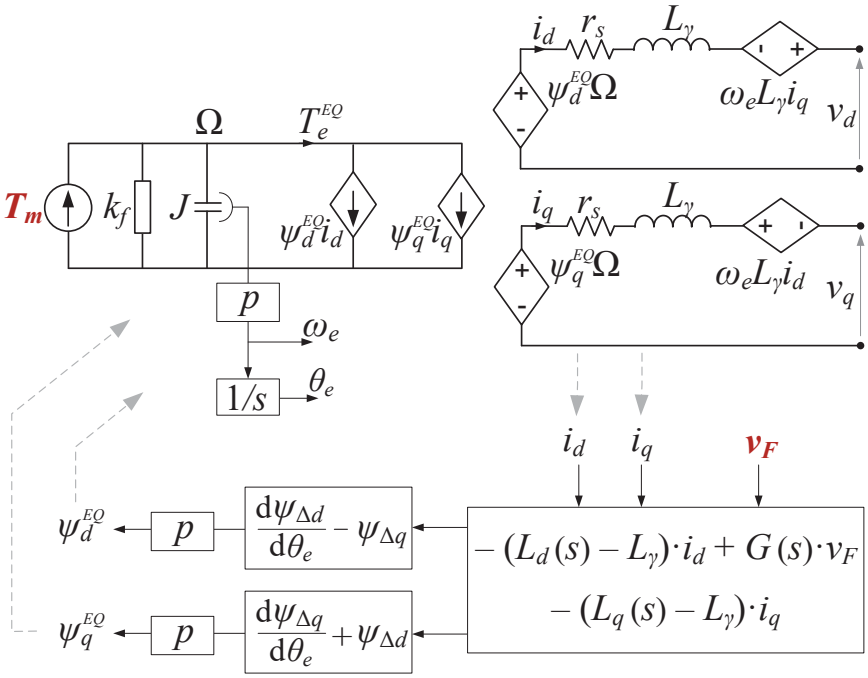

Figure 5-4: Generalized synchronous machine model

Equations (5.5)-(5.9) show the model with extracted leakage inductance L_γ. In fact, with no loss of generality, any value of L can be extracted out from the flux equations and added as an output inductor:

$$\psi_d = -(L_{\Delta d} + L)i_d + M_F i_F + M_D i_D = \psi_{\Delta d} - Li_d$$
$$\psi_q = -(L_{\Delta q} + L)i_q + M_Q i_Q = \psi_{\Delta q} - Li_q \tag{5.12}$$

As it will be seen later, this is especially important for emulation of the specific synchronous machine using a power converter that has a fixed value (L) of an output inductor – as illustrated in Figure 5-1.

Additionally, although magnetic saturation is neglected in this model, it can be added to flux equations (5.10) and (5.11) without difficulty.

5.2 An Electronic Synchronous Generator - Virtual Synchronous Machine

Being organized in a way that fully resembles a converter model, the machine model from Figure 5-4 already offers better understanding on what has to be done in order to imitate the behavior of a particular synchronous machine. This is especially obvious for the machine electrical subsystem, however, the mechanical subsystem needs some more clarification. This will be addressed in this subsection.

5.2.1 Mechanical-Electrical Subsystem Duality

Table 5.1 describes duality of mechanical/electrical units [169].

Table 5.3 Dual Units

Mechanical systems		Electrical systems
Torque $\boldsymbol{T}$	≡	Current $\boldsymbol{i}$
Angular speed $\boldsymbol{\Omega}$	≡	Voltage $\boldsymbol{v}$
Moment of Inertia $\boldsymbol{J}$	≡	Capacitance $\boldsymbol{C}$
Friction $\boldsymbol{k_f}$	≡	Conductance $\boldsymbol{G}$

With this, DC-link voltage equation (2.4) and Newton's motion equation (2.13) can be made directly equivalent leading to:

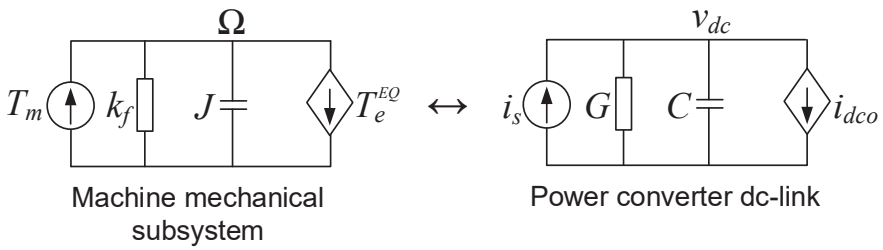

Figure 5-5: Electromechanical-electrical duality

For two subsystems from Figure 5-5 to be statically and dynamically identical, DC-link voltage v_{dc} [V] must be numerically equal to Ω [rad/s], input current i_s [A] must be numerically equal to the input torque T_m [Nm], and so on. However, since in voltage source converters the DC-link voltage has to be higher than peak line-to-line voltage on the AC side (modulation index lower than 1), it can be expected that v_{dc} [V] takes values (numerically) multiple times higher than Ω [rad/s]. This will be addressed below by defining constant K as the ratio between the DC-link voltage and grid angular frequency:

$$K = \frac{v_{dc}}{\omega_s} \tag{5.13}$$

where ω_s is the angular frequency of the system (grid) to which the converter connects. In most cases that would be 120π [rad/s] for a 60 Hz system, or 100π [rad/s] for a 50 Hz system.

There is already a similar relationship between mechanical and electrical angular frequency in machines:

$$p = \frac{\omega_e}{\Omega} = \frac{\omega_s}{\Omega} = \text{ a whole number; cannot be less than 1} \tag{5.14}$$

Figure 5-7 illustrates relationships (5.13) and (5.14):

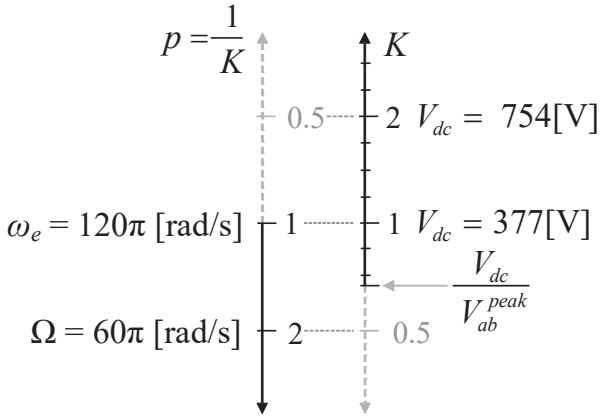

Figure 5-6: Graphical relationship between DC-link voltage, system angular frequency, and actual mechanical angular frequency of the synchronous machine

Consequently, (5.15) shows how the choice of the DC-link voltage level influences other parameters. In other words, in the attempt to completely mimic machine dynamics with the

converter (one-to-one mapping), one can choose the following values for input current, output admittance, and capacitance.

$$i_s \equiv \frac{T_m}{pK}, \quad i_{dco} \equiv \frac{T_e^{EQ}}{pK}, \quad G \equiv \frac{k_f}{p^2K^2}, \quad C \equiv \frac{J}{p^2K^2} \tag{5.15}$$

Although possible, installing a capacitor with a value C from (5.15) on the DC-link in order to emulate machine behavior would be completely impractical in all cases. Instead, this problem can be solved by means of control as will be seen in the virtual inertia subsection later.

5.2.2 Synchronization Loop

Once connected to the grid and operating at the particular operating point, synchronous machines self-synchronize to the system frequency and precisely follow its changes with a zero steady-state error. This is their inherent feature due to the physics behind the power balance [135] and is described by Newton's motion law (2.13).

This feature can be emulated in the converters as well allowing them to "synchronize" their DC-link voltages with the system frequency. Hence, it is possible to obtain internal converter angle in the same way it is obtained in the synchronous machines, only by integrating DC-link voltage of the converter:

$$v_{dc} \equiv K\omega_e \quad \rightarrow \quad \frac{\mathrm{d}\theta_e}{\mathrm{d}t} = \omega_e \quad \rightarrow \quad \theta_e = \int \frac{v_{dc}}{K}\mathrm{d}t + \theta_o \tag{5.16}$$

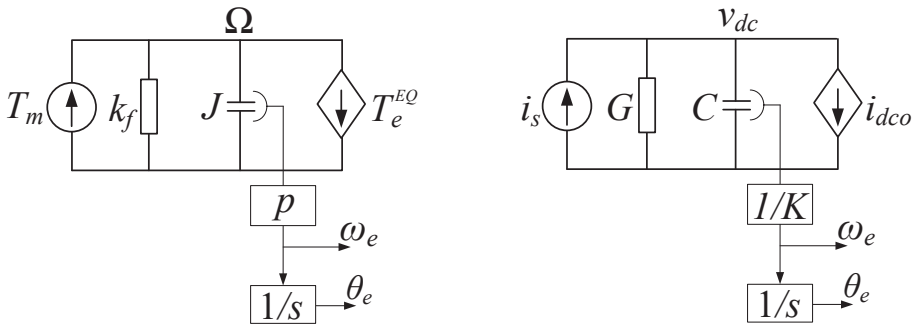

Figure 5-7: Internal angle generation (left – machine, right – converter)

Implementation of DC-link voltage integration is an essential technique for machine-like operation of power converters. In fact, to realize a very basic machine emulation with power converters, this frequency-locked loop is all that should be implemented (for instance, permanent

magnet machine emulation can be successfully realized only with this loop and fixed duty-cycles that correspond to a fixed-value rotor flux).

5.2.3 Frequency Droop

When grid-connected, the speed of synchronous machines will be in synchronism with the grid frequency and therefore no action on the speed controller will change the machine speed, it will instead change the active power flow. To allow paralleling /power sharing, many generators feature frequency droop where their governors deliver more active power when machine (system) speed (frequency) decreases, and vice versa. This can be emulated in power converters by either fully assigning the droop functionality to a front-end converter (as described in the flowing subsection), or changing parameter K during operation in order to achieve enhanced control over the active power flow (active droop control). This is illustrated in Figure 5-8.

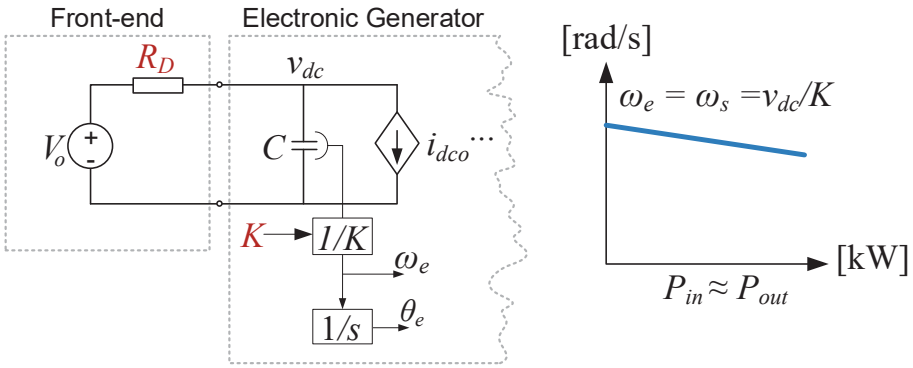

Figure 5-8: Droop implementation at the DC-link

5.2.4 Virtual Inertia

Subsection 5.2.1 shows that in order to match dynamics of the machine mechanical system, or more precisely, to mimic rotational moment of inertia of the machine - J, one (unacceptable) option is to choose the capacitor with the value of $C=J/(pK)^2$. The goal of this work is to show that this challenge can be resolved by means of control, not through hardware modification.

5.2.4.1 Method 1; front-end converter emulates virtual inertia

Boost converters are used [170],[171] in many practical realizations of converters that interface batteries, photovoltaics, or other renewable and non-renewable energy sources to the grid.

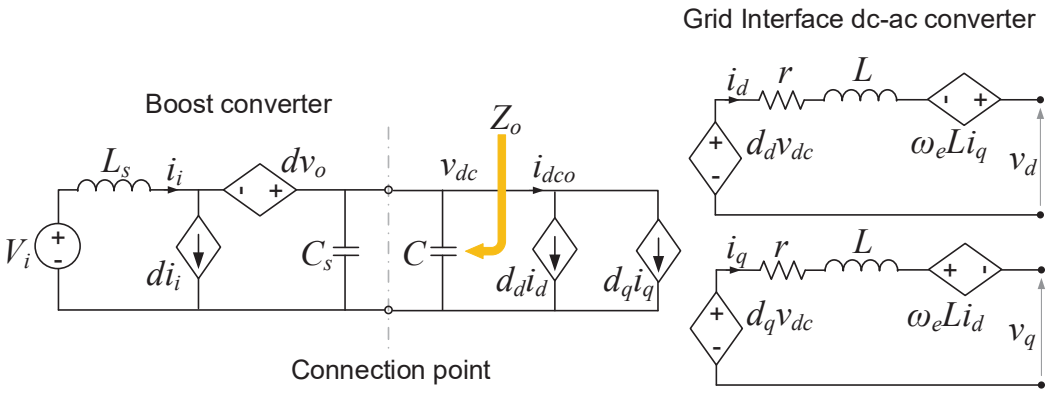

Figure 5-9: DC-DC boost converter as a front-end converter

Figure 5-9 illustrates the connection of a DC-DC boost converter to serve as a front-end power source to the grid interface converter (in this case the virtual synchronous machine). The interconnection point is clearly marked which emphasizes the existence of the boost output capacitor C_s, and DC-link capacitor C of the grid-interface converter. Obviously, the total installed DC-link capacitance is a sum of these two, nevertheless, that total value might not be a desired one which is needed to match the required moment of inertia. Therefore, some control actions have to be implemented at the boost converter level in order to shape up the desired aggregated output impedance seen from the marked orange arrow in Figure 5-10 (to the left).

Being usually fed by a steam or hydro turbine, synchronous generators in most cases operate in a speed droop mode. As speed in mechanical systems corresponds to voltage in electrical systems, the following structure can be drawn and represents the simplified prime mover.

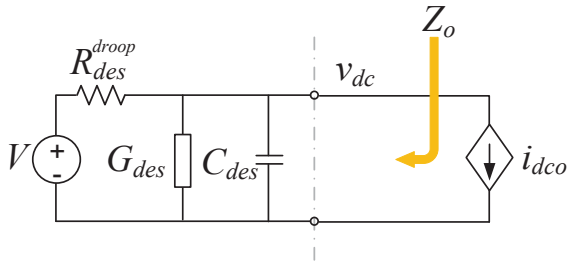

Figure 5-10: Simplified prime mover equivalent circuit

where

R_{des}^{droop} - desired droop resistance,

G_{des} - desired shunt conductance / friction,

C_{des} - desired output capacitance / moment of inertia

V - ideal voltage source

The Figure 5-11 shows one simple control structure of the boost converter needed to achieve desired output impedance.

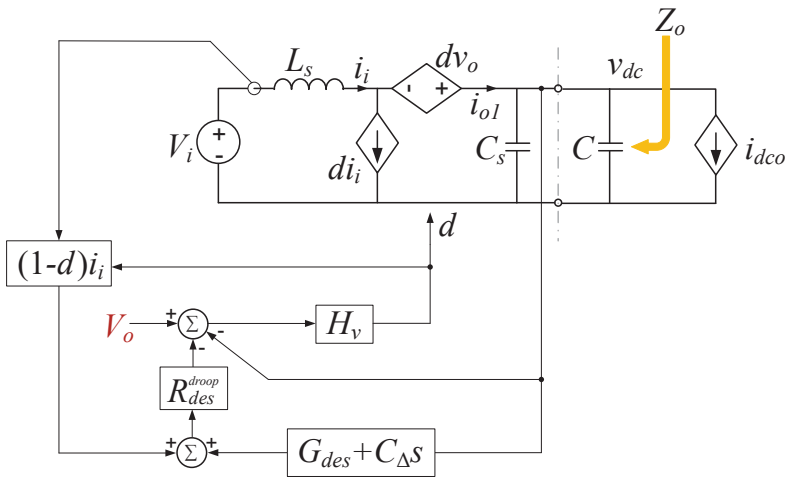

Figure 5-11: Closed-loop boost converter of virtual inertia and virtual droop

Value of the delta-capacitance shown in the circuit above, $C_\Delta = C_{des} - (C + C_s)$, represents the difference between the desired value (virtual inertia) and the combined installed capacitance at the converter output (aggregate value including both C and C_s).

The current i_{o1} in front of the capacitor C_s can be calculated out as:

$$i_{o1} = i_i(1-d) \tag{5.17}$$

and has a value:

$$i_{o1} = C_s s v_{dc} + C s v_{dc} + i_{dco} \tag{5.18}$$

Adding two more "virtual" shunt branches, (5.18) becomes:

$$i_{o1}^{'} = C_s s v_{dc} + C s v_{dc} + i_{dco} + \overbrace{C_\Delta s v_{dc} + G v_{dc}}^{\text{----virtual part----}} \tag{5.19}$$

Finally, the droop expression is:

$$v_o^{ref} = V_o - R_{des}^{droop} i_{o1}^{'} = V_o - R_{des}^{droop}\left(i_i(1-d) + C_\Delta s v_{dc} + G v_{dc}\right) \tag{5.20}$$

v_o^{ref} is then compared to the measured output voltage v_{dc}, and the error goes through the controller H_v achieving a relatively good response. Figure 5-12 shows the output impedance of the open-loop and closed-loop boost with the virtual inertia and droop implemented.

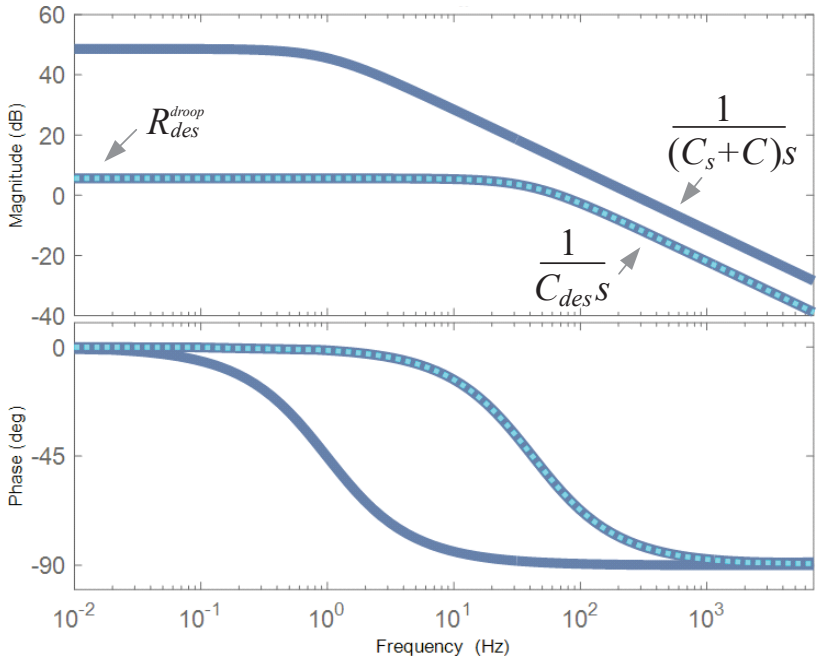

Figure 5-12: Output impedance of the boost front-end converter with virtual output impedance (dark blue – output impedance of the boost in open-, and closed-loop case; the latter overlaid with the output impedance of the simplified circuit 5-14 – shown in light blue dots)

5.2.4.2 Method 2; cancelation and replacement of DC-link dynamic

In the case when there is no access to the front-end converter (or its control), the virtual inertia can be implemented with the grid-interface converter (virtual synchronous machine) itself.

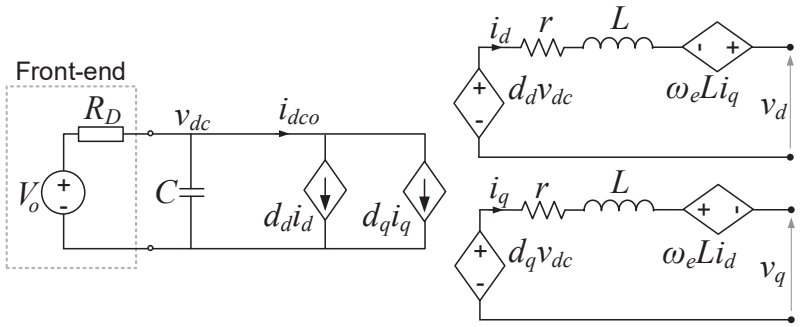

Figure 5-13: Front-end with the droop feeding voltage source converter

If the converter is supplied from the front-end featuring droop R_D, it can be written:

$$i_{dco} = \frac{V_o}{R_D} - \frac{1+sR_DC}{R_D} v_{dc}; \quad \text{where} \quad \tilde{i}_{dco} = -\frac{1+sR_DC}{R_D} \tilde{v}_{dc} \tag{5.21}$$

As this converter may not feature a desired DC-link capacitor, the following can be written for the desired dynamics:

$$\tilde{i}_{dco(desired)} = -\frac{1+sR_DC_{desired}}{R_D} \tilde{v}_{dc(desired)} \tag{5.22}$$

Now, in order for the converter from Figure (5-13) to demonstrate the same dynamics at the output side (as it would if it featured capacitor $\underline{C_{desired}}$ on the DC-link), the small-signal active power at the output has to be the same in both cases. Assuming a lossless conversion from input to output:

$$\begin{aligned} p_{out} \approx p_{in} = P_{in} + \tilde{p}_{in} = V_{dc}I_{dco} + \tilde{v}_{dc}I_{dco} + V_{dc}\tilde{i}_{dco} \quad \Rightarrow \\ \tilde{v}_{dc}I_{dco} + V_{dc}\tilde{i}_{dco} = \tilde{v}_{dc(desired)}I_{dco} + V_{dc}\tilde{i}_{dco(desired)} \end{aligned} \tag{5.23}$$

Plugging (5.21), and (5.22) into (5.23),

$$\tilde{v}_{dc(desired)} = \frac{\alpha - (1+sR_DC)}{\alpha - (1+sR_DC_{desired})} \tilde{v}_{dc}, \quad \text{where} \ \ \alpha = const. = \frac{R_DI_{dco}}{V_{dc}} \tag{5.24}$$

Including (5.24) into the synchronization loop will alter the dynamics of the voltage measured at the DC-link and generate ω_e (and θ_e) according to the new dynamics. Figure 5-14 shows the implementation of this methodology.

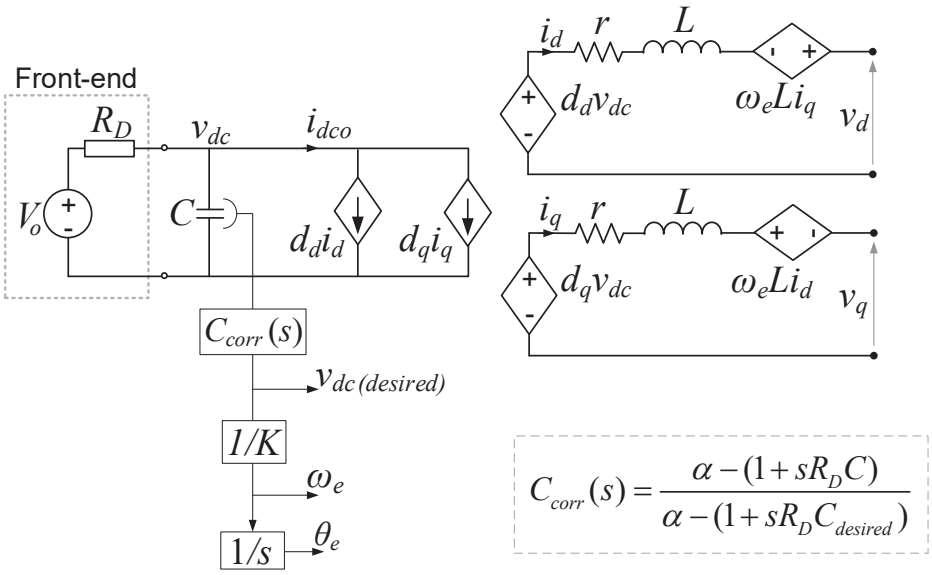

Figure 5-14: Changing DC-link voltage dynamics in the synchronization loop

However, Figure 5-14 is not enough to provide dynamics on the AC side exactly the same as it will be if the converter has a much larger capacitor installed on the DC-link. To achieve that duty-cycles d_d and d_q have to be altered as well:

$$d_d^{new} v_{dc} = d_d v_{dc(desired)} \quad \text{and} \quad d_q^{new} v_{dc} = d_q v_{dc(desired)} \quad \Rightarrow$$
$$d_d^{new} = d_d \frac{v_{dc(desired)}}{v_{dc}} \quad \text{and} \quad d_q^{new} = d_q \frac{v_{dc(desired)}}{v_{dc}} \tag{5.25}$$

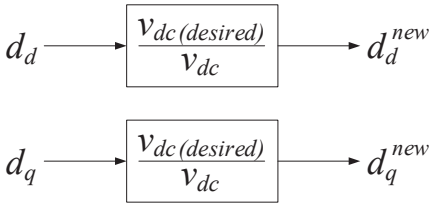

Figure 5-15: Duty-cycle adjustment for replacement of DC-link voltage dynamics

Finally, implementing (5.24), and (5.25) allows any virtual capacitor (inertia) to be emulated by means of control as long as there is a sufficient energy in the primary source (front-end).

5.2.5 Output Voltage Controller

There are many different ways and types of generator voltage control implementation commonly used in practice. However, all are based on the standard principles of regulation by comparing the measured voltage with the reference value and sending the error signal into the compensator structure to adjust the field voltage and consequently achieve output voltage regulation.

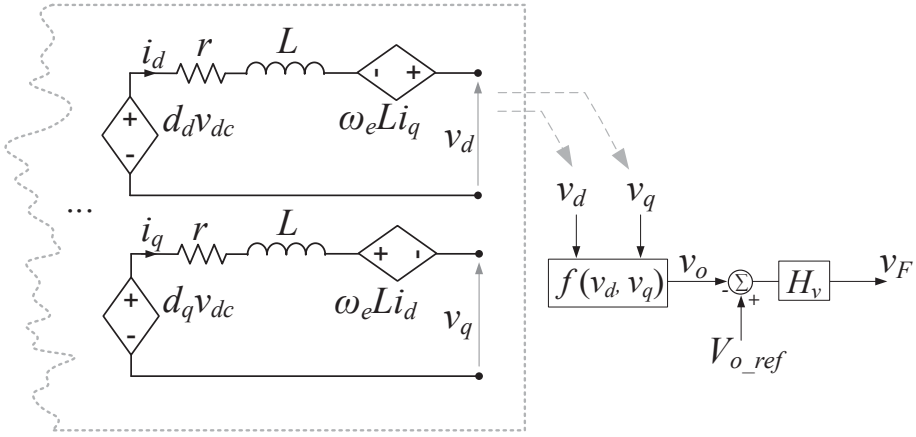

Figure 5-16: Output voltage controller

There will be more details given on the actual output voltage regulator implementation in the experimental demonstration part of this dissertation.

5.2.6 Complete Model of the Electronic Synchronous Generator - Virtual Synchronous Machine

Summarizing all the details from the previous subsections, the complete dynamic model of a virtual generator is shown in Figure 5-17. It comprises front-end stage with a droop function (for simplicity illustrated as a Thevenin equivalent with R_D output impedance to denote droop). The model also contains output voltage regulation loop and well as virtual inertia function.

It was important to develop a detailed and dual model of the synchronous machine and its virtual counterpart as the one shown in Figure 5-17, not only for the purpose of the academic exercise, but also for practical engineering reasons. Developing this model offers a good understanding of how to control power converters in order to mimic the machine behavior well, and what is more important - find a way to extend the grid-interface converter capabilities beyond the traditional synchronous machine operation.

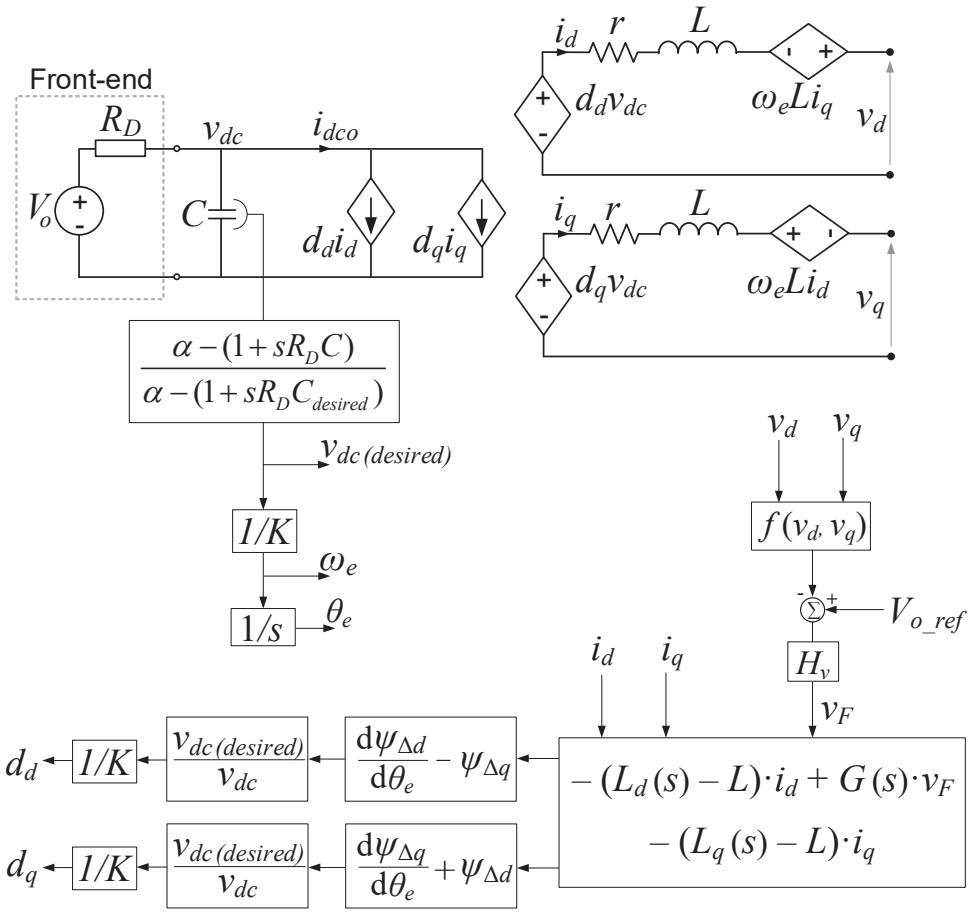

Figure 5-17: Complete dynamic model of a virtual synchronous machine

For instance, self-synchronization feature offers new possibilities for synchronization of grid-tied converters and, together with the virtual inertia concept, deserves to be further explored and improved for practical implementations. However, need for exact imitation of the other dynamics shown here (e.g. impedance and flux emulation) requires to be studied more to fully understand their potential. As a consequence of, difficulty associated with the exact machine dynamics mimicry is the derivative term for fluxes in *d* and *q* axes as shown in the model description in Figure 5-17 and (5.9); there are known problems with derivative terms in the control loops as they amplify noise and affect control bandwidth [205].

5.3 Virtual Synchronous Machine Model Verification

In order to perform a verification of the virtual synchronous machine model and proceed with hardware implementation of the concept, it is required to match the machine model with the experimental results obtained using real synchronous machine.

5.3.1 Synchronous Machine Testbed

The 30 kW testbed used in this work comprises a 30 HP variable speed drive [172], a 22 kW induction motor [173], and a four-pole 27 kW synchronous generator with field and damper windings [174]. Figure 5-18 shows the testbed. Limited information about the machine parameters is provided by the manufacturer, and the process of machine characterization (parameter extraction) is done according to the IEEE guide for standstill frequency response (SSFR) testing - Std. 115A-1987 [175].

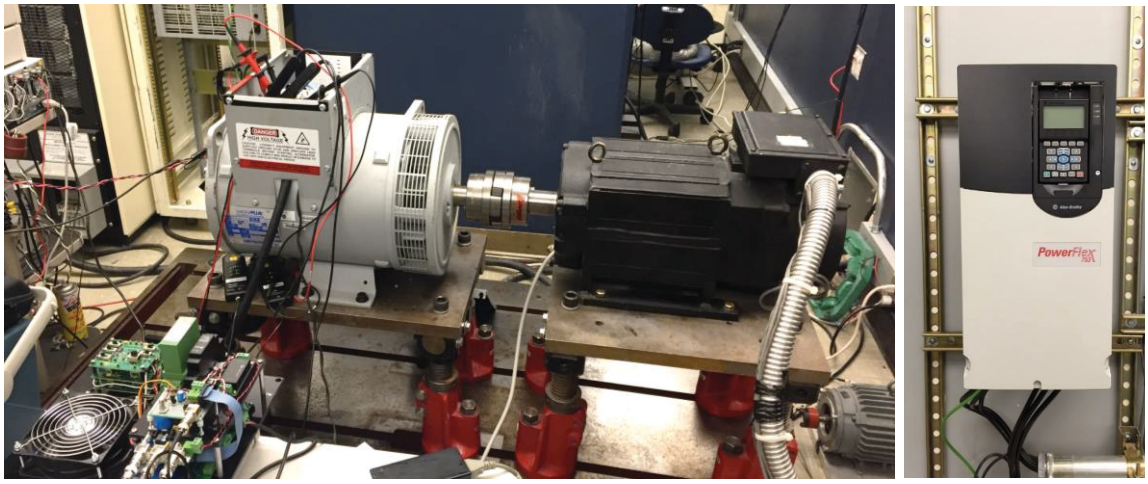

Figure 5-18: 30 kW synchronous machine testbed

5.3.2 Dynamic Characterization of the Synchronous Machine (Identification of the Machine Electrical Subsystem)

The IEEE SSFR standard proposes the measurement of several frequency response curves while the machine is at standstill. Some type of a frequency response analyzer with an amplifier is required to perturb the machine in the frequency range from a few mHz to a few hundred Hz. Most amplifiers only operate in the audible range (from about 20 Hz to 20 kHz) and may not be the best choice for machine characterization. Accordingly, a simple signal (function) generator was used

for this characterization task. The machine terminals are connected in series with the 50 Ω impedance, thus overloading the unit is prevented. Currents in the level of 50-70 mA are injected into machine, while terminal voltages are kept in the range of a few volts (10 V peak-to-peak max). Figure 5-19 illustrates the setup and measured variables.

The standard proposes a simple technique to position (by hand) the rotor of the machine in order to align it with the *d*- or *q*- axes, before performing the frequency sweep point-by-point (only the necessary steps and explanations will be given here for inclusiveness).

As seen in (5.10) and (5.11), three frequency response curves are needed in order to obtain full dynamic response of the machine.

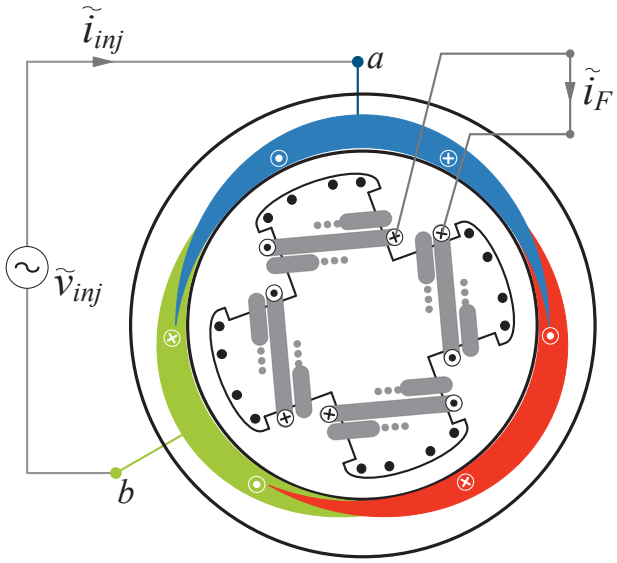

Figure 5-19: IEEE Std. 115A-1987 proposed measurement setup for machine characterization in *d*-*q*-axes

$L_d(s)$ is the direct-axis operational inductance. It represents the ratio of the direct-axis armature flux linkages to the direct-axis current with the field winding shorted:

$$L_d(s) = -\frac{\tilde{\psi}_d}{\tilde{i}_d}\bigg|_{v_F=0} \tag{5.26}$$

$G(s)$ is the armature to field transfer function. It represents the ratio of the direct-axis armature flux linkages to the field voltage with the open armature.

$$G(s) = \left. \frac{\tilde{\psi}_d}{\tilde{v}_F} \right|_{i_d=0} \tag{5.27}$$

$L_q(s)$ is the quadrature-axis operational inductance. It represents the ratio of the quadrature-axis armature flux linkages to the quadrature-axis current:

$$L_q(s) = -\frac{\tilde{\psi}_q}{\tilde{i}_q} \tag{5.28}$$

The transfer functions (5.26), (5.27), and (5.28) cannot be directly measured. Instead, they are calculated out from the measured frequency responses.

If the rotor of the machine is aligned in the *d*-axis and the measurement is set up as shown in Figure 5-19, the output impedance in the d-axis is obtained point-by-point by injecting perturbation with a resolution of about 10 frequency points per decade and ranging from 10 mHz to 1000 Hz (in 51 points). Figure 5-20 shows the measured frequency response.

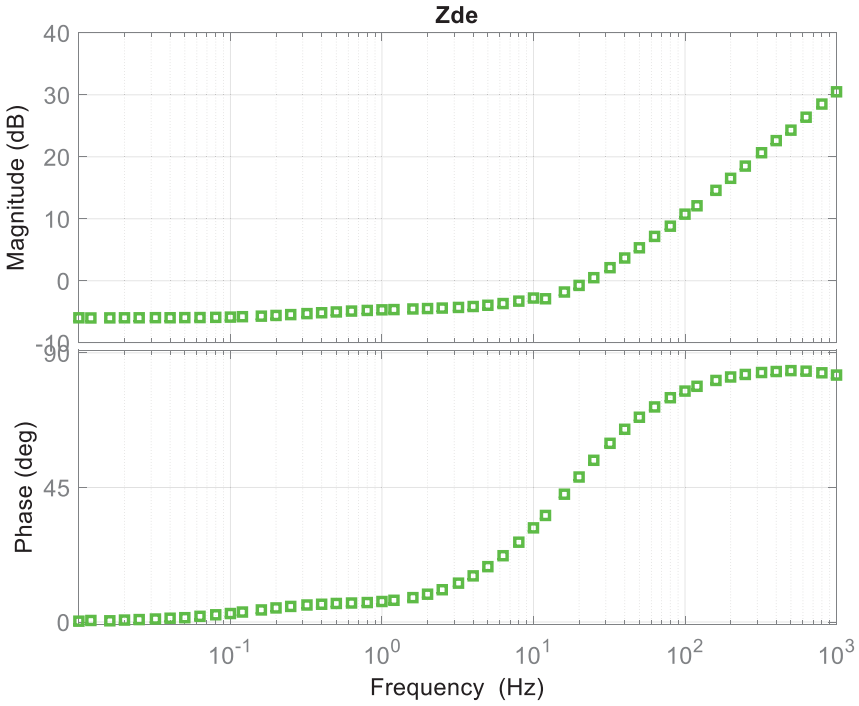

Figure 5-20: *d*-axis impedance frequency response

Since the impedance between terminal *a* and terminal *b* is measured (Figure 5-19), the obtained measurement result represents two Z_d impedances in series. The *d*-axis impedance is then:

$$Z_d(\mathrm{j}\omega) = \frac{1}{2}\frac{v_{inj}(\mathrm{j}\omega)}{i_{inj}(\mathrm{j}\omega)} = \frac{1}{2}Z_{de}(\mathrm{j}\omega) \tag{5.29}$$

Simultaneously with $Z_{de}(\mathrm{j}\omega)$, $\mathrm{j}\omega G_e(\mathrm{j}\omega)$ can be measured. That transfer function has a form:

$$\mathrm{j}\omega G_e(\mathrm{j}\omega) = \left.\frac{i_F(\mathrm{j}\omega)}{i_{inj}(\mathrm{j}\omega)}\right|_{v_F=0} \tag{5.30}$$

$$\mathrm{j}\omega G(\mathrm{j}\omega) = \sqrt{\frac{2}{3}}\mathrm{j}\omega G_e(\mathrm{j}\omega) = \left.\frac{i_F(\mathrm{j}\omega)}{i_d(\mathrm{j}\omega)}\right|_{v_F=0} = \left.\frac{v_d(\mathrm{j}\omega)}{v_F(\mathrm{j}\omega)}\right|_{i_d=0} \tag{5.31}$$

As shown in Figure 5-19, current i_F can be measured at the same time as i_{inj}. It is easy to prove the two transfer functions from (5.31) are equal, and the $G(s)$ can be straightforwardly obtained.

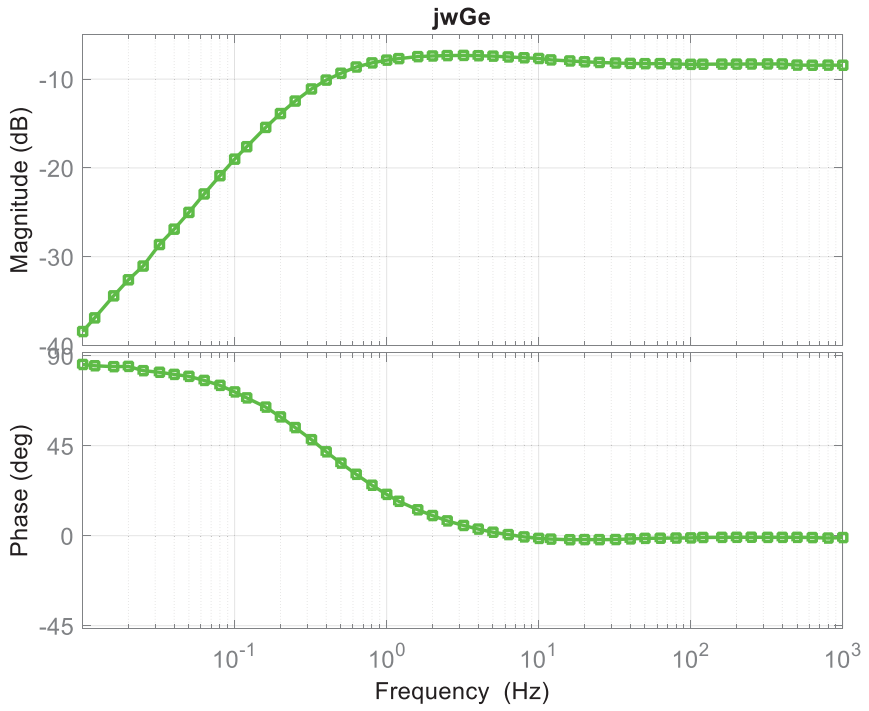

Figure 5-21: Armature to field frequency response

If the rotor of the machine is aligned in the *q*-axis and the measurement is set up as shown in Figure 5-19, the output impedance in the *q*-axis is obtained point-by-point by injecting

perturbation in 51 points from 10 mHz to 1000 Hz. Figure 5-22 shows the measured frequency response.

Similarly, as in the case of the *d*-axis impedance, the frequency response between terminals *a* and *b* is measured and the obtained measurement result represents two Z_q impedances in series; the *q*-axis impedance is then:

$$Z_q(\mathrm{j}\omega) = \frac{1}{2}\frac{v_{inj}(\mathrm{j}\omega)}{i_{inj}(\mathrm{j}\omega)} = \frac{1}{2}Z_{qe}(\mathrm{j}\omega) \tag{5.32}$$

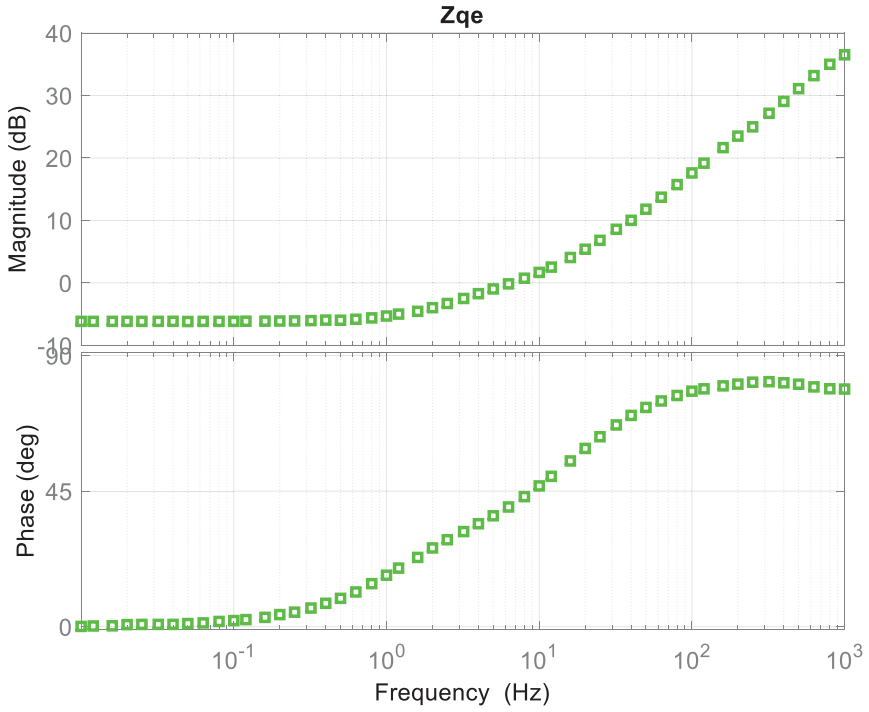

Figure 5-22: *q*-axis impedance frequency response

$L_d(\mathrm{j}\omega)$, $G(\mathrm{j}\omega)$, and $L_q(\mathrm{j}\omega)$ can now be obtained in the following way:

$$L_d(\mathrm{j}\omega) = \frac{Z_d(\mathrm{j}\omega) - R_a}{\mathrm{j}\omega} \tag{5.33}$$

$$G(\mathrm{j}\omega) = \frac{\mathrm{j}\omega G(\mathrm{j}\omega)}{\mathrm{j}\omega} \tag{5.34}$$

$$L_q(\mathrm{j}\omega) = \frac{Z_q(\mathrm{j}\omega) - R_a}{\mathrm{j}\omega} \tag{5.35}$$

where R_a is the stator resistance. The IEEE SSFR standard suggests using a Ω-meter with very good accuracy (measurement resolution of 1 part in 1000 is required), as this parameter significantly influences the calculated operational inductances L_d(s), and L_q(s) in the low frequency range (consequently, this influences synchronous inductances L_d, and L_q).

Using (5-33)-(5-35), the required transfer functions can finally be extracted from the measured data. Results are shown in (5.36) – (5.38) and below in Figures 5-23 – 5-25.

$$L_d(s) = 0.0438\frac{(1+s7.289)(1+s0.062)}{(1+s15.618)(1+s0.450)} \tag{5.36}$$

$$G(s) = 0.193\frac{(1+s15.54)}{(1+s15.618)(1+s0.450)} \tag{5.37}$$

$$L_q(s) = 0.0135\frac{(1+s0.016)}{(1+s0.038)} \tag{5.38}$$

Expressions (5.36) – (5.38) actually contain information about machine time constants in the following form:

$$L_d(s) = L_d\frac{(1+sT_d^{'})(1+sT_d^{''})}{(1+sT_{do}^{'})(1+sT_{do}^{''})} \tag{5.39}$$

$$G(s) = G_o\frac{(1+sT_{kd})}{(1+sT_{do}^{'})(1+sT_{do}^{''})} \tag{5.40}$$

$$L_q(s) = L_q\frac{(1+sT_q^{''})}{(1+sT_{qo}^{''})} \tag{5.41}$$

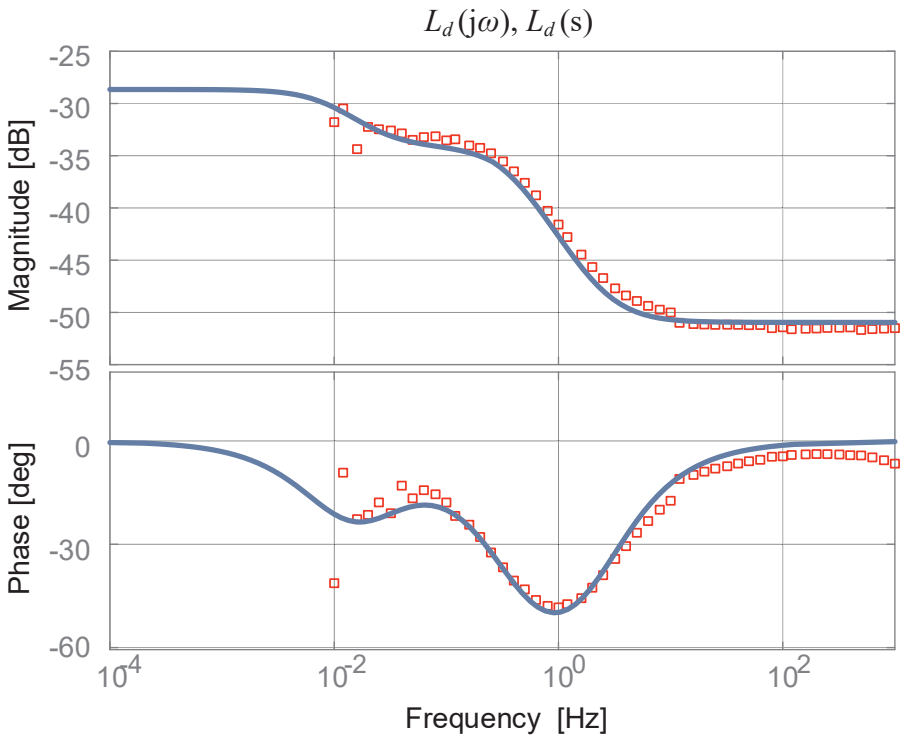

Figure 5-23: *d*-axis operational inductance;
dots – frequency response date, blue – s-domain identification (curve fitting)

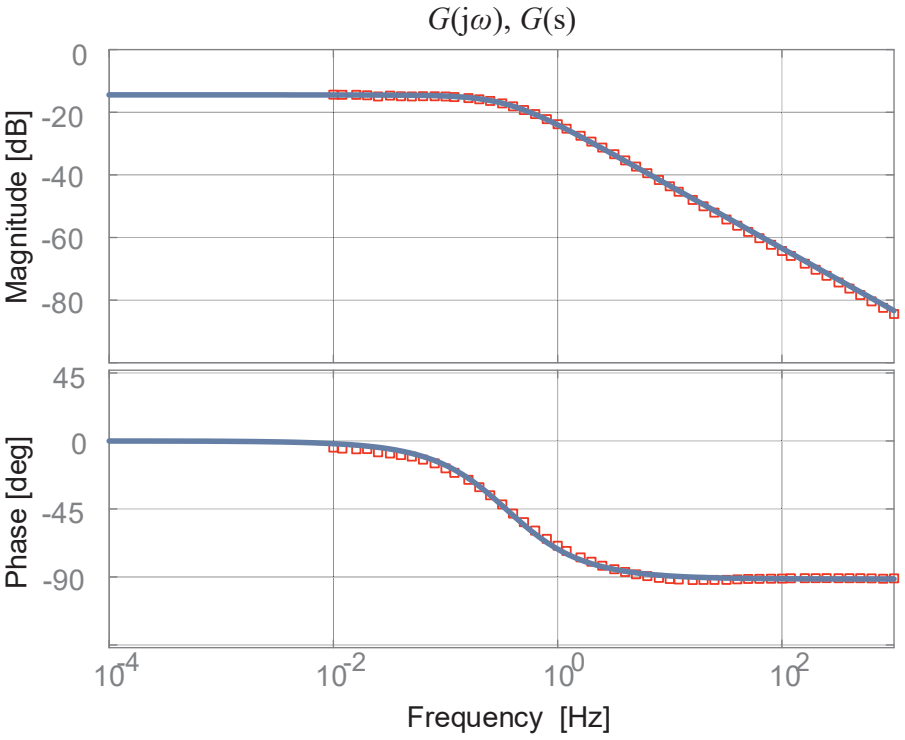

Figure 5-24: *q*-axis operational inductance;
dots – frequency response date, blue – s-domain identification (curve fitting)

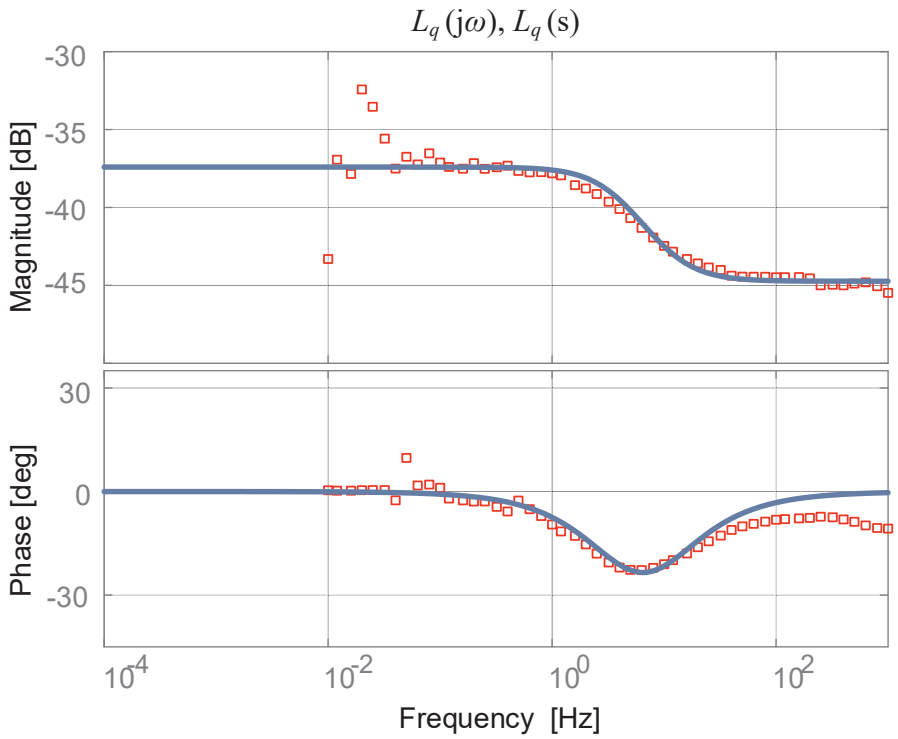

Figure 5-25: *q*-axis operational inductance;
dots – frequency response date, blue – s-domain identification (curve fitting)

Figure 5-26 depicts above relationships [167].

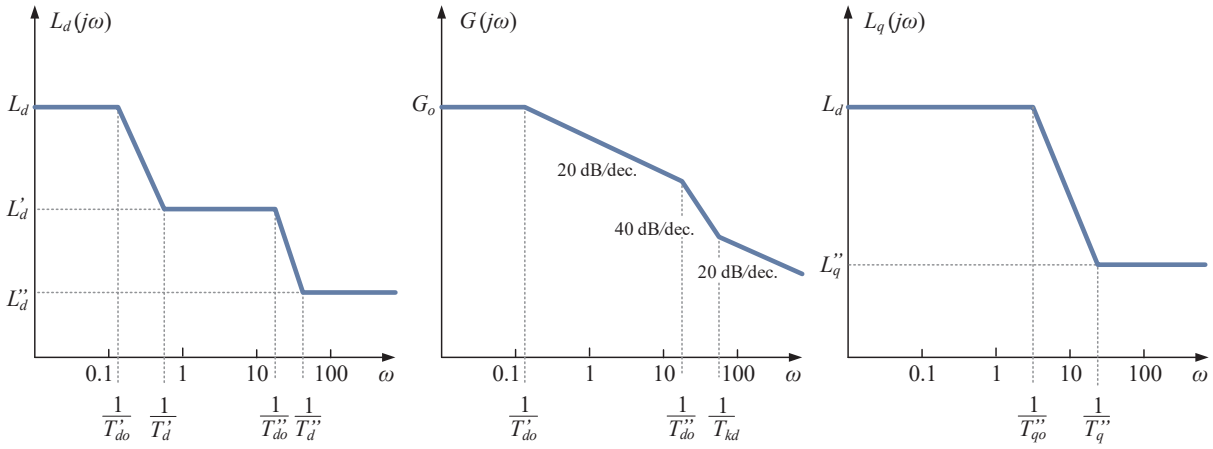

Figure 5-26: Simplified representations of L_d, G, and L_q emphasizing time constants of the machine

The transfer functions shown above unquestionably match the chosen machine model from Figure 2-5. As the rotor of the synchronous machines can be represented with multiple damper windings in both *d*- and *q*- axes, the order of the transfer functions (5.36) - (5.38) will reflect that. Consequently, the *d*-axis comprises one field and one damper winding, thus the transfer functions

L_d(s) and G(s) are second order (with the same denominator), while the q-axis features only one damper winding, therefore L_q(s) is the first order transfer function.

5.3.3 Identification of Machine Mechanical Parameters

In order to complete the machine characterization procedure, the machine moment of inertia J and the friction coefficient k_f have to be estimated (2.18). Figure 5-27 illustrates a simple measurement setup.

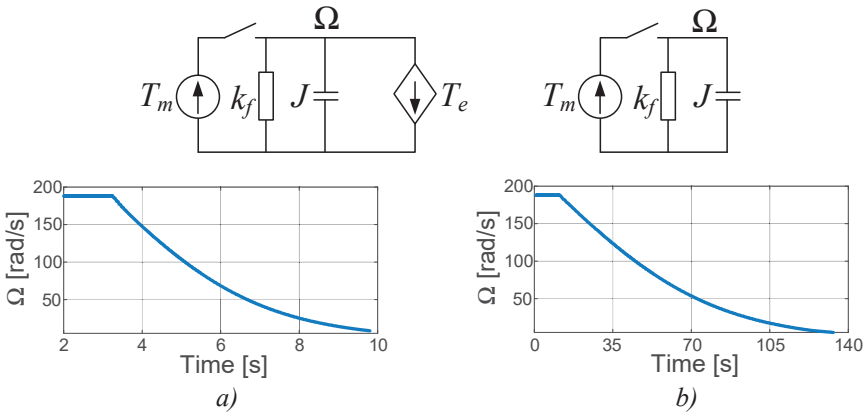

Figure 5-27: Simplified representation of two independent tests performed on the machine and corresponding speed *a)* loaded, and *b)* unloaded

Two independent measurements are performed on the machine: disconnecting the primary source (drive) after the loaded machine is spun to the nominal speed and repeating the same test for the unloaded machine. The parameters are estimated to be $J = 0.32$ [kg·m^2] and $k_f = 0.01$ [kg·m^2/s], respectively. It should be noted here that J and k_f encompass both generator and motor shafts due to being mechanically coupled.

5.3.4 Experimental Verification of the Restructured Machine Model

Once the electrical and mechanical parameters of the machine are estimated, the restructured machine model from Figure 5-4 can now be experimentally verified. If used exactly as identified (5.36)-(5.38), the transfer functions L_d(s), G(s), and L_q(s) do not automatically give a good match with the experimental results. Reasons for the lack of a good match include measurement accuracy, insufficient core excitation, and a standstill machine measurement. Therefore, measured frequency responses in the standstill may require some tuning before satisfactory results can be achieved [175]-[177]. After a series of iterations are performed over the measured data, new values for

L_d(s), G(s), and L_q(s) are determined. It can be noticed in Figure 5-28 the operational inductance L_d(s) is now a first order transfer function. This is done in order to simplify the model, as time constants associated with the original transfer function L_d(s) (5.36) are quite long.

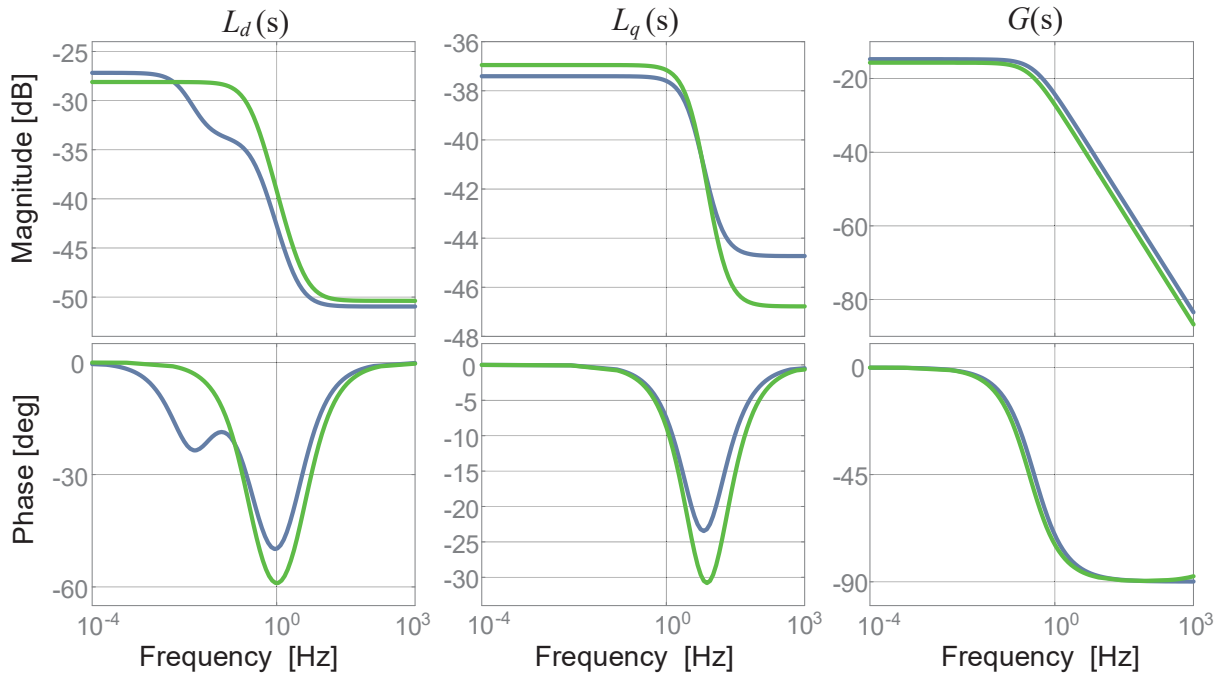

Figure 5-28: Original (blue), and modified (green) machine transfer functions

As will be seen later, the consequences of such a simplification are minimal.

The new transfer functions are now:

$$L_d(s) = 0.0393\frac{(1+s0.0438)}{(1+s0.5685)} \tag{5.42}$$

$$G(s) = 0.164\frac{(1+s6.44\cdot10^{-6})}{(1+s0.5685)} \tag{5.43}$$

$$L_q(s) = 0.0142\frac{(1+s0.0119)}{(1+s0.037)} \tag{5.44}$$

By having all of the necessary parameters available, simulation of the circuit shown in Figure 5-29 can be performed in the MATLAB/Simulink. As shown in the same figure, the generator model is loaded with an *R-L* load of L_L=1.6 mH, R_L=10 Ω, and ΔR_L=5 Ω. The choice of the load parameters is made according to the values used in the machine testbed experiments.

Similarly, the value used for the field voltage is chosen to be 4.4 V since it produces an output of 208 V line-to-line at a fixed 60π rad/s mechanical (120π rad/s electrical) speed. The following figures show model and simulation results.

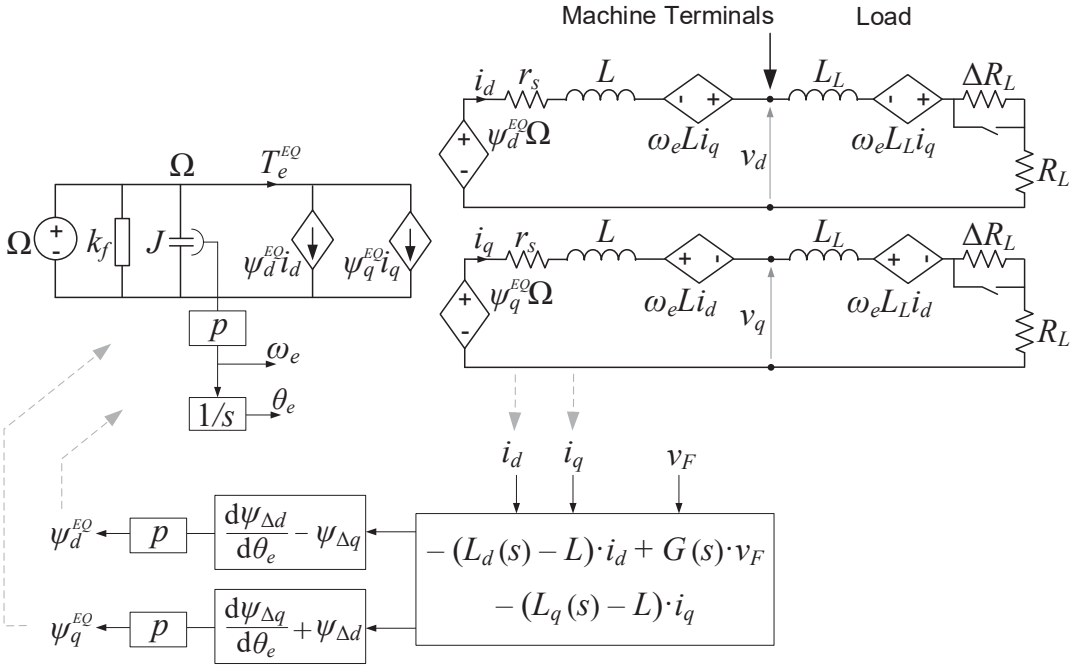

Figure 5-29: Converter-like machine model

Figure 5-30 shows simulation results of the model depicted in Figure 5-29 with measured machine parameters described. Two simulations results are plotted one over the other to show the influence of the flux derivative terms ($d\psi_{\Delta d}/d\theta_e$, and $d\psi_{\Delta q}/d\theta_e$). While simple to implement in simulation, these derivative terms are challenging to implement in practice due to inherent (noise) amplification at higher frequencies that can lead to circuit instability [205]. As noticeable in figure below, there is a negligible difference between the simulation case when these derivatives are included and the case when they are neglected due to large time constants that dominate in this circuit. Although these derivative terms will be neglected in the practical implementation of the virtual synchronous machine control throughout this dissertation, it is important to emphasize that full impact of these terms is not explored enough (here only showed in one case), and requires additional research effort before strong claims about their importance and impact can be made.

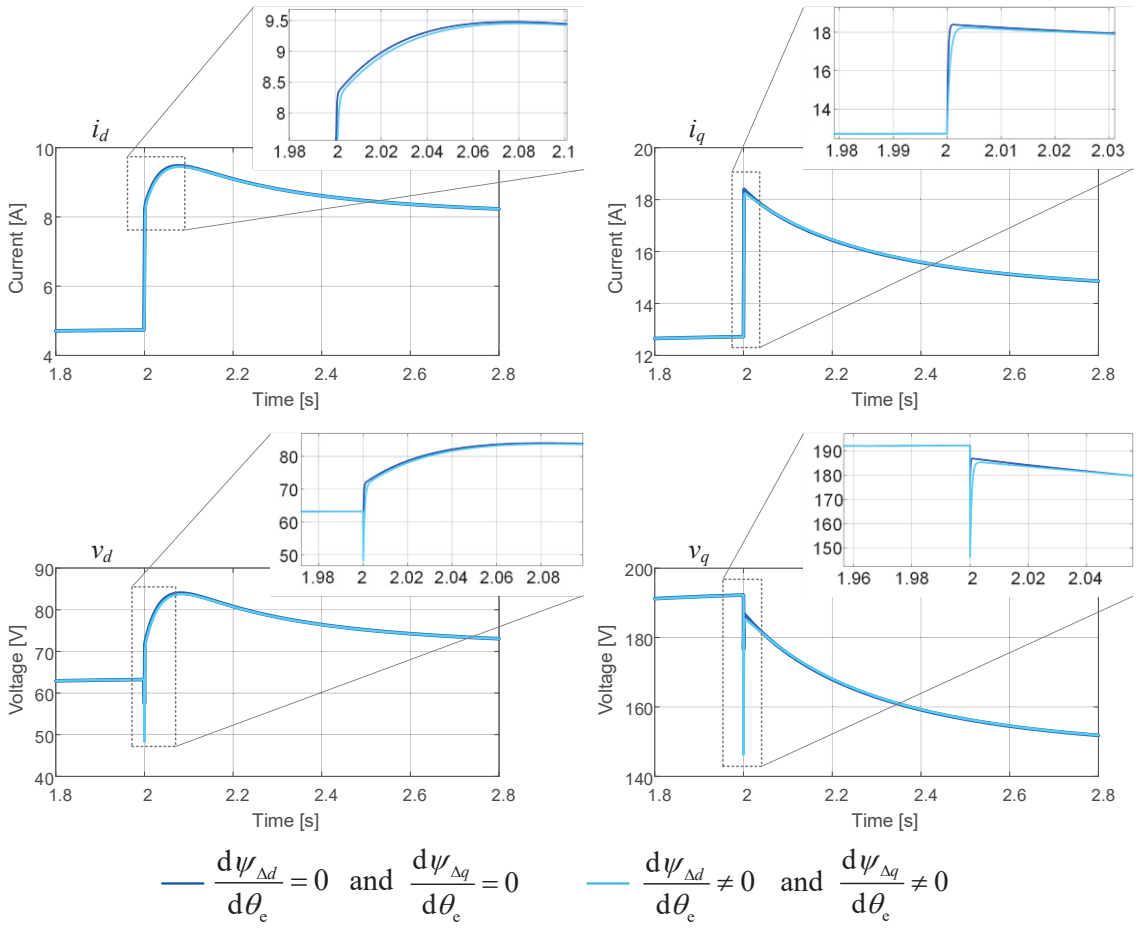

Figure 5-30: Simulation results (model from Figure 5-29) with and without flux derivative terms included

The machine transient test is now performed with the generator loaded with the real *R-L* load with values very close to those used in the simulation above. The motor-generator setup is illustrated in Figure 5-31.

The load switch (SW) was installed between two sets of resistors (R_L=10 Ω, ΔR_L=5 Ω) and the motor drive is set to operate in the constant speed mode with the reference speed of 60π rad/s (60 Hz). The field voltage is supplied from the laboratory power supply and set to the value of 4.4 V in order to achieve generator output voltage (line-to-line) of 208 V. Even though the nominal rating of the generator is 480 V, all the tests in this dissertation are performed at 208 V, assuming the magnetic saturation effect is negligible at less than half the nominal voltage. This choice is not completely without merit since 208 V is the standard voltage in the U.S.

The load step is introduced and transient waveforms are recorded. Two phase currents and two line-line voltages are measured (the third one is calculated out assuming the system is well

balanced). The phase voltages are then calculated out from the measured line-to-line ones, as phase the variable-based *d-q* transformation is used throughout this dissertation.

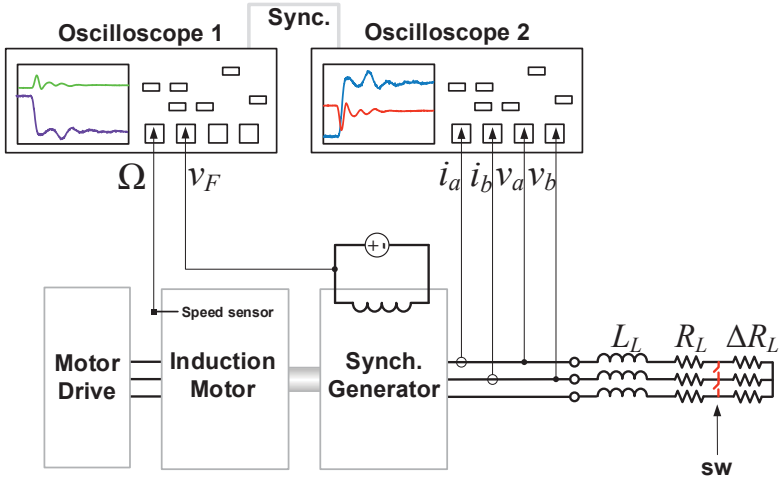

Figure 5-31: Setup for machine transient test

Figure 5-32 shows generator output voltage and output phase current captured on the scope during the load step transient.

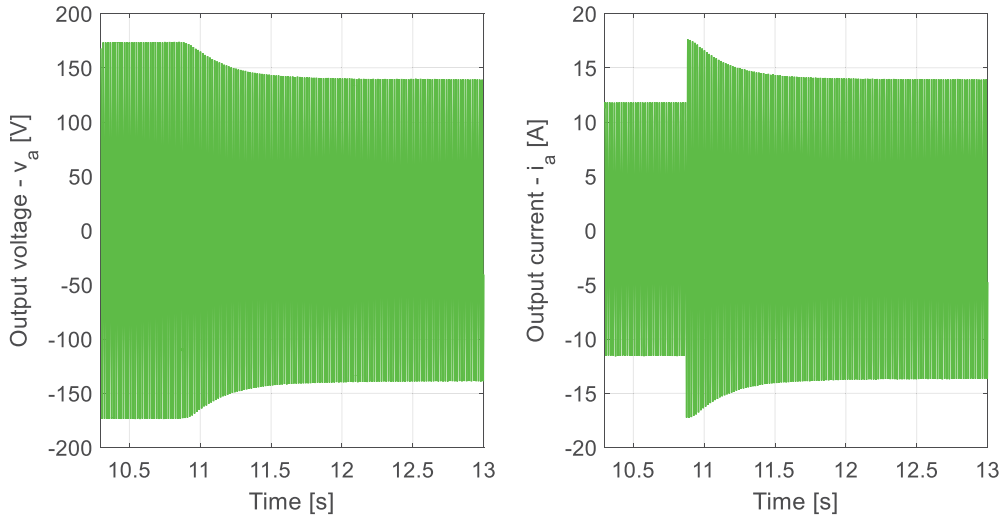

Figure 5-32: Time domain waveforms during load step transient; left - generator output (phase) voltage; right – output current

The generator speed captured and shown in Figure 5-33 experiences a negligible change after the load transient at 10.85 s because the motor drive operates in a speed regulation mode (stiff front-end).

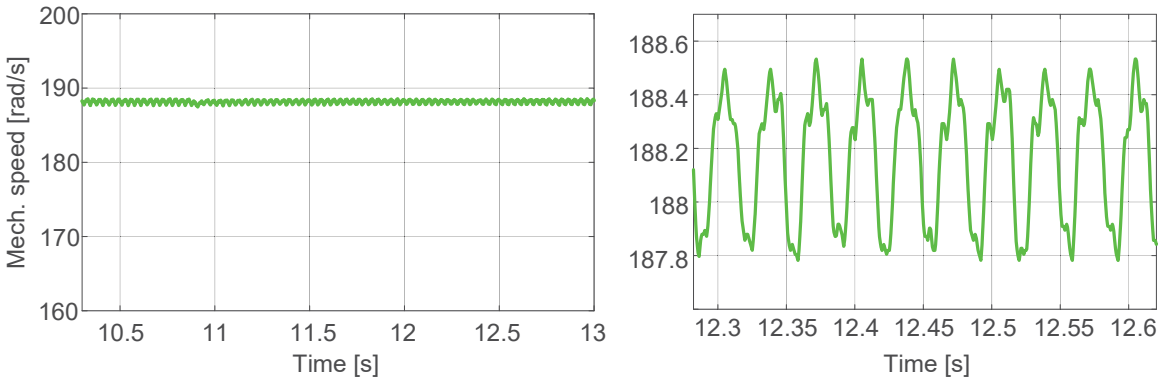

Figure 5-33: Left - Generator mechanical speed during transient; right - blown-up detail

It can be noticed that the generator speed contains 30 Hz ripple with about 0.7 rad/s peak to peak speed variation. This is caused by some anomaly in the mechanical system of the motor-generator group (bearings or misalignment) and is observed at various speeds including the very low speeds. Fortunately, the effects of it are minimal so the repair of the motor-generator testbed is postponed to not delay the progress of the research reported in this dissertation.

Once recorded, the time domain waveforms ($v_{a,b,c}$ and $i_{a,b,c}$) from the transient test are transformed to *d-q* for comparison with the restructured converter-like machine model derived earlier in this dissertation. Power-invariant *d-q* transformation (2.6) is performed on the measured variables by using measured machine mechanical speed (Figure 5-33).

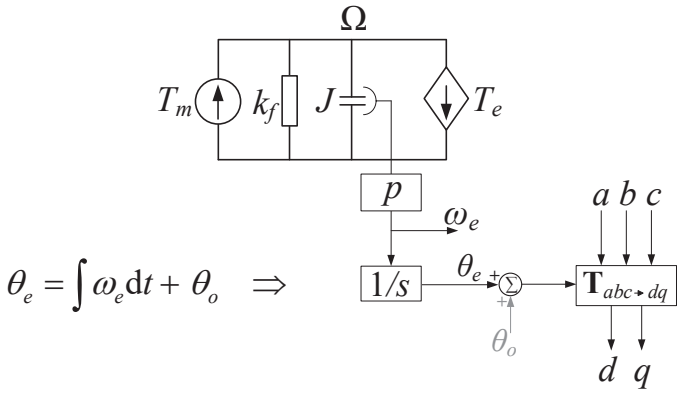

Figure 5-34: *d-q* transformation of the measured variables

Figure below shows generator output currents and voltages in *d-q* obtained experimentally and overlaid with simulation results for better comparison.

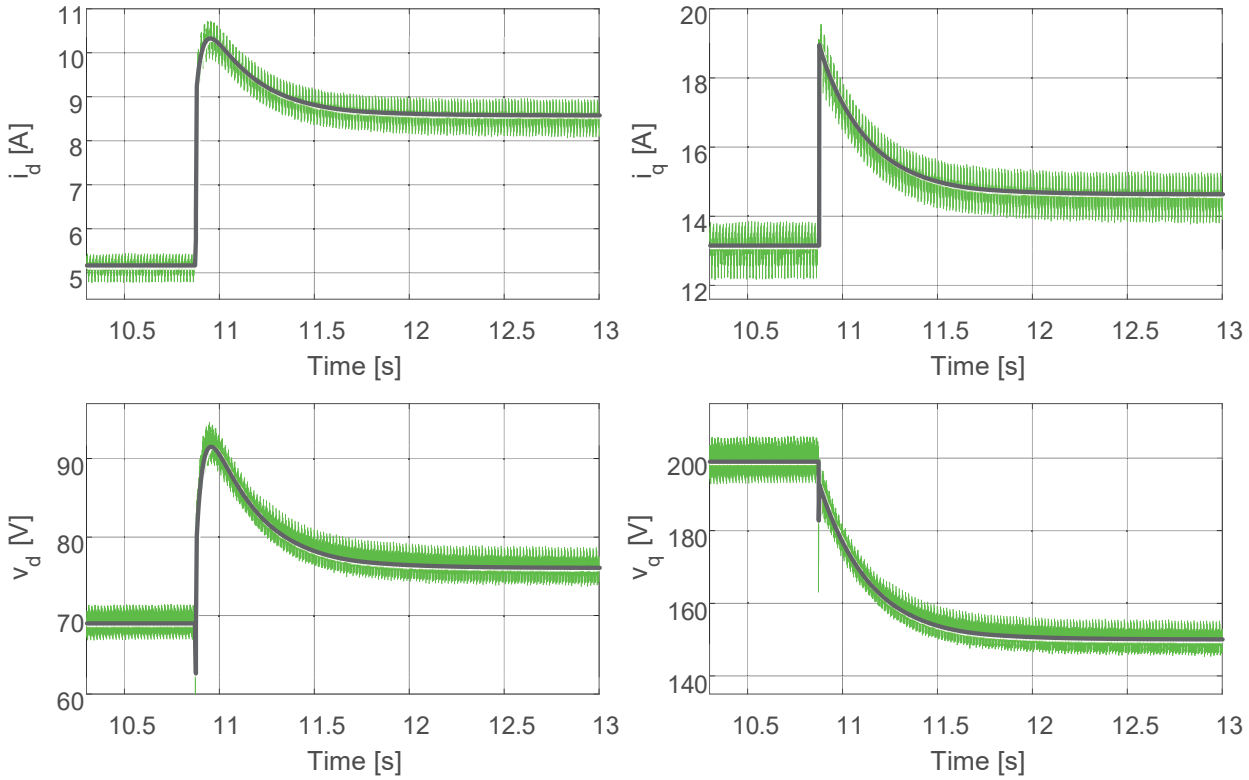

Figure 5-35: Experimental results overlaid with simulation for the load step transient; experiment - (green), simulation - (gray)

As apparent in Figure 5-35, a very good match between measured and simulated results is achieved. However, it can be noticed that *d*-*q* currents and voltages contain considerable ripple due to the DC offset and harmonics (specifically 3rd, 5th, and 7th) in the measurement results.

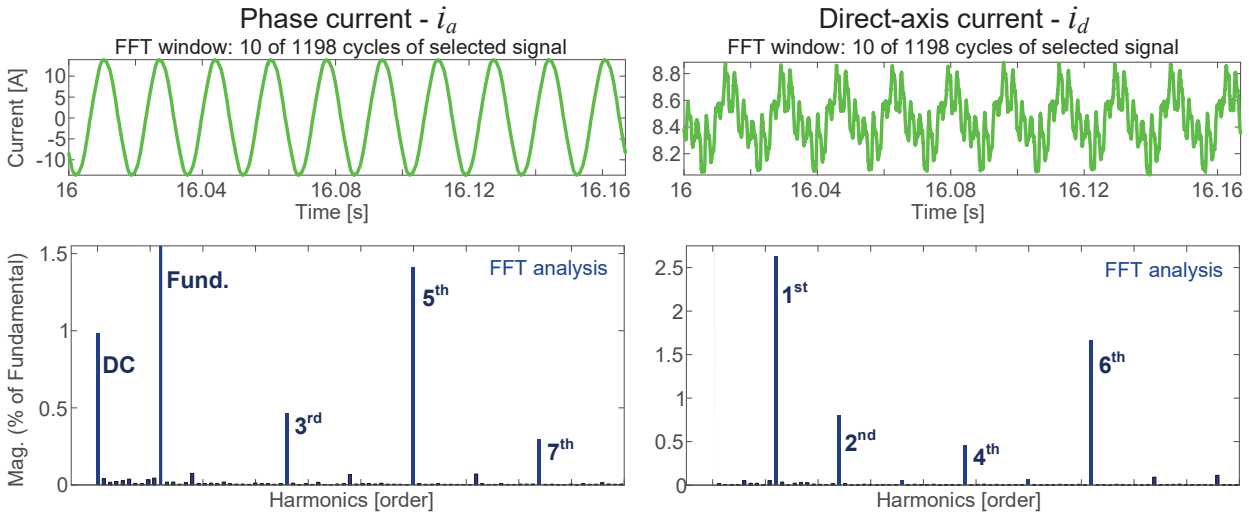

Figure 5-36: Harmonic content in phase and *d*-axis current (measurements)

FFT analysis of the *d*-axis current shown in Figure 5-36 confirms this; 60 Hz, and 360 Hz component dominate in the frequency spectrum of this current.

In order to transform measured *abc* variables to *d-q* (as shown in Figure 5-35 for comparison with results obtained via simulation), knowledge of the initial rotor position is required (rotor flux aligned with *d*-axis). Because there was no position sensor available on either machine in the testbed, the initial angle θ_o had to be determined either iteratively, by performing a manual adjustment, or by using the initial angle from the simulation to transform measured *abc* variables. The second solution requires very precise synchronization of the measured and simulated variables through either *abc* variables or transient events, and is used for results shown above, where reasonable matching is achieved between simulation and measurement results.

One alternative to the problem with the transformation angle, when comparison of the results obtained by different means is of interest (simulation – experiment or experiment – experiment), is the use of instantaneous current (or voltage) magnitude. Figure 5-37 demonstrates this alternative.

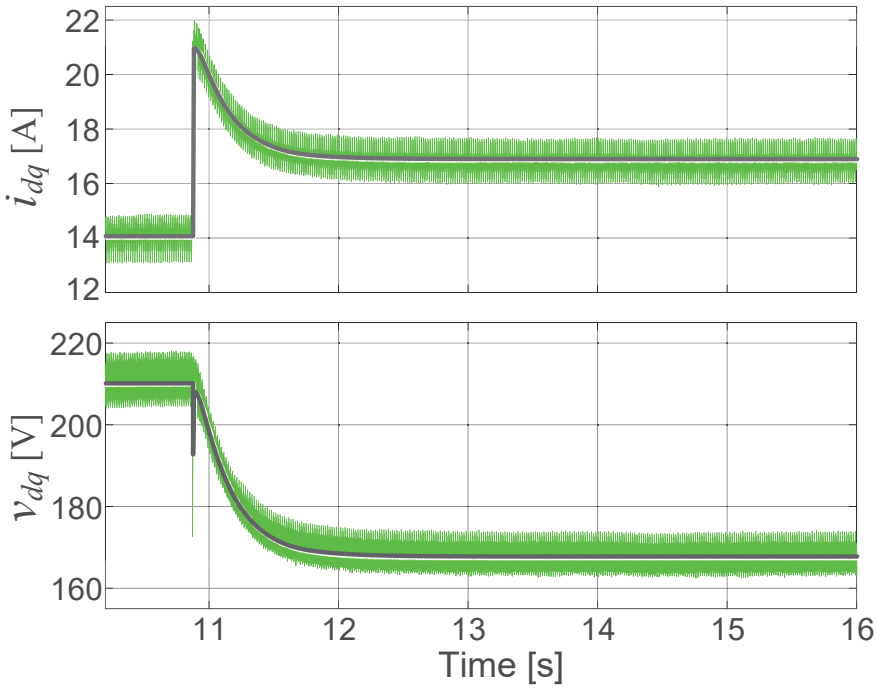

Figure 5-37: Instantaneous magnitude current and voltage comparison; experiment - (green), simulation - (gray)

The quantities are measured directly in *abc*, and are angle independent (5.45).

$$i_{dq} = \sqrt{i_d^2 + i_q^2} = \sqrt{i_a^2 + i_b^2 + i_c^2} = \sqrt{2}\sqrt{i_a^2 + i_b^2 + i_a i_b} = \sqrt{3}\, i_{RMS}$$
$$v_{dq} = \sqrt{v_d^2 + v_q^2} = \sqrt{v_a^2 + v_b^2 + v_c^2} = \sqrt{2}\sqrt{v_a^2 + v_b^2 + v_a v_b} = \sqrt{3}\, v_{RMS} \tag{5.45}$$

The above relationship between *abc* and *d-q* quantities does not require any scaling factor since the chosen *d-q* transformation is power invariant. Moreover, assuming the three-phase system is balanced, two voltage (v_a and v_b), and two currents (i_a and i_b) quantities are enough to obtain instantaneous current and voltage magnitudes. This form will be dominantly used throughout Chapters 5 and 6.

5.4 Experimental Demonstration of the Electronic Synchronous Generator

The same 30 kW voltage source converter described earlier is used here as well for experimental verification. Figure 5-38 illustrates basic electronic synchronous generator implementation.

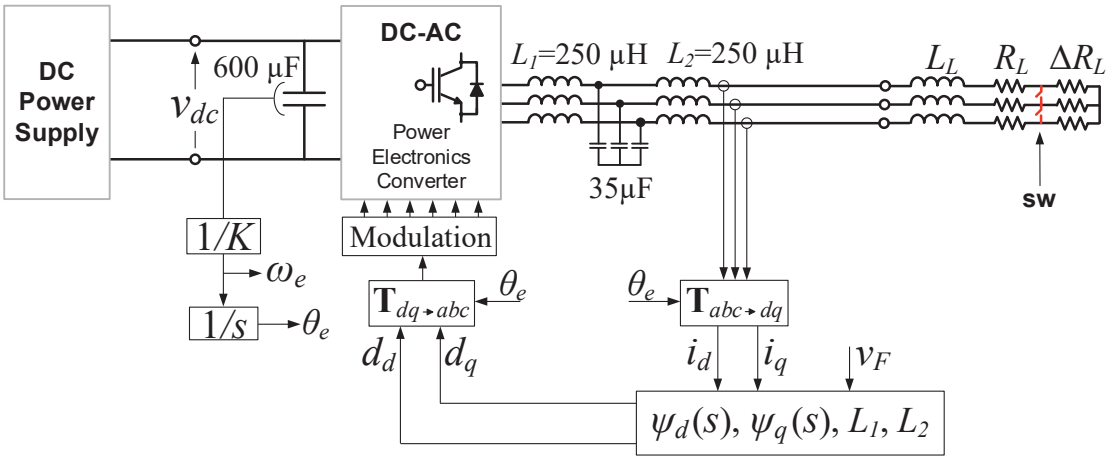

Figure 5-38: An electronic synchronous generator

The flux calculating block in Figure 5-38 takes into account the existing output inductors of the power electronics converter (L_1 and L_2) as shown in (5.46).

$$\psi_{\Delta d}(s) = -(L_d(s) - L_1 - L_2)\cdot i_d + G(s)\cdot v_F$$
$$\psi_{\Delta d}(s) = -(L_q(s) - L_1 - L_2)\cdot i_q \tag{5.46}$$

The mid-point capacitor can be neglected because it does not have a significant impact on the dynamics within the frequency range of interest (up to 1 kHz), as a result total filter inductance (L_1+L_2) is taken into account in (5.46). Flux equations, *d-q* transformation, and synchronization loop are programed into the DSP of this converter. The same load applied in the generator test is used here as well. Finally, Figure 5-39 shows the obtained experimental results overlaid with simulation. A relatively good match is achieved.

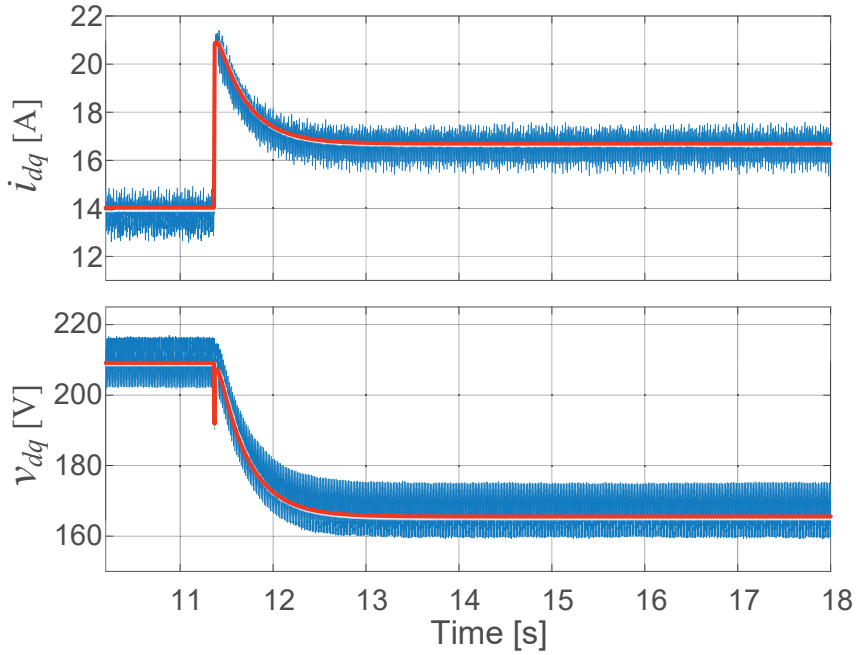

Figure 5-39: Instantaneous current and voltage magnitude comparison; experiment - (blue), simulation - (red)

5.4.1 Voltage Control of the Electronic Synchronous Generator

The previous tests are performed on the generator with no output voltage regulation. This subsection shows design and implementation of the voltage controller designed for the generator used in this testbed [174].

Three line-to-line voltages are measured, squared, and summed up in order to obtain time invariant measurement (5.47). Figure 5-40 shows analogue implementation of this function.

$$v_{om}^2 = \frac{1}{K_S}\left(v_{ab}^2 + v_{bc}^2 + v_{ca}^2\right) = \frac{1}{K_S} 3 v_{RMS}^2 \tag{5.47}$$

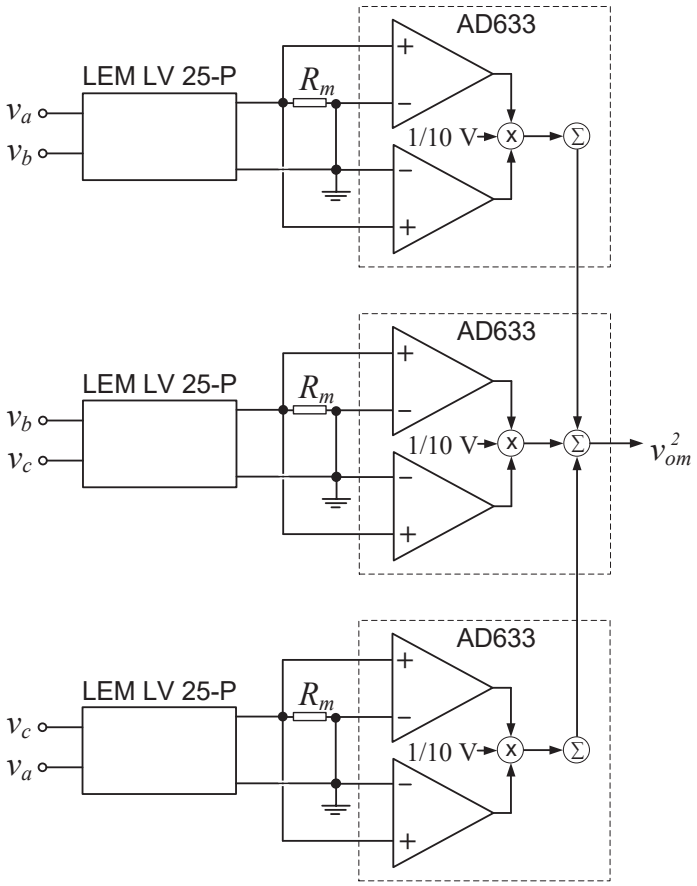

Figure 5-40: Terminal voltage magnitude measurement system

After voltages are measured using LEM LV 25-P, their scaled-down values are fed into three AD633 analog multipliers in order to obtain voltage magnitude squared (5.47). K_S is the scale factor that depends on the sensor property and value of the measurement resistor R_m (here 100 Ω). The measured voltage magnitude (squared) is then fed into the PI regulator developed using an operational amplifier OPA551PA and RC network as shown in Figure 5-41.

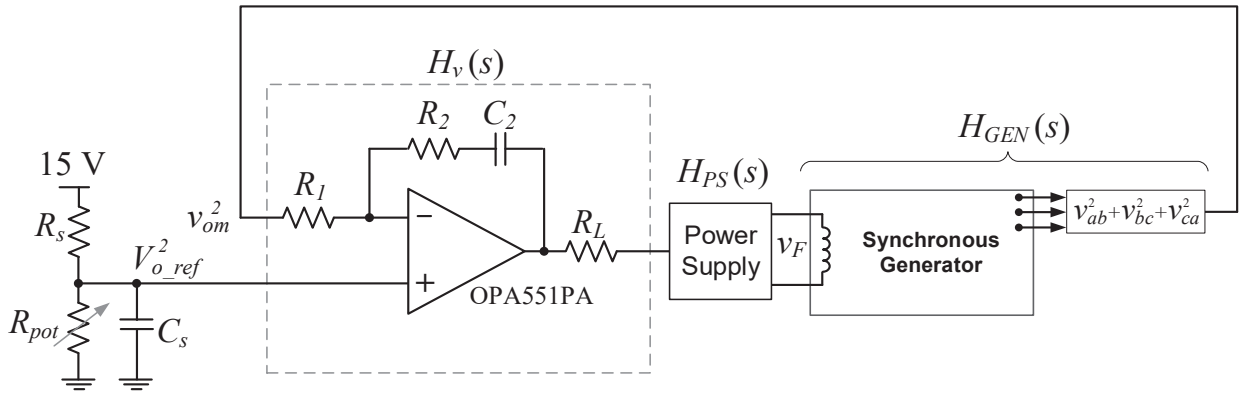

Figure 5-41: PI voltage regulator in analog implementation

The output of the operational amplifier is fed into the analog input of the ZUP60-14 power supply (60 V, 14 A) which serves as a master and operates in the voltage mode. In order to increase current capability, another ZUP60-14 which serves as a slave (operating in the current regulation mode) is connected in parallel with the master.

The next step is to obtain the power supply transfer function $H_{PS}(s)$ and the transfer function from the generator field voltage v_F to output squared voltage magnitude v_{om}^2 - $H_{GEN}(s)$, in order to design the control compensator $H_v(s)$. The power supply frequency response $H_{PS}(j\omega)$ is measured in the range from 10 Hz to 1 kHz using the network analyzer Agilent 4395A, and later curve-fitted in MATLAB to obtain the power supply transfer function. Figure 5-42 shows both results overlaid.

The transfer function $H_{GEN}(s)$ is obtained from the simulation due to the complexity associated with accurate *in-situ* measurements at very-low frequencies. Sensor and multiplier structure gains are simulated and linearized in MATLAB/Simulink together with the machine model (verified earlier). Figure 5-43 shows the linearization result – transfer function $H_{GEN}(s)$.

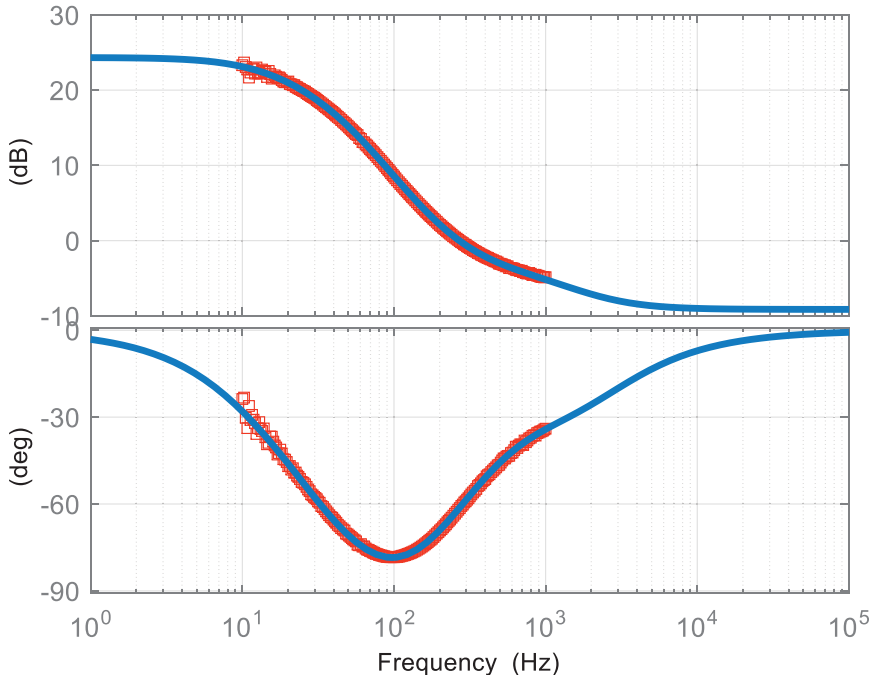

Figure 5-42: Frequency response $H_{PS}(j\omega)$ (red points), and transfer function $H_{PS}(s)$ (blue line)

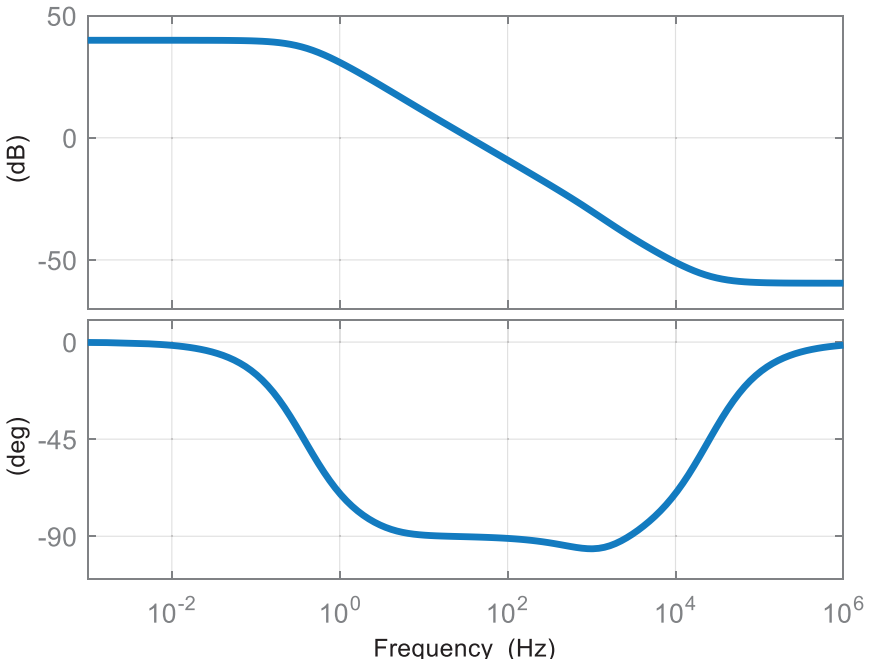

Figure 5-43: Generator transfer function (plant) $H_{GEN}(s)$

The designed compensator is a one-pole, one-zero (simple PI structure), with the transfer function (5.48) shown in Figure 5-44.

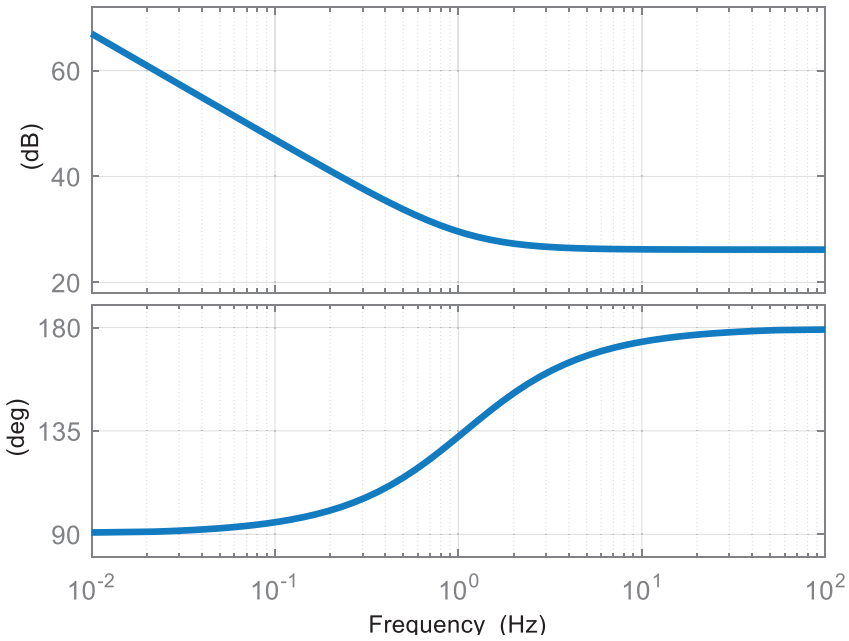

Figure 5-44: Compensator transfer function $H_v(s)$

$$H_v(s) = -\frac{20.425(s+6.847)}{s} \tag{5.48}$$

The result is the bandwidth of 2.3 Hz as shown in the loop gain below (Figure 5-45), with the phase margin of 65 degrees and the gain margin of 68 dB. The compensator values used with the operational amplifier from Figure 5-41 and corresponding to (5.48) are:

Table 5.4 Voltage compensator parameters

Parameter	Value	Parameter	Value
R_1	9.8 kΩ	R_s	20 kΩ
R_2	202 kΩ	R_{pot}	0-1 kΩ
C_2	720 nF	C_s	1 µF
R_L	24 Ω	-	-

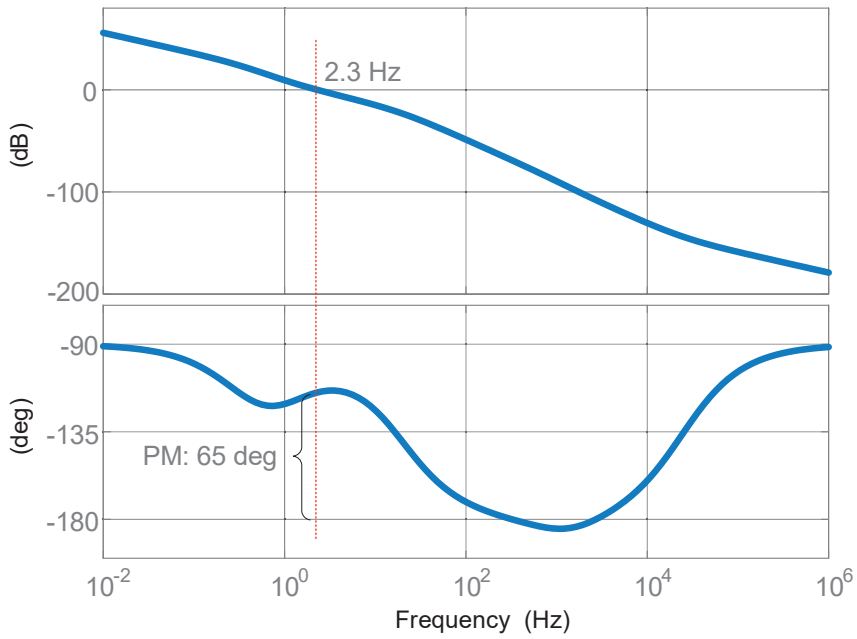

Figure 5-45: Output voltage control loop gain

Figure 5-46 shows hardware realization of the analog voltage regulator for the synchronous machine used in this testbed.

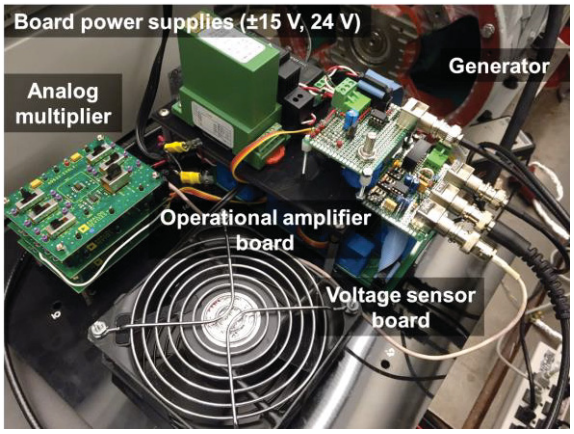

Figure 5-46: Hardware realization of synchronous machine voltage regulator

This voltage regulator is implemented in the machine, and as well, modeled in simulation together with the synchronous machine model. The load transient step (Figure 5-31) is imposed, and the response captured on the oscilloscope shown in Figure 5-47 is overlaid with the simulation result.

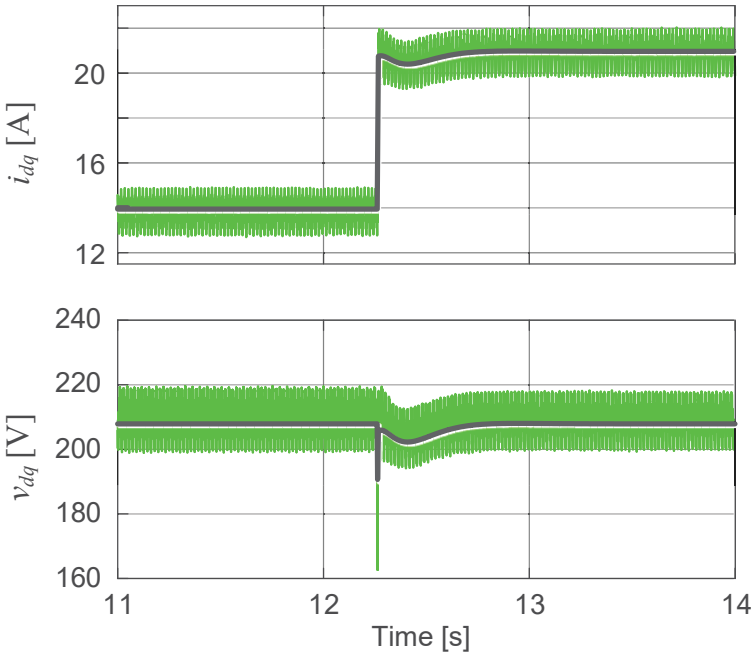

Figure 5-47: Instantaneous current and voltage magnitude comparison; experiment - (green), simulation - (gray)

It can be noticed that very good matching of experimental and simulation results is achieved.

The above described voltage regulator is also implemented digitally into the power converter, as illustrated in Figure 5-48.

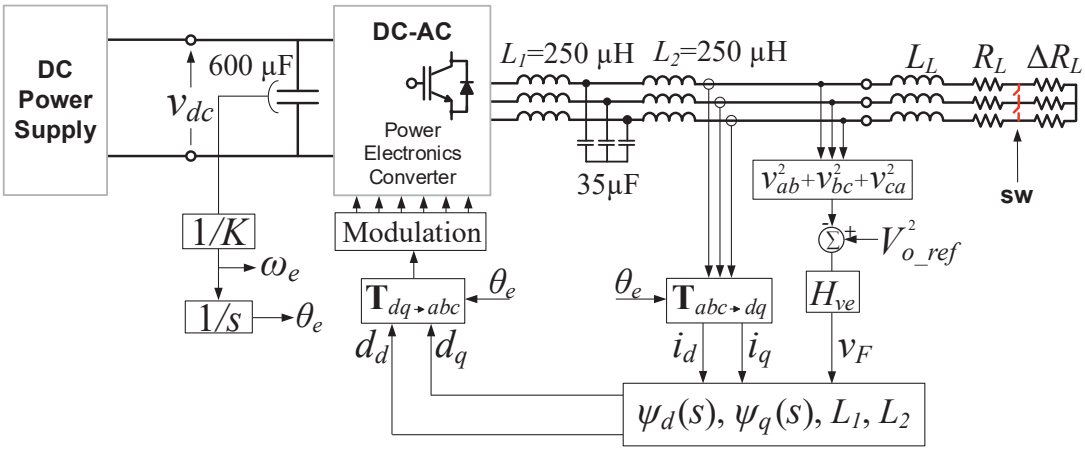

Figure 5-48: An Electronic synchronous generator with output voltage regulation

Implemented compensator H_{ve} (s) includes both power supply transfer function H_{PS} (s) and compensator H_v (s) in order to accurately emulate the complete system implemented on the machine.

$$H_{ve}(s) = H_v(s) \cdot H_{PS}(s) \tag{5.49}$$

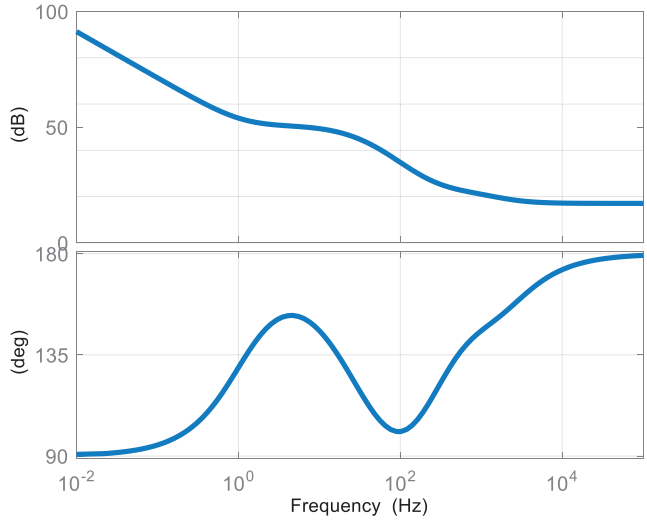

Figure 5-49: Modified compensator to include power supply dynamics

A transient (load step) test is now performed with the electronic synchronous generator and the waveforms recorded. Figure 5-50 shows these overlaid with machine transient waveforms and simulation results (from Figure 5-47) which illustrates a very good match.

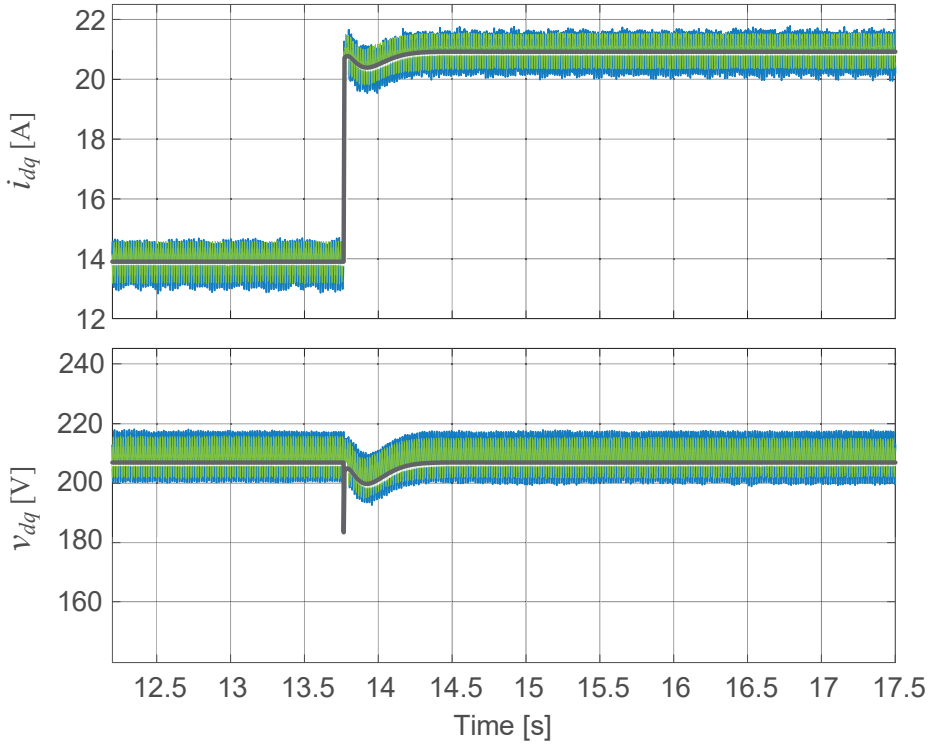

Figure 5-50: Instantaneous current and voltage magnitude comparison; experiment machine - (green), experiment converter - (blue), simulation - (gray)

5.5 Summary

This chapter starts with the introduction of the electrical model of the synchronous machine that is dual to the conventional electromechanical dynamic model commonly used in engineering practice and academia. The restructured model resembles the dynamic average model of the two-level voltage source converter by replicating electromechanical and electromagnetic processes in the machine, including saliency, field, and damper windings.

The particular generator from the laboratory testbed is dynamically characterized with three main frequency responses obtained covering machine dynamics in the frequency range from 10 mHz to 1 kHz. As demonstrated, experimental results match with the simulation relatively well.

An electronic synchronous generator is then implemented in the hardware using measured frequency responses, and it is shown that these can be used to accurately emulate the desired machine. Additionally, an output voltage regulator is designed and implemented in analog form for the synchronous machine, digitally for the electronic synchronous generator, and in simulation; a relatively good match between all systems is shown.

The test and simulations in this chapter are performed under a stiff front-end in all the cases. In the generator case the motor drive is set in the speed regulation mode dominating the dynamics on the shaft, while a DC-voltage source with low output impedance is connected to the DC-link of the electronic synchronous generator (voltage controlling converter). In order to start observing the dynamics effects of both, the inertia in the machine and the DC-link capacitor in the power converter, their front-ends will need to be made less stiff, where one way to do so is to introduce the speed and DC-voltage droop functions on the machine and converter front-ends, respectively. The next chapter will address that, as well as virtual inertia implementation and system-level operation.

6. Virtual Inertia and Multi-Source System Operation

The work described in the last chapter assumed (theoretically) an infinitely strong front-end, where neither the mechanical subsystem of the synchronous machine (inertia) nor the electrical subsystem of the power converter (DC-link capacitor) has any impact on their dynamics. Indeed, the synchronous machine is fed from the induction machine, which is fed from the motor drive operating in the speed regulation mode. Similarly, the power converter behaving as machine was fed from the power supply operating as a strong and low impedance voltage source.

To address the impact of the inertia/DC-link capacitor, speed/voltage droop will be implemented in both cases. As will be shown, the two systems feature quite different dynamics which calls for the need to implement virtual inertia into the electronic generator in order to accurately emulate the particular synchronous machine. The chapter will end with the system-level operation demonstrated experimentally, and additionally showing a simulated example of instability mitigation using the virtual inertia concept.

6.1 Virtual Inertia Implementation

The motor drive from the machine testbed has an option for a user to set a speed droop to a desired value through the drive graphical user interface. The entered value represents how many revolution/minute will drive slow-down when maximal output current (torque) is achieved. The chosen value of 500 revolution/minute corresponds to a droop of 0.11 [rad/Nm·s] as illustrated in Figure 6-1.

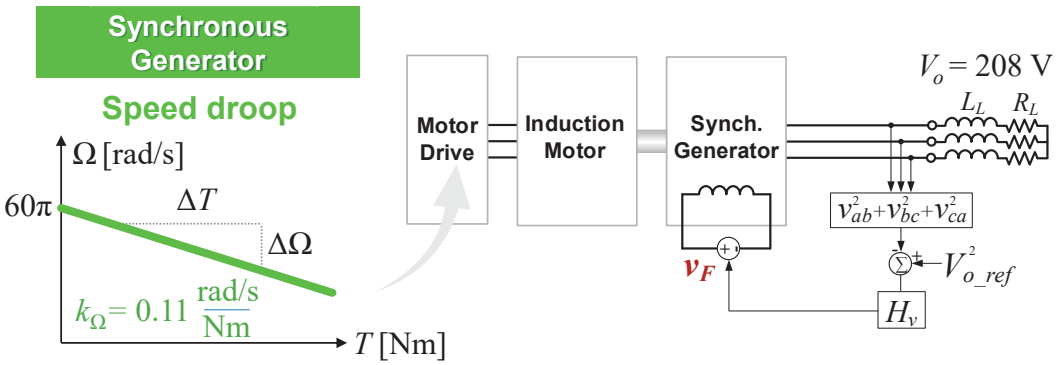

Figure 6-1: Speed droop implementation in the motor-drive

The laboratory DC power supply used as a front-end to the machine emulating converter did not feature a programmable droop option, hence a series resistor R_D is added on a DC-link between the power supply and the converter as illustrated in Figure 6-2. The value of 2.2 Ω is equivalent to 0.11 [rad/Nm·s] speed droop from above.

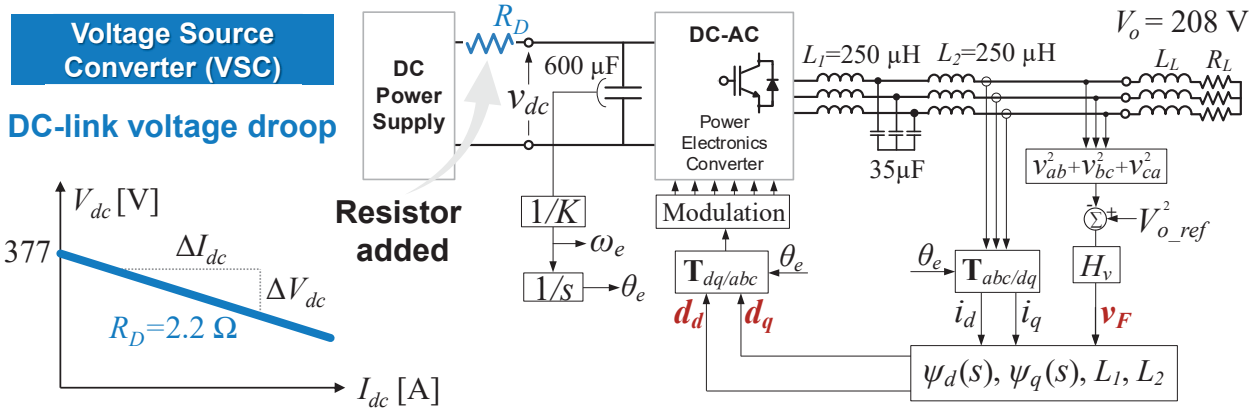

Figure 6-2: Voltage droop implementation

The same load step experiment is now repeated with both a generator and a power converter. Results are shown in Figure 6-3. It can be seen that the dynamic response is quite different in the two cases with the droop function implemented in their front-ends.

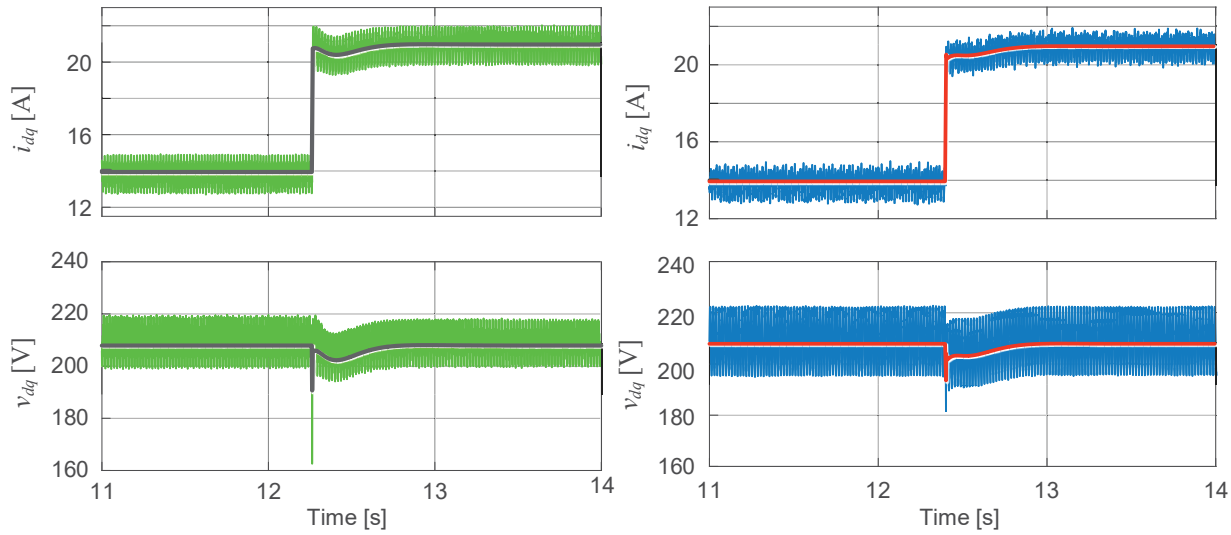

Figure 6-3: Instantaneous current and voltage magnitude comparison;
left: experiment machine - (green), simulation - (gray),
right: experiment converter - (blue), simulation - (red)

The figure on the left side shows machine waveforms due to the load step transient, while the figure on the right side shows electronic generator waveforms. Both figures are overlaid with

simulation results. In addition to voltages and currents, speed (and DC-link voltage) dynamics are now quite prominent (for comparison, in the case of a stiff front-end, both speed and DC-link voltage feature negligible dynamics and steady-state value change after the transient). The machine speed and electronic generator DC-link voltage change is now shown in Figure 6-4 overlaid with simulation results.

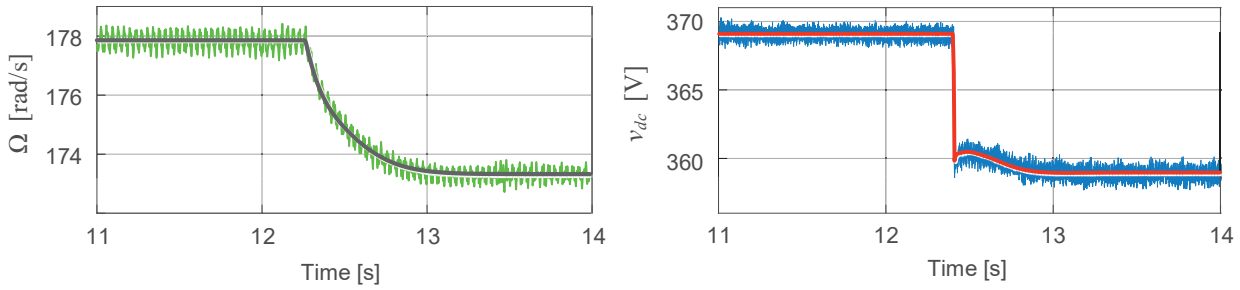

Figure 6-4: Instantaneous speed/DC-link voltage change during transient; left: experiment machine – (green), simulation – (gray), right: experiment converter – (blue), simulation – (red)

It is obvious and quite expected that these two systems experience different dynamics. Machine moment of inertia is 0.32 [kg·m^2] and translated to capacitance (for the same energy: $(1/2)CV^2 = (1/2)J\Omega^2$) it gives 80 mF - calculated for the DC-link voltage of 377 V. On the other hand, real capacitor residing at the DC-link of the electronic generator is 600 µF, featuring a more than 130 times smaller value. The reason dynamics differ slightly and not significantly between the two cases shown in Figure 6-3 is the high energy available from the primary source (front-end). In general, as long as there is sufficient energy in the primary source, the moment of inertia (or DC-link capacitor) cannot make a large impact on the dynamics of the system.

Perhaps the biggest difference in the experiment above is the frequency change of AC-side currents and voltages in two cases. As shown earlier in this dissertation, angular frequency of AC-variables is directly proportional to the dynamics of the front-end. In synchronous machines (generators) angular frequency of AC-variables is p times higher than the instantaneous mechanical speed Ω, while in the case of electronic generators, it is K times smaller than the instantaneous value of DC-link voltage. If high-bandwidth phase-locked loop (PLL) is applied on the AC-variables from the experiment above, the ω output will very closely resemble waveforms shown in Figure 6-4.

Going back to different waveforms from Figure 6-3, one way to make the right side waveforms (electronic generator) dynamically equal to the left side waveforms (machine) is to implement the virtual inertia concept into the electronic generator. The concept described in 5.2.4.2 is applied here with C = 600 µF, and $C_{desired}$ = 80 mF.

Figure 6-7 shows output impedances (obtained from simulation) of the synchronous generator (Figure 6-5) and electronic generator (Figure 6-6). The latter is shown in both cases, with no virtual inertia implemented (blue waveforms) and with virtual inertia implemented (white dotted waveforms). Virtual inertia implementation is emphasized with orange boxes in Figure 6-6.

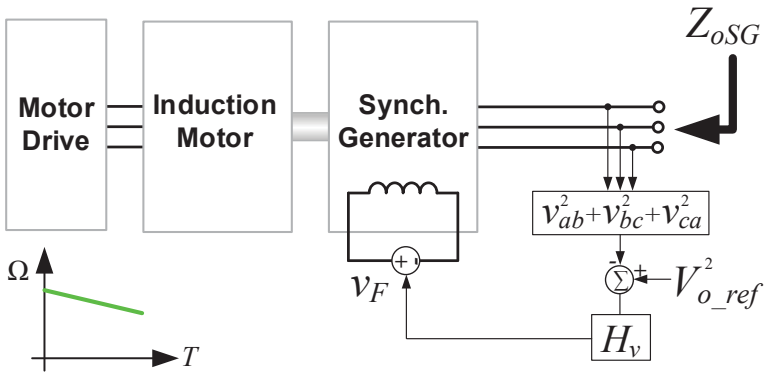

Figure 6-5: Output impedance measurement (synchronous generator)

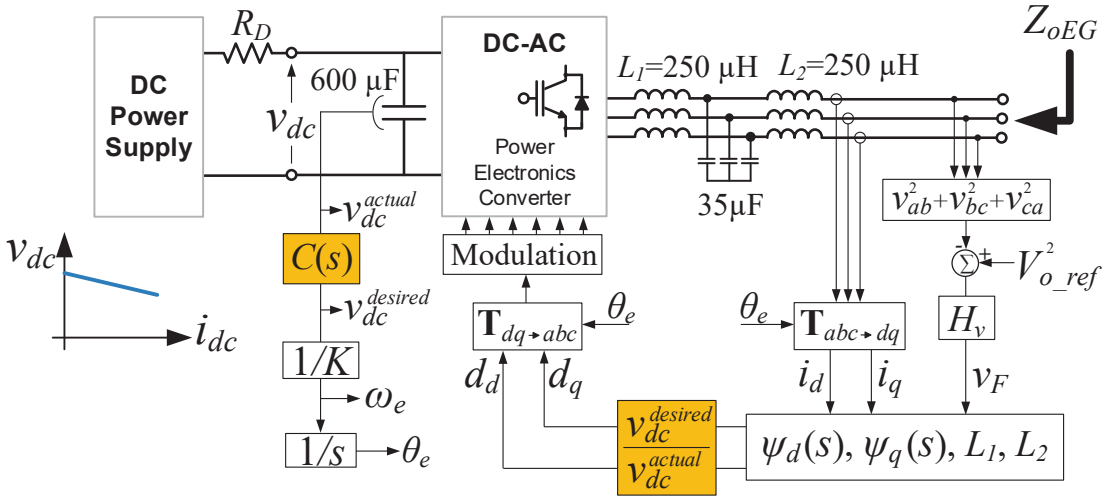

Figure 6-6: Output impedance measurement (synchronous generator)

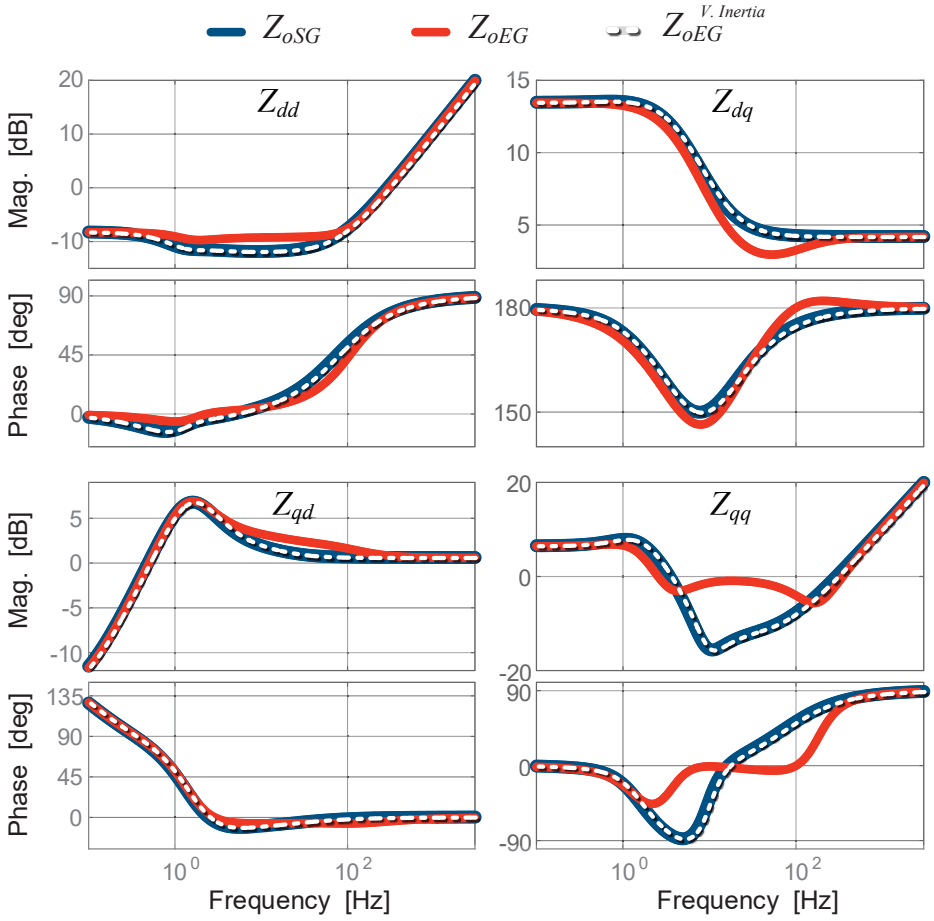

Figure 6-7: Output impedance measurement

Output impedances plotted in Figure 6-7 shows the difference caused by the presence of a much smaller capacitor on the DC-link of the electronic generator. However, the same figure shows how implementation of virtual inertia in the electronic generator compensates the difference and practically ideally emulates the real generator. Looking from the AC terminals, output impedance of the generator and output impedance of the electronic generator with virtual inertia implementation are identical. Finally, virtual inertia is implemented in the power converter (electronic generator) and the load step transient is repeated. Results are shown in Figure 6-8. Very good matching is achieved which experimentally verifies the virtual inertia concept. The bottom plot in Figure 6-8 shows generator speed overlaid with the DC-link voltage of the electronic generator with the virtual inertia implemented. These two still feature very different dynamics. However, unlike the case from Figures 6-3 and 6-4, the frequency of the electronic generator AC-variables is not directly proportional to DC-link voltage shown. Instead, correction (5.24) is

applied (as a necessary step for virtual inertia implementation) defining altered ω_e, and consequently θ_e, for PWM modulation. This is illustrated in Figure 6-9.

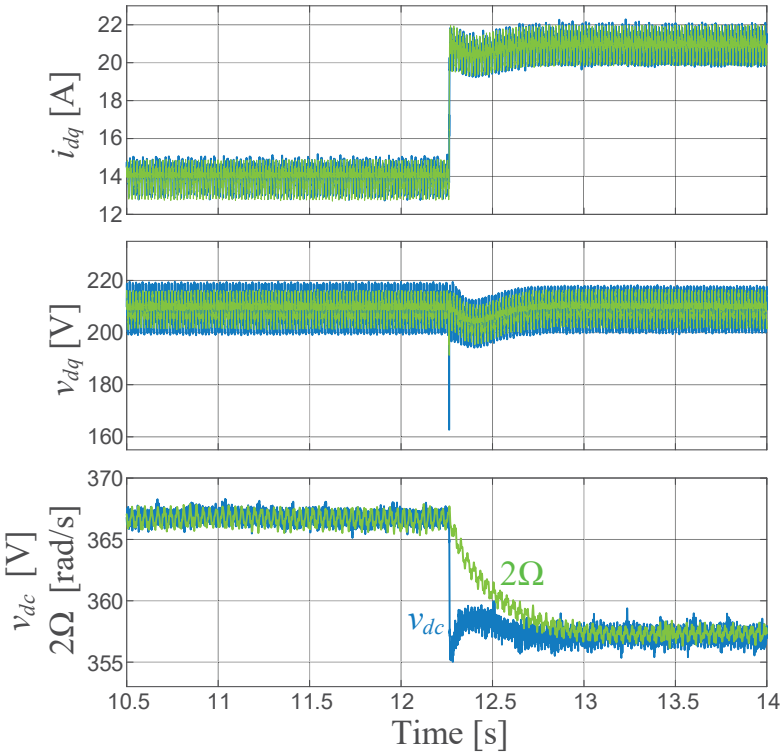

Figure 6-8: Machine - (green), converter - (blue) experiment. Top two: Instantaneous current and voltage mag. comparison; Bottom plot: Overlaid generator speed and converter DC-link voltage

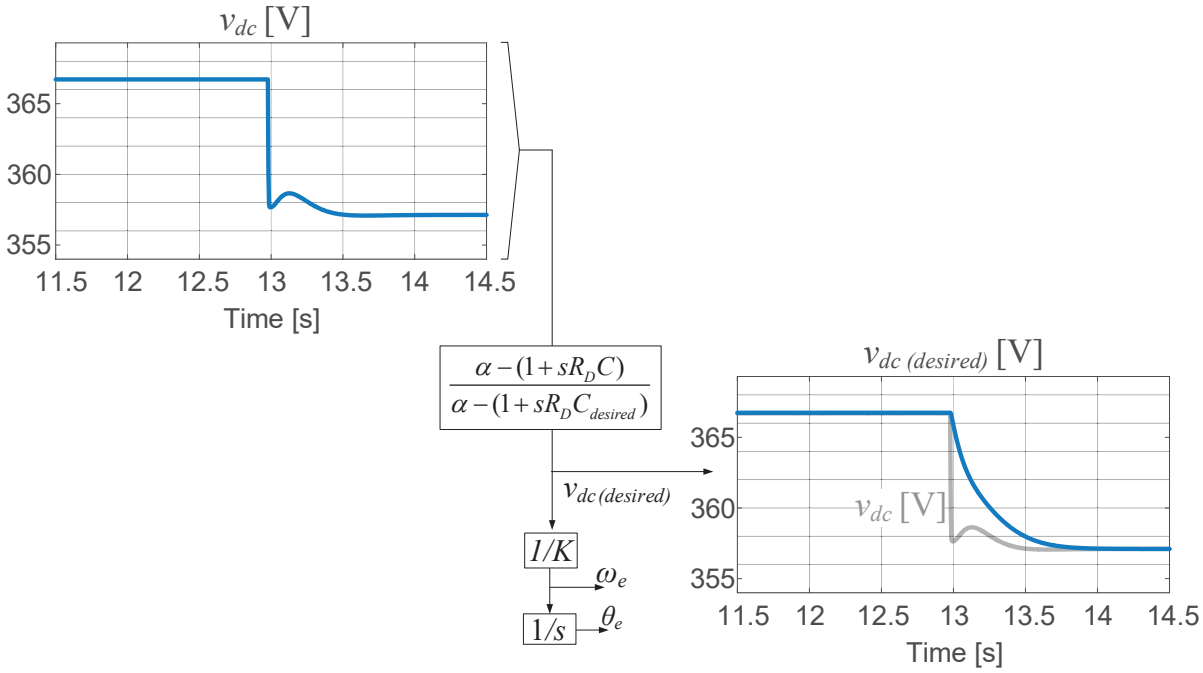

Figure 6-9: Illustration of DC-link voltage modification required for virtual inertia

6.2 Demonstration of System-level Operation with Voltage Controlling Converters

A system-level operation where a real and an electronic generator are coupled is simulated and demonstrated experimentally. Figure 6-10 illustrates connections and test conditions. The real generator features an output voltage regulator and the speed droop as described earlier. On the other side, the electronic synchronous generator additionally features output voltage regulation and DC-link voltage droop. Virtual inertia algorithm is not implemented for these tests.

The two systems are interconnected via the passive network shown in Figure 6-10, with the shunt load on each side. Both sources are started separately with the switch sw 1 open (the controllable three-phase relay). The oscilloscope is connected across it for monitoring voltages on both sides.

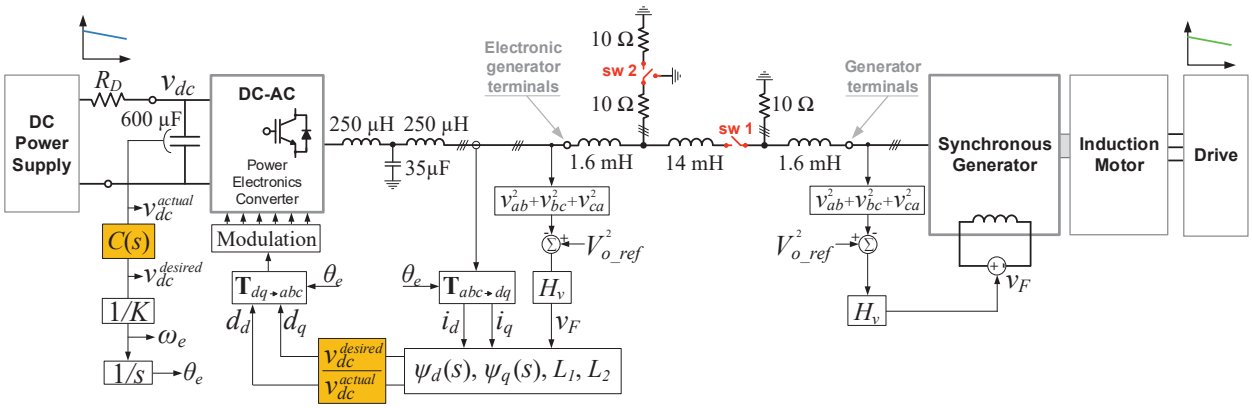

Figure 6-10: Real and electronic generator in system-level operation

After reaching the steady state, the DC-power supply is manually fine-adjusted so the electronic generator output voltages match those on the real generator side. Once in harmony (both amplitude and phase), sw 1 is manually closed and system reaches the new steady state with no significant transient at the moment of the relay closure since the voltage difference across the relay contacts is insignificant. The system is then coupled and operations continues until the switch sw 2 (controllable three-phase relay as well) is closed imposing the transient.

Figure 6-11 shows generator mechanical speed and electronic generator DC-link voltage captured during the transient. Dynamics of the generator speed exhibits the first order response and are dominantly influenced by the moment of the inertia of the machine. Due to the fact two systems (real and electronic generator) are electrically coupled, that will be reflected on the DC-link of the electronic generator, where slow first order response is evident towards the end of the

transient. However, as it can be seen in the right side of Figure 6-11, there is a sharp transient in the DC-link voltage caused by the capacitor discharge occurring immediately after the step (as described in Chapter 5, this capacitor is about 130 times smaller than the electrical equivalent of the real generator moment of inertia).

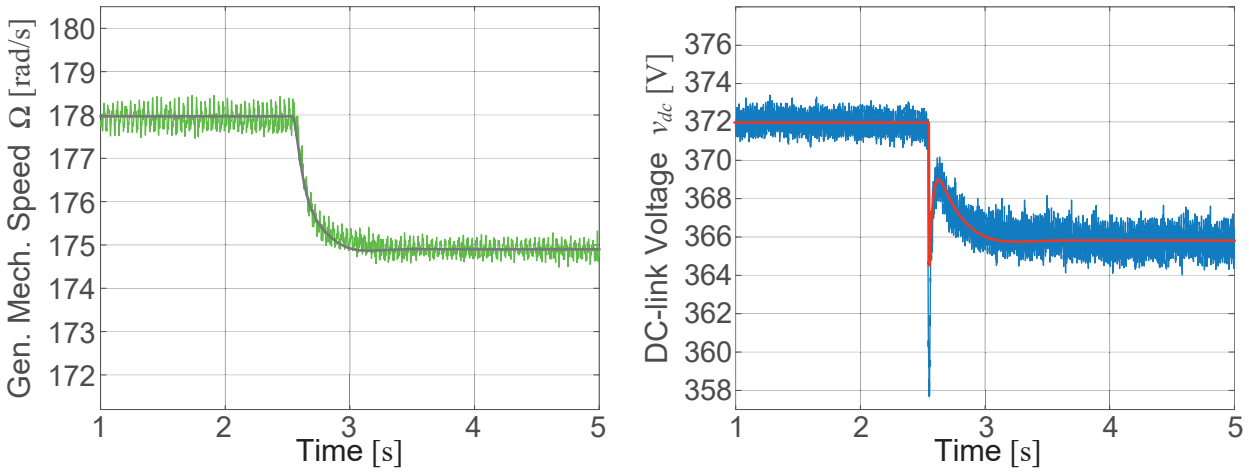

Figure 6-11: Left) Generator mechanical speed (experiment - (green), simulation - (gray)); right) electronic generator DC-link voltage (experiment converter - (blue), simulation - (red));

As a result of the coupled operation, frequency of the AC variables is directly proportional to either generator speed (via parameter *p*) or to DC-link voltage (via parameter *K*). Figure 6-12 shows overlaid real and electronic generator output currents recorded during the transient.

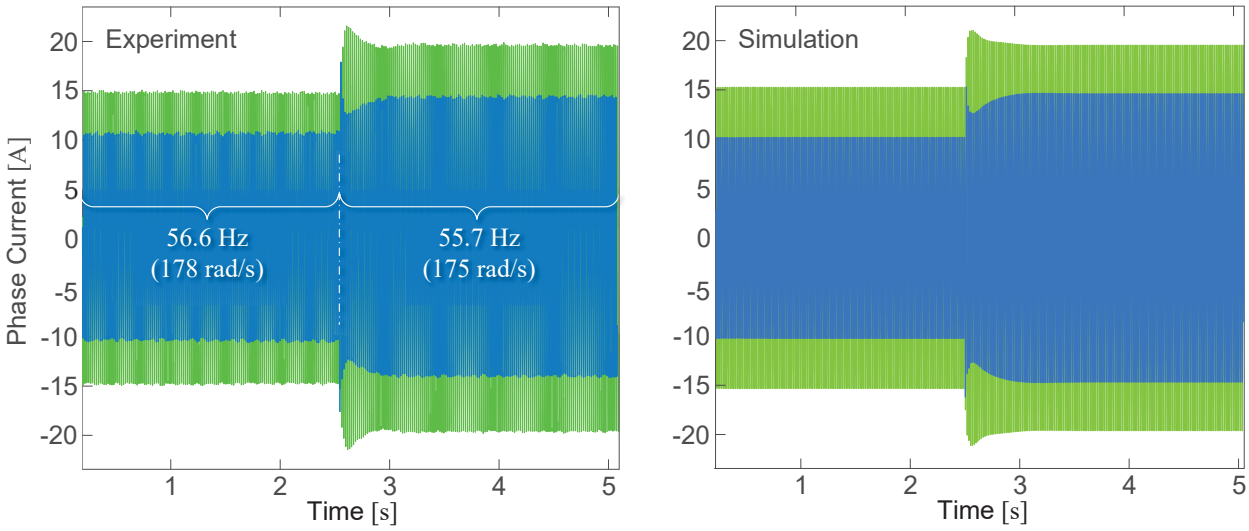

Figure 6-12: Real and electronic generator output current during transient; left) experimental waveforms: generator current - (green), electronic generator current - (blue)); right) simulation: generator current - (green), electronic generator current - (blue));

As noticed, a relatively good match between the measurements and simulation is achieved. However, looking at Figure 6-11 (both generator speed and electronic generator DC-link voltage) there is a small discrepancy between the measured and simulated waveforms between approximately 2.8 s and 3.2 s. The reason for this is the dynamics of the motor drive droop control. Although a very good match of the restructured machine model and experiments with the droop function is demonstrated earlier in Chapter 5, the situation here is quite more complex due to the coupled system dynamics. However, considering the mismatch is not that severe in Figure 6-11, excluding the (unknown) motor drive dynamics can be taken as a reasonable simplification.

6.3 System-Level Operation with Multiple Sources

Now that models represent real and electronic generators well, system-level simulations under many different cases can be performed. Figure 6-13 illustrates one such multi-source system comprising two real and one electronic generator interconnected through the passive network. Generator 3 (top right) represents the strongest source determining the frequency of the system. No speed droop was modeled in the front-end of this generator in order to impose the desired frequency step in the system. The frequency was stepped from 115π rad/s (57.5 Hz) to 120π rad/s (60 Hz).

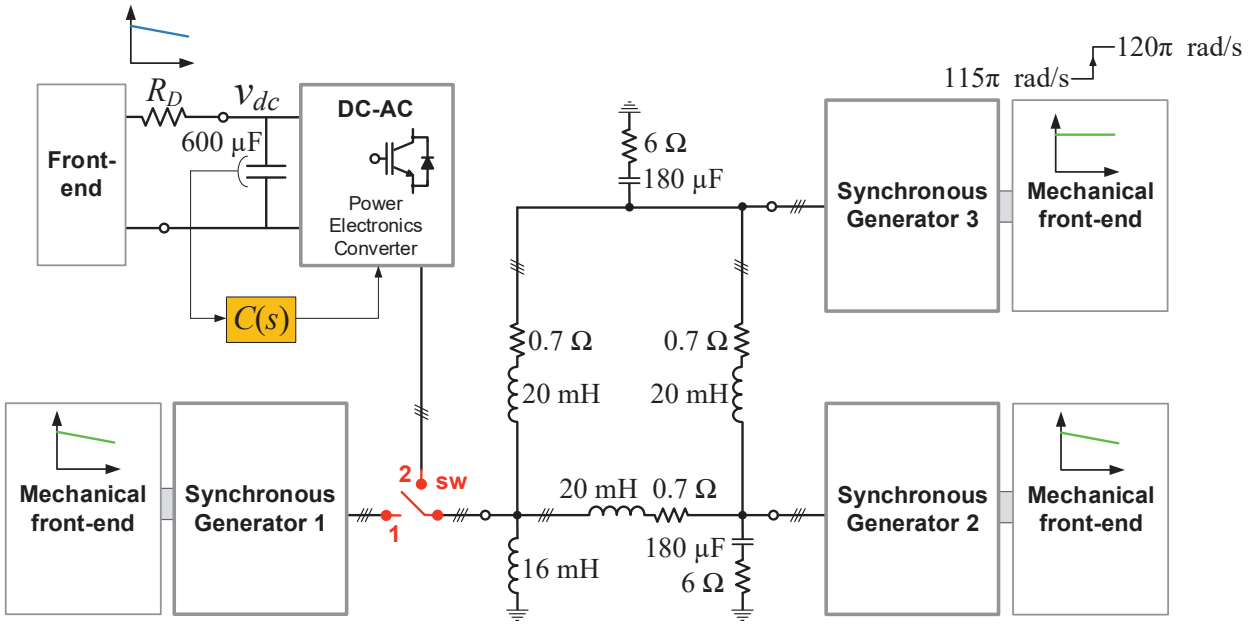

Figure 6-13: Simulated multi-source system (simplified, one-line representation)

Figure 6-14 shows the current magnitude transient captured at the output of generator 1 prior to and after the system frequency change. The switch (sw) is put in position 1 and generator 1 is simulated with inertia of 0.84 kg·m^2. After the frequency step is imposed by generator 3 at time 7 s, generator 1 with such large inertia is not capable of synchronizing, and lost the synchronism pulling the whole system (tightly coupled) to lose synchronism as well.

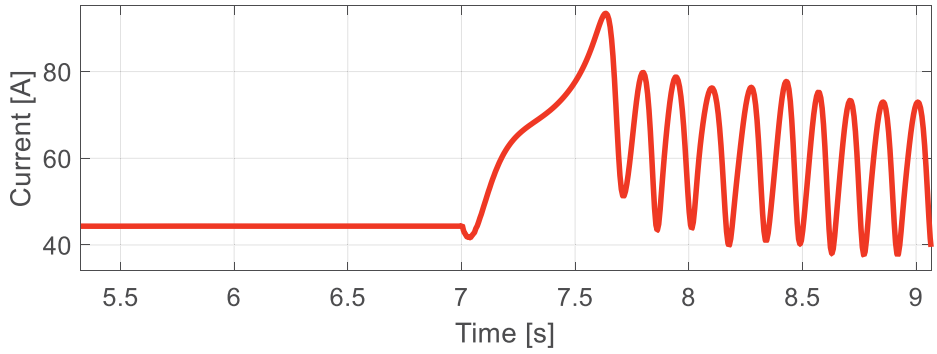

Figure 6-14: Generator output current for inertia of 0.84 kg·m^2

The switch (sw) is then put in position 2 and the whole simulation repeated with an electronic generator instead of generator 1, as illustrated in Figure 6-13. The electronic generator also operated with the large (virtual) DC-link capacitor by value equivalent to inertia of 0.84 kg·m^2 (C=210 mF, obtained from $(1/2)CV^2 = (1/2)J\Omega^2$). As evident in Figure 6-15, the same instability happened again, but now with the electronic generator.

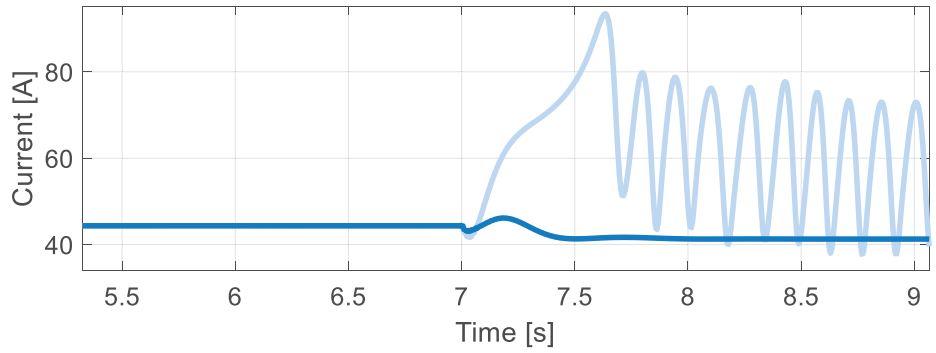

Figure 6-15: Electronic generator output current for DC-link capacitor of 210 mF (light blue), and 600 µF (blue)

The reason for this instability is the electronic generator featured the exact same (virtual) inertia as the generator above. Now, since the electronic generator can operate with practically any value of virtual inertia as long as there is enough energy available in the primary source, simulated is the

case when DC-link capacitor value was lowered down to 600 μF (equivalent to inertia of 0.0024 kg·m^2), leading to a stable transient in Figure 6-15. This level of inertia is impossible to achieve with the actual synchronous machine due to machine physics, hence the advantage of virtual inertia implementation in electronic generators is unquestionable.

6.4 Summary

This chapter presents a virtual inertia implementation as the final step towards complete machine emulation. It is shown that as long as there is a sufficient energy available in the primary source, practically any desired inertia can be implemented.

System-level operation is shown next, with the real and electrical generator coupled via inductive impedance and resistive shunt load on each side. Both units feature droop in their front-ends and exhibit a smooth synchronization after the system operating point is changed, demonstrating the ability of the synchronous machine-like frequency-locked loop to maintain the synchronism between the real generator and its electronic replica.

Finally, a multi-source system is simulated using a now already verified model of the electronic generator, demonstrating its capability to suppress system oscillations through the change of (virtual) inertia.

The next and final chapter in this dissertation offers additional insights into machine emulation and discusses a possibility for the concept improvement.

7. Discussion, Summary, and Future Work

The following sections will further discuss reported methodologies and their practical significance, as well as show alternatives that could possibly further improve proposed concepts.

7.1 Discussion on Terminal-Behavioral Modeling

The small-signal, low-frequency terminal behavioral modeling indeed offers a means for simpler system-level studies. Although limited to up to half of the switching frequency, most of the dynamic interactions between two converters happens in the frequency range that falls within the control bandwidths of the two converters, which is, in most cases, much lower than the converter switching frequency (1/5-1/10)·f_{sw}. With the addition of another factor, the simplicity associated with interconnecting these models one to another [190], terminal-behavioral modeling undeniably has a potential to become a very useful tool for system-level analysis.

7.1.1 Terminal-Behavioral Modeling of Electric Machines

Not only can power converters be modeled using this method, electric machines can be as well. Figure 7-1 illustrates how a synchronous generator can be represented using a three-port network terminal-behavioral model shown with the simplified circuit (with variables in the matrix form), and terminated with its governor and three-phase grid/load. The way to obtain unterminated transfer functions is completely equivalent to the process described for an inverter (section 3.1).

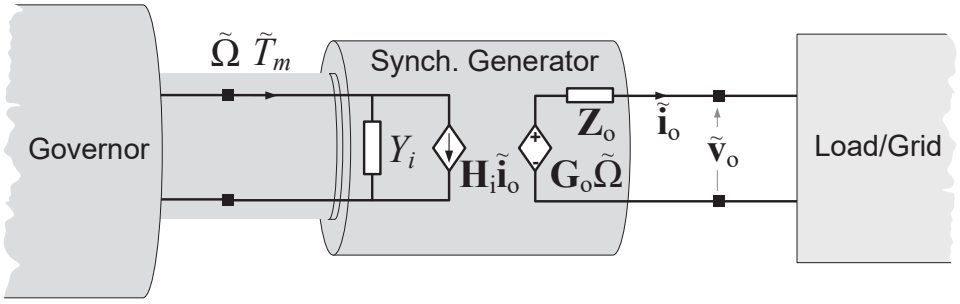

Figure 7-1: Terminal-Behavioral Model of the Synchronous Generator

The only difference is instead of measuring DC-link voltage and current during perturbations on the primary and secondary side, the user must measure mechanical speed and torque from the resolver and torque-meter located at the mechanical shaft of the machine. One difficulty associated with the primary side perturbations on the mechanical shaft is the need to generate the

perturbations in the governor itself, which is not a simple task in many cases. However, the solution to this problem is a characterization procedure described in the Chapter 5 of this dissertation. Once a good model of the particular machine is available, the unterminated transfer functions can be obtained from the simulation. Then, the small-signal terminal behavioral model of a synchronous generator becomes:

$$\left[\begin{array}{c|cc} G_d & -Z_{dd} & -Z_{dq} \\ G_q & -Z_{qd} & -Z_{qq} \\ \hline Y_i & H_d & H_q \end{array}\right] \cdot \begin{bmatrix} \Omega \\ i_d \\ i_q \end{bmatrix} = \begin{bmatrix} v_d \\ v_q \\ T_m \end{bmatrix} \tag{7.1}$$

where the matrix on the left comprises all nine unterminated transfer functions. Time domain simulation of the synchronous generator [174] is now performed using the large-signal model from Chapter 5. Recorded input and output variables during the mechanical speed step down of 0.25 rad/s at 8 s are shown in Figure 7-2.

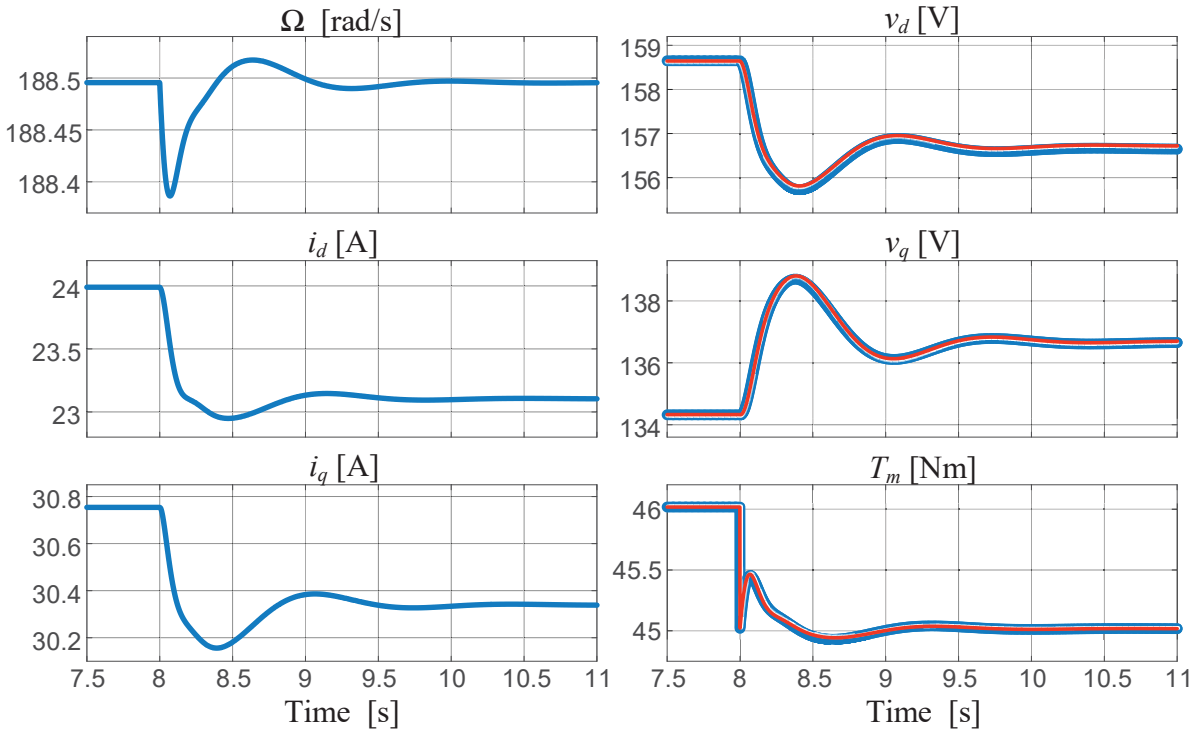

Figure 7-2: Time-domain waveforms of the synchronous generator modeled using large-signal model (blue), and terminal-behavioral model (red)

Variables Ω, i_d, and i_q are input into the model (7.1), with an expectation the model output variables v_d, v_q, and T_m will closely resemble the transient responses previously captured using the

large-signal model. As apparent, this is already done in Figure 7-2, displaying two sets of variables v_d, v_q, and T_m, which are overlaid with each other in a good match.

7.1.2 System-Level Modeling

Figure 7-3 illustrates an example of how complicated systems can be modeled using simplified terminal behavioral models. Consider that engineers can relatively and accurately capture and simulate the low-frequency behavior of the system, they can also prescribe the desired dynamic behavior of both the systems and the converters. This new paradigm opens completely new opportunities and will definitely aid with high performance system design, from portable electronics to nano-, and micro-grids.

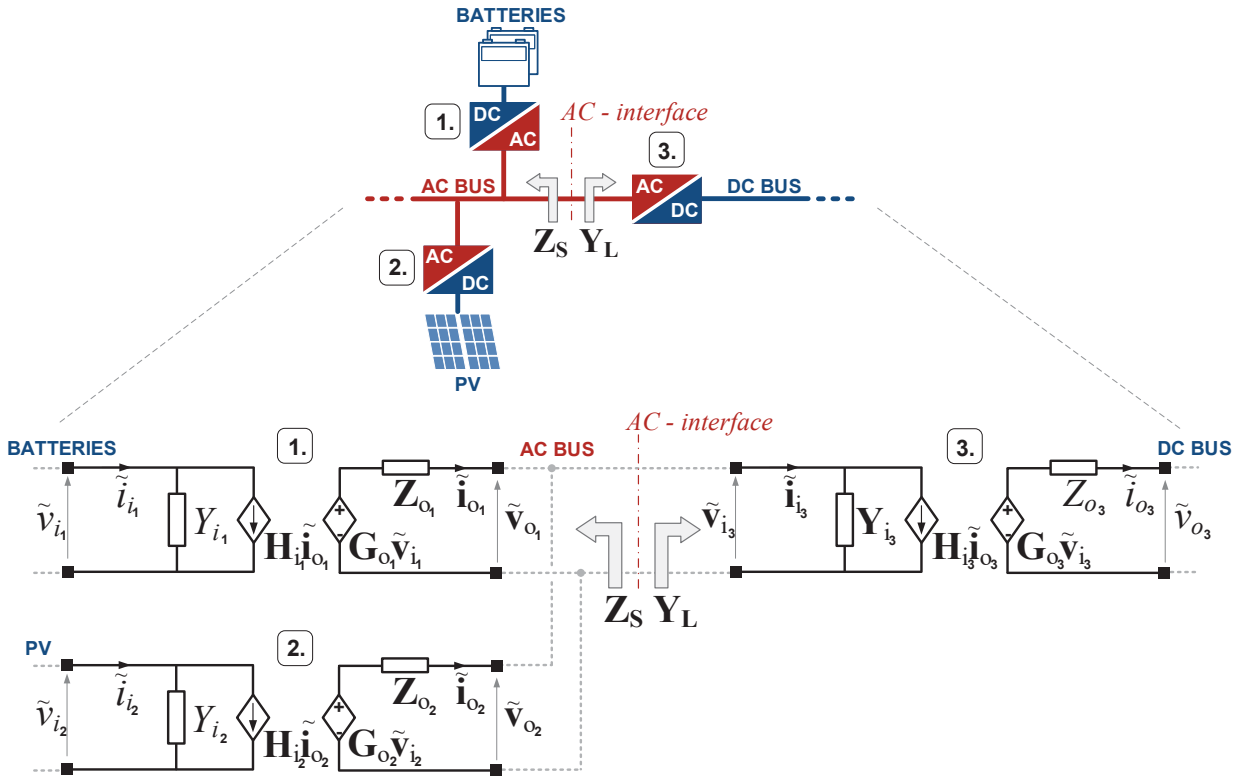

Figure 7-3: An example of system-level simulation using terminal-behavioral models

Moreover, converter manufacturers can, in addition to datasheets, provide small-signal behavioral models of the converters they produce. These models (frequency characteristics) will capture critical dynamics within the control bandwidth of the converter necessary for stability assessment. At the same time, the models will not disclose any information on the internal structure

and applied control concepts to its users allowing for full protection of intellectual property while highly benefiting the system integrators at all application levels.

However, to achieve this, it is not enough to perform characterization of converters at only one operating point and to use only one set of unterminated transfer functions to simulate all possible operating modes in which one converter can operate. Numerous sets of these transfer functions must be obtained and at as many operating points as possible, in order for these models to show a full potential. Figure 7-4 clearly illustrates this problem.

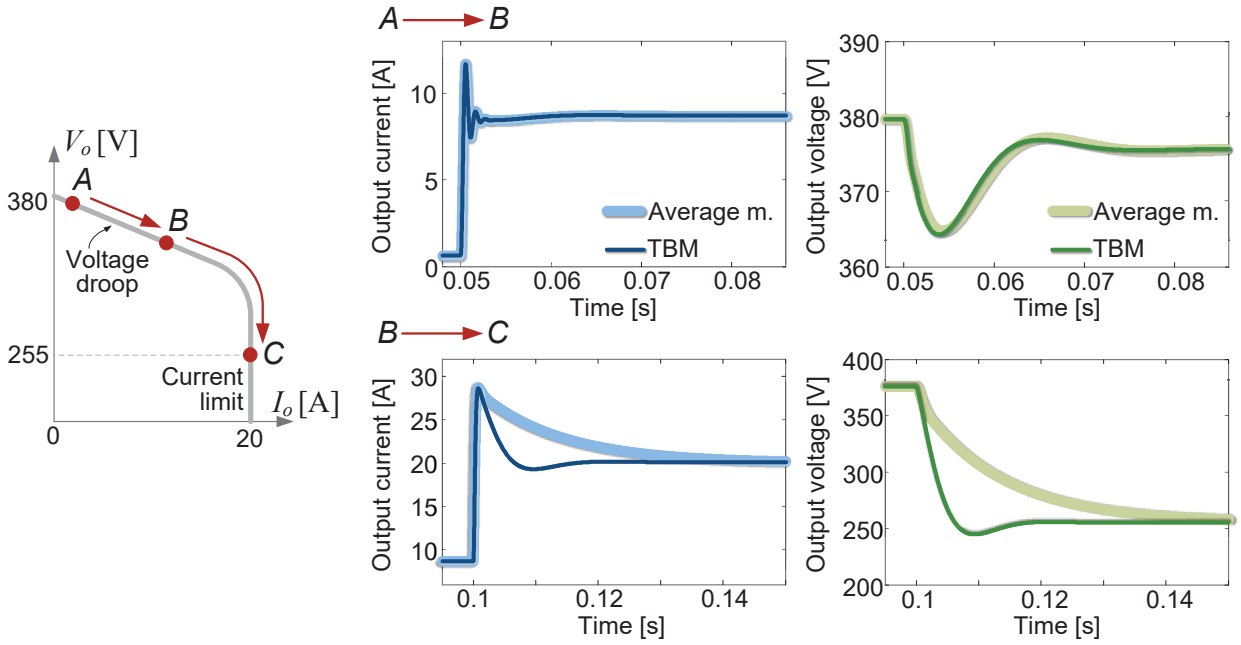

Figure 7-4: left) static V-I curve of the bus converter; right) time domain waveforms during transients corresponding to A,B, and C points; TBM – Terminal-Behavioral Model

Assuming the intermediate bus converter (No.3) from Figure 7-3 features the static V_o-I_o curve at its *DC*-output as shown in Figure 7-4 (left), only one set of unterminated transfer functions obtained at point "A" is used to define the terminal-behavioral model of this converter. If the load on the *DC*-bus suddenly increases at the time 0.05 s, the operating point of the converter moves to "B" on the output voltage droop curve. Two corresponding transient waveforms on the right top side of Figure 7-4 shows the associated dynamics captured during this transient using two simulation forms, the average model and the small-signal terminal behavioral model. It can be noticed the two models exhibit very similar dynamics with negligible discrepancy in the output voltage dynamics since the intermediate bus converter is a boost rectifier type still operating in the voltage mode when moving from point "A" to "B" on the static linear V_o-I_o curve. However, if the

bus converter load significantly increases taking the converter to point "C" and where it operates in the current-mode, the converter dynamics features a very different behavior as shown on the right bottom side of Figure 7-4, demonstrating that large-signal behavior cannot be accurately captured using a small-signal model obtained by means of circuit linearization at only one operating point (static nonlinearity was here taken into account [77],[95] hence the zero steady-state error).

Another matter particularly important for system-level terminal behavioral modeling of three-phase converters and systems, is unification of the used *d-q* transformation and PLL angle alignment. The transfer functions describing a particular converter are angle-variant. It is very important that every model comes with the information of which *d-q* transformation is used (for instance, power-invariant, line-to-line, *d* axis leads *q*, and is aligned with v_{ab}).

However, possibly the biggest hold-back of the terminal behavioral modeling is inaccessibility of the measurement equipment; frequency response analyzers for higher power converters and systems are not yet commercially available, and the need for high availability of such equipment is evident.

7.2 Discussion on an Online System Observation and Stability Assessment

If known, the unterminated frequency responses discussed above (transfer functions) can be programed in the converter before deployment in the field (in the form of the look-up table, for example). While performing the online, *in-situ* impedance measurements, the converter will now be able to "see through itself" (see aggregate input admittance from the primary terminals and aggregate output impedance from the secondary terminals), which gives the converter an opportunity to periodically perform small-signal stability assessment and apply online Generalized Nyquist Criteria. Assuming there is enough memory available on its control board, practically any digitally controlled converter can be programed to perform an online stability assessment *in-situ*. The same can be achieved with the analog-controlled converters as well, although in this case the engineer will be involved in the process (initiating external or internal perturbations and collecting responses for post processing). As a consequence, digital-controlled converters themselves can re-tune control loops when necessary in order to assure system stability, or even start operation in the open-loop mode the first time they are turned-on. Additionally, digital-controlled converters can observe the surroundings by performing online measurements and close appropriate control loops

online, taking into account some of the many stability criteria [55], [182]-[188]. Having this capability in the embedded form, without the user (engineer) being involved, can have an immense impact on the system performance and stability.

7.2.1 Online Observation of Electrical and Mechanical Interactions in Synchronous Generators

Subsection 7.2.1 addresses the possibility to model synchronous generator using a small-signal terminal-behavioral model. Having an unterminated dynamic model of the machine available provides opportunity to perform *in-situ* system observation and stability assessment with machines as well as with power electronics converters, as proposed in Chapter 4 of this dissertation. To achieve this, it is required to induce some perturbations internally in the machine, and probably the most practical way will be to perturb the field voltage of the machine, either directly if the machine operates open-loop or via a voltage reference set point if a machine output voltage controller exists. The latter is the more likely scenario in the majority of applications where synchronous generators are employed.

Figure 7-5 illustrates a small-signal model of the machine by highlighting impedances and admittances at both the machine input and output. The governor is modeled with its electrical equivalent, as a simple low-pass filter followed by droop resistance R_D. Perturbing machine field voltage reference, the output impedance of the mechanical system (governor) can be obtained as shown in (7.2). Figure 7-6 shows its bode plot together with mechanical (rotor) input admittance.

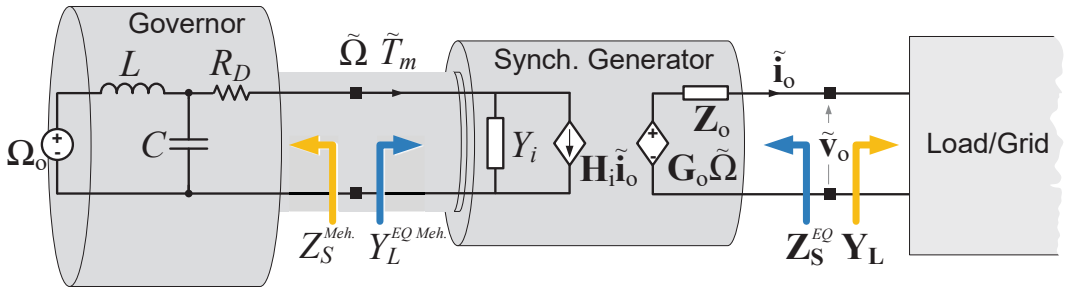

Figure 7-5: Inward and outward immittances at mechanical and electrical terminals

$$Z_S^{Meh.} = \frac{\tilde{\Omega}}{\tilde{T}_m} \tag{7.2}$$

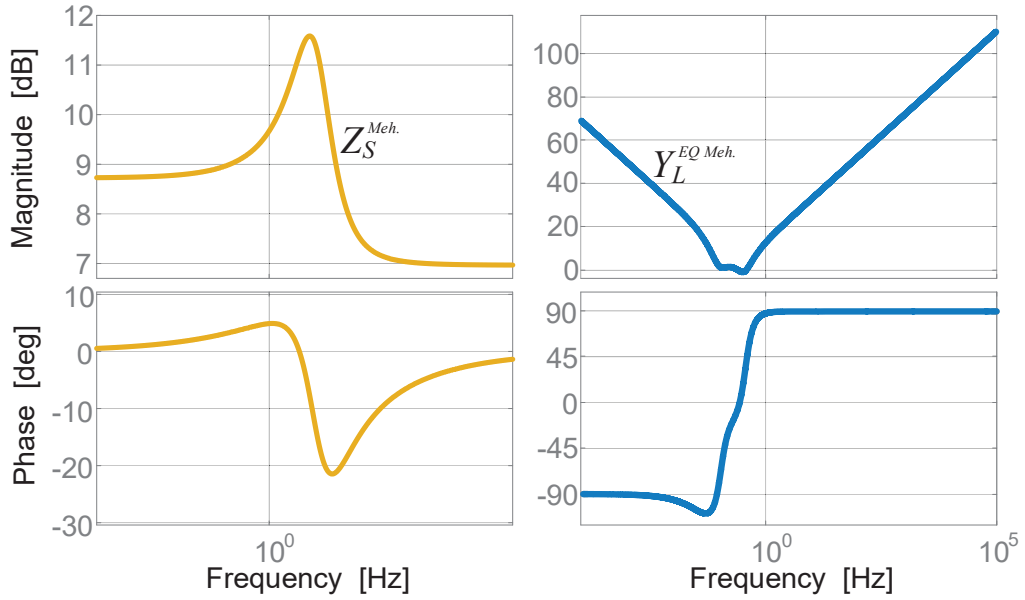

Figure 7-6: Exaggerated mechanical immittances at the machine shaft

Completely equivalent to the procedure described in 4.1.2, all other terminal impedances can be obtained which offers the possibility to perform an online stability assessment using synchronous generator itself as a perturbation source, and possibly apply the mechanical impedance-based Nyquist stability criterion as well to the machine mechanical subsystem [191]-[193]. Additionally, this capability can undoubtedly be of high importance in practice, as it is offering new insights into dynamic interactions of the mechanical system, the governor (turbine) control design in ships, aircrafts, and even the grid.

7.2.2 Small-Signal Active and Reactive Power

The commonly used procedure for the small-signal stability evaluation in large power distribution systems is done through the examination of system eigenvalues and their location in the complex plane [194]-[198]. An alternative method to access system eigenvalues by measuring small-signal active and reactive power can give similar insights. Although very limited information has been published on this topic so far, Paszek and Pruski [199],[200] observed deviation of the instantaneous active power waveform after the transient to extract the eigenvalues in simulation. This can be a convenient method if the impedance measurement unit or the unterminated transfer functions of the converter are not available. Then, an online monitoring and stability assessment can be performed by causing internal perturbations in the same way as the method described in Chapter 4 suggests, but instead of measuring impedances, measure the instantaneous, small-signal

active and reactive power frequency responses in the *abc* coordinates. This is possible since active and reactive powers are time invariant in balanced three-phase systems, and any internally-caused perturbation will appear in the time-domain measurement of all power variables, as illustrated in Figure 7-7.

Taking as an example the bus converter from the notional system used throughout this dissertation, the small-signal active and reactive power at the input and the small-signal active power at the output, all contain the complete dynamic information of the system (Figure 4-4), and feature impedance return-ratio in their denominator (7.3).

$$\frac{\tilde{p}_{in}}{\tilde{d}_d} = \frac{F_{pi}(\mathbf{Z}_S, \mathbf{Y}_i, \mathbf{H}_i, \mathbf{G}_o, Z_o, Y_L)}{1 + \mathbf{Z}_S \mathbf{Y}_L^{EQ}} \qquad \frac{\tilde{p}_{out}}{\tilde{d}_d} = \frac{F_{po}(\mathbf{Z}_S, \mathbf{Y}_i, \mathbf{H}_i, \mathbf{G}_o, Z_o, Y_L)}{1 + Z_S^{EQ} Y_L} \qquad (7.3)$$

$$\frac{\tilde{q}_{in}}{\tilde{d}_q} = \frac{F_{qi}(\mathbf{Z}_S, \mathbf{Y}_i, \mathbf{H}_i, \mathbf{G}_o, Z_o, Y_L)}{1 + \mathbf{Z}_S \mathbf{Y}_L^{EQ}}$$

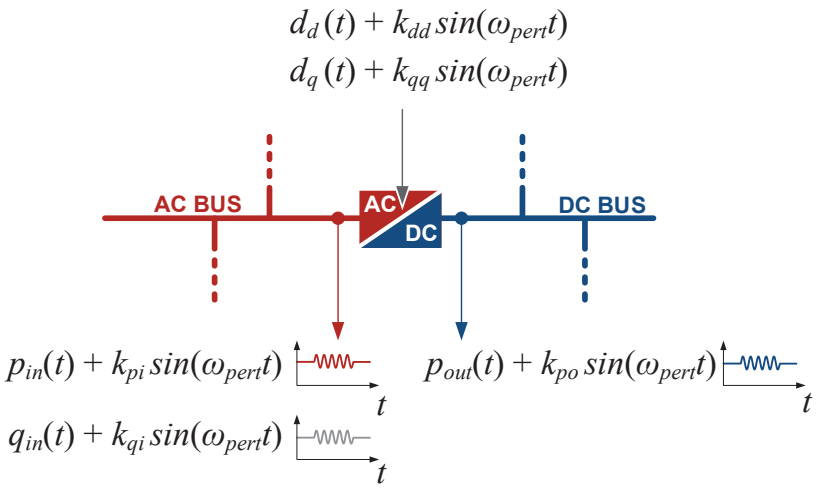

Figure 7-7: Online stability monitoring through small-signal power response

Therefore, if unterminated transfer functions (7.3) are not known, internal perturbation (*AC* sweep) of the duty cycle (or current/voltage references if converter operates as closed loop) will provide power frequency responses for the *AC* side as shown in Figure 7-8; actually shown are the transfer functions that can be obtained by curve fitting in the frequency domain which is similar to the technique used in Chapter 3 for unterminated transfer functions. It is now a straightforward effort to extract eigenvalues from the obtained power transfer functions.

Figure 7-9 shows eigenvalues extracted from those given in Figure 7-8, depicting two pairs of complex conjugate eigenvalues.

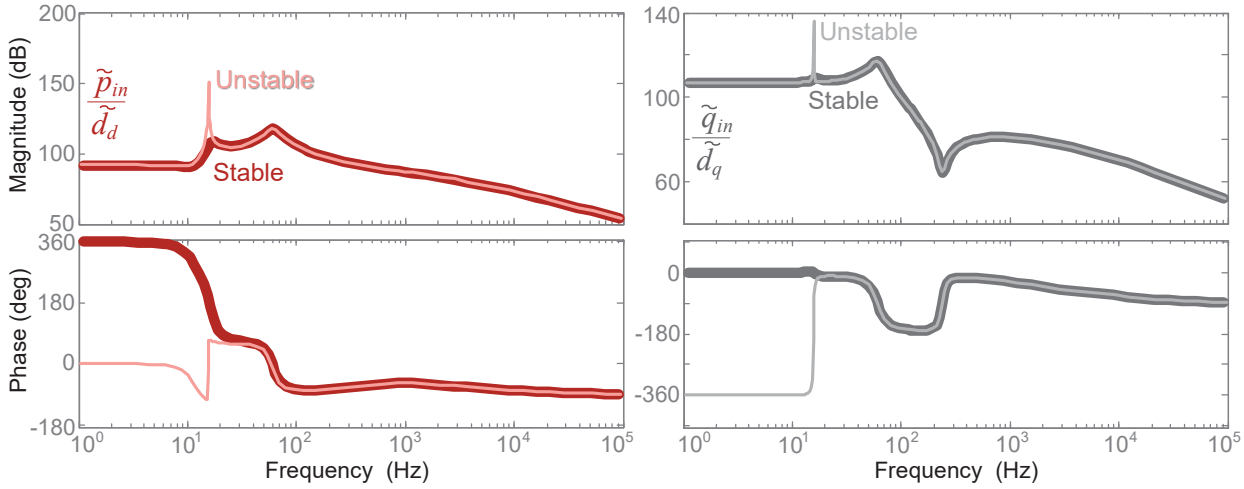

Figure 7-8: Bode plots of small-signal active (left), and reactive power (right) for both, stable and unstable case

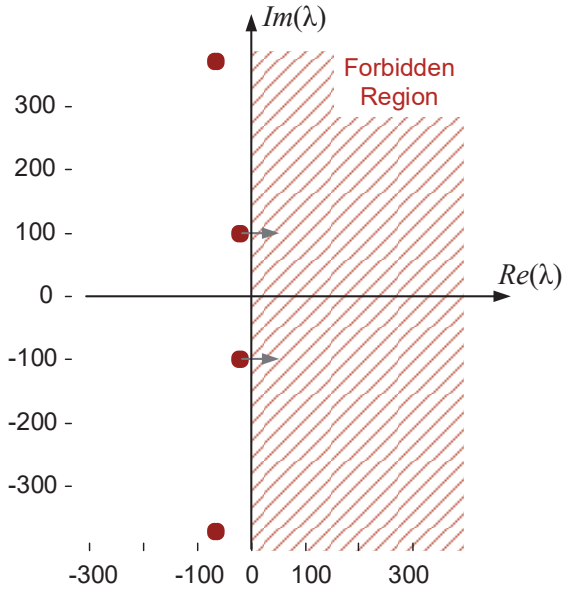

Figure 7-9: Complex conjugate eigenvalues extracted from small-signal active and reactive power

The double pole located at around 16 Hz in Figure 7-8 (both active and reactive power transfer functions contain it, as expected), has low damping and is very close to the vertical axis in the complex plane (Figure 7-9). A small load step (increasing the load of the bus converter) forces this double pole to cross the imaginary axis leading to instability that is reflected in the active and

reactive power transfer function as well (plotted using the state-space model, changing value of the resistive load).

This example only illustrates yet another possible methodology for online stability monitoring.

7.3 Discussion on Synchronous Machine Emulation

As seen in Chapters 5 and 6, power converters can very well imitate behavior of the synchronous machines via simple control means. Although these chapters present a way how to model and emulate a particular synchronous machine with the power electronic converter featuring as close as possible dynamic similarity with one another, the exact need for such accurate imitation is not a focus of this dissertation, and certainly needs to be researched further. The goal was to develop a detailed model of the synchronous machine and its virtual counterpart in order to form a good understanding of duality, and find a way to extend the grid-interface converter capabilities beyond the traditional synchronous machine operation. As demonstrated, machine-like, self-synchronization feature of power electronics converts implemented by integration of the DC-link voltage and virtual inertia offer new possibilities for performance improvement of grid-tied converters and validate further exploration on their advantage and practical implementation. On the other hand, exact imitation of other dynamics such as impedance and precise machine flux emulation need to be studied more before their advantage can be clearly seen.

The literature review reported in the Chapter 1 of this dissertation shows that there are numerous research groups who recognized that opportunity, and are highly focused on achieving exactly that - concept improvement beyond the conventional practice.

The following subsections summarize the methodology, and show some potential areas for further concept improvement by discussing simulation results. It should be noted that all of the following simulations are performed using the electronic generator model developed in Chapter 5 of this dissertation, and the goal of the next several simulation examples is to show phenomena qualitatively rather than quantitatively.

7.3.1 Electronic Generator Control Means

Figure 7-10 shows the simplified form of the virtual synchronous machine (electronic generator). It represents the grid-tied converter that features the machine-like frequency locked loop and has duty cycles d_d and d_q accessible for control (either open-loop, or closed -loop with flux calculation for full machine emulation as done in Chapter 5).

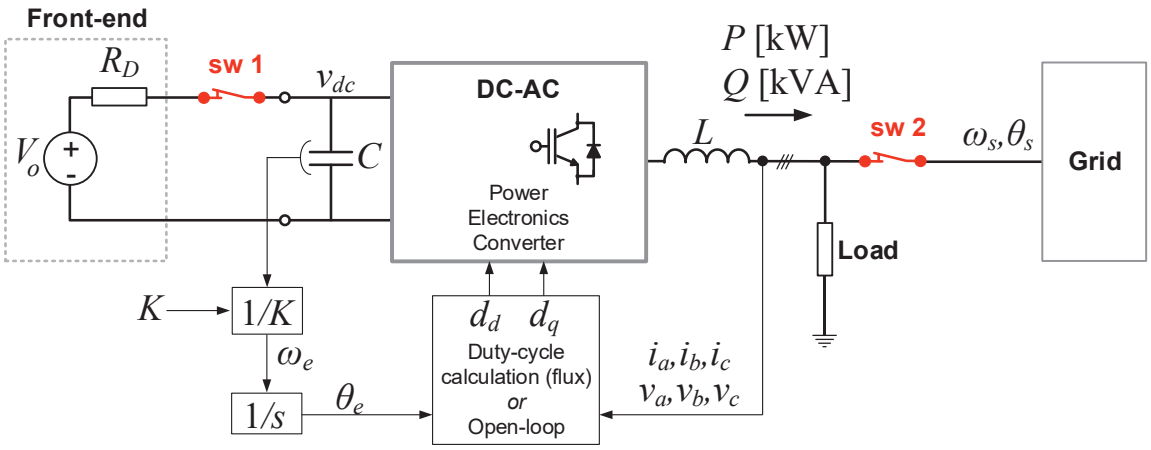

Figure 7-10: Simplified representation of the electronic generator

Synchronous machines can receive and deliver active power (motor and generator, respectively) only when their speed is in perfect synchronism with the frequency of the grid voltage. For this reason, the same happens here with the electronic generator. When the frequency locked-loop is implemented in the simple form as shown in Figure 7-10, controllability of the DC-link voltage is lost due to an enforced power balance. Frequency-locked loop will automatically set the DC-link voltage to the value $K\omega_s$, adjusting power angle δ as required to enable seamless active power transfer from the DC-side of the converter to the grid. It is apparent in Figure 7-11 that actions on the duty cycles do not have any impact on either active power or DC-link voltage, influencing only reactive power (reported simulation performed with direct access to the duty cycles, with no output current/voltage feedback from the AC – side).

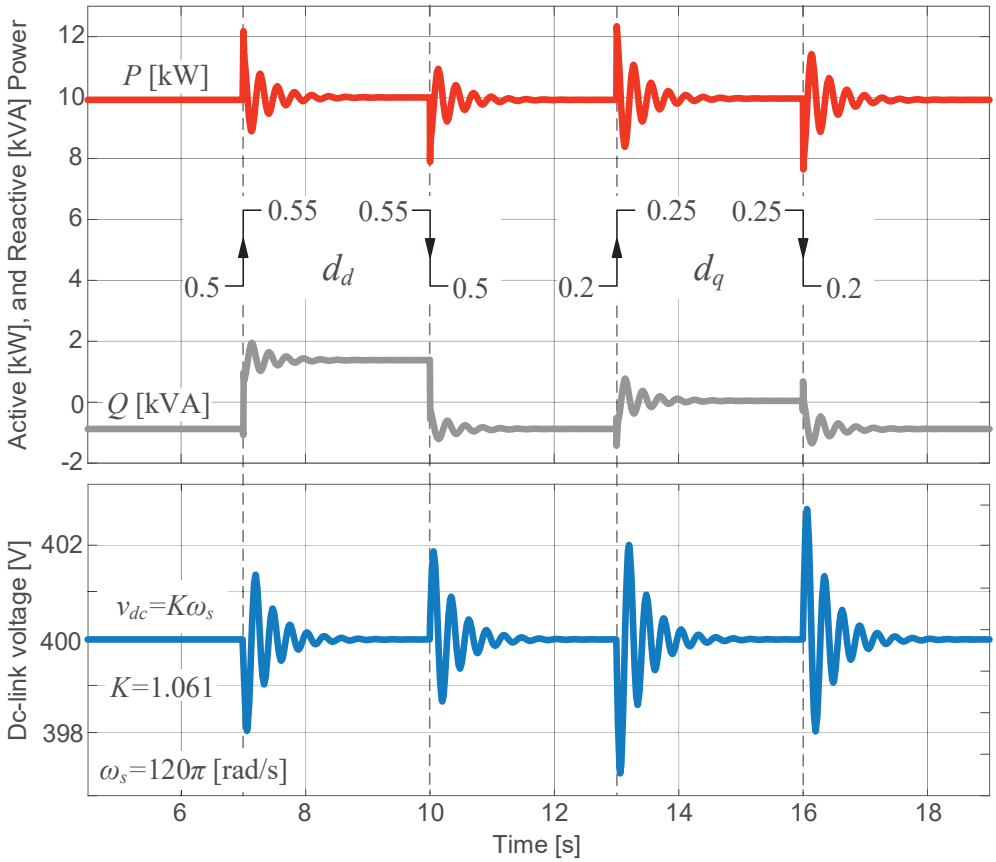

Figure 7-11: Active, reactive power, and DC-link voltage time-domain waveforms as a consequence of duty cycles changes

In any synchronous machine that operates grid-connected, active power flow is controlled by the primary source of energy (governor). The torque on the shaft will increase in an effort to increase the machine speed. As known, this cannot happen since the machine speed must stay in synchronism with the grid side frequency, resulting in power angle change and delivery of higher active power instead. Figure 7-12 shows the same effects happening in the electronic generator from Figure 7-10. With the duty cycles still being constant (d_d = 0.5, d_q = 0.2), the input voltage V_o is now increased at 20 s resulting in the greater active power delivery, while the DC-link voltage still remains constant until the grid frequency changes at 26 s. Immediately following that event, the DC-link voltage changes and follows the grid angular frequency change very closely as emphasized on the bottom of Figure 7-12. Active power also changes during the frequency step-down from the effect of the voltage droop (R_D in Figure 7-10).

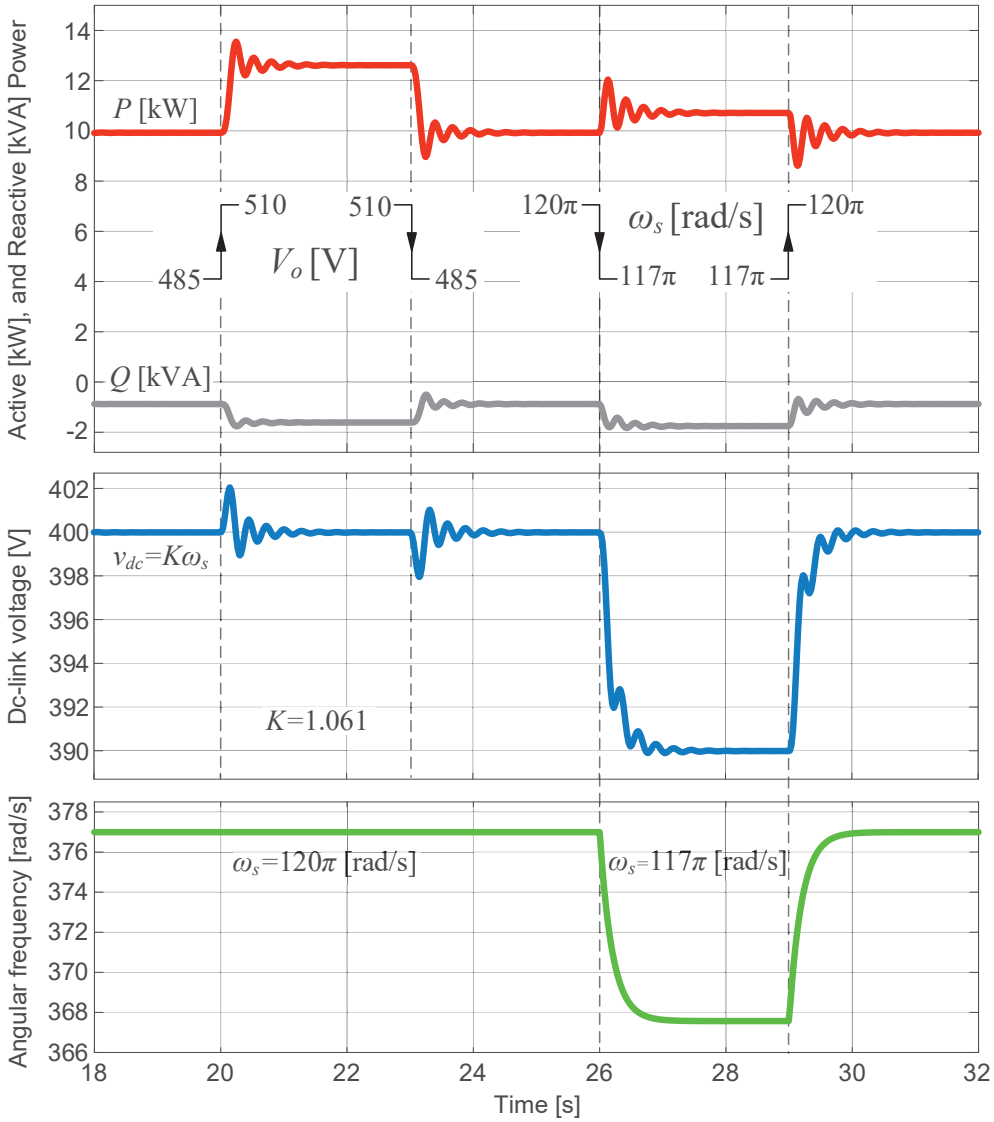

Figure 7-12: Active, reactive power, and DC-link voltage time-domain waveforms as a result of the input voltage and grid angular frequency change

7.3.2 An Alternative Control of the Active Power in Electronic Generators

Although there are no means to control the active power flow in the grid-tied synchronous machines other than changing the input torque from the governor, that action can be effectively done with the electronic generators simply via the scaling parameter K. In a way, frequency locked-loop emphasized in Figure 7-10 behaves as a DC-link voltage regulator, allowing the voltage to be set at any desired value (with the lower limits shown on Figure 5-6, and the upper limits being the rating of the applicable semiconductor devices, or DC-side system rating). Figure 7-13 illustrates this capability. It should be noted that for this simulation, duty cycles d_d and d_q are

still kept constant (0.5 and 0.2, respectively) with no output current/voltage feedback from the *AC* – side, and the below reported transients were obtained purely by stepping up and down scaling parameter *K*.

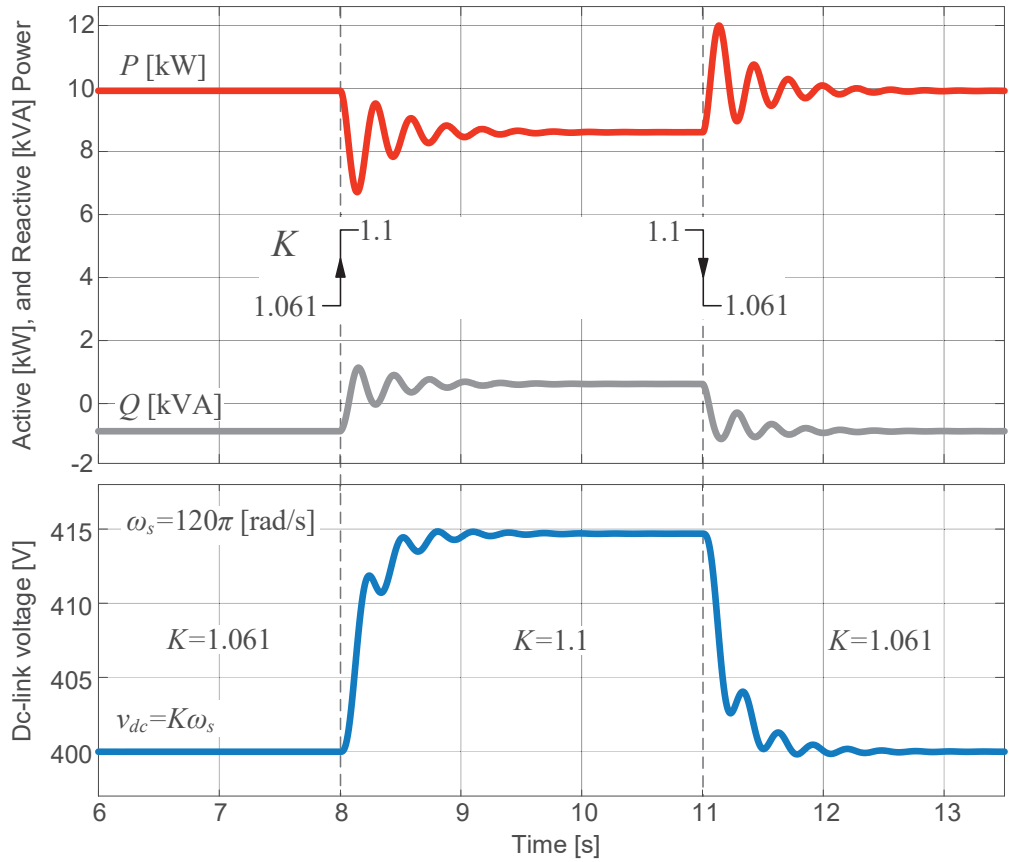

Figure 7-13: Active, reactive power, and DC-link voltage time-domain waveforms as a consequence of parameter *K* change

7.3.3 Loss of the Primary Generation

In the case when the primary energy source is lost, the electronic generator still continues to operate and, as in the real machines, automatically starts behaving as an unloaded synchronous motor. This is simulated by opening switch No.1 (sw 1) from Figure 7-10, while the electronic generator operates with active *AC*-side voltage/current feedback emulating a synchronous machine [174]. As shown in Figure 7-14, DC-link voltage recovers after the transient and resumes back to the previous value $K\omega_s$. This is once more the effect of the machine-like frequency locked loop and its effort to maintain the synchronization and power balance.

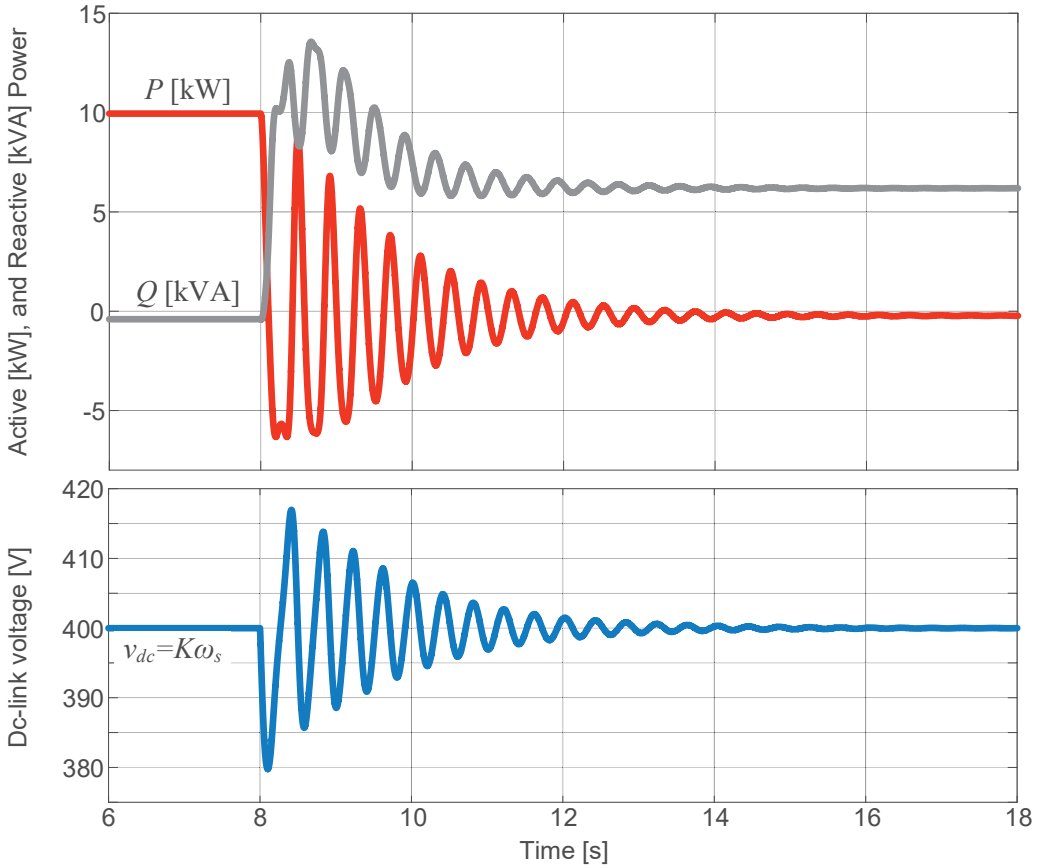

Figure 7-14: Active, reactive power, and DC-link voltage time-domain waveforms as a result of the primary energy source loss

7.3.4 Loss of the Grid (Islanding)

The islanding event is simulated by opening switch No.2 (sw 2) illustrated in Figure 7-10. Although the output voltage on the AC side still remains unchanged due to active regulation loop (via duty cycles), the predictable consequence of islanding is the DC-link voltage now becomes regulated by the primary source, and does not depend on the AC-side frequency anymore. Instead, the opposite happens due to the power-balance assured via the implemented frequency locked-loop; the AC-side frequency will now become proportional to the DC-link voltage: $\omega_s = v_{dc}/K$. To ensure that the load operates under nominal conditions, output frequency can be easily adjusted via the scaling factor K. This is illustrated in Figure 7-15 with the time-domain waveforms representing the loss of the grid at 8 s.

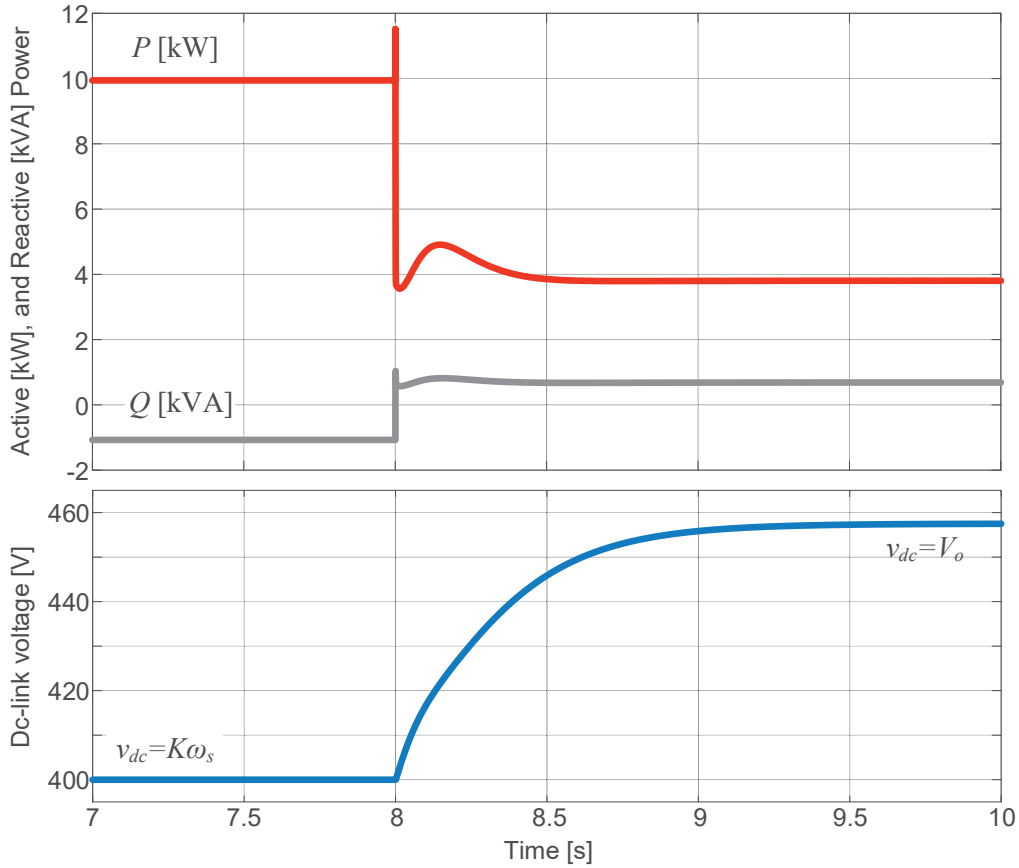

Figure 7-15: Active, reactive power, and DC-link voltage time-domain waveforms as a result of the grid loss

7.4 Dissertation Summary

The content of this dissertation is divided into seven chapters, starting with the introduction that expounds the motivation and objectives of this work, with an emphasis put on the research overview and here reported contributions.

The terminal behavioral modeling of three-, and four- port networks is presented next, proposing a generalized decoupling matrix that can be used with any type of AC-converters or networks (AC-DC, DC-AC, and AC-AC), to completely decouple source and load dynamics from the measured, terminated frequency responses, or transfer functions. The result of this methodology was an un-terminated behavioral model of the converter which was valid to half of the switching frequency, that can now be used in different system-level simulations, terminated with unknown source and load dynamics, while still preserving original and inherent dynamic

behavior. Several examples via simulations and experiments successfully demonstrated this concept.

After introduction of the terminal-behavioral modeling and decoupling procedure of three-phase converters, an alternative way to access small-signal stability on-line is proposed. The idea is that a converter already operating in the system can, via internal perturbations, perform an *AC*-sweep and obtain all terminal immittances online. Although the methods for obtaining outward impedances from converter terminals are well known, the contribution of the work reported here was the possibility to obtain inward terminal immittances by using an unterminated behavioral model. This allows an accurate estimation of how outward immittances reflect to the opposite side of the converter and an opportunity to perform an *in-situ* stability assessment. Methodology was successfully demonstrated by simulation and experiments.

Following an online small-signal stability assessment, the dissertation advances into the synchronous machine emulation with the power electronics converter. It was successfully shown how to establish electromechanical-electrical duality between the electric machine and the power converter, and re-structure the well-known machine model to fully resemble a power converter average model. This model not only allows for any type of machine to be accurately simulated, it also gives an insight into what needs to be done in order to successfully emulate the machine with the power electronics converter. It was further shown how converter synchronization can now be achieved by measuring and integrating its own DC-link voltage. Dynamic characterization of the particular machine was performed, and successful emulation was demonstrated using power electronics converter prototype. By using no other means of synchronization other than DC-link voltage integration, system-level operation with two coupled components, real and virtual synchronous machine, was simulated and experimentally demonstrated. Finally, a virtual inertia implementation method was proposed, and its capability to mitigate system-level instability was demonstrated in simulation.

The last chapter, synergistically discusses proposed methodologies by opening the space for new applications, and further improvement in the future, related work.

7.5 Future Work

Although confirmed on a minimal-relevant system comprising three-phase converter terminated with the source and the load, terminal-behavioral modeling reported in this dissertation did not focus on the simulation of larger, more complex systems comprising several sources and loads. Showing that in the future work, including nonlinearity and smooth transition between different operating points using time varying transfer functions, will undoubtedly strengthen the methodology reported in this dissertation, and presents an important and challenging next step towards higher adoption of this modeling practice.

Online monitoring and stability assessment reported in this dissertation certainly supports an effort towards future power distribution systems with increased "embedded awareness". Nevertheless, these efforts will heavily depends on the unterminated transfer functions, assuming each converter can have them obtained for numerous operating points and stored into memory. Hence, solving the nonlinearity problem stated above in the first paragraph will directly impact this method as well. Also, perturbation injection method used here is closely tied to the particular microprocessor family, and was not done in an embedded form, thus limiting the resources and wide endorsement of the methodology. Additionally, the time required to perform the full *AC* sweep is too long to assume the operating point is static and does not change during the injection period. Hence, future work should focus on the use of the embedded wide bandwidth frequency response functionality using other injection types (e.g. multi-tone, impulse, etc.), and applying certain stability criteria online, with an adequate action taken automatically on re-tuning converter control loops in order to increase stability margins.

In order to truly enhance the operation of multi-source power systems, power electronics converter emulating synchronous machines should also be capable of performing online monitoring and stability assessment in addition to its original functionality, hence part of the future work related to this topic should be implementation of the online monitoring function into the converter emulating a synchronous machine.

However, there are challenges in the area of improved control of the electronic generators themselves with the higher priority than embedded online monitoring functionality. Although this dissertation addresses relatively precise machine emulation and the advantage of utilizing the synchronous frequency-locked loop, it does not address current regulation, limit, and protection – functionalities of a very high importance for the grid-tied converters. Now that basic emulation of

the synchronous machines is better understood, the most logical future step would be a systematic comparison between the conventional *d*-*q* control of grid-tied converters and a virtual synchronous machine, including a methodical study that will clearly show an advantage (or disadvantage) of the machine-like synchronization presented in this dissertation. Furthermore, it is very important to improve the machine emulation algorithm by including high-bandwidth current regulation functionality instead of fully utilizing the exact machine operational inductances and field to stator dynamics.

References

[1] US Energy Information Administration: *Annual Energy Outlook 2017: With Projections to 2050*, January 2017.

[2] D. Boroyevich, I. Cvetkovic, R. Burgos, and D. Dong, "Intergrid: A Future Electronic Energy Network?," *IEEE Journal of Emerging and Selected Topics in Power Electronics,* vol. 1, pp. 127-138, 2013.

[3] G. Bakke: *The Grid: The Fraying Wires Between Americans and Our Energy Future*, Bloomsbury USA, 2016.

[4] D. Tan, "Electronictization - A foundation for grid modernization," *Chinese Journal of Electrical Engineering,* vol. 1, pp. 1-8, 2015.

[5] M. Guarnieri, "The Beginning of Electric Energy Transmission: Part One [Historical]*," Industrial Electronics Magazine*, IEEE, vol. 7, pp. 50-52, 2013.

[6] J. Wirfs Brock, "Data: Explore 15 Years of Power Outages," Inside Energy, 2014.

[7] U.S. Department of Energy. Quadrennial Energy Review Energy Transmission, Storage, and Distribution Infrastructure, 2015. Available online at: http://energy.gov/sites/prod/files/2015/08/f25/QER%20Summary%20for%20Policymakers%20April%202015.pdf.

[8] N. G. Hingorani and L. Gyugyi: *Understanding FACTS: Concepts and Technology of Flexible AC Transmission Systems*. New York: IEEE Press, 2000.

[9] N. G. Hingorani, "Power electronics in electric utilities: role of power electronics in future power systems", *Proceedings of the IEEE*, vol. 76, pp. 481-482, 1988.

[10] R. Abe, H. Taoka, and D. McQuilkin, "Digital Grid: Communicative Electrical Grids of the Future," *Smart Grid, IEEE Transactions on,* vol. 2, pp. 399-410, 2011.

[11] US Department of Energy: *GRID 2030,* July 2003.

[12] S. Bifaretti, P. Zanchetta, A. Watson, L. Tarisciotti, and J. C. Clare, "Advanced Power Electronic Conversion and Control System for Universal and Flexible Power Management," *Smart Grid, IEEE Transactions on,* vol. 2, pp. 231-243, 2011.

[13] P. Fairley, "Germany jump-starts the supergrid," *Spectrum, IEEE,* vol. 50, 2013.

[14] P. Juanuwattanakul and M. A. S. Masoum, "Increasing distributed generation penetration in multiphase distribution networks considering grid losses, maximum loading factor and bus voltage limits," *Generation, Transmission & Distribution, IET,* vol. 6, pp. 1262-1271, 2012.

[15] S. Xu, A. Q. Huang, S. Lukic, and M. E. Baran, "On Integration of Solid-State Transformer With Zonal DC Microgrid," *Smart Grid, IEEE Transactions on,* vol. 3, pp. 975-985, 2012.

[16] D. Boroyevich, R. Burgos, L. Arnedo, and W. Fei, "Syndissertation and Integration of Future Electronic Power Distribution Systems", *in Power Conversion Conference - Nagoya. PCC '07*, 2007, pp. K-1-K-8.

[17] M. G. Lauby, "Enabling the power system of the future", *in Advances in Power System Control, Operation and Management (APSCOM 2009), 8th International Conference on*, 2009, pp. 1-8.

[18] M. Smith and D. Ton, "Key Connections: The U.S. Department of Energy's Microgrid Initiative," *Power and Energy Magazine, IEEE,* vol. 11, pp. 22-27, 2013.

[19] I. A. Hiskens, "What's smart about the smart grid?", *in Design Automation Conference (DAC), 2010 47th ACM/IEEE*, 2010, pp. 937-939.

[20] O. HyungSeon, "Optimal Planning to Include Storage Devices in Power Systems," *Power Systems, IEEE Transactions on,* vol. 26, pp. 1118-1128, 2011.

[21] F. Blaabjerg, A. Consoli, J. A. Ferreira, and J. D. van Wyk, "The future of electronic power Processing and conversion", *Power Electronics, IEEE Transactions on*, vol. 20, pp. 715-720, 2005.

[22] A. Atputharajah and T. K. Saha, "Power system blackouts - literature review*", in Industrial and Information Systems (ICIIS), 2009 International Conference on*, 2009, pp. 460-465.

[23] M. Molinas and J. Kondoh, "Power electronic loads as providers of reactive power ancillary service to the grid: Analytical and experimental study", *in Power Electronics and Applications, 2009. EPE '09. 13th European Conference on*, 2009, pp. 1-10.

[24] European Center for Power Electronics, "Position Paper on Energy Efficiency – the Role of Power Electronics," March 2008.

[25] P. K. Steimer, "Power electronics, a key technology for future more electrical energy systems", *in Energy Conversion Congress and Exposition, 2009*. ECCE 2009. IEEE, 2009, pp. 1161-1165.

[26] Dyke, K.J., Schofield, N., Barnes, M., "The Impact of Transport Electrification on Electrical Networks", *Industrial Electronics, IEEE Transactions on*, Vol. 57, No. 12, pp. 3917 - 3926, Dec. 2010.

[27] P. K. Steimer, "*Enabled by high power electronics - Energy efficiency, renewables and smart grids*", in Power Electronics Conference (IPEC), 2010 International, 2010, pp. 11-15.

[28] P. K. Steimer, "Power electronics, a key technology for future more electrical energy systems", *in Energy Conversion Congress and Exposition, 2009*. ECCE 2009. IEEE, 2009, pp. 1161-1165.

[29] T. F. Garrity, "Innovation and trends for future electric power systems", *in Power Systems Conference, 2009. PSC* '09, 2009, pp. 1-8.

[30] D. Abbott, "Keeping the Energy Debate Clean: How Do We Supply the World's Energy Needs?", *Proceedings of the IEEE*, vol. 98, pp. 42-66, 2010.

[31] A. Ipakchi and F. Albuyeh: *Grid of the future*, Power and Energy Magazine, IEEE, vol. 7, pp. 52-62, 2009.

[32] F. Blaabjerg, Z. Chen, R. Teodorescu, and F. Iov, "Power Electronics in Wind Turbine Systems", *in Power Electronics and Motion Control Conference*, 2006. IPEMC 2006. CES/IEEE 5th International, 2006, pp. 1-11.

[33] F. Blaabjerg, C. Zhe, and S. B. Kjaer, "Power electronics as efficient interface in dispersed power generation systems", *Power Electronics, IEEE Transactions on*, vol. 19, pp. 1184-1194, 2004.

[34] C. Rahmann, H. J. Haubrich, A. Moser, R. Palma-Behnke, L. Vargas, and M. B. C. Salles, "Justified Fault-Ride-Through Requirements for Wind Turbines in Power Systems", *Power Systems, IEEE Transactions on*, vol. 26, pp. 1555-1563, 2011.

[35] C. C. Davidson, "Power Transmission with Power Electronics", *in IEEE EPE 2011-14th European Conference on Power Electronics and Applications*, 2009.

[36] R. S. Whitehouse, "Technical Challenges of Realising Multi-terminal Networking with VSC", *in IEEE EPE 2011-14th European Conference on Power Electronics and Applications*, 2009.

[37] T. J. Hammons, V. F. Lescale, K. Uecker, M. Haeusler, D. Retzmann, K. Staschus, and S. Lepy, "State of the Art in Ultrahigh-Voltage Transmission," *Proceedings of the IEEE,* vol. 100, pp. 360-390, 2012.

[38] J. S. Contreras-Jimenez, and F. Rivas-Davalos, "Reliability and availability of VSC-HVDC links: A state of the art," in *2015 IEEE International Autumn Meeting on Power, Electronics and Computing (ROPEC)*, 2015, pp. 1-8.

[39] M. M. Alamuti, C. S. Saunders, and G. A. Taylor, "A novel VSC HVDC active power control strategy to improve AC system stability," in *2014 IEEE PES General Meeting | Conference & Exposition*, 2014, pp. 1-5.

[40] C. A. B. Karim and M. A. Zamee, "Design and analysis of pole-placement controller for dynamic stability improvement of VSC-HVDC based power system," in *Strategic Technology (IFOST), 2014 9th International Forum on*, 2014, pp. 272-275.

[41] A. Lesnicar and R. Marquardt, "An innovative modular multilevel converter topology suitable for a wide power range," *in Power Tech Conference Proceedings,* 2003 IEEE Bologna, 2003, p. 6 pp. Vol.3.

[42] S. Allebrod, R. Hamerski, and R. Marquardt, "New transformerless, scalable Modular Multilevel Converters for HVDC-transmission," *in Power Electronics Specialists Conference*, 2008. PESC 2008. IEEE, 2008, pp. 174-179.

[43] J. Wang, R. Burgos, D. Boroyevich, “A Survey on the Modular Multilevel Converters - Modeling, Modulation and Controls,” *Accepted for publication at Energy Conversion Congress and Exposition, ECCE 2013.*

[44] H. Lee Willis, “ Power Distribution Planning Reference Book,”, CRC 2004.

[45] N. Sokal, “System oscillations from negative input resistance at power input port of switching-mode regulator, amplifier, dc/dc converter, or dc/ac inverter,” In proc. IEEE PESC’73, pp. 138–140, June 1973.

[46] R. D. Middlebrook, “Input filter considerations in design and application of switching regulators,” In proc. of IEEE IAS ’76, pp. 366−382, 1976.

[47] R. D. Middlebrook, “Design techniques for preventing input-filter oscillations in switched-mode regulators,” In proc. of *PowerCon 5*, *the Fifth National Solid State Power Conversion Conference*, May 1978.

[48] B. Wen, “Stability analysis of three-phase AC power systems based on measured d-q frame impedances,” Electrical Engineering, Dissertation, Virginia Tech, 2014.

[49] M. Karimi-Ghartema, "Synchronous Reference Frame PLL," in *Enhanced Phase-Locked Loop Structures for Power and Energy Applications*, ed: Wiley-IEEE Press, 2014, p. 250.

[50] D. Dong, D. Boroyevich, P. Mattavelli, and Y. Xue, “Analysis of Phase-Locked Loop Low Frequency Stability in Three-Phase Grid-Connected Power Converters Considering Impedance Interactions,” *IEEE Trans. on Industrial Electronics*, vol. 62, no. 1, pp. 310-321, Jan. 2015.

[51] X. Wang, F. Blaabjerg, and W. Wu, "Modeling and Analysis of Harmonic Stability in an AC Power-Electronics-Based Power System," *IEEE Transactions on Power Electronics,* vol. 29, pp. 6421-6432, 2014.

[52] F. Wang, J. Duarte, M. Hendrix, and P. Ribeiro, “Modelling and analysis of grid harmonic distortion impact of aggregated DG inverters,” IEEE Trans. Power Electron., vol. 26, no. 3, pp. 786–797, Mar. 2011.

[53] X. Wang, F. Blaabjerg, M. Liserre, Z. Chen, J. He, and Y. Li, “An active damper for stabilizing power-electronics-based AC systems,” IEEE Trans. Power Electron., vol. 29, no. 7, pp. 3318–3329, July 2014.

[54] A. MacFarlane and I. Postlethwaite, “The generalized Nyquist stability criterion and multivariable root loci,” *International Journal of Control*, vol. 25, pp. 81-127, Jan. 1977.

[55] M. Belkhayat, “Stability criteria for ac power systems with regulated loads,” *Purdue University, PhD Dissertation*, 1997.

[56] G. Francis, “An algorithm and implementation system architecture for measuring impedances in the d-q domain,” Ph.D. Dissertation, Virginia Tech, Jan. 2010.

[57] G. Francis, R. Burgos, D. Boroyevich, F. Wang, K Karimi, "An algorithm and implementation system for measuring impedance in the D-Q domain," *Energy Conversion Congress and Exposition (ECCE), 2011 IEEE* , pp. 3221-3228.

[58] Z. Shen, "Online measurement of three-phase ac power system impedance in synchronous coordinates," Ph.D. Dissertation, Virginia Tech, Jan. 2013.

[59] H. Shi, F. Zhuo, D. Zhang, Z. Geng, and F. Wang, "Modeling, analysis, and measurement of impedance for three-phase AC distributed power system," in *2014 IEEE Energy Conversion Congress and Exposition (ECCE)*, 2014, pp. 4635-4639.

[60] Y. L. Familiant, K. A. Corzine, J. Huang, and M. Belkhayat, "AC Impedance Measurement Techniques," in *IEEE International Conference on Electric Machines and Drives, 2005.*, 2005, pp. 1850-1857.

[61] Z. Shen, M. Jaksic, P. Mattavelli, D. Boroyevich, J. Verhulst, and M. Belkhayat, "Design and implementation of three-phase AC impedance measurement unit (IMU) with series and shunt injection," *APEC '13 – IEEE Appl. Power Elec. Conf.*, pp. 2674-2681, Mar. 17-21, 2013.

[62] Z. Shen, M. Jaksic, I. Cvetkovic, R. Burgos, and D. Boroyevich, "Small-signal impedance measurement in medium-voltage dc power systems," *ESARS 2015 – IEEE International Conf. on Electrical Systems for Aircraft, Railway, Ship Propulsion and Road Vehicles*, Mar. 2015.

[63] Z. Shen, I. Cvetkovic, M. Jaksic, C. DiMarino, D. Boroyevich, R. Burgos, and F. Chen, "Design of a modular and scalable small-signal dq impedance measurement unit for grid applications utilizing 10 kV SiC MOSFETs," *in Power Electronics and Applications (EPE'15 ECCE-Europe), 2015 17th European Conference on*, pp.1-9, Sep. 8-10, 2015.

[64] I. Cvetkovic, Z. Shen, M. Jaksic, C. DiMarino, F. Chen, D. Boroyevich, and R. Burgos, "Modular scalable medium-voltage impedance measurement unit using 10 kV SiC MOSFET PEBBs," *in Electric Ship Technologies Symposium (ESTS), 2015 IEEE*, pp.326-331, June 21-24, 2015.

[65] M. Jaksic, D. Boroyevich, R. Burgos, Z. Shen, I. Cvetkovic, P. Mattavelli, "Modular Interleaved Single-Phase Series Voltage Injection Converter Used in Small-Signal DQ Impedance Identification," *ECCE 2014 – IEEE Energy Conversion Congress and Expo.*, pp. 3036-3045, Pittsburgh, PA, Sep. 14-18, 2014.

[66] M. Jaksic, Z. Shen, I. Cvetkovic, D. Boroyevich, R. Burgos, and P. Mattavelli, "Multi-level single-phase shunt current injection converter used in small-signal dq impedance identification," *APEC '14 – IEEE Appl. Power Elec. Conf.*, pp. 2775-2782, Mar. 16-20, 2014.

[67] B. H. Cho, "Modeling and analysis of spacecraft power systems," *Virginia Polytechnic Institute and State University, PhD Dissertation*, 1985.

[68] B. H. Cho and F. C. Y. Lee, "Modeling and analysis of spacecraft power systems," *Power Electronics, IEEE Transactions on,* vol. 3, pp. 44-54, 1988.

[69] P. G. Maranesi*, et al.*, "Two-part characterization of PWM voltage regulators at low frequencies," *Industrial Electronics, IEEE Transactions on,* vol. 35, pp. 444-450, 1988.

[70] L. Arnedo, R. Burgos, F. Wang, and D. Boroyevich, "Black-box terminal characterization modeling of dc-to-dc converters," *IEEE APEC '07*, pp. 457-463, Feb. 2007.

[71] J. A. Oliver, R. Prieto, V. Romero, and J. A. Cobos, "Behavioral modeling of dc-dc converters for large-signal simulation of distributed power systems," in *Applied Power Electronics Conference and Exposition, 2006. APEC '06. Twenty-First Annual IEEE*, 2006, p. 6 pp.

[72] V. Valdivia, A. Barrado, A. Lazaro, C. Fernandez, and P. Zumel, "Black-box modeling of DC-DC converters based on transient response analysis and parametric identification methods," in *Applied Power Electronics Conference and Exposition (APEC), 2010 Twenty-Fifth Annual IEEE*, 2010, pp. 1131-1138.

[73] V. Valdivia, A. Barrado, A, Lazaro, M. Sanz*, et al.*, "Black-Box Behavioral Modeling and Identification of DC-DC Converters With Input Current Control for Fuel Cell Power Conditioning," *IEEE Transactions on Industrial Electronics,* vol. 61, pp. 1891-1903, 2014.

[74] M. Riva, F. Belloni, and D. D. Giustina, "Dynamic characterization of power converters: Methods and actuators," in *2010 IEEE International Workshop on Applied Measurements for Power Systems*, 2010, pp. 95-99.

[75] I. Cvetkovic, D. Boroyevich, P. Mattavelli, F. C. Lee, and D. Dong, "Unterminated Small-Signal Behavioral Model of DC-DC Converters," *IEEE Transactions on Power Electronics,* vol. 28, pp. 1870-1879, 2013.

[76] J. A. Oliver, R. Prieto, J. A. Cobos, O. Garcia, and P. Alou, "Hybrid Wiener-Hammerstein Structure for Grey-Box Modeling of DC-DC Converters," in *Applied Power Electronics Conference and Exposition, 2009. APEC 2009. Twenty-Fourth Annual IEEE*, 2009, pp. 280-285.

[77] I. Cvetkovic, D. Boroyevich, P. Mattavelli, F. C. Lee, and D. Dong, "Non-linear, hybrid terminal behavioral modeling of a dc-based nanogrid system," in *Applied Power Electronics Conference and Exposition (APEC), 2011 Twenty-Sixth Annual IEEE*, 2011, pp. 1251-1258.

[78] L. Arnedo, D. Boroyevich, R. Burgos, and F. Wang, "Polytopic black-box modeling of dc-dc converters," in *2008 IEEE Power Electronics Specialists Conference*, 2008, pp. 1015-1021.

[79] L. Arnedo, "System Level Black-Box Models for DC-DC Converters," *Virginia Polytechnic Institute and State University, PhD Dissertation*, 2008.

[80] X. Zheng, H. Ali, X. Wu, H. Zaman, and S. Khan, "Non-Linear Behavioral Modeling for DC-DC Converters and Dynamic Analysis of Distributed Energy Systems," *Energies, 2017, 10-63.*

[81] A. Francés, R. Asensi, O. García, R. Prieto, and J. Uceda, "A black-box modeling approach for DC nanogrids," in *2016 IEEE Applied Power Electronics Conference and Exposition (APEC)*, 2016, pp. 1624-1631.

[82] S. Hiti, D. Boroyevich, and C. Cuadros, "Small-signal modeling and control of three-phase PWM converters," in *Proceedings of 1994 IEEE Industry Applications Society Annual Meeting*, 1994, pp. 1143-1150 vol.2.

[83] V. Valdivia, R. Todd, F. J. Bryan, A. Barrado, L. A. Lazaro, and A. Forsyth, "Behavioral Modeling of a Switched Reluctance Generator for Aircraft Power Systems," *IEEE Transactions on Industrial Electronics,* vol. 61, pp. 2690-2699, 2014.

[84] V. Valdivia, L. A, zaro, A. Barrado, P. Zumel, C. Fern*, et al.*, "Black-box modeling of three phase voltage source inverters based on transient response analysis," in *Applied Power Electronics Conference and Exposition (APEC), 2010 Twenty-Fifth Annual IEEE*, 2010, pp. 1279-1286.

[85] V. Valdivia, A. Lazaro, A. Barrado, P. Zumel, C. Fernandez, and M. Sanz, "Black-Box Modeling of Three-Phase Voltage Source Inverters for System-Level Analysis," *IEEE Transactions on Industrial Electronics,* vol. 59, pp. 3648-3662, 2012.

[86] G. Ala, A. Spagnuolo, and F. Viola, "A local linear black-box identification technique for power converters modeling," in *2009 IEEE Vehicle Power and Propulsion Conference*, 2009, pp. 257-264.

[87] Aapro, A.; Messo, T.; Suntio, T. "An accurate small-signal model of a three-phase VSI-based photovoltaic inverter with LCL-filter", *Power Electronics and ECCE Asia (ICPE-ECCE Asia), 2015 9th International Conference on,* On page(s): 2267 – 2274.

[88] H. Bishnoi, P. Mattavelli, R. Burgos, D. Boroyevich, "EMI filter design of DC-fed motor-drives using behavioral EMI models," *in Power Electronics and Applications (EPE'15 ECCE-Europe), 2015 17th European Conference on*, pp.1-10, Sep. 8-10, 2015.

[89] C. Cuellar and N. Idir, "Determination of the insertion loss of EMI filters using a black-box model," in *2015 IEEE Energy Conversion Congress and Exposition (ECCE)*, 2015, pp. 2644-2649

[90] G. Frantz, D. Frey, J. L. Schanen, B. Revol, H. Bishnoi, and P. Mattavelli, "EMC models for power electronics: From converter design to system level," in *2013 IEEE Energy Conversion Congress and Exposition*, 2013, pp. 4247-4252.

[91] Bishnoi, A. C. Baisden, P. Mattavelli, and D. Boroyevich, "EMI modeling of half-bridge inverter using a generalized terminal model," in *Applied Power Electronics Conference and Exposition (APEC), 2011 Twenty-Sixth Annual IEEE*, 2011, pp. 468-474.

[92] A. C. Baisden, D. Boroyevich, and F. Wang, "EMI Terminal Modeling," in *Industry Applications Society Annual Meeting, 2008. IAS '08. IEEE*, 2008, pp. 1-8

[93] I. Cvetkovic, M. Jaksic, D. Boroyevich, P. Mattavelli, F. C. Lee, Z. Shen, S. Ahmed, and D. Dong, "Un-terminated, low-frequency terminal-behavioral d-q model of three-phase converters," in *2011 IEEE Energy Conversion Congress and Exposition*, 2011, pp. 791-798.

[94] L. Arnedo, D. Boroyevich, R. Burgos, and F. Wang, "Un-terminated frequency response measurements and model order reduction for black-box terminal characterization models," in *Applied Power Electronics Conference and Exposition, 2008. APEC 2008. Twenty-Third Annual IEEE*, 2008, pp. 1054-1060.

[95] I. Cvetkovic, "Modeling, Analysis and Design of Renewable Energy Nanogrid Systems," *Virginia Polytechnic Institute and State University, MS Dissertation*, 2010.

[96] H. Bishnoi, P. Mattavelli, R. Burgos, D. Boroyevich, "EMI filter design of DC-fed motor-drives using behavioral EMI models," *in Power Electronics and Applications (EPE'15 ECCE-Europe), 2015 17th European Conference on*, pp.1-10, Sep. 8-10, 2015.

[97] C. Cuellar and N. Idir, "Determination of the insertion loss of EMI filters using a black-box model," in *2015 IEEE Energy Conversion Congress and Exposition (ECCE)*, 2015, pp. 2644-2649

[98] G. Frantz, D. Frey, J. L. Schanen, B. Revol, H. Bishnoi, and P. Mattavelli, "EMC models for power electronics: From converter design to system level," in *2013 IEEE Energy Conversion Congress and Exposition*, 2013, pp. 4247-4252.

[99] Bishnoi, A. C. Baisden, P. Mattavelli, and D. Boroyevich, "EMI modeling of half-bridge inverter using a generalized terminal model," in *Applied Power Electronics Conference and Exposition (APEC), 2011 Twenty-Sixth Annual IEEE*, 2011, pp. 468-474.

[100] A. C. Baisden, D. Boroyevich, and F. Wang, "EMI Terminal Modeling," in *Industry Applications Society Annual Meeting, 2008. IAS '08. IEEE*, 2008, pp. 1-8.

[101] Y. Familiant, "Ac Impedance Measurement Techniques in Power Systems," *Ph.D. Dissertation, University of Wisconsin-Milwaukee, May 2006.*

[102] Marko Jakšić, "Identification of small-signal dq impedances of power electronics converters via single-phase wide-bandwidth injection," *Virginia Polytechnic Institute and State University, PhD Dissertation*, November 2014.

[103] Huang Jing and K. A. Corzine, "Ac impedance measurement by line-to-line injected current," in *Conference Record of the 2006 IEEE Industry Applications Conference Forty-First IAS Annual Meeting*, 2006, pp. 300-306

[104] Huang Jing, K. A. Corzine, M. Belkhayat, “Small-signal impedance measurement of power-electronics-based AC power systems using line-to-line current injection,” *IEEE Transactions on Power Electronics*, vol. 24, no. 2, 2009, pp. 445-455.

[105] V. Valdivia, A. Lazaro, A. Barrado, P. Zumel, C. Fernandez, M. Sanz, “Impedance Identification Procedure of Three-Phase Balanced Voltage Source Inverters Based on Transient Response Measurements,” *IEEE Transactions on Power Electronics*, vol. 26, no. 12, pp. 3810-3816, Dec. 2011.

[106] A. Barkley and E. Santi, "Online Monitoring of Network Impedances Using Digital Network Analyzer Techniques," in *2009 Twenty-Fourth Annual IEEE Applied Power Electronics Conference and Exposition*, 2009, pp. 440-446.

[107] M, Cespedes, and J. Sun, "Online grid impedance identification for adaptive control of grid-connected inverters," in *2012 IEEE Energy Conversion Congress and Exposition (ECCE)*, 2012, pp. 914-921.

[108] M. Cespedes and J. Sun, "Adaptive Control of Grid-Connected Inverters Based on Online Grid Impedance Measurements," *IEEE Transactions on Sustainable Energy,* vol. 5, pp. 516-523, 2014.

[109] B. Wen, D. Boroyevich, P. Mattavelli, R. Burgos, and Z. Shen, "Impedance-based analysis of grid-synchronization stability for three-phase paralleled converters," in *2014 IEEE Applied Power Electronics Conference and Exposition - APEC 2014*, 2014, pp. 1233-1239.

[110] A. Riccobono, S. K. A. Naqvi, A. Monti, T. Caldognetto, J. Siegers, and E. Santi, "Online wideband identification of single-phase AC power grid impedances using an existing grid-tied power electronic inverter," in *2015 IEEE 6th International Symposium on Power Electronics for Distributed Generation Systems (PEDG)*, 2015, pp. 1-8.

[111] A. Riccobono, E. Liegmann, A. Monti, F. C. Dezza, J. Siegers, and E. Santi, "Online wideband identification of three-phase AC power grid impedances using an existing grid-tied power electronic inverter," in *2016 IEEE 17th Workshop on Control and Modeling for Power Electronics (COMPEL)*, 2016, pp. 1-8.

[112] D. Martin, I. Nam, J. Siegers, and E. Santi, "Wide bandwidth three-phase impedance identification using existing power electronics inverter," in *Applied Power Electronics Conference and Exposition (APEC), 2013 Twenty-Eighth Annual IEEE*, 2013, pp. 334-341.

[113] http://sites.ieee.org/gms-pes/files/2017/02/IEEE-1547-Vermont-Chapter.pdf.

[114] G. J. Schaeffer and P. Vaessen, "Future power system transition - step into the light", *in Future Power Systems, 2005 International Conference on*, 2005, pp. 6 pp.-6.

[115] R. E. Brown and L. A. A. Freeman, "Analyzing the reliability impact of distributed generation", *in Power Engineering Society Summer Meeting*, 2001. IEEE, 2001, pp. 1013-1018 vol.2.

[116] I. A. Hiskens, "What's smart about the smart grid?", *in Design Automation Conference (DAC)*, 2010 47th ACM/IEEE, 2010, pp. 937-939.

[117] W. El-khattam and T. S. Sidhu, "Resolving the impact of distributed renewable generation on directional overcurrent relay coordination: a case study", *Renewable Power Generation, IET*, vol. 3, pp. 415-425, 2009.

[118] J. H. R. Enslin and P. J. Heskes,"Harmonic interaction between a large number of distributed power inverters and the distribution network*", IEEE Transaction on Power Electronics,* vol. 19, no. 6, pp. 1586-1593, 2004.

[119] M. Cespedes and J. Sun, "Renewable Energy Systems Instability Involving Grid-Parallel Inverters*", in Applied Power Electronics Conference and Exposition*, 2009. APEC 2009. Twenty-Fourth Annual IEEE, 2009, pp. 1971-1977.

[120] M. Liserre, R. Theodorescu and F.Blaabjerg, "Stability of photovoltaic and wind turbine grid-connected inverters for a large set of grid impedance values", *IEEE Transactions on Power Electronics*, vol. 21, no.1, pp. 263-272, 2006.

[121] *IEEE Recommended Practices and Requirements for Harmonic Control in Electrical Power Systems*, IEEE Std 519-1992, p. 0_1, 1993.

[122] "Proposed terms and definitions for flexible AC transmission system (FACTS)," *IEEE Transactions on Power Delivery,* vol. 12, pp. 1848-1853, 1997.

[123] H. P. Beck and R. Hesse, "Virtual synchronous machine," in Electrical Power Quality and Utilisation, 2007. EPQU 2007. *9th International Conference* on, 2007, pp. 1-6.

[124] J. Driesen and K. Visscher, "Virtual synchronous generators," in Power and Energy Society General Meeting - *Conversion and Delivery of Electrical Energy in the 21st Century*, 2008 IEEE, 2008, pp. 1-3.

[125] Q. C. Zhong and G. Weiss, "Static synchronous generators for distributed generation and renewable energy," in *2009 IEEE/PES Power Systems Conference and Exposition*, 2009, pp. 1-6.

[126] Z. Qing-Chang and G. Weiss, "Synchronverters: Inverters That Mimic Synchronous Generators," *Industrial Electronics, IEEE Transactions on*, vol. 58, pp. 1259-1267, 2011.

[127] L. Zhang, L. Harnefors, and H. P. Nee, "Power-Synchronization Control of Grid-Connected Voltage-Source Converters," *IEEE Transactions on Power Systems,* vol. 25, pp. 809-820, 2010.

[128] F. Blaabjerg, R. Teodorescu, M. Liserre, and A. V. Timbus, "Overview of Control and Grid Synchronization for Distributed Power Generation Systems," *IEEE Transactions on Industrial Electronics,* vol. 53, pp. 1398-1409, 2006.

[129] P. Rodriguez, J. Pou, J. Bergas, J. I. Candela, R. P. Burgos, and D. Boroyevich, "Decoupled Double Synchronous Reference Frame PLL for Power Converters Control," *IEEE Transactions on Power Electronics,* vol. 22, pp. 584-592, 2007.

[130] A. Luna, J. Rocabert, J. I. Candela, J. R. Hermoso, R. Teodorescu, F. Blaabjerg, and P. Rodríguez, "Grid Voltage Synchronization for Distributed Generation Systems Under Grid Fault Conditions," *IEEE Transactions on Industry Applications,* vol. 51, pp. 3414-3425, 2015.

[131] Z. Qing-Chang, N. Phi-Long, M. Zhenyu, and S. Wanxing, "Self-Synchronized Synchronverters: Inverters Without a Dedicated Synchronization Unit," *Power Electronics, IEEE Transactions on*, vol. 29, pp. 617-630, 2014.

[132] Z. Qing-Chang and N. Phi-Long, "Sinusoid-locked loops based on the principles of synchronous machines," *in Control and Decision Conference* (CCDC), 2012 24th Chinese, 2012, pp. 1518-1523.

[133] S. D. Arco and J. A. Suul, "A synchronization controller for grid reconnection of islanded virtual synchronous machines," in *2015 IEEE 6th International Symposium on Power Electronics for Distributed Generation Systems (PEDG)*, 2015, pp. 1-8.

[134] I. Cvetkovic, D. Boroyevich, R. Burgos, C. Li, and P. Mattavelli, "Modeling and control of grid-connected voltage-source converters emulating isotropic and anisotropic synchronous machines," in *2015 IEEE 16th Workshop on Control and Modeling for Power Electronics (COMPEL)*, 2015, pp. 1-5.

[135] I. Cvetkovic, D. Boroyevich, R. Burgos, Y. H. Hsieh, F. C. Lee, C. Li, and P. Mattavelli, "Experimental verification of a virtual synchronous generator control concept," in *2016 IEEE 17th Workshop on Control and Modeling for Power Electronics (COMPEL)*, 2016, pp. 1-8.

[136] M. Ashabani, F. D. Freijedo, S. Golestan, and J. M. Guerrero, "Inducverters: PLL-Less Converters With Auto-Synchronization and Emulated Inertia Capability," *IEEE Transactions on Smart Grid,* vol. 7, pp. 1660-1674, 2016.

[137] M. Amin, A. Rygg, and M. Molinas, "Self-Synchronization of Wind Farm in an MMC-Based HVDC System: A Stability Investigation," *IEEE Transactions on Energy Conversion,* vol. 32, pp. 458-470, 2017.

[138] T. V. Van, K. Visscher, J. Diaz, V. Karapanos, A. Woyte, M. Albu, et al., "Virtual synchronous generator: An element of future grids," *in Innovative Smart Grid Technologies Conference Europe* (ISGT Europe), 2010 IEEE PES, 2010, pp. 1-7.

[139] P. Rodriguez, I. Candela, and A. Luna, "Control of PV generation systems using the synchronous power controller," *in Energy Conversion Congress and Exposition* (ECCE), 2013 IEEE, 2013, pp. 993-998.

[140] P. Rodriguez, C. Citro, I. Candela, J. Rocabet, and A. Luna, "Flexible grid connection and islanding of SPC-based PV power converters," in *2015 IEEE Energy Conversion Congress and Exposition (ECCE)*, 2015, pp. 450-459.

[141] C. Verdugo, J. I. Candela, and P. Rodriguez, "Grid support functionalities based on modular multilevel converters with synchronous power control," in *2016 IEEE International Conference on Renewable Energy Research and Applications (ICRERA)*, 2016, pp. 572-577.

[142] W. Zhang, D. Remon, and P. Rodriguez, "Frequency support characteristics of grid-interactive power converters based on the synchronous power controller," *IET Renewable Power Generation,* vol. 11, pp. 470-479, 2017.

[143] D. Remon, A. M. Cantarellas, J. M. Mauricio, and P. Rodriguez, "Power system stability analysis under increasing penetration of photovoltaic power plants with synchronous power controllers," *IET Renewable Power Generation,* vol. 11, pp. 733-741, 2017.

[144] C. Li, R. Burgos, I. Cvetkovic, D. Boroyevich, L. Mili, and P. Rodriguez, "Analysis and design of virtual synchronous machine based STATCOM controller," in *2014 IEEE 15th Workshop on Control and Modeling for Power Electronics (COMPEL)*, 2014, pp. 1-6.

[145] C. Li, R. Burgos, I. Cvetkovic, D. Boroyevich, and L. Mili, "Design, analysis and experimental evaluation of a virtual-synchronous-machine-based STATCOM with LCL filter," in *2015 IEEE Energy Conversion Congress and Exposition (ECCE)*, 2015, pp. 5771-5778.

[146] C. Li, R. Burgos, I. Cvetkovic, and D. Boroyevich, "Active and reactive power flow analysis of a STATCOM with virtual synchronous machine control," in *2015 IEEE 16th Workshop on Control and Modeling for Power Electronics (COMPEL)*, 2015, pp. 1-8.

[147] N. Phi-Long, Q. C. Zhong, F. Blaabjerg, and J. M. Guerrero, "Synchronverter-based operation of STATCOM to Mimic Synchronous Condensers," in *2012 7th IEEE Conference on Industrial Electronics and Applications (ICIEA)*, 2012, pp. 942-947.

[148] M. A. Torres L., L. A. C. Lopes, L. A. Moran T, and J. R. Espinosa C, "Self-Tuning Virtual Synchronous Machine: A Control Strategy for Energy Storage Systems to Support Dynamic Frequency Control," *IEEE Transactions on Energy Conversion,* vol. 29, pp. 833-840, 2014.

[149] M. P. N. v. Wesenbeeck, S. W. H. d. Haan, P. Varela, and K. Visscher, "Grid tied converter with virtual kinetic storage," in *2009 IEEE Bucharest PowerTech*, 2009, pp. 1-7.

[150] J. Alipoor, Y. Miura, and T. Ise, "Power System Stabilization Using Virtual Synchronous Generator With Alternating Moment of Inertia," *IEEE Journal of Emerging and Selected Topics in Power Electronics,* vol. 3, pp. 451-458, 2015.

[151] Y. Hirase, K. Sugimoto, K. Sakimoto, and T. Ise, "Analysis of Resonance in Microgrids and Effects of System Frequency Stabilization Using a Virtual Synchronous Generator," *IEEE Journal of Emerging and Selected Topics in Power Electronics,* vol. 4, pp. 1287-1298, 2016

[152] W. Wu, Y. Chen, A. Luo, L. Zhou, X. Zhou, L. Yang, Y. Dong, and J. M. Guerrero, "A Virtual Inertia Control Strategy for DC Microgrids Analogized With Virtual Synchronous Machines," *IEEE Transactions on Industrial Electronics,* vol. 64, pp. 6005-6016, 2017.

[153] M. Torres and L. A. C. Lopes, "Virtual synchronous generator control in autonomous wind-diesel power systems," *in Electrical Power & Energy Conference (EPEC*), 2009 IEEE, 2009, pp. 1-6.

[154] K. Sakimoto, Y. Miura, and T. Ise, "Stabilization of a power system with a distributed generator by a Virtual Synchronous Generator function," *in Power Electronics and ECCE Asia (ICPE & ECCE)*, 2011 IEEE 8th International Conference on, 2011, pp. 1498-1505.

[155] M. Torres and L. A. C. Lopes, "Frequency control improvement in an autonomous power system: An application of virtual synchronous machines," *in Power Electronics and ECCE Asia* (ICPE & ECCE), 2011 IEEE 8th International Conference on, 2011, pp. 2188-2195.

[156] C. Yong, R. Hesse, D. Turschner, and H. P. Beck, "Improving the grid power quality using virtual synchronous machines," *in Power Engineering, Energy and Electrical Drives (POWERENG)*, 2011 International Conference on, 2011, pp. 1-6.

[157] C. Yong, R. Hesse, D. Turschner, and H. P. Beck, "Investigation of the Virtual Synchronous Machine in the island mode," *in Innovative Smart Grid Technologies* (ISGT Europe), 2012 3rd IEEE PES International Conference and Exhibition on, 2012, pp. 1-6.

[158] J. Alipoor, Y. Miura, and T. Ise, "Distributed generation grid integration using virtual synchronous generator with adoptive virtual inertia," *in Energy Conversion Congress and Exposition* (ECCE), 2013 IEEE, 2013, pp. 4546-4552.

[159] S. D'Arco and J. A. Suul, "Virtual synchronous machines- Classification of implementations and analysis of equivalence to droop controllers for microgrids," *in PowerTech* (POWERTECH), 2013 IEEE Grenoble, 2013, pp. 1-7.

[160] A. Vassilakis, P. Kotsampopoulos, N. Hatziargyriou, and V. Karapanos, "A battery energy storage based virtual synchronous generator," *in Bulk Power System Dynamics and Control* - IX Optimization, Security and Control of the Emerging Power Grid (IREP), 2013 IREP Symposium, 2013, pp. 1-6.

[161] C. Debruyne, S. Derammelaere, J. Desmet, and L. Vandevelde, "Using general synchronous machine theory to integrate PLL controller dynamics into a static power electronic converter model," *in Industry Applications Soc.Annual Meeting* (IAS), 2012 IEEE, 2012, pp. 1-7.

[162] R. Pena-Alzola, D. Campos-Gaona, and M. Ordonez, "Control of flywheel energy storage systems as virtual synchronous machines for microgrids," in *2015 IEEE 16th Workshop on Control and Modeling for Power Electronics (COMPEL)*, 2015, pp. 1-7.

[163] C. F. d. Santos, F. B. Grigoletto, and M. Stefanello, "Power quality improvement in a grid connected voltage source inverter using the concept of virtual synchronous machine," in *2015 IEEE 13th Brazilian Power Electronics Conference and 1st Southern Power Electronics Conference (COBEP/SPEC)*, 2015, pp. 1-5.

[164] D. Chen, Y. Xu, and A. Q. Huang, "Integration of DC Microgrids as Virtual Synchronous Machines into the AC Grid," *IEEE Transactions on Industrial Electronics,* vol. PP, pp. 1-1, 2017.

[165] Q. C. Zhong, "Virtual Synchronous Machines: A unified interface for grid integration," *IEEE Power Electronics Magazine,* vol. 3, pp. 18-27, 2016.

[166] I. Cvetkovic, D. Boroyevich, R. Burgos, F. C. Lee, and Q. C. Zhong, " Synchronous generator-based grid-interface converter for energy storage systems integration," *in Proceedings of the Grand Challenges on Modeling and Simulation Conference, GCMS '13*, Article No. 22, July 2013.

[167] P. Kundur, *Power System Stability and Control*, McGraw Hill, 1994.

[168] S. N. Vukosavic, *Electrical Machines*, Springer, 2013.

[169] H.F. Olson, Dynamical Analogies, 2nd ed., Van Nostrand, pp. 27–29., 1958.

[170] G. R. C. Mouli, J. H. Schijffelen, P. Bauer, and M. Zeman, "Design and Comparison of a 10-kW Interleaved Boost Converter for PV Application Using Si and SiC Devices," *IEEE Journal of Emerging and Selected Topics in Power Electronics,* vol. 5, pp. 610-623, 2017.

[171] F. Reverter and M. Gasulla, "Optimal Inductor Current in Boost DC/DC Converters Regulating the Input Voltage Applied to Low-Power Photovoltaic Modules," *IEEE Transactions on Power Electronics,* vol. 32, pp. 6188-6196, 2017.

[172] http://ab.rockwellautomation.com/Drives/PowerFlex-753.

[173] https://www.yaskawa.com/products/motion/spindle-products/spindle-motors. Mod. UAASKA.

[174] http://www.marathonelectric.com. Model MagnaPlus Synchronous Generator 283PDL1706.

[175] "IEEE Standard Procedures for Obtaining Synchronous Machine Parameters by Standstill Frequency Response Testing (Supplement to ANSI/IEEE Std 115-1983, IEEE Guide: Test Procedures for Synchronous Machines)," *IEEE Std 115A-1987,* p. 0_1, 1987.

[176] M. E. Coultes and W. Watson, "Synchronous Machine Models by Standstill Frequency Response Tests," *IEEE Transactions on Power Apparatus and Systems,* vol. PAS-100, pp. 1480-1489, 1981.

[177] J. Huang, K. A. Corzine, and M. Belkhayat, "Online Synchronous Machine Parameter Extraction From Small-Signal Injection Techniques," *IEEE Transactions on Energy Conversion,* vol. 24, pp. 43-51, 2009.

[178] B. Zhou, "d-q impedance identification in three phase systems using multi-tone perturbation," MS Dissertation, Virginia Tech, 2013.

[179] https://www.mitsubishielectric-mesh.com/products/pdf/pm100cl1a060_e.pdf.

[180] http://www.ti.com/product/TMS320C28343.

[181] http://www.latticesemi.com/Products/FPGAandCPLD/MachXO2.aspx.

[182] C. Wildrick, F. Lee, B. Cho, and B. Choi, "A method of defining the load impedance specification for a stable distributed power system," *IEEE Transactions on Power Electronics*, vol. 10, no. 3, pp. 280-285, May 1995.

[183] X. Feng, Z. Ye, K. Xing, F. Lee, and D. Borojevic, "Impedance specification and impedance improvement for DC distributed power system," in *30th Annual IEEE Power Electronics Specialists Conference*, pp. 889-894, 1999.

[184] X. Feng, J. Liu, and F. Lee, "Impedance specifications for stable DC distributed power systems," *IEEE Transactions on Power Electronics*, vol. 17, no. 2, pp. 157-162, Mar 2002.

[185] X. Wang, R. Yao, and F. Rao, "Three-step impedance criterion for small-signal stability analysis in two-stage DC distributed power systems," *IEEE Power Electronics Letters*, vol. 1, no. 3, pp. 83-87, Sep 2003.

[186] F. Liu, J. Liu, B. Zhang, and H. Zhang, "Unified stability criterion of bidirectional power flow cascade system," in *28th Annual IEEE Applied Power Electronics Conference and Exposition*, pp. 2618-2623, 2013.

[187] F. Liu, J. Liu, H. Zhang, D. Xue, and Q. Dou, "Terminal admittance based stability criterion for multi-module DC distributed system," in *IEEE Applied Power Electronics Conference and Exposition*, pp. 580-586, 2014.

[188] X. Zhang, X. Ruan, and C. Tse, "Impedance-Based Local Stability Criterion for DC Distributed Power Systems," *IEEE Transactions on Circuits and Systems I: Regular Papers*, vol. 62, no. 3, pp. 916-925, Mar 2015.

[189] http://www.ti.com/tool/sfra.

[190] Konstantin P. Louganski, "Modeling and Analysis of a DC Power Distribution System in 21st Century Airlifters," Virginia Polytechnic Institute and State University, MS Dissertation, 1999.

[191] P. A. W. Walker and A. S. Aldred, "Frequency response analysis of displacement governing in synchronous power systems," *Proceedings of the IEE - Part C: Monographs,* vol. 108, pp. 471-477, 1961.

[192] H. Woo and K. Kong, "Controller Design for Mechanical Impedance Reduction," *IEEE/ASME Transactions on Mechatronics,* vol. 20, pp. 845-854, 2015.

[193] R. Priesner and S. Jakubek, "Mechanical Impedance Control of Rotatory Test Beds," *IEEE Transactions on Industrial Electronics,* vol. 61, pp. 6264-6274, 2014.

[194] G. C. Verghese, I. J. Perez-Arriaga, and F. C. Schweppe, "Selective modal analysis with applications to electric power systems, Part II: The Dynamic Stability Problem", IEEE Trans. PAS, Vol. 101, No. 9, pp. 3126-3134, Sept. 1982.

[195] H. Hiraiwa, H. Saitoh, E. Tsukada, K. Minazawa, and J. Toyoda, "System-response-based eigenvalue estimation for on-line assessment of power system stability," in *Electric Utility Deregulation, Restructuring and Power Technologies, 2004. (DRPT 2004). Proceedings of the 2004 IEEE International Conference on*, 2004, pp. 366-371 Vol.1.

[196] T. Yonezu, T. Nitta, and J. Baba, "On-line identification of real parts of eigenvalues of power system by use of superconducting magnetic energy storage," in *Power and Energy Society General Meeting - Conversion and Delivery of Electrical Energy in the 21st Century, 2008 IEEE*, 2008, pp. 1-7.

[197] A. Pal and J. S. Thorp, "Co-ordinated control of inter-area oscillations using SMA and LMI," in *2012 IEEE PES Innovative Smart Grid Technologies (ISGT)*, 2012, pp. 1-6.

[198] D. Remon, A. M. Cantarellas, J. M. Mauricio, and P. Rodriguez, "Power system stability analysis under increasing penetration of photovoltaic power plants with synchronous power controllers," *IET Renewable Power Generation,* vol. 11, pp. 733-741, 2017.

[199] S. Paszek, A. Nocoń: The method for determining angular stability factors based on power waveforms. AT&P Journal Plus2, Power System Modeling and Control, Bratislava, Slovak Republic 2008, pp. 71-74.

[200] P. Pruski and S. Paszek, "Calculations of electromechanical eigenvalues based on instantaneous power waveforms," *Przegląd Elektrotechniczny,* vol. 90, pp. 214-217, 2014.

[201] https://venable.biz

[202] Network analyzers - https://www.keysight.com

[203] http://www.ridleyengineering.com/hardware/ap310-analyzer/intro-ap-analyzer.html

[204] V. Kaura and V. Blasko, "Operation of a phase locked loop system under distorted utility conditions," *IEEE Transactions on Industry Applications*, vol. 33, no. 1, pp. 58-63, 1997

[205] T. Caldognetto, L. D. Santa, P. Magnone, and P. Mattavelli, "Power Electronics Based Active Load for Unintentional Islanding Testbenches," *IEEE Transactions on Industry Applications,* vol. 53, no. 4, pp. 3831-3839, 2017.

[206] K. N. Areerak, S. V. Bozhko, G. M. Asher, L. D. Lillo, and D. W. P. Thomas, "Stability study for a hybrid ac-dc more-electric aircraft power system," *IEEE Trans. Aerosp. Electron. Syst*., vol. 48, no. 1, pp. 329–347, Jan. 2012.

[207] Y. Panov and M. M. Jovanovic, "Stability and dynamic performance of current-sharing control for paralleled voltage regulator modules," *IEEE Trans. Power Electron*., vol. 17, no. 2, pp. 172-179, Mar. 2002.

[208] J. Morroni, R. Zane, and D. Maksimovic, "An online stability margin monitor for digitally controlled switched-mode power supplies," *IEEE Trans. Power Electron.*, vol. 24, no. 11, pp. 2639-2648, Nov. 2009.

[209] J. Castello and J. M. Espi, "DSP implementation for measuring the loop gain frequency response of digitally controlled power converters," *IEEE Trans. Power Electron.*, vol. 27, no. 9, pp. 4113-4121, Sep. 2012.

[210] R. D. Middlebrook, "Measurement of loop gain in feedback systems," *Int. J. Electron.,* vol. 38, pp. 485–512, 1975.

[211] S.D. Sudhoff, S. F. Glover, P. T. Lamm, D. H. Schmucker, and D. E. Delisle,"Admittance space stability analysis of power electronic systems," IEEE Trans. Aerosp. Electron. Syst., vol. 36, no. 3, pp. 965–973, Jul. 2000.

Appendix

The following are the estimated transfer functions that represent terminal-behavioral model of the voltage source converter from Chapter 3 (all are reduced to the 4th order using MATLAB function *modred*).

Voltage Source Inverter mode:

$$\left[\begin{array}{c|cc} G_d & -Z_{dd} & -Z_{dq} \\ G_q & -Z_{qd} & -Z_{qq} \\ \hline Y_i & H_d & H_q \end{array}\right] \cdot \begin{bmatrix} v_{dc} \\ i_d \\ i_q \end{bmatrix} = \begin{bmatrix} v_d \\ v_q \\ i_{dc} \end{bmatrix}$$

$$G_d(s) = \frac{0.002s^4 + 501s^3 + 5.52\cdot10^5 s^2 - 2.26\cdot10^{11} s - 1.83\cdot10^{16}}{s^4 + 2.03\cdot10^4 s^3 + 5.59\cdot10^8 s^2 + 3.42\cdot10^{12} s + 3.86\cdot10^{16}}$$

$$G_q(s) = \frac{0.004s^4 - 209.6s^3 + 9.33\cdot10^6 s^2 + 4.93\cdot10^{10} s + 9.1\cdot10^{15}}{s^4 + 1.44\cdot10^4 s^3 + 4.89\cdot10^8 s^2 + 2.48\cdot10^{12} s + 3.34\cdot10^{16}}$$

$$Y_i(s) = \frac{13.44s^4 + 2.99\cdot10^5 s^3 + 9.55\cdot10^9 s^2 + 3.56\cdot10^{13} s + 2.83\cdot10^{13}}{s^4 + 4.9\cdot10^4 s^3 + 9.92\cdot10^8 s^2 + 1.75\cdot10^{13} s + 5.9\cdot10^{16}}$$

$$Z_{dd}(s) = \frac{0.3s^4 - 1.86\cdot10^5 s^3 - 6.1\cdot10^8 s^2 - 2.59\cdot10^{13} s - 5.55\cdot10^{15}}{s^4 + 3.9\cdot10^4 s^3 + 5.24\cdot10^8 s^2 + 4.91\cdot10^{12} s + 3.63\cdot10^{16}}$$

$$Z_{dq}(s) = \frac{-0.009s^4 + 898s^3 - 2.57\cdot10^7 s^2 - 2.18\cdot10^{10} s + 1.17\cdot10^{11}}{s^4 + 3838s^3 + 8.19\cdot10^7 s^2 + 7.22\cdot10^{10} s + 3.5\cdot10^{11}}$$

$$Z_{qd}(s) = \frac{0.001s^4 + 3796s^3 - 3.09\cdot10^7 s^2 - 1.92\cdot10^{11} s + 1.33\cdot10^{11}}{s^4 + 7135s^3 + 8.5\cdot10^7 s^2 + 2.9\cdot10^{11} s + 1.4\cdot10^{12}}$$

$$Z_{qq}(s) = \frac{-0.84s^4 - 1.97\cdot10^5 s^3 - 1.94\cdot10^{10} s^2 - 4.28\cdot10^{13} s - 2.79\cdot10^{13}}{s^4 + 1.6\cdot10^5 s^3 + 3.65\cdot10^9 s^2 + 3.2\cdot10^{13} s + 1.6\cdot10^{14}}$$

$$H_d(s) = \frac{0.004s^4 + 1923s^3 - 2.98\cdot10^7 s^2 - 5.36\cdot10^{11} s - 1.36\cdot10^{10}}{s^4 + 1.5\cdot10^4 s^3 + 1.4\cdot10^8 s^2 + 1.11\cdot10^{12} s + 2.6\cdot10^{10}}$$

$$H_q(s) = \frac{3.1\cdot10^{-5} s^4 + 5560s^3 - 9.25\cdot10^8 s^2 + 2.18\cdot10^{13} s + 1.6\cdot10^{14}}{s^4 + 7.8\cdot10^5 s^3 + 4.11\cdot10^9 s^2 + 8.6\cdot10^{13} s + 6.3\cdot10^{14}}$$

Active Rectifier mode:

$$\left[\begin{array}{cc|c} G_d & G_q & -Z_o \\ \hline Y_{dd} & Y_{dq} & H_d \\ Y_{qd} & Y_{qq} & H_q \end{array}\right] \cdot \begin{bmatrix} v_d \\ v_q \\ i_{dc} \end{bmatrix} = \begin{bmatrix} v_{dc} \\ i_d \\ i_q \end{bmatrix}$$

$$G_d(s) = \frac{0.012s^4 - 128s^3 - 1.86\cdot10^4 s^2 - 2.76\cdot10^5 s + 3.84\cdot10^7}{s^4 + 619s^3 + 8.2\cdot10^4 s^2 + 7.26\cdot10^6 s + 2.05\cdot10^8}$$

$$G_q(s) = \frac{0.009s^4 + 42.78s^3 - 472.9s^2 + 1.85\cdot10^5 s - 9.39\cdot10^6}{s^4 + 412.4s^3 + 3.48\cdot10^4 s^2 + 2.03\cdot10^6 s + 8.34\cdot10^7}$$

$$Z_o(s) = \frac{-0.44s^4 - 1830s^3 - 4109s^2 - 1308s - 27.36}{s^4 + 174.6s^3 + 1.15\cdot10^4 s^2 + 2.33\cdot10^4 s + 273.3}$$

$$Y_{dd}(s) = \frac{-0.27s^4 - 106s^3 + 3.71\cdot10^4 s^2 + 1.84\cdot10^6 s + 1.31\cdot10^8}{s^4 + 3210s^3 + 6.4\cdot10^5 s^2 + 3.44\cdot10^7 s + 1.9\cdot10^9}$$

$$Y_{dq}(s) = \frac{0.02s^4 - 78.7s^3 - 4.86\cdot10^4 s^2 - 9.86\cdot10^5 s - 1.89\cdot10^8}{s^4 + 2004s^3 + 6.87\cdot10^5 s^2 + 2.29\cdot10^7 s + 2.48\cdot10^9}$$

$$Y_{qd}(s) = \frac{0.01s^4 - 74.27s^3 - 4.74\cdot10^4 s^2 - 1.11\cdot10^6 s - 1\cdot10^8}{s^4 + 1673s^3 + 5.36\cdot10^5 s^2 + 1.35\cdot10^7 s + 1.04\cdot10^9}$$

$$Y_{qq}(s) = \frac{-0.12s^4 - 46.6s^3 - 1180s^2 - 1.61\cdot10^5 s - 1.27\cdot10^6}{s^4 + 714.9s^3 + 3.3\cdot10^4 s^2 + 3.06\cdot10^6 s + 2.38\cdot10^7}$$

$$H_d(s) = \frac{118.7s^3 + 1.23\cdot10^5 s^2 + 1.29\cdot10^7 s + 8.37\cdot10^6}{s^4 + 641.4s^3 + 1.07\cdot10^5 s^2 + 7.63\cdot10^6 s + 4.9\cdot10^6}$$

$$H_q(s) = \frac{-77.6s^3 - 5.04\cdot10^4 s^2 - 2.28\cdot10^6 s - 4.77\cdot10^6}{s^4 + 401.8s^3 + 5.84\cdot10^4 s^2 + 2.4\cdot10^6 s + 5.02\cdot10^6}$$